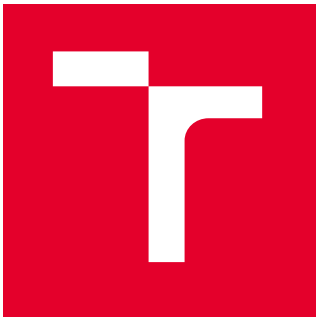

BRNO UNIVERSITY OF TECHNOLOGY

VYSOKÉ UČENÍ TECHNICKÉ V BRNĚ

FACULTY OF MECHANICAL ENGINEERING

FAKULTA STROJNÍHO INŽENÝRSTVÍ

INSTITUTE OF MATERIALS SCIENCE AND ENGINEERING

ÚSTAV MATERIÁLOVÝCH VĚD A INŽENÝRSTVÍ

INTERACTION OF PULSATING WATER JET WITH SURFACE OF STRUCTURAL MATERIALS

INTERAKCE PULSUJÍCÍHO VODNÍHO SVAZKU S POVRCHEM KONSTRUKČNÍCH MATERIÁLŮ

DOCTORAL THESIS

DIZERTAČNÍ PRÁCE

AUTHOR — **Ing. Jakub Poloprudský**

AUTOR PRÁCE

SUPERVISOR — **prof. Mgr. Tomáš Kruml, CSc.**

ŠKOLITEL

BRNO 2024

Abstract

The pulsating water jet (PWJ) is a hybrid technological modification of the continuous water jet (CWJ) working at the principle of impact pressure. PWJ is created by splitting the coherent stream of water into discrete clusters. The clusters create the so-called water hammer effect, which significantly increases the effectivity of erosion of the material subjected to PWJ. This work deals with the interaction of water clusters created by the PWJ with the surface of selected structural materials. The work focuses on the incubation erosion stage before the start of the material removal. The experimental materials used were austenitic 316L stainless steel and aluminium alloy AW-2014, due to their excellent corrosion resistance in tap water environment and their homogeneity and low hardness respectively. Both of these materials are according to literature review common for waterjet focused research. The PWJ is a novel technology with several technological parameters, which offers the potential for technology optimization and opens questions about its possibilities and limitations. The individual clusters of water are expected to act upon the surface in a similar way as liquid droplets. Under this approximation, the technology is currently a candidate for use as an erosion testing tool. The advantages of PWJ erosion testing compared to conventional erosion testing tools are the high frequency of impacts and control over the impact speed, droplet size, angle of droplet impacts and impact frequency.

The work focuses on the incubation erosion stage, which is the stage prior to macroscopic material removal. The incubation stages consist of plastic deformation of the material, surface deformation exposing the grain boundaries and the creation of surface steps. The goal is to tune the use of PWJ technology for erosion testing, surface roughening and surface strengthening. The main findings are as follows:

- 316L stainless steel and AW-2014 were treated with PWJ moving along a linear trajectory with different levels of pressure and cluster impact distribution. The influence of cluster impact distribution on the erosion stage was evaluated.
- The static PWJ with increasing erosion time was done on 316L steel. The subsurface changes corresponding with surface changes were documented using transmission electron microscopy. A new erosion stage was proposed between material roughening and macroscopic material removal stages. This stage precedes the formation of micropits and is defined by the presence of cracks at preferential sites.
- The surface hardening of 316L steel was measured on cross-sections after PWJ treatment. Hardening up to depth of 100 μm was observed before significant material removal started.
- A substantial increase of the fatigue life of 316L steel specimen after treatment by PWJ was found. This is a quite interesting and original finding, opening the possibility of developing a new way for surface engineering. The dependence between PWJ the feed rate and a number of cycles to failure was measured for two strain levels within the experimental design.
- Electron back scattered diffraction measurement was done before and after PWJ treatment. Changes in grain orientation were measured and kernel average misorientation was evaluated. The proposal of this new methodology for erosion incubation stage observation is the highlight of this work.

Keywords: Erosion, Wear, Plastic deformation, Water cluster, Pulsating water jet, Surface hardening, Surface roughening

Abstrakt

Pulzní vodní svazek je modifikace konvenčního kontinuálního vodního svazku. Principem technologie je vyvolání rozpadu koherentního vodního proudu na jednotlivé shluky vodních kapek. Shluky působí v momentě dopadu na povrch impaktním tlakem, což významně zvedá erozní vlastnosti proudu. Práce studuje interakci pulzního vodního svazku s povrchem konstrukčních materiálů. Práce se zaměřuje zejména na inkubační erozní etapa. Inkubační erozní etapa se projevuje plastickou deformací povrchu bez přítomnosti makroskopického úběru materiálu. Experimentální typy materiálů jsou austenitické korozivzdorná ocel 316L a hliníková slitina AW-2014. Pulzující vodní proud je poměrně nová technologie s množstvím propojených technologických parametrů. Množství parametrů poskytuje velký prostor pro optimalizaci technologie v závislosti na použití. Předpokládá se, že vodní shluky svazku působí na povrch podobně jako vodní kapky. Na základě tohoto zjednodušení se nabízí použití technologie na testování erozní odolnosti materiálů. Výhoda technologie oproti konvenčním metodám testování eroze je vysoká frekvence dopadu kapek až 40 kHz a možnost kontrolovat rychlost, velikost, úhel a frekvenci dopadajících kapek.

Zaměřením práce je zkoumání inkubačního erozního stádia předcházejícího úběru materiálu. Eroze se v tomto stádiu projevuje zdrsňováním povrchu v důsledku plastické deformace materiálu, deformací zrn vedoucímu k odhalování hranic zrn a vytváření povrchového reliéfu uvnitř zrn. Cílem práce je naladění a porozumění fungování pulzního vodního svazku a možné použití technologie pro erozní testování, zdrsňování a zpevňování povrchu. Hlavní dosažená zjištění jsou následující:

- Závislost změny distribuce dopadů vodních kapek s několika úrovněmi hydraulických parametrů byla pozorována na obou experimentálních materiálech (hliníková slitina AW-2014 a austenitická ocel 316L). Závislost distribuce dopadů vodních kapek na erozní efektivitu a erozní stádium byla popsána.
- Statické erozní testy byly provedeny na oceli 316L. Byly měřeny změny profilu způsobené interakcí s PWJ Podpovrchové změny korespondující se změnami povrchovými byli pozorovány pomocí transmisního elektronového mikroskopu. Bylo definováno erozní stádium mezi zdrsňováním povrchu a makroskopickým úběrem materiálu. Definováno bylo přítomností nespojitých mikro trhlin koncentrujících se zejména na hranicích zrn.
- Zpevňování povrchu oceli 316L bylo měřeno na řezu kolmém k ovlivněnému povrchu. Zpevnění bylo pozorované až do hloubky 100 μm, a předcházelo makroskopickému úběru materiálu.
- Nárůst únavové životnosti oceli 316L byl změřen po zpracování povrchu pomocí pulzujícího vodního svazku. V rámci zvolených experimentálních parametrů byla pozorována závislost rychlosti přejezdu pulzujícího vodního svazku a počtu cyklů do lomu pro dvě zkoumané úrovně řízené celkové deformace.
- Metodologie měření pomocí difrakce zpětně odražených elektronů před a po zpracování povrchu oceli 316L pulzním vodním svazkem byla použita. Metodologie umožňuje měřit vývoj změn v orientaci a deformace uvnitř konkrétních zrn. Otestování metodologie je hlavní příspěvek této práce.

Klíčová slova: Eroze, Opotřebení, Plastická deformace, Kapka vody, Pulzující vodní svazek, Zpevňování povrchu, Zdrsňování

Bibliography of the Thesis

POLOPRUDSKÝ, Jakub. *Interakce pulsujícího vodního svazku s povrchem konstrukčních materiálů.* Brno, 2024. Dostupné také z: https://www.vut.cz/studenti/zav-prace/detail/154870. Dizertační práce. Vysoké učení technické v Brně, Fakulta strojního inženýrství, Ústav materiálových věd a inženýrství. Vedoucí práce Tomáš Kruml.

Declaration

The figures presented in State of the art from literature are reused with permission based on one of the following:

-Agreement between the author and the publisher (Elsevier, Springer Nature, etc.) provided by Copyright Clearance Center:

Fig. 1	Fig. 2	Fig. 9	Fig. 10	Fig. 12	Fig. 13	Fig. 16	Fig. 17	Fig. 18	Fig. 19	Fig. 20	Fig. 23	Fig. 24	Fig. 25	Fig. 28	Fig. 29	Fig. 33

-Based on open access Creative Common CC BY licence:

Fig. 4	Fig. 14	Fig. 15	Fig. 22	Fig. 30	Fig. 31	Fig. 32	Tab. 1

-Personal agreement:

Fig. 21	Fig. 26	Fig. 27

-Retained author/coauthor right to reuse in thesis (Elsevier policy):

Fig. 8

- Original figures schematics based on information gathered during literature review

Fig. 3	Fig. 5	Fig. 6	Fig. 7	Fig. 11	Tab. 2	Tab. 3

The figures presented in experiment, results, and discussion are either reused based on Elsevier's right of authors of articles to include parts of it in thesis, or original work unpublished work.

I declare that I am the author of this doctoral thesis with topic INTERACTION OF PULSATING WATER JET WITH SURFACE OF STRUCTURAL MATERIALS. The thesis has been prepared under the guidance of my supervisor. The reported results are the outcome of original research conducted during my PhD study and consultations with experts in the field. I quoted all the resources including my own publications. The references are provided at the end of this thesis.

……

Brno, 30.4.2024 Jakub Poloprudský

Acknowledgement

I would like to express my gratitude to number of people who supported me through my strenuous doctoral studies. Firstly, I would like to thank my supervisor Prof. Mgr. Tomáš Kruml, CSc for his supervision during the whole study and his patience with all my ideas. I would also like to thank my supervisor specialist Ing. Ivo Kuběna, Ph.D. for his mental support during finishing of this thesis and to Ing. Alice Chlupová, Ph.D. for teaching me how to use scanning electron microscopy and how to organize my work. I also have to thank the rest of the low cycle fatigue group and Institute of Physics of Materials for inspiring and friendly environment.

I would also like to thank colleagues from the Institute of Geonics for allowing me access to Pulsating water jet technology and for numerous discussions about the results and future development. Namely I would like to thank Prof Sergej Hloch, Ing. for great leadership and theory explanation, Nag Akash, Ph.D. for discussing results and waterjet theory beyond my comprehension, Ing. Dagmar Klichová, Ph.D. for explaining to me metrology, Ing Gabriel Stolárik for perfect control of the PWJ machine allowing me to design very precise experiments, and all the other colleagues from the Fluid jets department.

I would also like to my family and especially my wife who has been with me, as the deadline for thesis was approaching and my anxiety was growing, and still somehow didn’t leave me.

Content

1. Introduction

The interaction of liquid droplets with the surface of structural materials leads to the start of the erosion process that changes surface properties of the materials. These changes caused by liquid droplet impacts are usually considered as a degradation phenomenon, but as shown in this Thesis, when applied in a controlled manner they may become effective way of targeted surface disintegration or modification. Droplet erosion is considered as an phenomenon which decreases the service life of engineering components such as wind turbine blades [1, 2], steam turbine blades [3], aircraft leading edges [4], steam pipes in nuclear power plants [5–7], etc. These surface changes caused by repeated water droplet impact can lead to material loss and cause potential failures. This is especially prevalent in the energy or transport industry. Repeated straining of the surfaces in contact with atmospheric liquid droplets at increased speed can lead even to surface material removal. This is problematic when a shape of the surface is of importance. Aerodynamic shape degradation of the steam turbine blades caused by erosion in combination with corrosion, leads to loss of its nominal power [8]. This is historically the reason why the research of the interaction of water droplets with surface started.

The same effect of a continuous stream of water or discrete water clusters impinging the surface can be used for controlled material disintegration, which is driving idea behind water jet technology. The effect of the water jet can be enhanced by an addition of abrasives [9–11] or by splitting continuous jet into discrete clusters. Controlling the parameters of water jet and therefore water clusters speed, the interaction can lead to surface roughening or hardening. Both hardening and roughening can be used to create functional surfaces. The hardening can be used for a treatment of welds [12], 3D printed materials or increasing of fatigue life of components. An example of highly complex and functional roughening is a preparation of human implants [13], where a rougher surface promotes osseointegration.

The effect of pulsating water jet (PWJ) (i.e. the jet broken in clusters and drops) is substantially stronger in comparison with continuous water jet (CWJ). Several types of approaches to create pulsating water jet exists. In this work, the formation of liquid clusters is achieved by the piezoelectric sonotrode induced PWJ device. The sonotrode creates pressure fluctuations in the chamber with pressurized water and these are transformed into velocity fluctuations when water jet leaves the nozzle. The velocity fluctuations lead to separation of the jet into the clusters of droplets [14]. The discrete clusters then cause repeated water hammer effect on the surface of treated material. The impact pressure caused by clusters is significantly higher than the Bernoulli stagnation pressure [15]. The repeated increase in pressure upon the material surface leads to changes in the surface and with increased time exposure even material removal. The PWJ technology shows significant increase in erosion intensity compared to CWJ. Currently water jet disintegration effectivity on hard materials is in industry mostly increased by addition of the abrasives. This is called Abrasive water jet (AWJ) which is a highly universal and widely used technology [16]. The abrasive use carries some disadvantages such as abrasive cost [17] and material contamination by grit embedment [18]. That is why disintegration of continuous jet is a promising alternative to AWJ which deserves detailed study.

The experimental part of this work is divided into two experimental sets:

Experimental set 1

- Parametric optimization
  The technology shows several new challenges and need tuning of several technology parameters. One of the main intricacies of the technology is the dependence of standoff distance (distance between the nozzle and material´s surface) on both hydraulic and the acoustic parameters of the process. The first experimental part of this work focuses on tuning the standoff distance for 316L stainless steel. Ideal standoff distance was established using stairs trajectory. Pressures set in the acoustic chamber were 30, 40, 50, and 60 *MPa*.
- Surface hardening
  PWJ was tested with a sonotrode frequency of 40 *kHz* and increasing exposure time. PWJ technology allows recalculation of exposure time (clusters impact per second) into feed rate (relative movement of the jet and the specimen,). Test of the various feed rate (1-40 *mm/s*) and pressure (20,40 *MPa*) were done on an aluminium alloy. The aluminium was chosen based on its low hardness. The low hardness makes it very responsive to changes in jet parameters.

Experimental set 2

The set of experiments was done with the pressure of 50 *MPa* at the frequency of 40*kHz*. The erosion stages range from initial material deformation to significant material removal. Austenitic 316L steel was used.

- Improving the fatigue life
  Based on the knowledge of erosion stages, the PWJ treatment of 316L steel fatigue samples was done with the aim to strengthen the surface and thus enhance the fatigue life of the material. It was shown that the experiment with the increasing number of impacts/mm led to a systematic increase in fatigue life. It is proposed that such treatment can be an alternative to the shot peening procedure.
- Time exposure experiment
  Surface was treated by PWJ with exposure time ranging from incubation erosion period to stages of material removal. In this work the focus is on early erosion stages that can be used for surface modification. The surface modifications achieved can be surface hardening or surface roughening. Both of these effects were observed in this work. The surface hardening focuses can prevent crack initiation and therefore increase the fatigue life of many technical components. The surface roughening is a critical step in the preparation of bioactive implants.
- Incubation erosion stage measurement
  The time exposure experiment was repeated only within the incubation interval. Since most of the works evaluate incubation only by surface profilometry, method for surface layer deformation is proposed. The method uses electron back scatter diffraction (EBSD) measurement before and after PWJ exposure on the same marked spot. This allows qualificative observation of changes in grain orientation and misorientation inside the grains. The EBSD measurement can be evaluated statistically to gain quantitative information about eroded areas.

2. State of the art

2.1. Droplet Erosion

The erosion phenomena are explained in this chapter. Then the various approaches for the PWJ technology are discussed. The erosion as an effect of liquid impinging solid is explained by the means of operating damage mechanisms. Conventional erosion testing tools are introduced. This chapter concludes with an overview of erosion mechanisms for model materials.

2.1.1 Droplet impact on surface

The research of water drop impact on the solid surface at the beginning of the last century was motivated by the erosion it caused and was treated as a negative effect. One of the first modern research [8] was driven by the loss of effectivity of steam turbines due to impact caused geometry changes. One of the earliest experimental results came from the observation of erosion of Parsons type steam turbine. The observation showed that the erosion was caused by water drops carried in the steam onto the turbine blades [19]. The pioneering research in the erosion mechanisms was done by Hancox and Brunton [20–22]. **Figure 1** shows testing machine used at these times consisting of spinning disc with a sample attached and a waterjet. With each rotation of the disc the sample was subjected to short impact by the waterjet. The erosion testing devices were made for the understanding of turbine erosion mechanisms [8]. It should be noted that similar type of spinning disc is still frequently used for erosion testing with only minor adjustments [23–25]. There are two main disadvantages of these types of devices. 1) the sample is submitted to tangential forces when running through the jet and therefore it's not simple uniaxial impact. 2) The number of impacts and frequency of impacts are connected to the number of rotations of the disc.

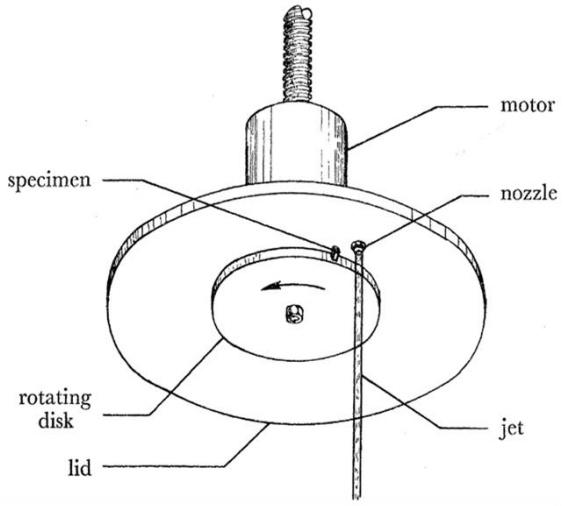

Figure 1 Schematics of early erosion testing machines a) wheel and jet apparatus used by Hancox and Brunton [20]

Using the wheel and jet apparatus Hancox and Brunton [20] described the mechanism of erosion in brittle polymers and ductile metals under various impact conditions. Wheel driven by an electric motor at 9000 rotations per minute (*rpm*) was driving the sample through water jet once per rotation. This results in 150 hits per second. Hancox divided tested materials into two categories, the first category fails in brittle manner in tension and the second category deform plastically in shear. The brittle materials fail under impact of water due to the propagation of

cracks from surface flaws. The stress levels necessary for propagation of these cracks are often lower compared to macroscopic breaking stress. Some materials, namely ceramics and inorganic single crystals, showed critical impact velocity under which no evident erosion was observed. In the case of ductile materials (metals), creation of surface depressions is the first significant surface change caused by erosion. With further impact, the depression gets deeper until material removal starts by ductile tearing or brittle fractures. Materials in this group that show good resistance to erosion have high hardness and yield strength homogenously distributed across the surface [20]. Experiments showed significant erosion dependence on the velocity of the droplets. Thomas and Brunton [21] created experimental curves for metallic materials showing a dependency of the impact velocity of the droplets with a number of impacts. These curves show similitude between the erosion and the fatigue [21]. The ability of water droplets to exceed the yield strength of metallic materials was of concern. Cook proposed a theory, that the pressure generated at the surface by water droplet moving by finite velocity is largely different from that produced by a steady stream moving at the same velocity [15]. The transient pressure created at the exact moment when the liquid droplet hits the surface is significantly higher than the Bernoulli stagnation pressure. One of the first calculations of this impact pressure was proposed by Cook [15], this phenomenon is called the water hammer effect. Cook defined the water hammer effect as follows: "The pressure generated on an element of the surface at its first encounter with water moving at finite velocity is different from that produced by the steady impact of a moving stream of water at the same velocity" [15]. When the moving column of water is abruptly stopped by a fixed surface, there is a sudden break of the front layer of the water column. If no layer of gas to cushion the blow is present, the velocity energy of the front of the column is transformed into the potential energy of the impact. The generated pressure is only limited by the slight compressibility of the impacted solid and the liquid medium [15].

The kinetic energy of the impacting water column is calculated by the Eq. (1):

$$E_k = \frac{1}{2}\rho v^2 \Delta h \tag{1}$$

where v is the water velocity, ρ is water density and Δh is the thickness of the layer of the water column [15]. This energy is then converted into potential energy, which is given by Eq. (2):

$$E_p = \frac{1}{2}\beta p^2 \Delta h \tag{2}$$

where β refers to compressibility and p is the pressure of the water column [15]. After considering that $\mathrm{E_p} = \mathrm{E_k}$, the pressure at the time of impact (water hammer pressure) can be calculated [15] by Eq. (3):

$$p_{WH} = v\sqrt{\rho/\beta} \tag{3}$$

The water hammer pressure Eq. (3) can be expressed as a means of the velocity of the compression wave [20] by Eq. (4):

$$p_{WH} = \rho C v \tag{4}$$

where *C* is the velocity of the compression wave in the liquid. When the continuous stream hits the solid surface, the stagnation pressure (p_S) applies [14] according to Eq. (5):

$$p_S = \frac{1}{2}\rho v^2 \tag{5}$$

The water hammer Eq. (4) includes the velocity of the water multiplied by the velocity of the compression wave in a given liquid and the liquid density. The stagnation pressure is square of the velocity of impinging water multiplied by the density of the liquid. From the comparison of p_{WH} and p_S, it follows that the water hammer effect is more dominant at lower speeds of impinging liquid. Another important finding from Eq. (3) is that the water hammer pressure itself is not influenced by the thickness of the layer or droplet *(*Δh). The thickness of the layer (Δh) affects the timespan of water hammer pressure in the case of droplets, as well as the size of the affected area. The equations above can be applied to droplets of regular spherical shape. In the case of the irregular shape of droplets there is a possibility that a small empty space is created between the front of the droplet and the impacted material. This would lead to the creation and collapse of the cavity on the impacted surface which would lead to much larger pressures in the impacted area [15]. Irregular droplets can be expected in several cases. There is not enough time for surface tension to fully form a spherical drop [15]. In natural conditions it is often caused by droplet size. In the case of larger droplet size, the droplet becomes unstable and creates a parachute shape and can shatter into smaller droplets [1].

The simplified water hammer Eq. (4*)* does not consider the effect of compressible deformation of the solid surface. The effect of the impacted solid deformation on the resulting water hammer pressure is considered [20] in Eq. (6):

$$p_{WH} = \rho C v \left[\frac{\rho_s C_s}{\rho_s C_s + \rho C}\right] \tag{6}$$

where ρ_s is the density in the impacted solid and C_s is the compression wave velocity in the impacted solid [20].

Calculations of the radius of the area affected by the water hammer effect were based on geometry analysis of the curved profile of the liquid front considering -spherical drop. The basis of the geometry analysis is shown in **Figure 2**. The line A-O is a flat solid surface moving - relatively to the drop - upwards at the speed of v. Curve O-B is the wave front of a spherical drop. Point B is the point where the rigid surface (the distance |AB|) meets the compression wave which propagates through the liquid at velocity C the distance of |OB|. Therefore, at a point closer to a solid surface than B such is the case for B′, the surface arrives in contact with waterfront before the stress wave. At a point further away however, the opposite is true. For the outward flow to start, the compression wave must reach the edge of the drop. Since at all points in the distance |AB| the solid surface reaches the edge of the drop first, the liquid in this region is compressed which results in high pressure in the area. The radius of the area is then given by the distance |AO|. This radius is affected by water hammer pressure and can be calculated [26] by Eq. (7):

$$|AO| = \frac{2rv}{C}[1 - v^2/C^2]^{\frac{1}{2}} \tag{7}$$

This solution only considers stress waves propagated from point O. Stress waves are propagating from all contact points. It is necessary to define new point B_f as the nearest point to O at which stress waves arrive at the same point as the solid surface. The point B_f is closer to point O than the original point B. The location of point B_f is the inclination α makes a tangent with the curve of the waterfront. This can be seen in **Figure 2** from which inclination can be calculated as $(\sin^{-1}(V/C)$. The radius of the line between B_f and O is then given [26] by Eq. (8):

$$x_0 = Rv/C \tag{8}$$

where x_0 is the radius of the area affected by the water hammer effect and R is the radius of impacting drop [26].

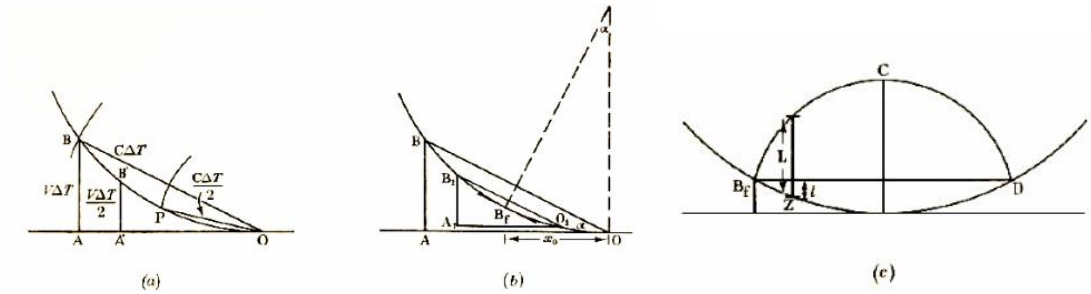

Figure 2 Schematic of curved waterfront interacting with the solid surface [26]

The duration of the water hammer effect for the spherical or cylindrical shape of the drop can be calculated [21] based on Eq.9:

$$T = \frac{R}{v}\left[1 - \sqrt{\left(1 - \frac{v^2}{C^2}\right)}\right] \tag{9}$$

after this time passes, the velocity wave reaches the edge of the droplet before solid surface and lateral outflow begins. The pressure falls to stagnation pressure calculated by Eq. (5). The schematic of pressure development for water column compared to repeated droplet impact is shown in **Figure 3**.

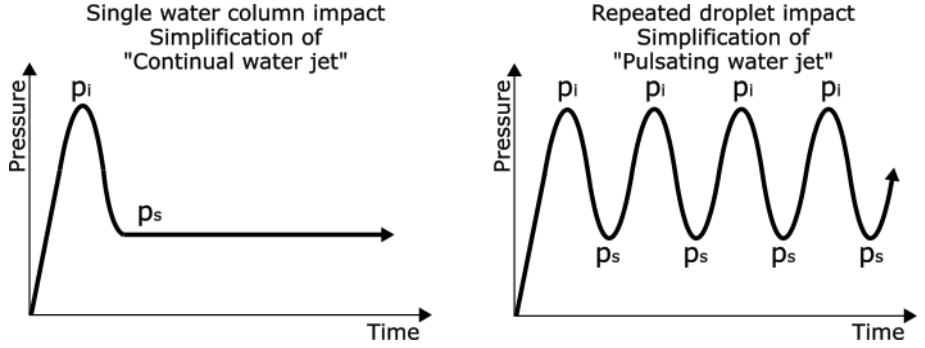

Figure 3 Pressure development based on time comparison of single water column impact and repeated droplet impact. Pressure developments can be under simplification assigned to continuous water jet and pulsating water jet

2.1.2 Droplet erosion

The forces causing deformation during impact of liquid drop and solid surface can be divided into initial load normal to the solid surface caused by fast deceleration of the droplet. The duration of the normal load can be calculated by Eq. (9). This is followed by shear force acting on surface caused by rapid outflow of liquid away from the impact point.

The first stage, known as the initial compressible stage, is the transient time when the droplet first hits the solid surface and behaves in a compressible manner [26]. The region of the compressed liquid is on the interface between solid and liquid. The compression is caused by the expansion of the contact periphery between liquid and solid which is faster than the motion of the shock front. This creates the high pressure on the impacted surface of the solid most referred to as water-hammer pressure.

The second stage called lateral outflow begins when the shock front reaches the edge of the solid/liquid interface. At this point, the release of compressed liquid starts. The release causes the high-velocity flow of liquid in the radial direction. The velocity of lateral flow is significantly higher than flow velocity in the impinging direction. The lateral outflow propagates from the solid/liquid interface. This can cause the material removal of uneven surfaces [27]. After these initial effects are depleted then the Bernoulli stagnation pressure takes place [28]. These two transient effects are the cause of four general erosion mechanisms of water droplets repeatable impinging solid surfaces. The erosion mechanisms divided by [28] are as follows:

1) Impact pressure, which describes the effect of repeated high water-hammer pressure acting on the surface of the material during the compressible stage. This loading is transient and dynamic. The erosion damage is then different based on the material properties. Surface depressions evolve in ductile materials while brittle materials usually show surface and subsurface damage due to tensile fractures.

2) Stress wave propagation is the second source of erosion damage. The high-pressure acting on the surface during the compressible stage creates stress waves propagating into the material (compression, shear, and Rayleigh). These waves then can interact with material structure, in-homogeneities, or grain boundaries, which can introduce tensile loading that could lead to further erosion damage.

3) The lateral outflow jetting is a phenomenon caused by high-velocity flow released during the secondary flow stage. The high-velocity lateral flowing can then interact with surface irregularities and create cracks or plastic deformation. The most important factors for this type of damage are believed to be surface roughness (profile) and velocity of the flow.

4) Hydraulic penetration governs the changes in the surface geometry of the solid due to the establishment of erosion pits or cracks, which then act as stress concentrators. These concentrators are the cause of accelerated erosion and tunnelling into the material [28].

It is important to note that lateral outflow jetting and hydraulic penetration modes require the presence of pre-existing cracks or surface irregularities. This means, that on flat polished material surfaces direct deformation and stress wave propagation are the most contributing effects [28].

2.1.3 Erosion conditions and testing tools

Considering water hammer pressure and erosion mechanisms even rain in natural conditions is a phenomenon worth to be examined. This problem is especially prevalent when water drop impinges surface rotating or moving at high speeds. Examples of linear movement based erosion are found in aviation [4], such as plane exterior or leading edge of plane wings. An example of erosion of rotating blades may be found in the energy industry. A highly researched topic is the erosion resistance of composite wind turbine blades [1, 2, 29, 30]. Water droplet erosion of corrosion resistant steels is also an important topic, due to their usage in steam turbines [3]. Different water droplet impact conditions affecting industrial applications were summarized in the review conducted by Ibrahim and Medraj [2]. Their summary is depicted in **Table 1**. Numerous types of erosion testing facilities are used to either simulate impact conditions during service or provide accelerated erosion tests by for example increasing impact speed or increasing the frequency of impacts.

Table 1 Droplet impact conditions in selected applications. Modified table from review by Ibrahim and Medraj [2].

Application	Affected Part	Impact speed	Droplet diameter	Ref
[-]	[-]	[mm/s]	[μm]	[-]
Steam Turbine	Blades of the low pressure stage	400-900	50-400	[3, 31, 32]
Gas Turbine	Compressor blades	100-600	200-600	[33]
Wind Turbine	The outer power producing part	70-150	500-5 000	[1, 29]
Nuclear power plant	Cooling pipes	~200	60-80	[34]
Aero engine	Fan blade	200-400	1 000 – 5 000	[35]
Civil airplanes	Rain erosion of different part	~250	1 000 – 5 000	[4]

Ibrahim and Medraj [2] divided, in their review, the erosion testing facilities into several categories shown in **Figure 4**. Ultrasonically induced pulsating water jet, which is the topic of this work, falls into water jet devices in multiple droplet categories, as it is currently not plausible to use this technique effectively to create a single impact. Separation of the jet into individual droplets, which is the basis of PWJ technology creates a possible candidate for erosion testing of structural materials. Gohardani [4] described the advantages and shortcomings of currently used erosion testing facilities. The selection of these is as follows: Whirling arms testing offers easy to replicate test conditions, the possibility of accelerated testing, the availability of quick change of the samples, and the possibility of heating of the sample.

Shortcomings are limitations in attainable speed, non-spherical droplet impact, centrifugal forces on the sample, and the effect of turbulences and shock waves produced. Rotating facilities are the primary device for investigation of leading edge erosion of wind turbine blades [2]. Single impact waterjet testing offers accelerated testing; however, it provides a non-

spherical droplet shape, unlike single droplet devices capable of spherical droplet. Multiple impact jet apparatus is used to provide damage threshold velocity for small samples and is also suitable for accelerated testing [4]. Finally, wind tunnel testing can test more complicated geometries and larger scale models. The conclusion is that single impact devices and jets are used to examine physics and fundamentals behind droplet impact, and multiple droplet facilities (rotating rigs, whirling arms, and rotating discs) are used to provide qualitative data about material erosion resistance [2].

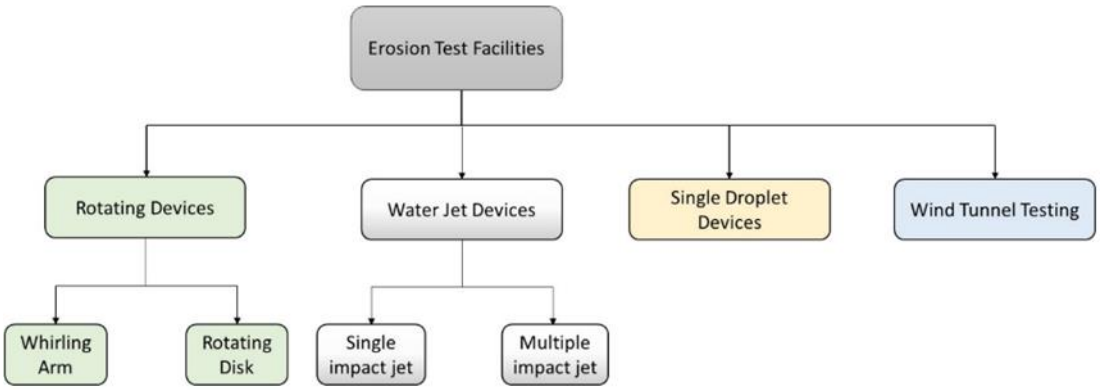

Figure 4 Classification of liquid droplet impact testing facilities divided by Ibrahim [2]

2.1.4 Erosion of structural materials

Fundamental erosion studies were conducted by Thomas and Brunton [20, 21]. During their research they tested a number of materials using rotating disk apparatus. The water in rotating disc apparatus interacts with the surface by repeated droplet impact rather than by a continual flow. Former research used continuous water jets to simulate erosion conditions because it was assumed that it has a more intense erosive effect. The rotating disc apparatus consists of a sample mounted onto a rotating disk. The sample is periodically (once per rotation) hit through a nozzle by a single CWJ flowing parallel to the axis of the rotation. Erosion of both non-metals and metallic materials was observed [20]. The most important result from the early observations is the definition of three stages of erosion. They were defined based on the erosion curve of different metallic materials (**Figure 5**) [21]. Stage I-**incubation period** corresponds to a period with no erosion in sense of material loss, but the material was subjected to macroscopic plastic deformation. During the second stage (stage II-**the maximum rate of erosion**), the material removal rate rises to a maximum and then remains constant for a certain period. This stage is characterized by the formation and merging of the erosion pits in the impacted area. The erosion pits are formed by erosion material removal in this stage The third stage (stage III-**the final steady state**) begins when most of the pits across the impacted area are merged to form a single erosion crater or kerf. This stage propagates by deepening the single erosion kerf/crater [21].

The erosion stage progression according to [21] in austenitic stainless steel will be discussed.

I. In the incubation stage, small surface depressions appear. Depressions are smooth and shallow with no preferred shape or orientation. Further impacts are causing the number of depressions to increase, and some of the depressions are increasing in size. During this stage, there is no evidence of the loss of material. The secondary deformation effect is assumed to be the tilting of the grain in a way that grain boundaries can be visible.

II. After certain droplet accumulation, the material starts to break away from the treated surface. The preferred larger depressions form small pits by material breakage. These small pits appear throughout the eroded area. These small pits then start merging into a kerf across the impacted area.

III. Repeated impact then serves to deepen the kerf and finally cause severe damage to the sample. Fractures can spread into the adjacent material from the sides and bottom of the kerf. The linking of these fractures accounted for most of the erosion during stage III [21]. Foldyna et al. [36] distinguished similar three stages of erosion in material treated by pulsating water jet.

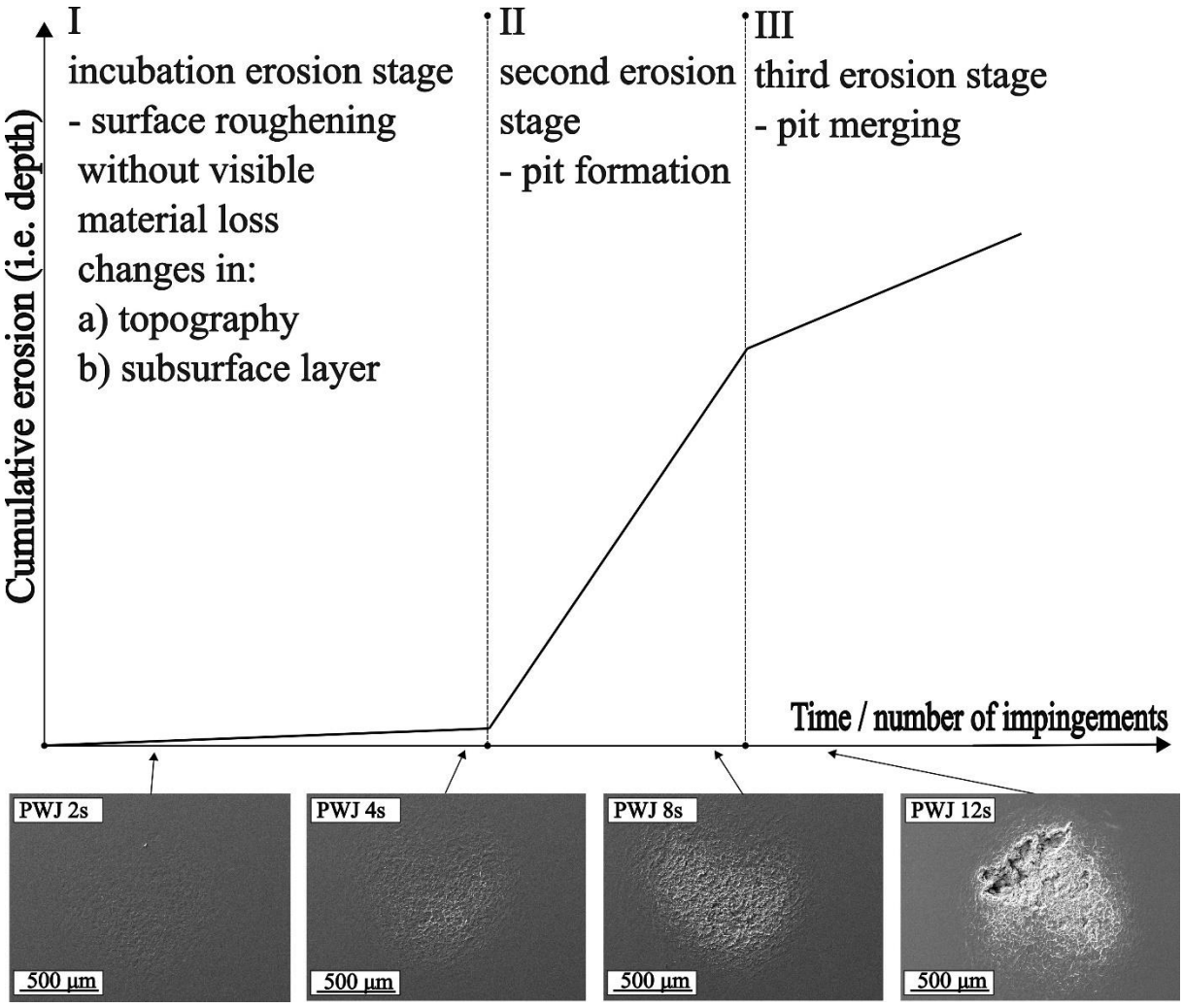

Figure 5 Theoretical erosion curve drawn according to [21] with added examples of eroded surfaces

The erosion curve was in the following studies further divided into 4 or in some cases 5 stages. The stages noted by Bargman et al. [27] are the incubation period followed by the acceleration phase, then the deceleration phase, and the final stationary stage with a constant erosion rate. The erosion curve is commonly divided into 5 erosion stages as done by i.e. Ibrahim and Medraj [2] and Ma et al. [37]. Compared to the 4 stages, the division of the erosion process into 5 stages includes the maximum rate period added between the acceleration period and the deceleration period. **Figure 6** shows the division of the erosion curve in 3 and 5 stages Introducing 5 stages

allows a better description of transitional areas that are described by their respective stages. On the other hand, using of only 3 stages requires a lower number of experimental points and is easier to distinguish [37]. The acceleration stage is characterized by an increasing rate caused by the merging of the erosion pits. At the end of the acceleration stage, the erosion rate reaches its maximum (maximum rate stage). The decline in the erosion rate marks the start of the deceleration period also known as the attenuation stage. The erosion rate decrease is commonly attributed to high roughness and irregularities changing the stress distribution caused by droplets [2].

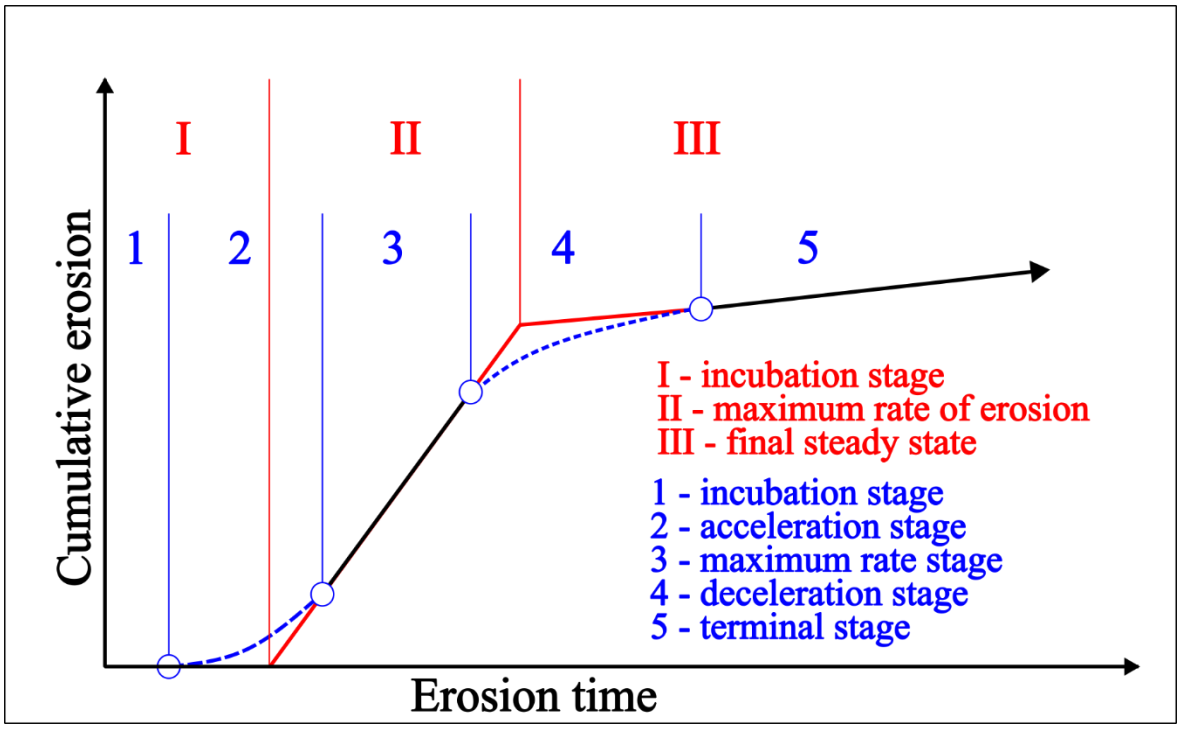

Figure 6 Schematic of a comparison between erosion curve divided into 3 erosion stages (redrawn according to [21]) and 5 erosion stages (drawn based on [2, 37])

2.2. Water jets

The history overview of industrial water jet apparatuses is described in this section. The typical uses of water jetting technology are also introduced. The water jets are then divided into several categories and each category is characterized.

2.2.1 Introduction and history

The power of flowing or impacting water can be seen acting in many places in nature. Rain may erode mountains and at the same time move the eroded rocks away from the area. The great river deltas show the carrying capacity of the water even at the low speeds of the water flow. The architecture across the world is eroded by rain droplets. These processes show three aspects of water capabilities, which play an important part in shaping the surface of the earth. These three aspects are breakage, mobilization, and removal of the material. These aspects have been widely used throughout history by humans. In ancient Egypt, they found a way to divert the flow of the river to wash the soil away from mineral deposits. In the Roman period, they used the same power by making water reservoirs on top of the hills and then directing the flow of water into the ore deposit below where it would break, remove, and carry away the rock and minerals to the place where the minerals could be easily extracted. The use of pipes to direct

the stream of water for coal mining was introduced in the Soviet Union and New Zealand [16]. With the development of various mining applications, waterjets were used for rapid cleaning of surfaces. Expansion in the cleaning industry led to the use of higher-pressure pumps. This led to further exploitation of the water jet for cutting applications. In the late 1960s, Robert Franz and his students found that at sufficient pressure of the jet it is possible to cut through wood. The cuts in the wood showed little damage to the material outside of the cut area. This led to the development of a cutting system with pressure up to 400 *MPa* as a new tool for the technical industry. Especially, the low reacting force of high-pressure water jets made it effective to use in the fast-developing process of robotic cutting. This type of water jet had limitations in cutting ceramics or metallic material. It was either slow or completely impractical. The effectivity of the water jet was increased by adding solid particles into a high-flow speed water stream. Therefore, an AWJ was developed [16].

Summers quoted: „Waterjetting is in its simplest form, concerned with the development, the transition and the application of power" [16]. Power is in the case of waterjet technology created in the liquid medium by the hydraulic system. The pressurized water then flows through a nozzle equipped with an orifice with a diameter smaller than the rest of the feed system. When the constant volume of water reaches the nozzle, the flow accelerates. After exiting the orifice, the jet travels through the environment and loses some of its energy due to atmospheric or environmental drag [16]. The acceleration of the pressurized water volume in the nozzle orifice has been described by Bernoulli's law [38] written in Eq. (10):

$$p_{at} + \frac{\rho_W}{2}.v_0^2 + \rho_W.g.h_1 = p + \frac{\rho_W}{2}.v_{pipe}^2.\rho_W.g.h_2 \qquad (10)$$

where p_{at} is atmospheric pressure, p is pump pressure, v_0 is effective water-jet velocity, v_{pipe} is flow velocity, g is gravity constant, h is the height and ρ_W is the density of water. When the height difference due to nozzle height is considered zero: $h_1 = h_2$, pump pressure is significantly higher than atmospheric pressure $p_{at} \ll p$, and effective water jet velocity is considered significantly larger than flow velocity $v_0 \gg v_{pipe}$, the theoretical velocity of the exiting waterjet (v_{0th}) can be estimated [38] by Eq. (11):

$$v_{0th} = \sqrt{\frac{2.p}{\rho_W}} \qquad (11)$$

Efficiency coefficient μ is often considered. The modified Eq. (12) is then written [38] as follows:

$$v_0 = \mu.v_{0th} = \mu.\sqrt{\frac{2.p}{\rho_W}} \qquad (12)$$

The coefficient characterizes momentum losses caused by several factors including wall friction, fluid flow disturbances and compressibility of water [38].

A range of achievable pressures available to WJ and relative ecology of the process (especially for pure water jets), predetermine both plain water jets and abrasive water jets for a plethora of industrial applications. Water jets are used for applications such as industrial cleaning, surface

preparation, paint, or coating striping, concrete hydro demolition, rock fragmentation, rock and soil drilling, decontamination, material recycling and number of manufacturing operations. Manufacturing operations include deburring and surface peening by plain water jet, cutting milling, 3D shaping, turning, piercing and polishing by AWJ [38].

2.2.2 Types of water jets

The water jet technology was divided by Momber [38] based on three criteria as can be seen in **Figure 7**. The first criterion is dividing jets by pressure ranges in the hydraulic system into low-pressure jets and high-pressure jets. The water pressure criterion divides the waterjet systems into systems pressurized with just a plunger pump and systems equipped with an intensifier. The border between low and high-pressure jets is increasing with advancements in hydraulic technology. Based on the jet medium, the jets can be divided into plain water jets, water jets with soluble additives (slurry jets) and water jets with added non-soluble abrasives (abrasive water jets). A combination of additives and abrasives may be also used (abrasive slurry jet). Abrasive water jets can be further divided into suspension abrasive water jets and injection-abrasive water jets based on the placement of the entry point of the abrasive particles [38].

The most important criterion for this work is dividing jets by the continuity of the stream into continuous and discontinuous jets. The first definition of discontinuous jets was: the discontinuous jet creates a discontinuous load on the impact site. However, it is necessary to point out, that every jet creates some discontinuous phases in the impact zone due to pressure fluctuations in the hydraulic system. The jet also shows droplet formation caused by the drag of the environment in which the water jet is working. Therefore, Momber suggested that discontinuous jets are artificially broken up by external conditions, while continuous water jets are not influenced by external conditions [38]. Vijay [39] similarly divided pulsed jets into “natural” and “forced”. The forced jets are divided into droplets by external energy source.

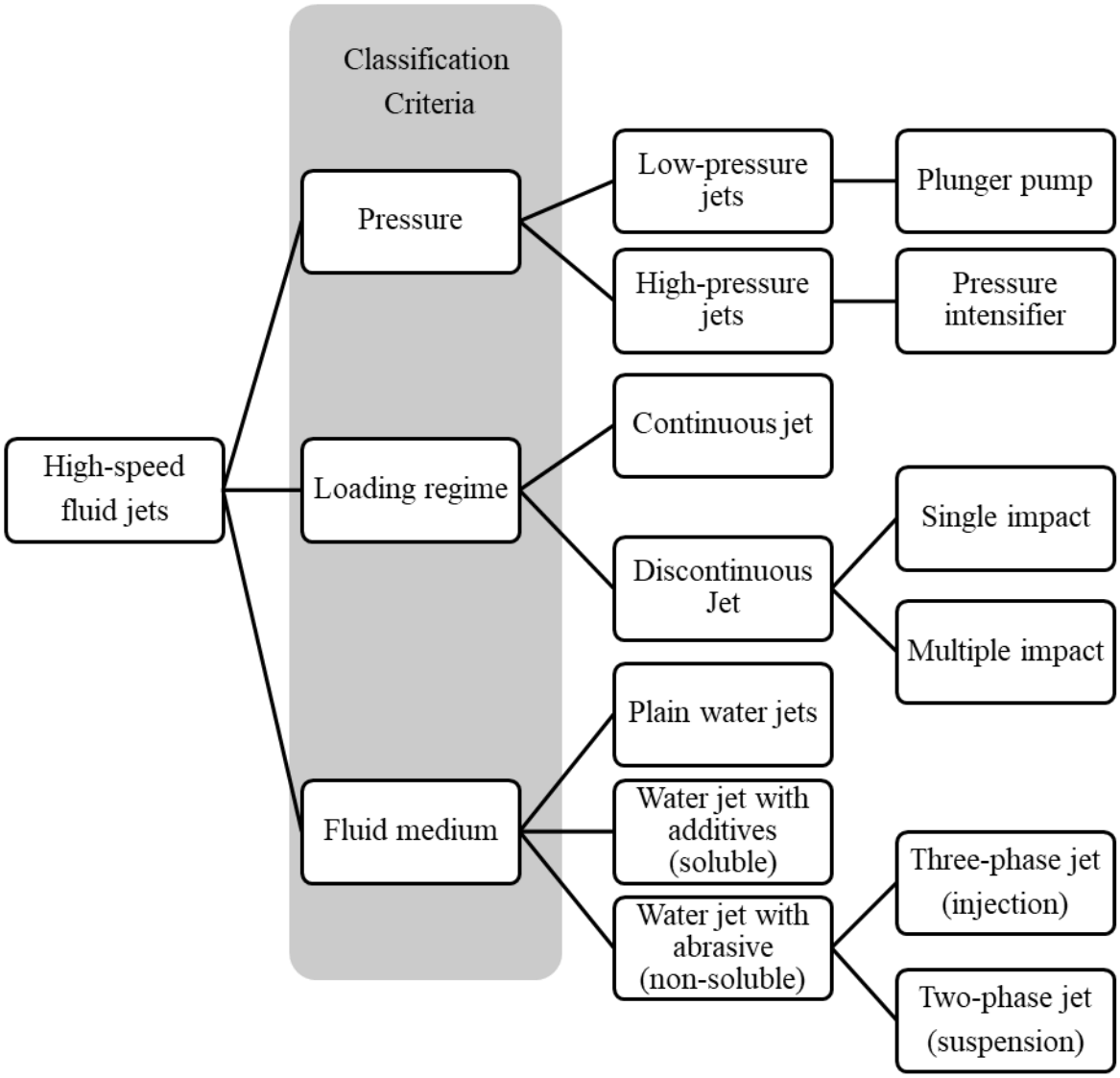

Figure 7 Basic water jet types Redrawn according to [38]

2.3. Basic types of pulsed jets

This section describes the ways of artificially splitting the jet into separate water droplets. The nonspherical coherent water droplets clusters produced by PWJ will be labelled **clusters**. At first, methods of forced jet separation are introduced and then two methods currently used in the Institute of Geonics CAS are described in detail, because one of them is used in this thesis.

The pulsating water jets (as described above) are divided into natural or forced types. The pulsating water jet is a water jet with a divided flow of water into separated clusters of water. The methods to achieve separate water clusters are depicted in **Figure 8**. The pulsed jets can be produced by accelerating the breaking of CWJ, by using an external jet separator or by dynamic modulation of continuous jet. Single pulse water jets (pulse cannons) are forced jets typically based on free piston impact or pressure extrusion [39]. The jet separation can be performed by e.g. a rotating disc (**Figure 8a**) or mechanic vibrations of nozzle body [39]. Another effective approach consists of using ultrasonically vibrating mechanical element inside of the jet chamber (depicted in **Figure 8b, c**). Finally, methods using self-excited oscillations to modulate the jet can be used. An example is Helmholtz resonator (**Figure 8d**) based on a rotationally symmetrical chamber with inlet and outlet. A similar principle is used by the fluidic nozzle

(**Figure 8e**), the main difference is the lack of rotational symmetry of the chamber as well as the jet. This method creates a flat jet with sweeping motion [40].

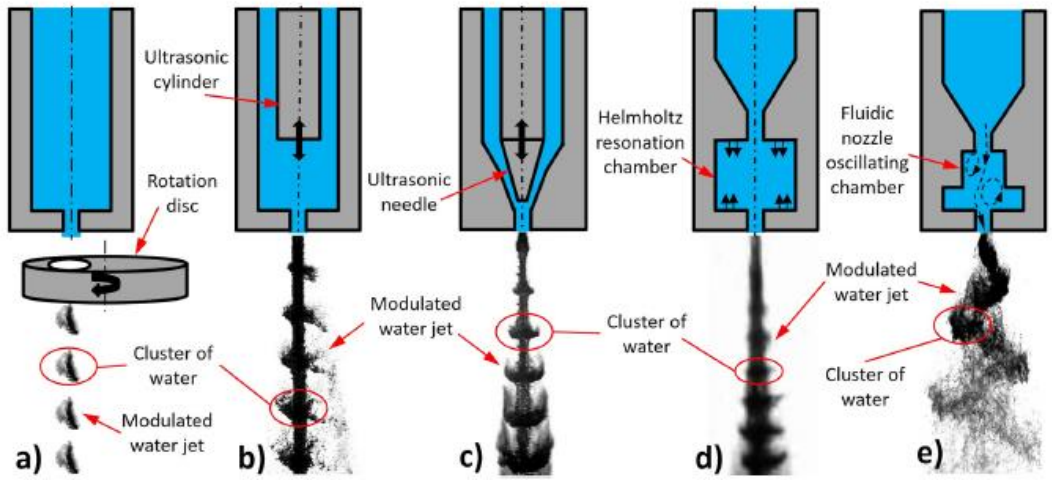

Figure 8 Different types of clusters generation for pulsating water jets a) perforated disk, b) pulsating ultrasonic cylinder, c) pulsating ultrasonic needle, d) Helmholtz resonator, e) fluidic nozzle [40]

The PWJ repeatedly impacts the surface of treated material with water clusters. The waterfront of the water clusters causes a peak in pressure (impact pressure) on the surface of the material due to the water hammer effect. Unlike CWJ which creates impact pressure only on first contact (**Figure 9a a$_1$**), the water cluster impact of PWJ is repeated based on the frequency of impacts given by jet morphology (**Figure 9b, b$_1$**). Due to repeated impact pressure (**Figure 9b$_2$**) PWJ achieves a larger erosion effectivity than a pure CWJ acting on a surface with Bernoulli stagnation pressure (**Figure 9a$_2$**). The PWJ can be an alternative to an AWJ, which uses solid particles to enhance the ability of pure water continual jet. This method offers an edge over the AWJ mainly due to the absence of the abrasive particles. From an economical point of view abrasive costs may reach 75% of the operating costs of AWJ devices [41]. However, the main concern of abrasive particles is the possibility of surface contamination caused by particle embedment [18, 42].

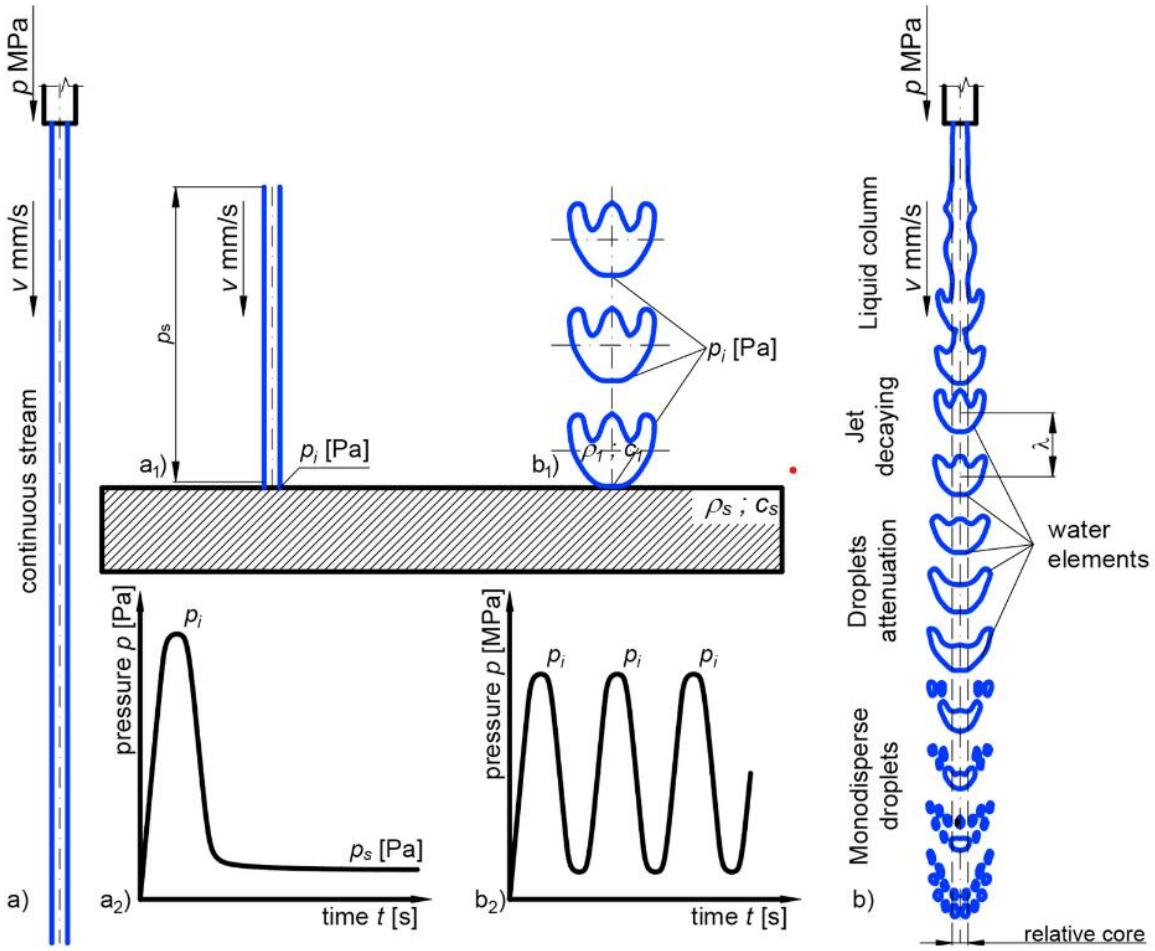

Figure 9 Difference in effect between continuous and pulsating water jet in a, b) jet morphology a1,b1) jet impact and a2 b2) jet effect on pressure/time development on the material surface [43]

2.3.1 Self-resonating nozzles

There are methods for the generation of the clusters without any mechanically moving parts inside the nozzle (see **Figure 8d, e**). These tools without moving parts are based on characteristic geometry inside of the nozzle.

The first type of this tool is based on the Helmholtz resonator, which creates self-excited pressure pulsations in the chamber. These pulsations split the jet after leaving the nozzle into PWJ. The system of the rotationally symmetrical chamber with variable diameters of inlet and outlet orifices was shown to create sufficient pressure oscillations for creating effective PWJ. Li et al. [44] observed the effect of feeding pipe diameter and the chamber length on axial pressure oscillation and standoff distance. It was found that the optimum chamber length decreases with increasing pump pressure regardless of the feeding pipe diameter. The relation between feeding pipe diameter and pressure oscillation peak, chamber length and standoff distance was well described in [44]. The correct function of the Helmholtz oscillator is therefore dependent on its exact geometry and properties of liquid medium (water) such as density and viscosity.

The second way of creating PWJ using only the nozzle's internal geometry is by a using fluidic nozzle (see **Figure 8e**). The unique shape of the chamber inside the nozzle can create sweeping side-to-side motion of the water stream as shown in **Figure 10**. The side-to-side motion is generated by water flow through a specially shaped chamber located between the feeding pipe and ending with an outlet orifice. Zeleňák et al. [45] visualized the motion of the jet outside of

the nozzle using a high-speed recording method in combination with front pulsed LED lighting illumination. Results can be seen in **Figure 10**. Visualisation of the jet shape is necessary for verification of fluid flow simulations. Říha et al. [40] compared the disintegration abilities of this type of modulated water with the ability of the CWJ. The side-to-side motion can be set perpendicular to the water jet head movement direction for wider cuts and higher material removal rates or parallel for more focused and deeper cuts at the same hydraulic powers. Other angles between the motion of the jet and the feed rate have not been documented yet.

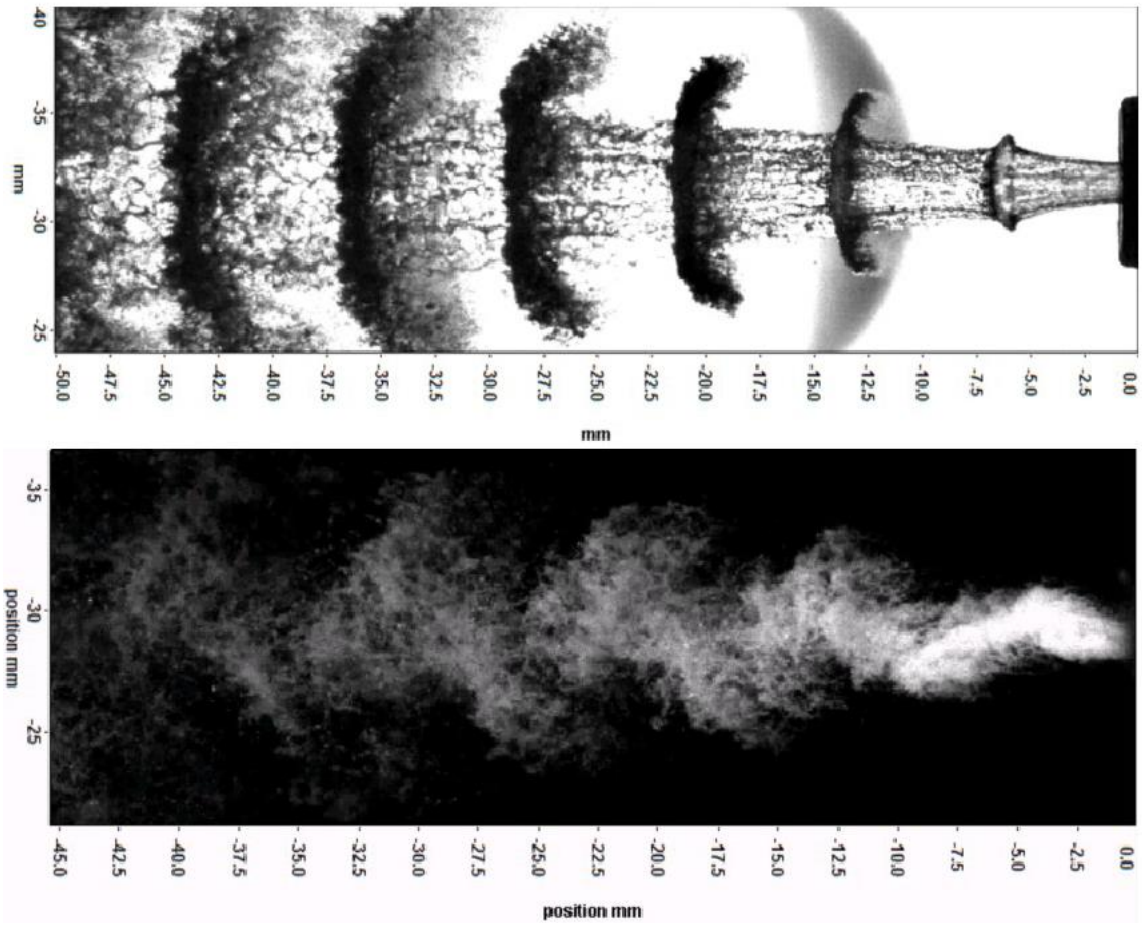

Figure 10 Comparison of the acoustically generated pulsating water jet (top) with jet generated by self-resonating hydrodynamic nozzle (bottom) [46]

2.3.2 Ultrasonically modulated pulsating water jet

This study used the formation of the PWJ by ultrasonic modulation of the jet caused by vibrations of the ultrasonic tool located in the acoustic chamber (see **Figure 11**) [14]. The high-pressure system with the integrated acoustic generator of pressure pulsations consists of an acoustic actuator inside a cylindrical acoustic chamber connected to the liquid waveguide. The liquid waveguide is fitted to a supply of pressurized water and ends with a selected nozzle. The acoustic actuator consists of a piezoelectric transducer and cylindrical waveguide. Pressure pulsations created by the acoustic actuator in an acoustic chamber are amplified by the mechanical amplifier of pulsations and transferred by a liquid waveguide into the nozzle. For effective transfer of the energy of the pulses from the generator to the nozzle, it is important to consider the compressibility of the water. The pressure pulsations created by the acoustic actuator transform into the velocity pulsation when the liquid exits the closed hydraulic system [36]. The ultrasonic modulation advantageously generates a forward oscillation in the direction

of water jet. The most of jet energy and volume flow rate is effectively used on eroded material in comparison to the perforated rotation disc method. The method may not be used at specific hydraulic conditions that would lead to cavitations inside the apparatus. These cavitations would be detrimental to the service life of the jet. These conditions entail lower water pressures (10 *MPa*) and frequencies up to 15 *kHz* [40]. On the other hand, sonotrode may not be effective enough to create efficient pulses for clusters separation at too high pressures (100 *MPa*). PWJ morphology with not-clearly separated clusters of water can be disadvantageous, because the water between the clusters may dampen the impact [40].

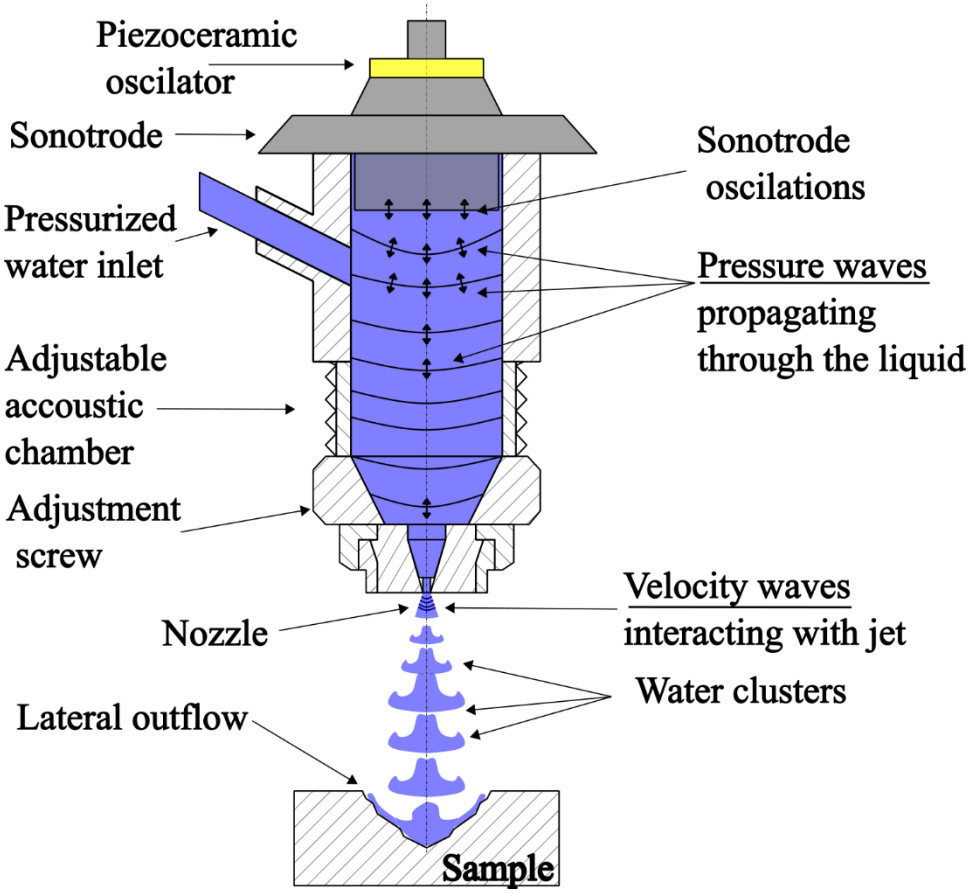

Figure 11 Schematic of the water jet with an acoustic generator of pressure pulsations and adjustable acoustic chamber

Although PWJ brings many advantages over the continual water jet it also introduces a number of new process parameters that need to be controlled and which have a significant effect on the resulting erosion of the material. The parameter with strong importance is a standoff distance, which needs to be set according to other parameters (pressure, frequency, etc.), to fully utilize the advantages of PWJ. The parameters can be divided into several key groups such as liquid properties (pressure, liquid density, and flow rate), the nozzle properties (nozzle diameter, nozzle geometry, and nozzle angle), the properties of the process (traverse speed and standoff distance) and the acoustic properties (frequency of the actuator, amplitude of sonotrode and acoustic chamber length). These properties are summarized in **Table 2**.Moreover the mechanical properties of the impacted material are of crucial importance for the effectivity of the erosion process.

Table 2 Process properties of pulsating water jet

Liquid parameters	Nozzle parameters	Technological parameters	Acoustic parameters
Pressure	Nozzle geometry	Standoff distance	Frequency
Liquid density	Nozzle diameter	Traverse speed	Amplitude
Flow rate	Nozzle angle	Impact angle	Chamber length

2.4. Effect of process parameters on ultrasonic PWJ

This chapter describes the effect of process parameters on erosion effectivity and jet morphology. Jet morphology has a significant effect on optimal standoff distance in the case of PWJ. Therefore, the majority of this chapter focuses on standoff distance correlation to other parameters. The parameters are divided into hydraulic parameters, acoustic parameters, and technological parameters.

2.4.1 Effect of hydraulic parameters on optimal standoff distance

Pressure and standoff distance are the most easily changeable parameters of the PWJ process. However, pressure has a significant effect on jet morphology and therefore on optimal standoff distance. A number of research is focused on the effect of different PWJ parameters on the optimal standoff distance of ultrasonic PWJ [47–54].

The pressure fluctuations of the liquid leaving the closed hydraulic system through the nozzle causes the velocity fluctuations. The velocity fluctuations then shatter the jet into separate water clusters. A certain travel distance from the nozzle is necessary before the formation of the discrete water clusters.

The erosion starts at higher standoff distances with an increase in pressure. The erosion potential of the jet is highest at the standoff distance (distance between nozzle and the material) of 21 *mm* for the pressure of 40 *MPa* and 43 *mm* at a pressure of 100 *MPa* for other process parameters being constant. This shows the dependence of optimal standoff distance on hydraulic pressure. An increase in pressure leads to an increase in optimal standoff distance for the full incubation of discrete water clusters as visible in the diagram (**Figure 12**). Hloch et al. [47] used stair trajectory for increasing standoff distance from 5 to 101 *mm* with a step of 2 *mm*. Five erosion regimes based on the dependency of PWJ morphology and erosion features on the standoff distance were established based on this research [47]. These regimes were classified as incubation, acceleration, culmination, depletion, and termination.

The lowest standoff distances cover the incubation regime, where the liquid column of PWJ is acting like the CWJ. There are no discrete clusters of water in this regime and stagnation pressure prevails over impact pressure. The length of this regime depends on supply pressure. It is important to distinguish between the incubation regime [47] based on jet morphology and the incubation stage based on erosion exposure time [21].

The second regime called the acceleration regime is defined by the acceleration of the erosion rate. Acceleration of erosion rate is caused by the increase in the amplitude of the axial velocity fluctuations of the jet at the distance of solid surface impact. The stress-induced by the impact of the jet locally exceeds the ultimate strength of the material and causes severe deformation

and erosion of the impacted area. In the acceleration regime, impact pressure prevails over stagnation pressure.

At an even higher standoff distance, the rate of erosion increases until it reaches its maximal value. This point is called the culmination regime. The jet morphology in the culmination regime consists of discrete clusters of water. Each of these clusters causes an impact pressure (water hammer effect) when its waterfront reaches the solid surface. The erosion rate is highest at this point and widening of the kerf may be observed due to lateral outflow jetting. Undercuts and micro channels are present in the eroded area in this regime.

After the further increase in standoff distance, the erosion rate starts to decrease. This regime is called the depletion regime. It is caused by the interaction of discrete clusters with the drag of the atmosphere. The aerodynamic drag causes radial wave de-concentration. It leads to a decrease in the PWJ impact pressure. kerf in this regime is shallower and wider. The presence of material deformation diminishes due to a decrease in lateral flow [47].

Upon further increase of the standoff distance, aerodynamic drag causes the breakup (termination) of the discrete clusters into solitary droplets. This regime is named as termination regime. The jet is at this point created from a monodisperse of water droplets. The mass of these droplets in the regime is lesser than the mass of the clusters in the acceleration or depletion regime. Some washing effects can be observed on the impacted surface.

A graphical representation of dependency of the depth of the erosion kerf and morphology of the jet on standoff distance is represented in **Figure 13**.

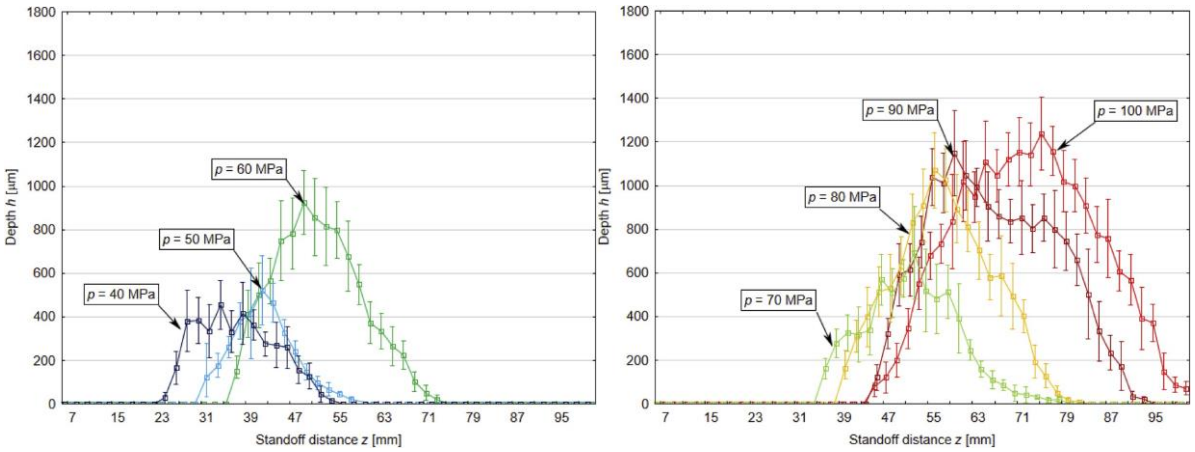

Figure 12 Depth dependence on pressure and standoff distance [47]

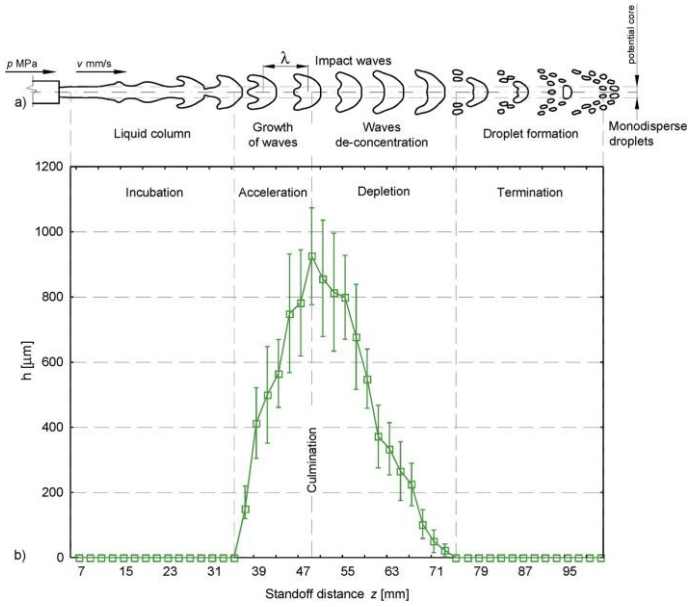

Figure 13 Schematic and measurement of dependence of erosion depth on standoff distance [47]

Recently, a switch occurred in the methodology of determining the effect of the optimal standoff distance of the PWJ. The standoff distance was increased continuously along the inclined trajectory with some predefined angle. This can be seen for example in research done by Hloch et al. [48], Raj et al. [49] or Nag et al. [50]. Srivastava et al. [51] examined differences between the inclined trajectory and step trajectory. Step trajectory consists of several discreet steps with a given increment of SOD between each measurement. This trajectory can be seen in **Figure 14**. The inclined trajectory doesn't consider the vertical velocity component $v_y = v.\sin\alpha\ \frac{mm}{s}$. This component decreases the impact force because it creates a decrement in jet velocity: $v = v_{PWJ} - v_y$. **Figure 14** includes a comparison between the inclined and step trajectory in terms of achieved erosion depth on the same type of sample. The researchers concluded based on **Figure 14**, that the step trajectory achieves higher erosion depth, and the inclined trajectory may have a detrimental effect on the results and optimal standoff distance evaluation [51]. This is the reason why stair trajectory is now used predominantly.

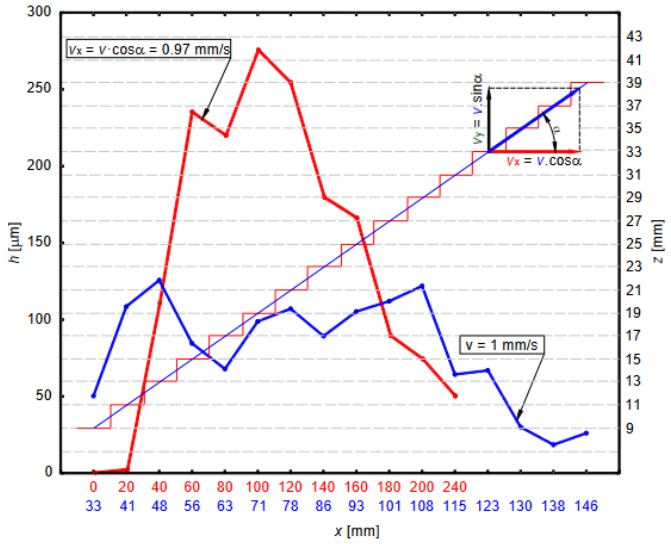

Figure 14 Comparison of stair and inclined trajectory with constant travel speed on the erosion depth [51]

Further research [55] dealt with the effect of standoff distance (15-47 mm) on the erosion of aluminium alloy using PWJ with 40 *MPa* and 20 *kHz*. The novelty was the adoption of X-ray computer micro-tomography. This measurement allowed non-destructive cross-sectional examination resulting in a 3D imaging of intricate cavities network under the eroded surface. The X-ray tomography allowed the classification of subsurface cavities into two categories:

- Blind cavities are the most abundant under the surface. The structure of these cavities shows a symmetrically stochastic character (**Figure 15**) [55]. The diameter and shape of these cavities are dependent on their location on the erosion kerf. Their penetrating ability is dependent upon water cluster kinetic energy. The cavity dimension is dependent on the jet penetrating ability resulting from water cluster kinetic energy.
- Transient cavities are characterized by the presence of both inlet and outlet of the cavity. The inlet was usually located in the lateral direction of the kerf while the outlet was often located behind the upheaved material (pile-up) in a direction away from the kerf [55].

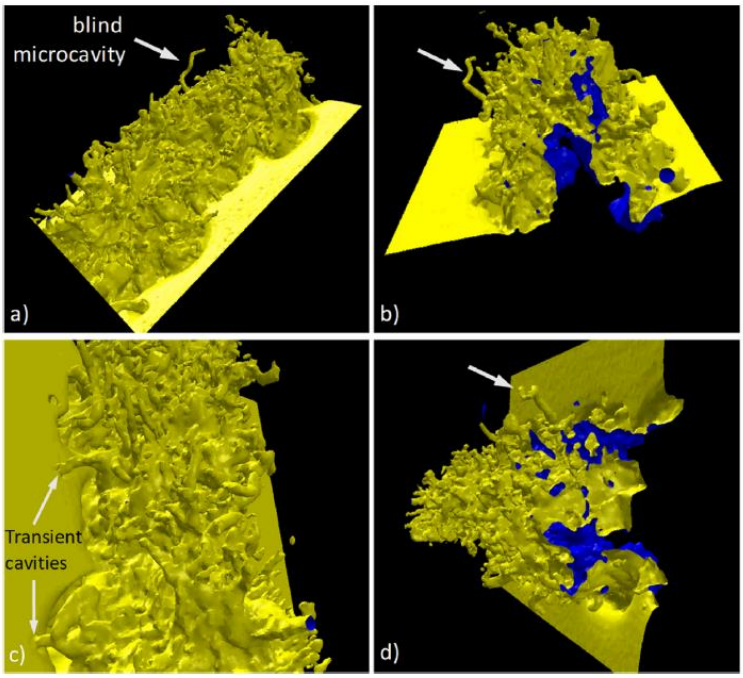

Figure 15 X-ray μ-CT observed an example of (a, b) blind micro-cavity and (c, d) transient cavity observed using [55]

A complex analysis of the effect of standoff distance of PWJ with other constant parameters on the surface of EA4T bainitic steel was done by Chlupová et al. [52]. A single pass of the PWJ moving on stair trajectory was evaluated. The experiment followed a step trajectory from 15 *mm* to 43 *mm* with an increment of 2 *mm*, a constant feed rate of 0.25 *mm/s* and a constant pressure of 40 *MPa*. The analysis consisted of light microscopy (depth evaluation), micro hardness measurement, SEM, EBSD, TEM and hardness analysis. The authors evaluated the effect of standoff distance on width and depth of the kerf. The plot of kerf depth and width dependence on standoff distance shown in **Figure 16** is a prime example of using stair trajectory for tunning of standoff distance for the highest erosion effectivity. The standoff distance setup creating highest erosion depth was 35 *mm* based on **Figure 16 a**. The width of the kerf the most

effective standoff distance was in interval from 29 *mm* to 35 *mm* as can be red from the **Figure 16 b**.

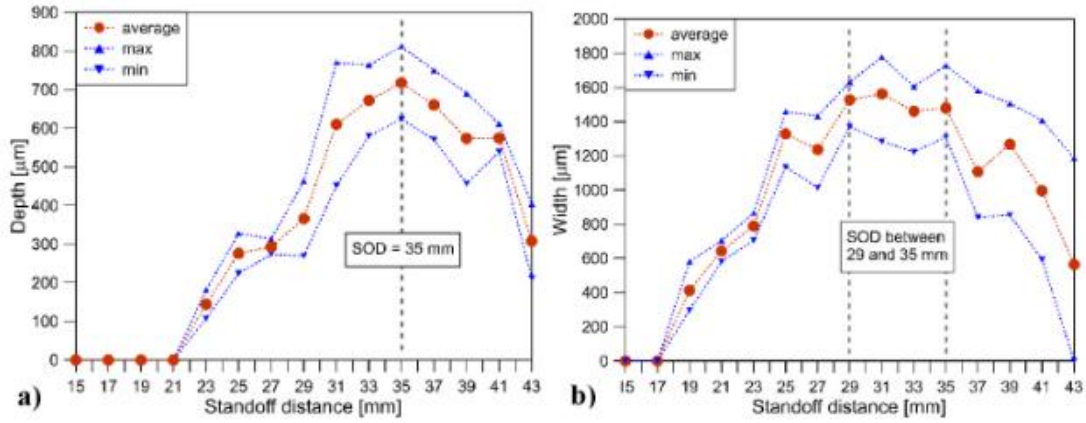

Figure 16 Influence of standoff distance on erosion of EA4T a) depth b)width [52]

The EBSD (Electron back scattered diffraction) analysis was performed on a cross-section of the material. EBSD data were used to evaluate the kernel average misorientation (KAM) profile under the kerf. The KAM results show misorientations accumulated within the grains **Figure 17a**. Significant misorientation is observed within grains under kerf created at a standoff distance of 19 *mm*. The region of increased misorientation closely follows the erosion kerf treated with a standoff distance of 39 *mm.* EBSD is supported by TEM analysis and hardness analysis. Locations with reduced hardness are observed in the hardness profile in **Figure 17 b**. These may be attributed to cavities underlying the measured area. Observed changes in material surface layer were attributed to the shear stresses subjected to the material due to the water hammer effect [52].

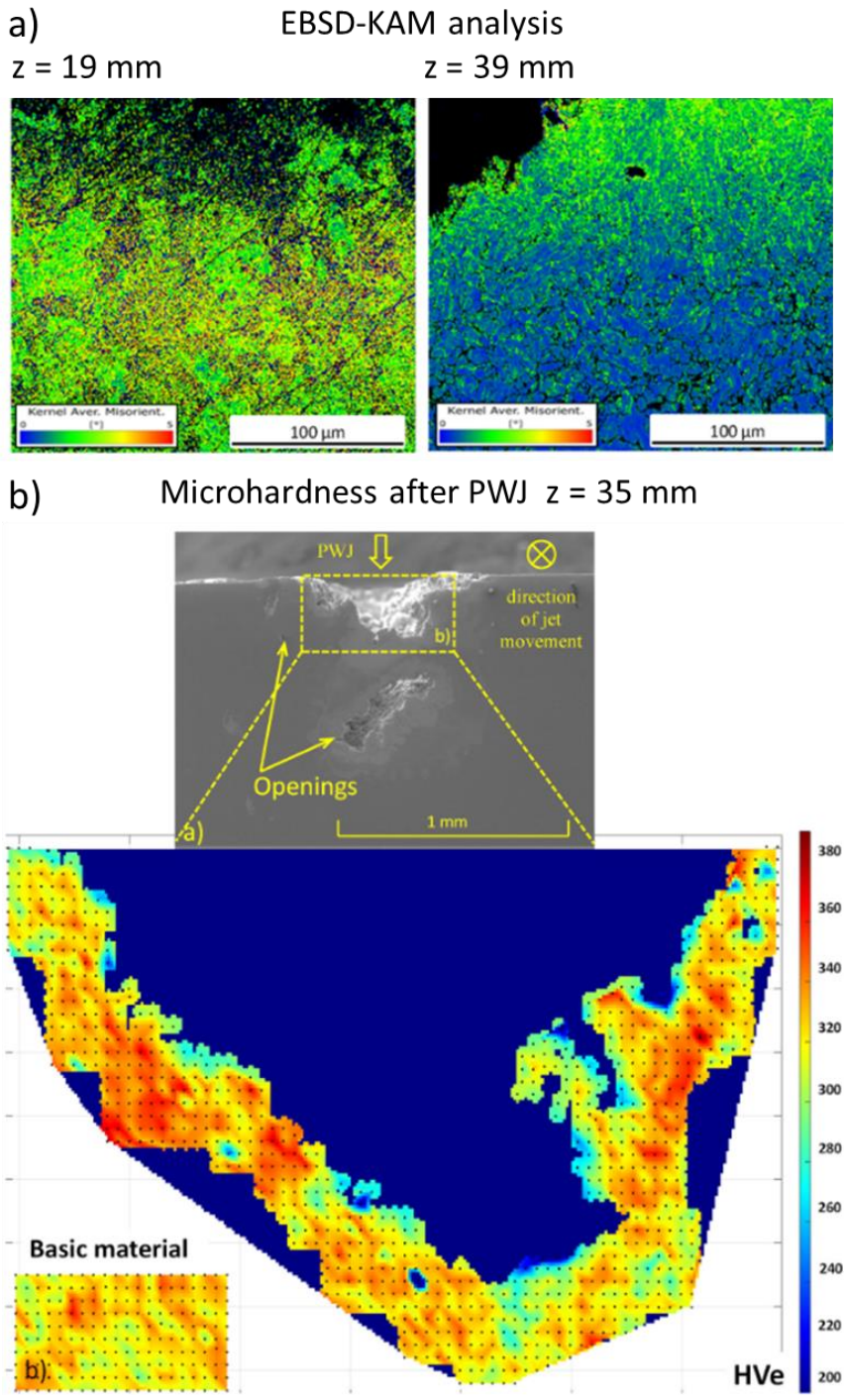

Figure 17 Complex analysis of single pass PWJ treatment at different standoff distances [52]

2.4.2 Effect of liquid cluster impact distribution

Technological parameters of PWJ including exposure time, feed rate, overlapping strategy and overlapping distance deal indirectly with cluster impact distribution on the treated surface. The next paragraph reviews the research of each of the aforementioned strategies for adjusting cluster distribution. The paragraph will be focused mainly on PWJ created by oscillating sonotrode excitation of pressurized liquid.

Exposure time can be described as a time during which PWJ acts, with water cluster impacts upon the stationary point of the surface. The stationary PWJ exposure experiment has been

done by Foldyna et al. [36] and Nag et al. on tantalum [43] and on aluminium alloy AW6060 [56] . The number of cluster impacts I_n of the surface is calculated by Eq. (13):

$$I_n = t.f \tag{13}$$

where I_n is the number of impacts, *t* is exposure time in *s*, and *f* is the frequency of the sonotrode in *Hz*. Static exposure tests are mostly done in research to elucidate the erosion mechanisms or to evaluate material erosion resistance. There is of course a possible use of stationary PWJ exposure for drilling applications.

The experiments considering PWJ head moving on a linear trajectory over the surface are currently the most abundant. Studies [47, 48, 52] focused on other PWJ parameters often use constant feed rate. Several studies focused mostly on the effect of feed rate on the erosion behaviour of treated materials [57, 58], and some studies consider multiple factorial approaches consisting of a combination of parameters including feed rate. Srivastava et al. [59] considered feed rate and nozzle type. In another study Srivastava et al. [12] examined the effect of feed rate on several hydraulic pressure levels, which is often researched parametric combination [60, 61]. Tripathi et al. [62] as well as [49] examined effect of feed rate on two frequency levels. Finally, Lehocká et al. [63] studied multiple parametric approach using Hadamard matrix considering inputs hydraulic power, feed rate, pressure, and nozzle diameter, and the selected output was mass material removal .In case of PWJ moving on the linear trajectory at constant feed rate *v mm/s*, impact distribution I_d can be calculated by Eq. (14):

$$I_d = \frac{f}{v} \tag{14}$$

where f is the frequency in *Hz* and I_d is in *i/mm*. The line based PWJ tests were either focused on erosion research or material disintegration. AWJ cutting is in industry common practice, therefore lot of studies considered PWJ use for material cutting and disintegration, too. However, previous studies as well as kerfs demonstrated in this work show very nonuniform rough edges compared to AWJ cuts. Therefore, other uses of PWJ technology were considered.

The effect of the overlapping strategy and overlap distance on the pure CWJ and AWJ has been researched [64–67]. Wang et al. [66] concluded that it is beneficial to use multiple passes of AWJ (e.g., 2 passes) to achieve more significant material removal (complete overlapping) within the same process time. The effect of overlapping multiple passes of PWJ has been studied just recently [13, 68, 69]. The main driving force for the overlapping study of PWJ is the possibility of treating functional surfaces in processes of roughening [68, 69], or peening [70, 71].

2.4.3 Effect of ultrasonic parameters

The effect of frequency changes on erosion effectivity is the rarely researched topic. Frequency change requires significantly more effort compared to standoff distance change. To change the frequency of the PWJ it is necessary to readjust the sonotrode system. This usually includes changing the sonotrode, readjusting of the acoustic chamber, and evaluating the new optimal standoff distance. This is one of the reasons why changing the frequency of PWJ is a less researched problem. The ultrasonic PWJ at UGN CAS has available 20 *kHz* sonotrode and 40

kHz sonotrode systems. This makes currently possible erosion test at only two frequency levels by PWJ at UGN CAS.

Tripathi et al. [62] evaluated the effect of frequency change of PWJ during sandstone erosion. The frequency was changed from 20 *kHz* to 40 *kHz*. They observed that the modulation of the frequency from 20 *kHz* to 40 *kHz* results in increased erosion depth (1.186 *mm* to 2.618 mm) with other parameters being constant. This can be attributed to the increased number of impacts in the treated area. For the feed rate of 200 *mm/s*, the number of impacts for 20 *kHz* ranged from 100 to 160 *i/mm* (impacts per milimetre) and for 40 *kHz* ranging from 200 to 320 impacts per millimetre. The change of frequency also affected the width of the highly eroded area. The increase in frequency from f = 20 *kHz* to 40 *kHz* led to the width of the erosion kerf decreasing from 10.49 to 8.14 *mm* (p = 40 *MPa* v = 200 *mm/s*). This decrement is attributed to the larger size of gaps between the clusters at the frequency of 20 *kHz* (see λ in **Figure 13**). The dispersed stream in this gap then impacts the wider surface affected along the erosion path. The pressure increase caused the increase in width of the erosion area; for the frequency of 20 *kHz*, the width increased from 8.99 *mm* to 10.49 *mm* and for the frequency of 40 *kHz* the width increased from 6.51 to 8.14. The width increase can be attributed to increase in the energy of the water clusters. Srivastava et al. [53] conducted a classic stair test (see **Figure 18**) on the steel AISI 304 with 70 *MPa* and standoff distance ranging from 5 *mm* up to 101 *mm* with a step size of 2 *mm.* During the test, the frequency was changed from 20.11 *kHz* to 20.27 *kHz*. Material loss (incubation regime) did not occur until standoff distance of 35 *mm* was reached for the frequency of 20.11 *kHz*. The standoff distance of 55 *mm* was needed for the first visible signs of material loss for a frequency of 20.27 *kHz*. The depth of the eroded kerf as the effect of standoff distance "z" was plotted for both frequencies (**Figure 18**) The frequency change which occurred during the experiment [53] is attributed to the wear of sonotrode. It is visible that even minor differences in frequency show a significant effect on optimal standoff distance (the position of the culmination regime) However, the synergy of frequency change with other process parameters needs to be studied further. The excitation amplitude of the sonotrode influences the material volume removal as well. It is possible to determine the optimum standoff distance yielding the maximum volume removal rate for a given excitation amplitude in combination with other hydraulic parameters. The break-up length of the PWJ is inversely related to the excitation amplitude [54].

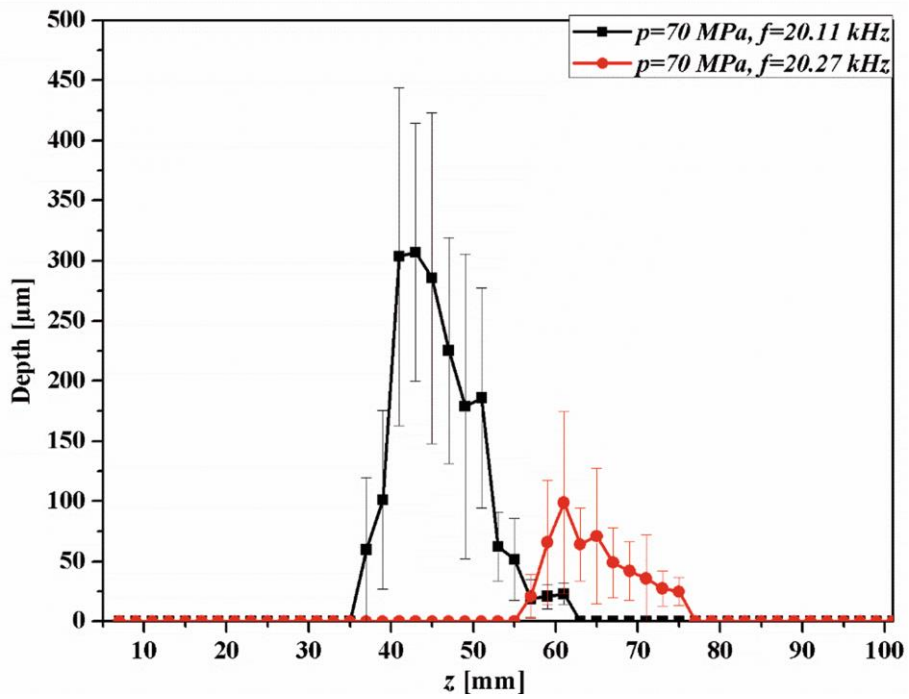

Figure 18 Depth of the kerf as a function of standoff distance for two different frequencies [53]

One of the basic principles of the PWJ created using ultrasonic sonotrode is the transformation of the pressure waves into velocity waves. This happens at the nozzle. However, the environment where the pressure waves travel has a significant effect on the effectivity of the jet. The acting of the turbulent flow of compressible water in the high-pressure system was numerically simulated by Foldyna et al. [72] The process consists of the generation and propagation of pressure pulsation in tens of kilohertz in a liquid environment pressurized to tens of *MPa*. The final part of the process is the discharge of the liquid affected by the pulsations through the nozzle into the gaseous atmosphere. Typologically similar models were created for fuel injection in combustion diesel engines. The computational fluid dynamic model was therefore used to calculate what happens in the acoustic chamber and the rest of the high-pressure system. The first result [72] is that the calculated pressure is dependent on the location inside the acoustic chamber. The acoustic actuator generated a standing wave in water pressurized to 30 *MPa* and the amplitude of the wave increased significantly towards the nozzle exit. The simulation results were in good agreement with the pressure measured experimentally. Furthermore, the effect of length of acoustic chambers were studied, and the optimal shape was proposed. The optimal function of the acoustic chamber is to increase the pressure fluctuations the most at the nozzle. The most significant and systematic experimental work in this area was created by Nag et. al. [50] The acoustic chamber of the experimental device in the Institute of Geonics Czech Academy of Sciences (UGN CAS), was equipped with the acoustic chamber with variable length of the acoustic chamber. The chamber length was varied by a mechanical screw. The length of the acoustic chamber was then varied from 5 to 22 *mm* while varying standoff distance from 5 to 101 *mm.* The experiment was done at two distinct pressure levels of 30 *MPa* and 40 *MPa*. The first significant conclusion is that the optimal standoff distance is dependent on the length of the acoustic chamber. With the increase in hydraulic pressure, the optimal standoff distance shifts to higher distances while other parameters remain the same. The most interesting result is that the maximal depth of the kerfs follows a convex pattern as the maximal depth starts high (449 μm for 30 *MPa*) and then decreases to 188 μm when the

acoustic chamber length was increased from 5 *mm* to 12 *mm*. The maximal depth then increases from 221 μm to 333 μm when the acoustic chamber length increases from 13 *mm* to 22 *mm*. The output power of the piezoelectric sonotrode is also influenced by the length of the acoustic chamber. The power value decreased from 243.5 *W* to 143.5 *W*, when the acoustic chamber length increased from 5 *mm* to 22 *mm* [50].

2.5. Utilisation of erosion stages

2.5.1 PWJ based erosion prediction

One of the current uses of PWJ technology is erosion research and testing. This topic consists of erosion testing of new materials, erosion mechanism observation and erosion prediction. The earliest prediction and understanding of the erosion process was made using a wheel and jet apparatus [20]. The one of key characteristic of this method is a frequency based on the number of rotations of the motor (i.e., 150 *Hz*). A high quantity of erosion tests uses moving samples impacting falling water droplets [20, 22, 73]. Water jet separated into water clusters by performed disc show similitude with ultrasonically modulated PWJ used in the institute of Geonics. The impact frequency of the performed disc separated jet is however given by the rotational speed of the disk and the number of perforations on the disk. The frequencies reached by both of these approaches are low in comparison to ultrasonically modulated PWJ working in tens of *kHz* (20 *kHz*, 40 *kHz*). Other methods of erosion testing are summarized in chapter **2.1.3**.

The research of ultrasonically modulated PWJ variant is still focused on the development of the technology. The focus of the development is finding optimal parameters and increasing the repeatability of the technology. However, PWJ technology is also used as a high frequency generator for single point or single line erosion tests. The recent experiments of Nag et al. [43] were focused on determining the erosion resistance of tantalum subjected to stationary PWJ with variable frequency and supply pressure. The impacted area was divided into three regimes based on the number of clusters. These exposure-based regimes (incubation, acceleration, and depletion) were observed in the range from 5 050 to 2 585 600 impacts for 20 *kHz* frequency and in the range from10 150 to 5 196 800 impacts for 40 *kHz* frequency. These obtained erosion stages were observed using SEM for the presence of microcracks, craters, material upheaving, and tearing. The curves describing depth evolution based on exposure time were evaluated for several pressure levels (20, 30, 40 *MPa*) and divided into erosion exposure-based regimes. Hloch et al. [48] also observed erosion mechanisms in aluminium alloy caused by PWJ on an inclined trajectory. This experiment has been described above. The novelty was the use of acoustic emission. The acoustic wave differences can be easily distinguished between the area without visible disintegration and the area with low and high levels of material disintegration (see **Figure 19**). The correlation between the measured depth profile and acoustic emission reveals ongoing interaction between the dynamic signal and deformation of the material. The PWJ is considered as the source of the carrier wave of a given frequency in this case 20 *kHz* [48]. The study of this correlation is still under investigation to use acoustic emission as an instrument for monitoring of erosion process.

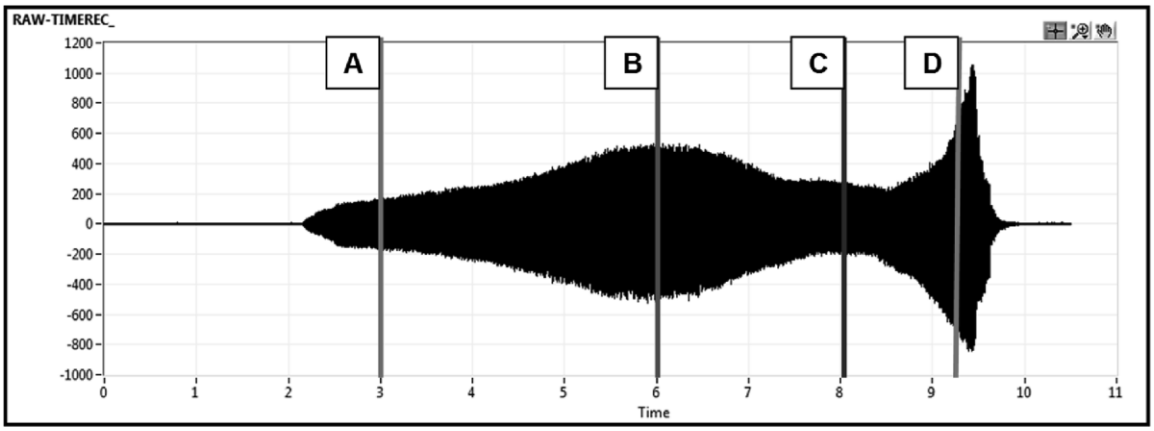

Figure 19 Acoustic signal of material subjected to clusters impact. Fast Fourier transformation spectra in dependence on time of the experiment a) initial section with no visible cracks b) area without significant plastic deformation c) area above the yield strength of the material, the region with a high density of signs of plastic deformation d) area above the ultimate strength of the material with strong material disintegration [48]

2.5.2 PWJ induced surface roughening

The highly studied potential use of this technology is surface roughening. The possibilities and advantages of using PWJ for this application are described in this chapter. A significant part of research concerning the application of PWJ for surface roughening belongs to the preparation of bioactive surfaces [74] or bone cement [75]. The surface with micron scale topography enhances the biological processes in both in vitro and in vivo conditions [76]. The PWJ technology is a very attractive method for use in surface roughening of joint implants. The main potential advantage is the lack of embedment or foreign particles introduced to the surface of joint replacement. Currently used grit blasting or AWJ can lead to some level of particle embedment causing a contamination [75] . Sourd et al. [9] used a pure water jet after an AWJ for a milled titanium surface to remove the aforementioned embedded particles. The researcher found out that plain water jet cleaning was effective in reducing the particle contamination by 65% for process parameters (SOD = 100 *mm* P = 254 *MPa* v = 2 *mm/min*). For the evaluation of contaminations, back scattered electron observation was used. Bergs et al. [42] compared the post-treatment by pure water jet suspension and injection abrasive water jets on the surface of 42CrMo4 steel. The post-treatment (P = 200 and 500 *MPa* v = 5000 and 2000 *mm/min*) showed the geometrical effect on the already treated surface. Surface embedded particles were removed; however, the research lacks a BSE or chemical analysis of the treated surface. Surface roughening without contamination of the roughened surface with foreign particles is very critical for the preparation of implants [77]. Barriuso et al. [78] used a pure water jet for surface roughening of titanium alloy and austenitic stainless steel to avoid contamination. However, the lack of abrasives needs to be compensated with high pressures (360 *MPa*) and low traverse speeds (0.05-0.1 *mm/s*). It is a generally accepted fact that rough surfaces have a beneficial effect on cellular activity compared to smooth surfaces [79]. This is the reason for joint replacement implants roughening by methods such as sandblasting or acid etching. Kalliecharan et al. [80] treated medical-grade titanium alloy Ti6Al4V using a PWJ to roughen the surface. The feed rate of 75 *mm/s* produced roughness of Sa = 5 μm, which is comparable to the typical roughness of used implants. The grain boundaries of titanium were exposed during the process and grain/phase boundaries emerged. This treatment contributed to the removal of the weaker β-phase. The β-phase was located around the α-phase grain boundaries. The PWJ treatment showed a promising increase in macroscale as well as nanoscale roughness. During

the experiment, only a small increase of TiO2 phase content was observed, which could improve the chemical inertness of the treated area. In vitro response of PWJ treated titanium alloy was observed by Steeves et al. [74]. The experiment examined the effect of surfaces treated by PWJ with varying feed rates (450; 500; 600; 800 *mm/s*) with pressure of 69 *MPa* and frequency of 40 *kHz*. The treated surfaces were compared to untreated surface (cold rolled, unpolished). The surface analysis was conducted using atomic force microscopy. The fibroblastic cells were then applied to the material surface. It was evaluated which surface is the most beneficial for cell cultivation and growth. While the relative proliferation was lowest for treatment with the feed rate of 450 *mm/s* then increased for the feed rate of 600 *mm/s* and further increased for feed rate of 800 *mm/s*. While the proliferation of the sample treated with feed rate of 800 *mm/s* was similar to that of the reference sample (cold rolled), the treated surface shows a higher degree of surface homogeneity [74].

2.5.3 PWJ induced surface hardening

PWJ based surface hardening is the third researched potential field of use of PWJ. The fatigue loading and stress corrosion cracking of engineering materials are effectively altered by a combination of surface roughness, residual stress distribution and degree of plastic work introduced to the surface [81]. Shot peening (SP) uses solid particles, to impinge the surface of the treated material at high velocity to change the surface and subsurface properties. The impact can be also generated by different physical phenomena such as the collapsing of cavitation bubbles [82], laser shock peening [83] and ultrasonic peening [84]. All these methods increase surface roughness and create compressive residual stress under the treated surface. The compressive residual stress leads to an increase in the hardness of the affected area. Furthermore, De Los Rios et al. [85] showed that compressive residual stresses reduced fatigue crack initiation and crack propagation, therefore enhancing fatigue life. This relationship between compressive residual stresses and fatigue life was studied by Torres et al. [86]. It is important to note that created roughness, as well as stress distribution, are different for different peening mechanisms [82]. Zhou et al. [87] observed that the fatigue life depends on compressive stresses induced near the surface and strain applied during the fatigue testing affects the relaxation of these residual stresses. Surface hardness increment can also increase further resistance to a number of wear mechanisms, such as abrasive wear [88]. It has been already proven that PWJ interaction with the surface increases the hardness of the surface layer and introduces compressive residual stresses [12, 13]. To understand and compare the results the conventional as well as new promising technologies of surface hardening will be introduced. These methods will be then in the last chapter compared to results considering PWJ technology.

In the next subchapters, the first conventional SP will be briefly described as it is longer researched method that show similitude to most non-conventional hardening types including pulsating water jet peening (PWJP). Next continuous water jet peening (WJP) and water jet cavitation peening (WJCP) will be described. This will be followed by a subchapter describing the most recent breakthroughs in PWJ peening research. Two competitive modern methods of surface hardening will be introduced and finally all described methods of surface hardening will be compared.

The conventional method of surface hardening will be introduced in following paragraphs. One of the most common methods to prolong the service life of engineering components is

surface hardening (peening). Surface hardening increases mainly high cycle fatigue life due to the induced crack closure phenomenon based on the underlying stress field [89, 90]. SP is the most prevalent from the wide array of peening methods [81]. SP is a cold working process during which the component surface is subjected to impact of small spherical media known as the shots. Each shot creates a small surface indentation, which deforms the surface in tension. The adjacent elastic material creates a residual compressive stress field [85]. This is caused by local misfit with unstrained material beneath normal surface. This causes elastic response, which generate in-plane compressive residual stresses near the surface. These are balanced by tensile residual stresses beneath [81]. However, the surface roughening created by the sum of small indentations can have detrimental effect. High surface roughness provides sites for crack initiation and leads to shortened fatigue life [91]. This means that the effectivity of SP is determined by resulting residual stress distribution, surface roughness and level of plastic work. The disadvantages of SP were described by Montross et al. [92]. The SP was in the past described semi quantitatively by peening intensity provided by treating Almen type gage. This method may not guarantee uniform SP intensity across the component. Another disadvantage is surface roughness and topology after the process. Finally, induced compressive stresses have a limited depth not exceeding 250 μm for soft metals and less for hard metals [92]. This has also given rise to modern methods of surface treatment competitive to SP.

De los Rios et al. [85] described near surface stress distribution by four parameters as seen on **Figure 20**. The surface stress (SS) is stress directly at the surface. The maximum compressive stress (CS_{max}) is found slightly below the surface. The depth at which residual stress changes orientation (d) and maximum tensile stress (TS_{max}). De los Rios et al. also observed the magnitude of residual stress dependency as primarily a function of material properties rather than peening properties, maximum compressive stress at half of the yield strength of material [85]. The depth is influenced by peening parameters and for steel and titanium are constant with intensity, while for aluminium being also dependent on shot size [85]. The compressive residual stresses increase the fatigue life making nucleation and propagation of fatigue cracks more difficult due to crack closure phenomena[89, 90].

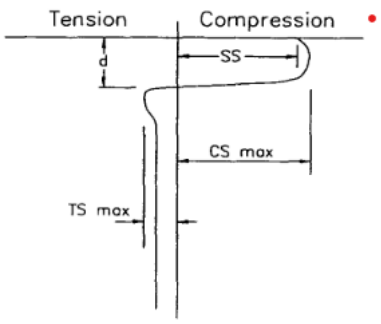

Figure 20 Schematic of residual stress distribution after shot peening [85]

Torres et all [86] observed on AISI 4340, that the compressive residual stress field pushed the crack sources beneath the surface of the material in a most medium and high cycle fatigue test. In the case of low cycle fatigue tests and untreated samples, cracks initiated from the surface. The results showed increased fatigue life of AISI 4340 due to compressive residual stress field. Maleki et al. [93] observed surface hardening of several carbon steels and observed hardening and grain refinement in subsurface layer based on peening parameters and material parameters.

Maleki processed hardness and surface measurements by a seven parameters neural network. Parameters describing the peening process were shot diameter, projection pressure, Almen intensity and peening duration. The parameters describing the material were carbon content, yield stress of the material and ultimate stress of the material. The results suggest that peening duration importance on the result from peening parameters has 59 % importance compared to shot diameter 17% and projection pressure 24 % if considering only these three parameters. From the material point of view of the three considered parameters, the ultimate stress has 40% significance, yield stress has 34 % significance and carbon content has 26 % significance [93]. Katsuji Tosha [94] observed the effect of hardness increment and compressive stress increment caused by SP. Tosha explained the relationship between compressive stress and hardness increment for SP and sheet bending. The results in the case of SP are shown in **Figure 21**. The measurement is done by measuring hardness and residual stress on the side opposite to the peened side, while after each measurement removing layer by layer of total sample thickness by etching. The hardness decrement plotted against the decrement of compressive residual stress shows that negative hardness decrement is in proportion to the decrement of compressive residual stress [94]. This describes the relationship between residual stresses and hardness. Therefore, a number of research of peening optimization of the effect of peening parameters used on surface hardness and roughness due to the availability, comparability, and reliability of these measurements. Omari et al. [95] used such a combination (hardness, roughness) for optimization of peening parameters (pressure, exposure time) on aircraft turbine blade material carbon steel 1070 [95]. The aim is again to maximize hardness while minimizing surface roughness.

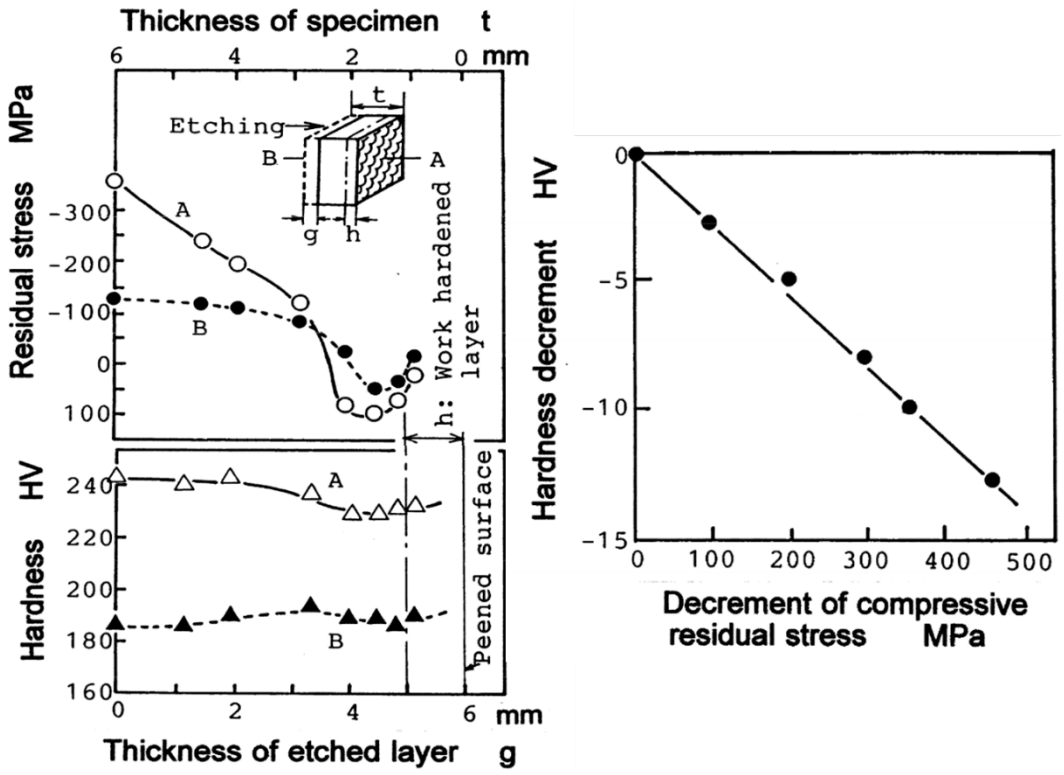

Figure 21 Comparison of residual stress evolution and hardness evolution in the shot peened sample [94]

Figure 22 shows parameters influencing the SP results. The parameters are divided into three logical groups: peening medium, peening device (process) and workpiece. The resulting parameters are material hardening (hardness increase), residual stress profile and roughness. In industry, most parameters are hard to control or are not controllable at all [96]. For this reason, in industrial praxis, the two parameters Almen intensity and peening coverage are used to control the SP process. Ahmed et al. evaluated the effect of ball size, Almen intensity, and coverage on the depth profile of 316L stainless steel [97]. He found that peening coverage and Almen intensity improve microhardness and compressive residual stresses of treated surface [97]. For numeric optimisation the most used objective function to determine the peening effect is the distribution of the residual stress and secondary surface roughness [96]. The most notable disadvantage of SP is relatively high surface roughness based on process parameters. The surface roughness must be even minimized by polishing, grinding or second peening step after peening in some applications. The second disadvantage is the inaccessibility of some structural areas to SP such as notches and fillets [98].

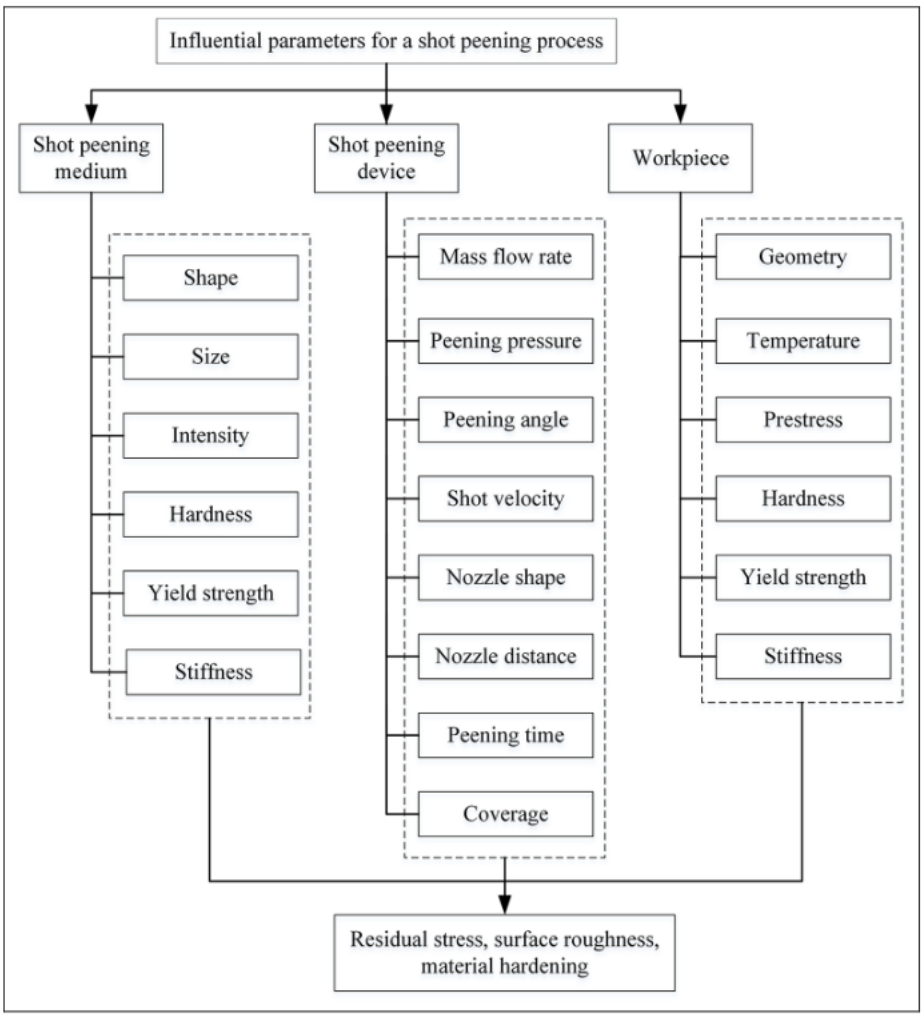

Figure 22 parameters influencing the result of shot peening process [96]

Continuous water jet based surface hardening can be divided into two categories: Water jet peening (WJP) and Abrasive water jet peening (AWJP). In the case of WJP the hardening is just due to the effect of pressure created by water impacting the surface. During the AWJP

hardening is a combination of the effects of pressure created by water impact and flow and pressure created by solid abrasive particles impacting the surface at high speed. The effect of single pass of the pure water jet on the solid material stress state was simulated by He et al. [99, 100]. He concluded that residual stress is induced due to unrecoverable elastic strain blocked by the plastic strain of the adjacent material. This led to an increase in microhardness and an improvement of fatigue life due to compressive residual stresses. **Figure 23** show the mechanism of residual stress field creation due to the single pass of the water jet. This analysis is related to the position C chosen at the surface. **Figure 23a** shows the jet approaching the position, hitting the exact position of C (**Figure 23b**), then leaving the examined position (**Figure 23c**). **Figure 23d** shows area after treatment. The effect of the jet is described as follows: as the jet approaches C the elastic strain is forming due to the effect of the water jet. As the jet draws closer the plastic strain is also formed under the jet. When the jet is above the C point a semi-circular region of elastic and plastic strain is created directly under the jet. When the jet leaves the induced stress decreases due to weakening of the pressure from the jet, as the jet moves further away. The elastic recovery occurs but the plastic strain remains. As the jet leaves the region of plastic strain remains the same and hinders full recovery of the elastic region. This creates a new stress equilibrium [100].

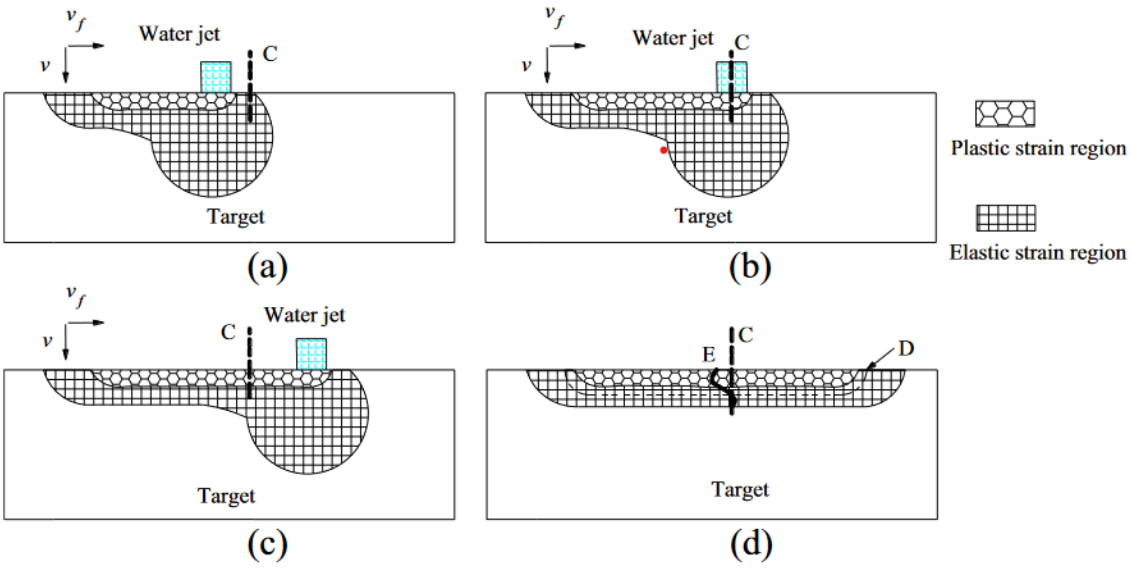

Figure 23 Schematic of single pass pure WJP residual stress field creation [100]

Azhari et al. [64] observed the effect of multiple passes of the pure water jet on the surface of the material. Azhari focused on several WJP parameters, namely pressure, number of passes and feed rate. Based on parameter inputs Azhari et al. [64] evaluated surface roughness, surface microstructure, and subsurface hardness of AISI 304 (X5CrNi18-10). Azhari et al. divided surface damage types into two levels initial damage and evolved damage. The surface roughness increased with an increase in pressure and number of passes and decreased with increase in feed rate. Pressure increase led to an increase in hardness (compared to untreated material) of 16%, 27% and 31% for pressures 100, 200 and 300 *MPa*, respectively. The thickness of the hardened layer also increased with the increase of pressure from 150 μm for the lowest pressure to 400 μm for the highest pressure [64].The Azhari et al. [64] also described the effect of feed rate on hardness with feed rate levels of 1000 *mm/min*, 2000 *mm/min* and 3000 *mm/min*. A slower feed rate results in higher surface hardness and higher hardened depth. The increase in maximum hardness of 27% 14% and 12% was achieved with feeds of 1000

mm/min, 2000 *mm/min* and 3000 *mm/min* and pressure of 200 *MPa*. Increase in number of passes leads to higher maximum hardness increase of 12%, 14% and 22% for a number of passes 2, 4, and 6 with the pressure of 200 *MPa* and feed rate of 2 000 *mm/min* [64]. Azhari et al. [65] followed with an experiment with similar scope in variables (pressure, feed rate, overlapping) on aluminium alloy 5005. The parameter ranges were the number of passes between 1 and 3, the pressure between 50 and 150 *MPa*, the feed rate ranged from 500 to 1500 *mm/min* and the standoff distance ranged from 20 to 60. The experiment parametrisation was designed by Box Behnken experimental design. The achieved roughness R_a μm after peening ranged from 0.51 to 16.42 compared to untreated material roughness of 0.49. The hardness increment was divided into three groups. At first, hardness increment of specimen with low roughness below 1 μm. This group shows almost no change in hardness values. Second is a group with intermediate roughness (1 μm to 10 μm) where an increase in hardness is significant close to the surface and decreases farther from the surface (up to 200μm). Finally, runs with high roughness above 10 μm showed significant hardness increase up to 300 μm. An interesting result is however that the highest measured hardness is not directly under the surface but at a depth of 80-120 μm [65]. Azhari et al. [65] created a predictive model for roughness (Eq. *(15)*) and hardness (Eq. *(16)*) based on 29 experimental runs:

$$R_a = -12.774 - 4.038n + 1.360 \times 10^{-1}p + 7.130 \times 10^{-3}u + 1.634 \times 10^{-1}h + 1.521 \times 10^{-1}nh - 3.0 \times 10^{-4}uh \quad (15)$$

and

$$HV = 47.908 + 1.016n + 1.092 \times 10^{-1}p + 3.15 \times 10^{-3}u - 3.3 \times 10^{-4}p^2 - 2.5 \times 10^{-6}u^2 \quad (16)$$

where n is a number of passes, p is pressure *MPa*, u is feed rate *mm/min* and h stands for standoff distance *mm* [65]. Modification of the pure water jet peening process was studied by Grinspan et al. [67]. Grinspan used oil ISO VG68 as a hydraulic medium instead of water. The oil properties are density of 884 kg/m^3 and kinematic viscosity of 62.5 to 73.5 mm^2/s. This experiment produced a work hardened surface similar to pure water peening. The introduced residual stresses to AA6063 are about 50 *MPa* varying with tested standoff distances [67]. The dependence of hardness can be seen in **Figure 24**. The highest hardness was achieved with the smallest standoff distance and with increasing standoff distances hardness decreased significantly. The highest hardness was also achieved directly under the surface and decreased to 400 μm.

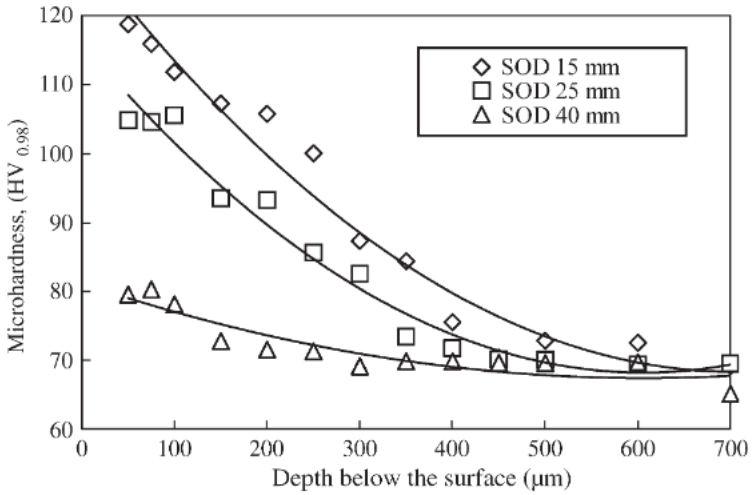

Figure 24 Oil jet peening dependence of hardness on depth below surface based on the standoff distance [67]

Arola et al. [101] studied the effect of AWJP on compressive residual stress, surface texture and fatigue strength of stainless steel (AISI 304) and titanium alloy Ti6Al4V. These materials are often used in orthopaedics. Arola et al. experiment showed that in case of AWJP of austenitic stainless steel both compressive residual stress magnitude as well as surface roughness increased primarily with increasing of the jet pressure and abrasive particle size. Arola et al. [101] used the AWJP method to treat the cylindrical fatigue samples. SEM observation showed surface contamination of the fatigue samples by abrasive particles. The achieved results in fatigue were summarised as increments in endurance strength. The fatigue testing was done at room temperature under fully reversed fatigue (R = -1) using a rotating bending machine. Untreated Ti6Al4V endurance strength was 680 *MPa*. AWJP conditions were selected from flat sample AISI 304 residual stress analysis, where one condition corresponds to minimal residual stress (low stress) created and the second condition (high stress) corresponds to maximal residual stress created. Treatment led to endurance strength (1×10^7) of 695 *MPa* and 724 *MPa* respectively. Increment in endurance strength (1×10^7) of Ti6Al4V samples was 3% and 6%. For 316L stainless steel untreated endurance strength (1×10^6) was 342 while after treatment the endurance strength rose to 370 and 382 *MPa* for low stress and high stress. The increment achieved was therefore about 10 % [101].

Cavitation based surface hardening can be confused with water jet peening. Both are produced using water jet technology and fast flow of water so some authors use these terms interchangeably [102, 103]. There is one significant difference, however. Water jet peening use water column impact to induce plastic deformations in the surface layer by liquid collision [104]. The cavitation peening uses shockwaves created by collapsing cavities, i.e. gas bubbles, created inside the water stream. The schematic of the water jet cavitation peening (WJCP) process can be seen in the **Figure 25**. The figure shows stream of water exiting the nozzle and at a given speed entering the body of water. The water jet produces cavitation bubbles under certain conditions. When the bubble collapses close to the material surface it produces a shockwave of significant pressure that is enough to cause plastic deformation in the material. The cavitation causes significant damage in hydraulic machinery, but the same effect can be used for peening by varying the exposure time of the surface to the cavitation phenomenon.

There are four stages of the cavitation phenomenon based on exposure time. These are the incubation stage, acceleration stage, maximum rate stage and deceleration stage. For the cavitation peening it is necessary to stay within the incubation stage of cavitation damage. Soyama et al. reported [105], that the processing time of cavitation peening lies in interval 4 % to 20 % of the incubation stage period [105]. The cavitation bubbles are created due to a phase change from liquid to gas by a decrement in pressure due to an increase in velocity [106]. This can be expressed [105] by the Bernoulli Eq. (17):

$$\frac{1}{2}\rho_L v^2 + p = const \tag{17}$$

where p is pressure ρ_L is the density of the liquid and v is the velocity of the liquid. Cavitation number σ_c the parameter describing cavitating flow can be described [105] by Eq. (18):

$$\sigma_c = \frac{p - p_v}{\frac{1}{2}\rho_L v^2} = \frac{p_2 - p_v}{p_1 - p_2} \approx \frac{p_2}{p_1} \tag{18}$$

In this case p_v is static pressure, p_1, p_2 are upstream and downstream pressures in the orifice or nozzle. Therefore, σ_c is the ratio of dynamic pressure defined with velocity and static pressure. In the cases of cavitating jet the simplification in Eq. (18) is possible because $p_1 >> p_2 >> p_v$ [106]. To generate cavitations by hydrodynamic effect for cavitation peening narrow flow passage is used, for example Venturi tube orifice or nozzle.

The cavitations can also be achieved using the acoustic cavitation effect. This happens when ultrasonic waves are propagated through the liquid and are causing mechanical vibrations of the liquid. This leads to cavitation nucleation in air bubbles contained in liquid [107]. This type of ultrasonic cavitation peening (UCP) was used for erosion testing by Janka et al. [108] who used this method for testing of erosion resistance of stainless steel EN 10088-3 (1.4301) and aluminium alloy EN AW 2030 T3. During the experiments they observed incubation period before the material loss. Significant surface hardening of both materials was observed. After the incubation period the material loss rate increases. The incubation period for experimental conditions was 90 min for stainless steel and 5 min for aluminium alloy [108]. The incubation period achieved using ultrasonic cavitation peening was also observed by [109]. The incubation period is the period best suited for peening as it creates hardening while not removing material on a macroscale. Bai et al. [109] observed the effect of current driven ultrasonic horn. The highest hardness was measured at the end of the incubation period for each experimental condition [109].

Balamurugan et al. [103] utilized the cavitation peening technique for residual stress increment of difficult to reach structures. Successful peening of the teeth root region of forming tool proved the usability of cavitation peening for hard-to-reach places. During the research, the effect of the impinging angle on the surface was studied. The maximum residual stress was caused by treatment at an angle of 45 degrees for pressure of 27 *MPa*. Seki et al. [110] achieved an increase in rolling contact fatigue life after cavitation peening comparable to fine (0.1 *mm* shot diameter) SP [110]. Kim et al. [111] observed the effect of cavitation peening on the electrochemical characteristics of Al/Mg alloy. Kim achieved lowering of corrosion current by applying cavitation jet peening [111] . This means that cavitation jet peening can influence the corrosion properties of the surface. Considering pure metals Ju et al. [112] observed

the effect of cavitation peening on commercially pure titanium. The researcher focused on residual stresses and hardness. The research also included OM and electron microscopy. The TEM study was focused on twinning formation, dislocation structure, and twinning interaction due to plastic deformation. The researcher found compressive residual stress to a depth of 150 μm and concluded that enhancement by cavitation peening is related to deformation twining as well as dislocation structure [112].

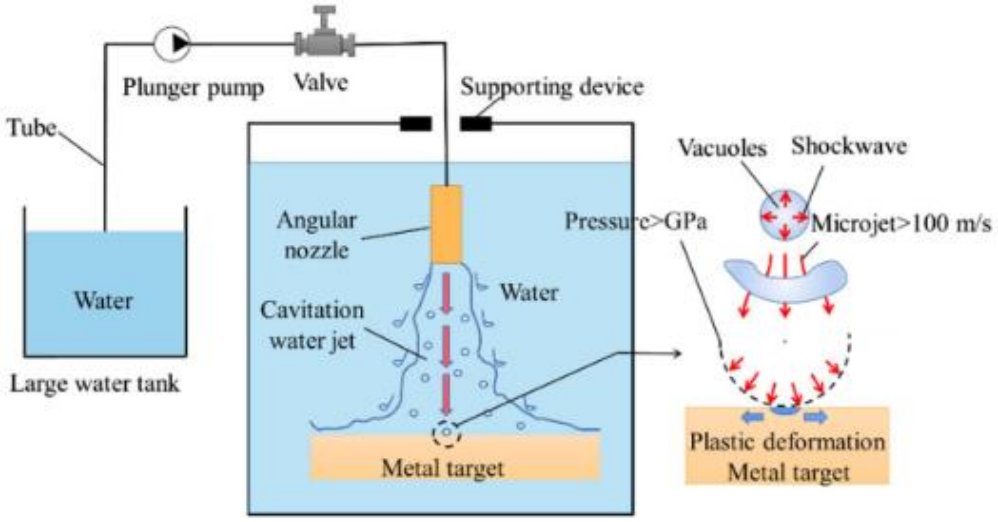

Figure 25 Schematic of cavitation affecting the surface [113]

PWJ based surface hardening will be described in the next paragraphs. Ultrasonically modulated PWJ is examined as a tool for surface hardening. Surface hardening is caused by plastic deformation of the subsurface generated by liquid cluster impact. Water jet surface hardening research considering pure water jets, abrasive water jets and cavitation jets was introduced. Finally, now the possibility of using PWJ as a tool for surface hardening is examined.

Surface hardening caused by PWJ also known as pulsating water jet peening (PWJP) has been examined in a small number of studies [12, 13, 114] compared to SP. SP uses solid particles, to impinge the surface of the treated material at high velocity. PWJP shows similitude as fast traveling liquid cluster hits the surface of the treated material. The plastic deformation caused by the first erosion (incubation) stage [36] is accompanied by an increase in dislocation density. This leads to the surface hardening. Similarly, to other methods of surface treatment the interplay between residual stress field, plastic strain and associated roughness determines the effectivity of the treatment [81]. Srivastava et al. [12] used PWJ for the treatment of welded joints from stainless steel AISI304. The pressure of the PWJ varied from 20 to 60 *MPa*. Each pressure level was assigned a specific standoff distance (20 *MPa* => 45 *mm*, 40 *MPa* => 70 *mm* and 60 *MPa* => 100 mm). The feed rate was also variable from 0.25 *mm/s* to 2 *mm/s* for 20 *MPa*, and up to 6 *mm/s* for 60 *MPa*. The resulting surface was then observed using optical microscopy, X-ray diffraction and roughness measurement. The optical microscopy found slip bands and twins created by sample preparation as well as plastically deformed zones at places of PWJ interaction. The PWJ treatment led to an increase in compressive residual stresses from -67 *MPa* to -322 *MPa* in the welded region and from -122 *MPa* to -499 *MPa* in the heat-affected zone (HAZ) at a pressure level of 20 *MPa*. The surface roughness increased the most (from Ra 1.48 μm up to Ra 3.47 μm) for the following parameters: pressure 40 *MPa*, SOD 70 *mm*, and

feed rate of 3 *mm/s*. The surface roughness then decreases with an increase in feed rate. The hardness increase was observed to the depth of 200-250 μm for higher pressures (40-60 *MPa*) and only to 150 μm for lower pressures. The maximum observed hardness increase was achieved by 40 *MPa* in HAZ from 3.12 *GPa* to 5.43 *GPa* [12]. The treatment of austenitic steel welded joints by PWJ proved to be effective in further study [115].

Srivastava et al. [12, 114] continued in this line of research and expanded previous knowledge for higher pressures 40-100 *MPa* at lower standoff distances: 15, 23 and 25 *mm* on step trajectory. Residual stress in this experiment changed significantly for all experimental conditions. The highest change was observed always for 40 *MPa* and then diminished with an increase in pressure. The observed change was from about 75 *MPa* tensile to about -525 *MPa* compressive stress achieved by treatment with 40 *MPa* at v 5 *mm/s*. The feed rate also showed a negative effect on induced compressive residual stress. The highest roughness was achieved similarly using the slowest feed rate of 5 *mm/s* and standoff distance of 31 *mm* at the lowest pressure of 40 *MPa*. Observed hardness increased from 350 HV for untreated material up to 550 HV. The most significant increase in hardness was induced by the lowest feed rate. Again, an increase in pressure lowers the hardness [114]. The author suggested that diminishing returns when increasing pressure is due to velocity fluctuations not being able to split the higher-pressure jet completely at small standoff distances. Lehocka et al. [116] compared the erosion of stainless steel EN X5CrNi18-10 in annealed state and aluminium alloy EN-AW 6060 in an artificially aged state. The jet parameters were set to 70 *MPa* for a nozzle diameter of 1.19 *mm*. Traverse speed was set to 100 *mm/s* (200 impacts per mm) for stainless steel and 660 *mm/s* (30 impacts per mm) for aluminium alloy. The observable deformation was observed for aluminium alloy. The stainless steel showed the beginning stage of deformation i.e. small erosion pits, depression and plastically deformed subsurface area. The important result however lies in the hardness observation. The stainless steel shows an 11% higher hardness value under the affected area compared to the centre of the sample. Furthermore, the observable plastic deformation zone is up to 200 μm. Compared to that decrease in hardness value of 18 % was observed on the treated aluminium surface [116]. Hloch et al. [47] observed the effect of PWJ on the surface of austenitic stainless steel AISI 304. During the experiment, SOD of 5-101 *mm* and waterjet pressure of 40-100 *MPa* varied. They observed not only depth and surface morphology but the hardness of the cross-section as well. The hardness measurements were performed for standoff distances of 37 *mm*, 53 *mm*, and 73 *mm*. The best increase in microhardness was achieved for p = 80 *MPa* and SOD 37 *mm*. The hardness of the material increased from the initial value of 192 HV0.05 to 393 HV0.05. The biggest measured microhardness was always at the closest point to the treated surface (50 μm). Interestingly SOD 37 *mm* is for 80 *MPa* closer to the incubation regime than to the culmination stage. The hardness decreases with an increase in distance from the surface. This is in the article attributed to changes in dislocation density, though the dislocation density was not observed in the article. For all pressure levels (40-100 *MPa*) the maximum hardness was measured at the standoff distance of 37 *mm* and then decreased for SOD 53 *mm* and increased again for SOD 73 *mm* [47]. The measured hardness was inversely correlated with the measured depth. The observed results were surface topography, microstructure, and microhardness on the cross-sectional cut.

Stolárik et al. [13] examined the effect of the PWJP treatment pattern as well as pressure on surface roughness and microhardness of treated aluminium alloy EN AW–1050A. The treated surface was analysed using measurement of surface roughness parameters and microhardness.

The appearance of erosion was observed by scanning electron microscopy. In the experiment, three distinct pressure levels 10, 20 and 30 *MPa* were selected. Chamber length, as well as standoff distances, were set accordingly. The variables are then feed rate *mm/s* and pattern type. Two pattern types were used linear-hatch pattern and crosshatch pattern. For the crosshatch pattern, the feed rate is twice the amount of the feed rate of the linear hatch. The roughness parameters increased with an increase in jet supply pressure. The lowest roughness value (Ra 1.89μm) was observed for the 10 *MPa* crosshatch pattern. The highest roughness value (Ra 4.11 μm) was achieved by a 30 *MPa* linear-hatch pattern. The mean microhardness shows an increasing trend with an increase in PWJP supply pressure. The maximum observed hardness increase was 16.62 % compared to unaffected material for the crosshatch pattern. Both the roughness and hardness may be attributed to an even distribution of impacts across the whole surface compared to the unidirectional distribution of the linear hatch pattern [13].

One of the first study of the ultrasonically induced PWJP fatigue life enhancement was carried out by Hlaváček et al. [117] The PWJ was applied to a cylindrical fatigue sample made of austenitic steel 316L. The parameters of the jet were set to achieve the first stage of erosion in the material, which corresponds to plastic deformation of the surface. The plastic deformation in the surface should create compressive residual stresses, which counteract the initiation of the fatigue cracks. On the surface of the impacted area, the number of slip bands was documented using SEM and AFM. The bands observed (**Figure 26**) differ from bands created during standard fatigue tests as they consist of sharp steps. These steps were recognized as preferable places for nucleation of the fatigue cracks. The hardness increment was not observed by the Vickers hardness testing method (**Figure 27a**). It can be interpreted that the increase in hardness is in the lesser depth below the surface than the closest indent (60 μm). However, the fatigue test (**Figure 27b**) shows that SN curves of samples treated by PWJP show more than 2.5 higher number of cycles to failure for the low-stress amplitude area. These results show a beneficial effect of PWJP analogical to SP. However, balance must be established between surface hardening due to plastic deformation and surface roughening creating preferential places for fatigue crack initiation [117].

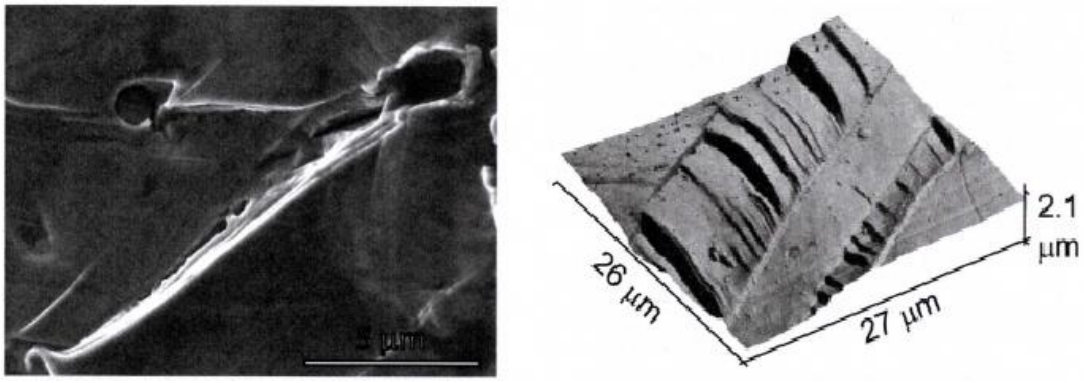

Figure 26 a) Detail of surface band containing small crack b) 3D mapping of surface bands created by AFM [117]

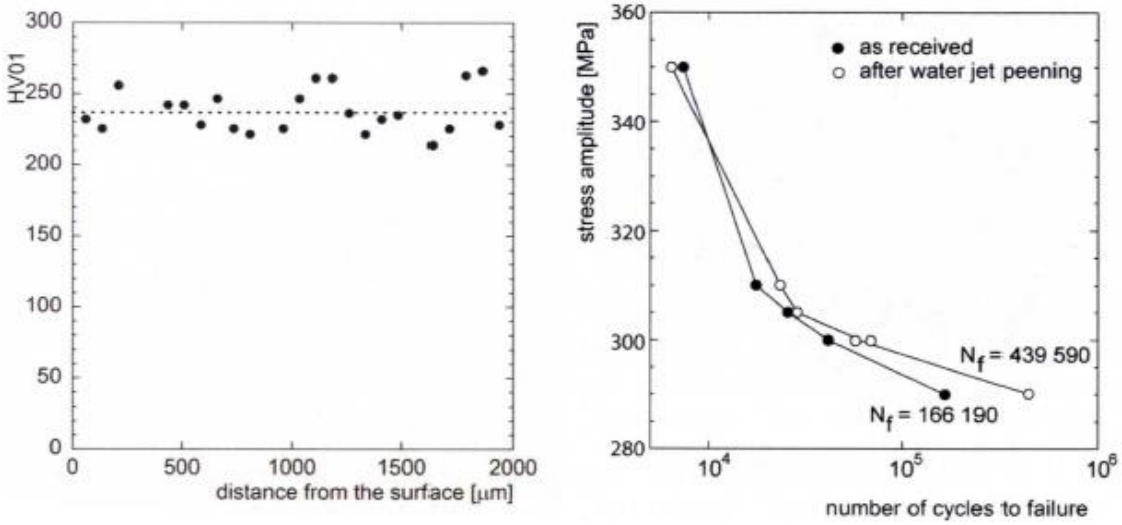

Figure 27 a) hardness measurement of the treated sample b) S-N curves of treated and as received sample [117]

Solid contact based surface hardening working on the principle of either continuous or discontinuous contact of the surface with the solid piece will be described. Some of the methods included are ultrasonic peening, hammer peening, and rolling. In his overview of hammer peening, Chan et al. [118] divided surface modification methods based on working mechanisms. Media-based processes include burnishing, deep cold rolling or hammer peening [118]. There is a considerable number of process parameters that need to be set for appropriate results including frequency, feed rate, amplitude angle of impact, indentation spacing, indentation diameter and overlapping. Hammer peening can be described as a process involving a hard hammer head oscillating at high frequency striking the surface and generating a deep layer of plastic deformation. The typical stress field and hardness field after the treated area are schematically shown in **Figure 28** [118]. The stress field and hardness field show a similar pattern as other hardening methods described in this work.

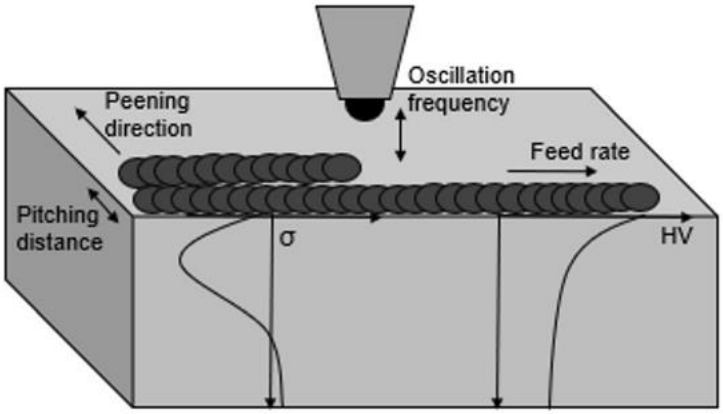

Figure 28 Hammer peening schematic of process and subsurface properties [118]

Ultrasonic peening treatment (UPT) works as follows. Low amplitude, high frequency ultrasonic oscillations are forced on the material through a number of rods or pins. The surface is subjected to severe plastic deformation that can lead to refinement of grain size, microstructure and even surface geometry. Surface microcracks are closed due to plastic

deformation and tensile residual stresses are eliminated. This means that UPT can increase microhardness, corrosion resistance, and fatigue life [119].

Deep rolling is another method that increases surface hardness by contact with a solid counterpart. In the case of deep rolling pressure is created by a hydraulic or mechanic source and transmitted through a ball or roller. In the case of thin parts that could bend two opposed rolling tools may be used. In the case of axially symmetrical components, three balls spaced by 120 ° may be used [120].

Laser shock based surface hardening most known as laser shock peening (LSP) is a technology that creates shock waves propagating through the material that alter subsurface material properties namely residual stress and hardness. The shock waves are created when the laser energy exceeds the ablation threshold of the material or coating. The layer is then evaporated. As the vapor continues to absorb energy from the laser, the vapor is converted to high temperature plasma. The shockwave is then caused by the rapid expansion of the plasma [121]. The schematic of this process is visible in **Figure 29**. The method can consist of placing an overlay on laser irradiated surfaces. The overlay can be a solid overlay or liquid water overlay combined with paint coating. The method using water liquid overlay was demonstrated by Fairand et al. [122]. The method can also be used without the protective overlay, this is then known as laser peening without coating [121]. The use of coatings transparent to the laser leads to increase in shock wave intensity by two orders compared to plasma generated by hitting metallic surface in a vacuum [123, 124]. The transparent coatings are known as overlays. Under overlay laser absorbent sacrificial coating can be placed to further increase the shockwave magnitude and protect the metal surface from ablation or melting. These coatings can be metallic such as copper, zinc, or aluminium. The organic sacrificial coatings such as black paint are used, too. The LSP process with sacrificial coating and confining medium generates a uniaxial compressive stress along the shockwave direction. The plastic deformation occurs up to the depth at which the peak pressure doesn't exceed the Hugoniot elastic limit. This constant is related to dynamic yield strength [92]. It has been observed that laser shock processing can produce compressive residual stresses in commercially pure aluminium alloys to depth of more than 1 *mm* [92]. The ability of the laser shock process to increase hardness was observed on many commercial metallic materials such as stainless steels, carbon steels, aluminium alloys, titanium alloys, and nickel based superalloys [92]. Nakano et al. [125] used hardness measurement with load of 0.1 *N* for 30 *s* at the side and top surface to measure the effect of process parameters of femtosecond laser. The process parameters observed were laser fluence *J/cm2*, and coverage *%* with a pulse duration of 191 fs at a wavelength of 800 nm. The maximum hardness increase was achieved from 200 HV up to 409 HV [125]. Similarly, Ebrahimi et al. [126] observed the effect of LSP on the hardness of ANSI 316L stainless steel. The effect of process parameters overlapping percentage, impact size and impact intensity was studied. The author used overlapping percentages to calculate average number of peening. The author reports increment of hardness up to 35% and an increment of corrosion results of about 100 *%* [126]. Zhou et al. reported surface nanocrystalization and martensite transformation due to LSP treatment, also on austenitic stainless steel 316L [127]. Kashaev et al. [128] observed the effect of LSP on thin AA2024 aluminium alloy. Kashaev observed similarities between residual stress profile and hardness profile in LSP treated area.

The LSP method is used in extent on titanium alloys for applications such as rotor blades where a combination of high hardness and low density is often required. Lu et al. [129] examined the effects of LSP on commercially pure titanium. Significant hardening of up to 41.42% was observed after three LSP impacts with hardened depth reaching up to 650 μm. By conducting the TEM analysis grain refinement due to LSP was proven. Four types of deformation induced features were observed in compression deformation zones, including layered slip bands, inverse transformation martensite, micro twin grating and micro twins [129].

Hongchao et al. [130] examined the effect of LSP on the surface of TiAl alloy (Ti-45.5Al-2Cr-2Nb-0.15B) and achieved hardness improvement of 30 % with laser pulse energy of 9 J. Interestingly, in this experiment is reported depth of hardened layer that is staggering 1.4 *mm.* Hongchao also tested the stability of the hardened layer and reported stability of 4 hours at a temperature of 700 °C [130]. Hongchao et. al. [131] continued with the investigation of the effect of LSP on Ti17 titanium alloy (Ti–5Al–2Sn–2Zr–4Cr–4Mo) varied a number of laser impact times and laser energy and achieved hardness increase from 320HV to up to 415HV for most severe experimental conditions. Hongchao also achieved significant fatigue life improvement of almost 14 times at a stress level of 250 *MPa* after LSP treatment[131]. In the case of Ti6Al4V, Kumar et al. [132] observed the effect of LSP on tribological properties of Ti alloy of the surface, namely fretting wear resistance. The treated surface showed an increase in hardness based on laser fluence and coating system from a base material hardness of 2.8 *GPa* up to 4 *GPa*. The depth of the layer was also dependent on laser fluence and coating system (in water, in air, in water with coating, in air with coating). Fretting was tested using chromium bearing steel AISI E52100 sphere ball (d = 6 *mm*) as a counterpart with a load of 10 *N* and 20 *N*. The fretting performance reported (displacement 100 μm at 10 *Hz* and 10 000 cycles) is of 89 % for LSP in air and 91% for treatment in water [132]. Zhang et al. [133] used LSP to improve fatigue life of Ti6Al4V alloy. The bending fatigue test was performed and an increase in fatigue strength (2×10^6) from 216 *MPa* up to 306 *MPa* was achieved using two successive laser shocks [133] .

Zhang et al. [134] is working on development of a method for the detection of hardness increase caused by LSP. The driving force behind the development of this new method is that conventionally used methods of hardness measurement result in damage to the workpiece or exhibit long detection cycles with low detection efficiency. The typically used methods are X-Ray stress measurement and microhardness tests as well as high cycle fatigue testing and hole drilling strain method. Zhang et al. [134] proposed method of hardness on-line monitoring based on extracting data using acoustic emission.

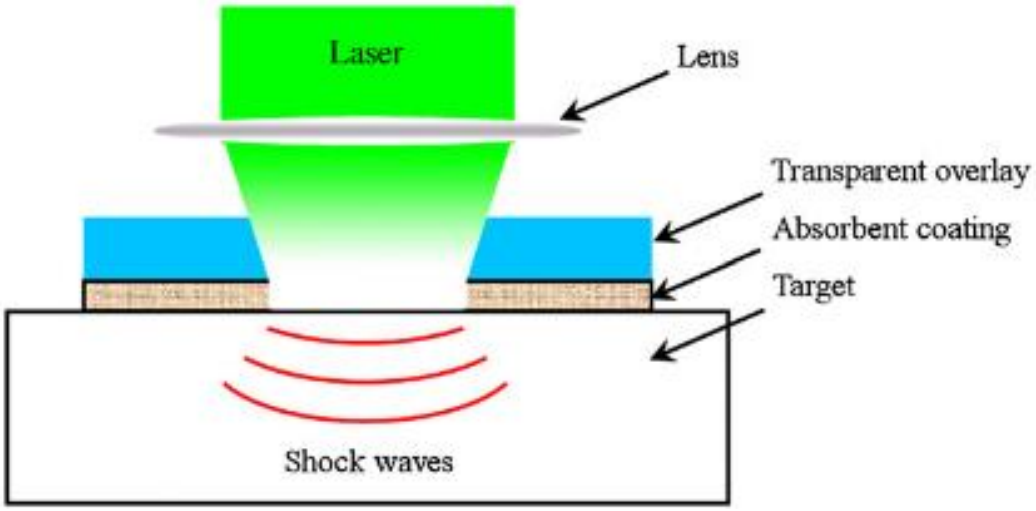

Figure 29 schematic of laser shot peening process creating shock waves in the material [133]

2.5.4 Comparison of different surface hardening methods

A number of methods are used to achieve the same thing, which is surface hardening due to increment of residual compressive stresses, while maintaining reasonable surface roughness. The differences can be summarized in the ratio of hardness increment and roughness increment and the depth profile of hardness or residual stress increment. The hardness and roughness development of the discussed peening applications is given in the **Table 3**. The graph below (**Figure 30**) shows a comparison of hardened depth for deep rolling, hammer peening, shot peening, and laser peening based on the work of Chan et al. [118] and Świetlicki et al. [107]. Seki et al. [110] compared SP with fine and normal (0.1 and 0.3 *mm* shot diameter) cavitation peening under similar achieved roughness. He found that in the case of contact fatigue life the normal shot peening is superior while cavitation peening and fine shot peening are comparable [110]. Soyama et al. [104] compared different surface hardening using compressive residual stress distribution based on the distance from the surface. Based on the results it can be concluded the high depth of compressive stress layer achieved by shot peening and cavitation hardening show more gradual gradient compared to the steeper gradient of the laser surface hardening. The **Figure 31** show effect of different surface hardening methods on the bending fatigue life. The positive effect of all tested surface hardening methods can be concluded from the graph. Shot peening show highest fatigue life at higher normalized bending stresses (1.5-1.6), while laser surface hardening and especially cavitation peening show increase in significant increase in fatigue limit. Waterjet peened sample showed closest behaviour to not peened samples with slightly higher fatigue limit. Most importantly, Soyama and Korsunsky [135] evaluated corelation between introduced compressive residual stresses and surface hardness in case of shot peened and cavitation peened surfaces as seen in **Figure 32**. Kumagai et al. [136] compared shot peening with laser peening and cavitation peening by residual stress development based on distance from the treated surface. Alongside stress analysis the research was expanded by nano-hardness measurement and EBSD analysis of cross-sections. The EBSD analysis **Figure 33** shows cross-sections of treated surfaces. The bottom line of the figure shows angular disorientation inside the angles. The misorientation is shown using grain reference orientation deviation (GROD). The GROD is high for the SP method for 80 μm examined. This contrasts with CP and LSP samples where GROD is the highest closest to the surface up to the first 40 μm. This is proof of different strain gradients based on the treatment methods observed.

Kumagai et al. also concluded that dislocation density after SP is about 2.5 times larger than CP or LP [136]. Wang et al. [137] compared the cross-sectional hardness profile created by ultrasonic impact peening (UIP) and LSP on 316L stainless steel. The depth profiles measured show significant hardness increase from 192 HV up to 433±16HV for UIP compared to 246 ±16HV of triple LSP. The conclusion was that UIP creates a larger micro-hardness increase compared to LSP[137]. The hardness profiles in his work show hardening caused by UIP deeper than 800 μm. LSP reaches the hardness of untreated material in depth slightly over 600 μm [137].

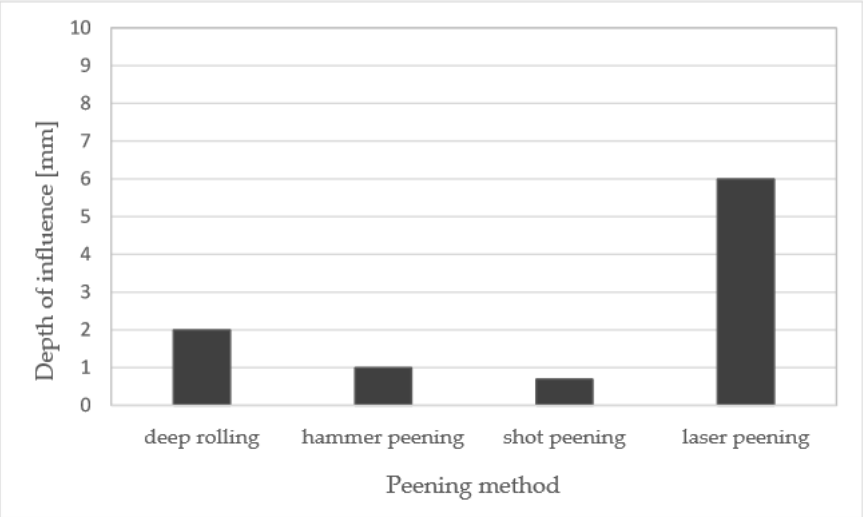

Figure 30 Affected layer depth based on the peening method [107]

Table 3 Comparison of different surface treatment methods and setups focused on surface roughness parameter and surface hardness achieved

Peening method	Material	Hardness initial	Roughness initial	Maximum hardness achieved	Correlative Roughness achieved	Source
SP	AISI 316L	~220 HV0.1	Ra 0.05	~405 HV0.1	Ra 0.77	[97]
SP	JIS: SCM415	760 HV 0.1	Ra 0.13	975 HV 0.1	Ra 0.27	[110]
SP$_{(FPP)}$	JIS: SCM415	760 HV 0.1	Ra 0.13	1170 HV 0.1	Ra 0.33	[110]
UPT	AISI 316L	192 HV 0.2	--	433 HV 0.2	--	[137]
WJP	AISI 304	230 HV0.01	Ra 0.15	~300 HV 0.01	--	[64]
WJP	Al alloy 5005	53.6 HV 0.01	Ra 0.49	61.3 HV 0.01	Ra 15.93	[65]
WJP	316 LVM	210 HV 0.01	--	300 HV 0.01	Ra 13	[78]
WJP	Ti6Al4V	320 HV 0.01	--	320 HV 0.01	Ra 11	[78]
WJP	AA6061-T6	111.5 HV 0.05	Ra 0.56	203 HV 0.05	Ra 2.79	[138]
AWJP	Inconel 718	490 HV 0.3	Sa 7.7	590 HV 0.3	Sa 9.06	[139]
AWJP	AA6063	91.2 HV 0.1	Ra 2.98	141.3 HV 0.1	Ra 4.06	[140]
AWJP	2205 DSS	306 HV 0.05	Ra 0.35	396 HV 0.05	Ra 3.8	[141]
UCP	Al alloy 5005	50 HV 0.2	Ra 0.1	76 HV 0.2	~Ra 6.6	[109]
UCP	EN 10088-3	~250 HV 0.02	Ra 0.8	547 HV 0.02	--	[108]
UCP	EN AW-2030 T3	~160 HV 0.02	Ra 0.8	184 HV 0.02	--	[108]
UCP	Com. pure Ti	151.6 HV 1	--	168.7 HV 1	--	[112]
WJCP	M2HSS	698.2 HV 0.1	Ra 0.110	1058.3 HV0.1	Ra 0.49	[103]
WJCP	5456-H116	98.0 HV 1	--	114.6 HV 1	--	[111]
WJCP	5083-H321	91.1 HV 1	--	112.0 HV 1	--	[111]
WJCP	JIS: SCM415	760 HV 0.1	Ra 0.13	888 HV 0.1	Ra 0.27	[110]
LSP	C. pure Ti	~173.5 HV 0.2	Ra 0.03	239 HV 0.2	--	[129]
LSP	Ti6Al4V	335 HV 0.05	--	~432 HV 0.05	--	[133]
LSP	TiAl alloy	~280 HV 0.2	0.05	377 HV 0.2	0.37	[130]
LSP	Ti17	320 HV0.2	Sa 0.082	415 HV 0.2	--	[131]
LSP	SUS 304	200HV0.01	--	409HV0.01	--	[125]
LSP	AISI 304	216 HV0.5	Ra 0.3	279 HV0.5	--	[127]

LSP	AISI 316L	192 HV0.2	--	246 HV0.2	--	[137]
LSP	AA2024	150 HV0.1	--	175 HV0.1	--	[128]
LSP	Al-6061-T6	~52HV0.05	Ra 0.72	~62HV0.05	Ra 2.60	[142]
PWJP	Ti6Al4V	349 HV0.05	--	437.3 HV0.05	Sa 2.96	[69]
PWJP	Ti6Al4V	349 HV0.05	--	376.7 HV0.05	Sa 3.14	[69]
PWJP	EN AW-1050A	40.3 HV0.05	Ra 0.852	47.5 HV0.05	Ra 3.78	[13]

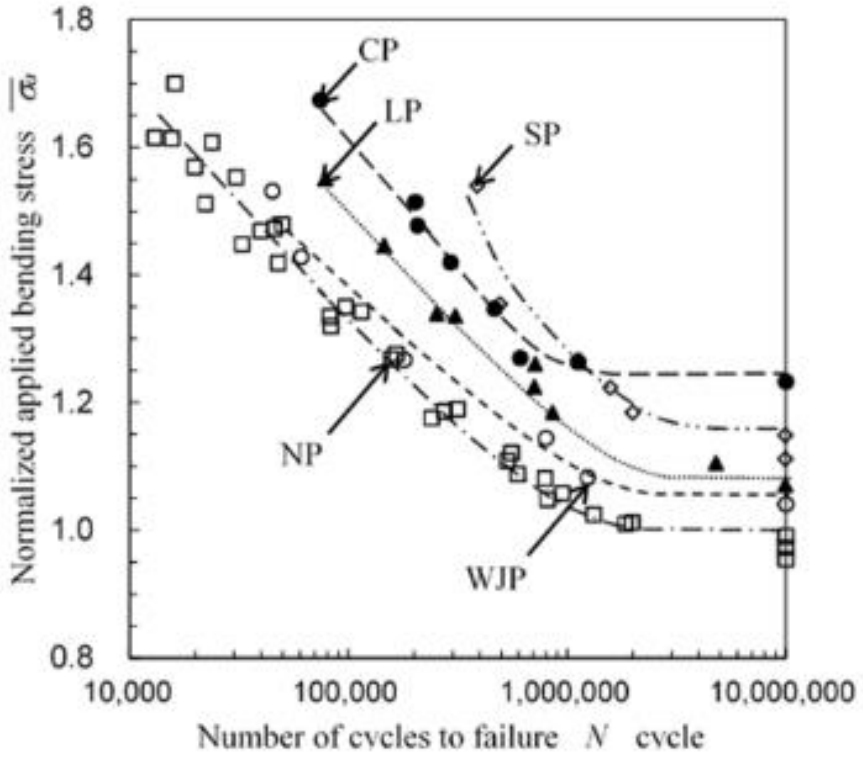

Figure 31 comparison of different surface peening methods on bending stress fatigue [105]

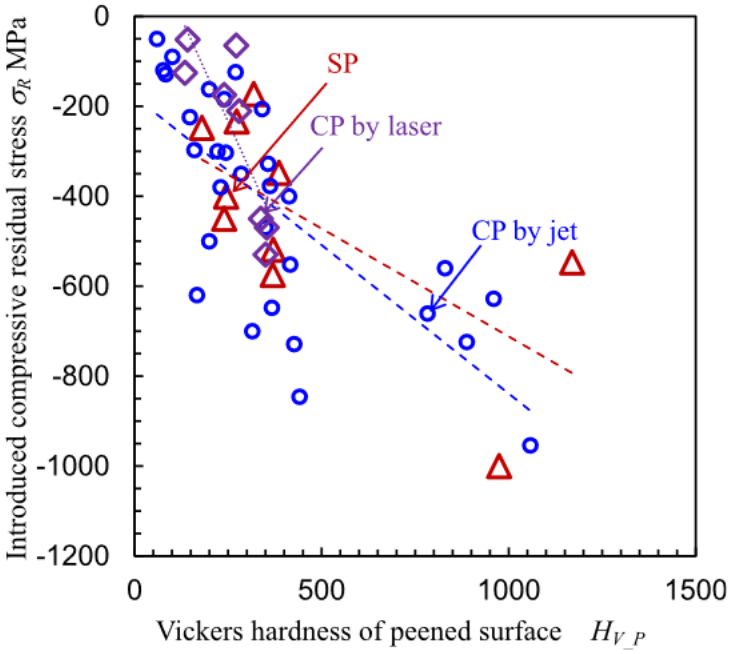

Figure 32 correlation between hardness of peened surface and induced compressive stresses by shot peening and cavitation peening [135]

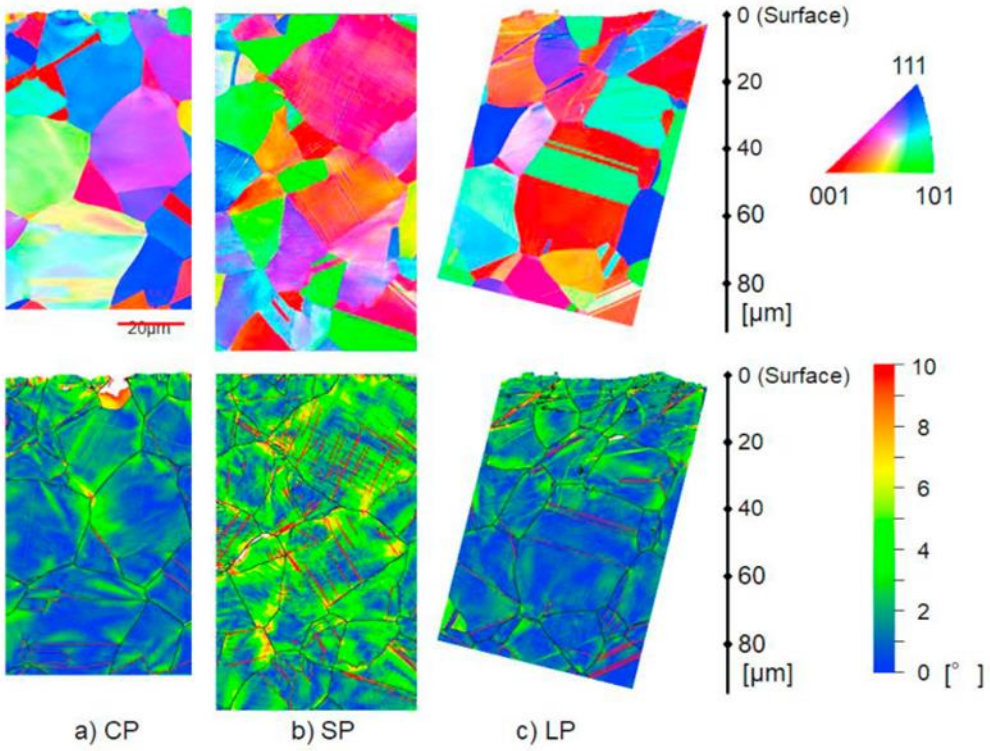

Figure 33 EBSD analysis of cross-section after a) cavitation peening b) shot peening and c) laser peening [136]

2.6. Research gap and plan of the experiments

Based on the literature summary presented above, considering the effect of liquid clusters impact on the surface of structural materials, the incubation erosion stage is mostly evaluated by roughness measurements while further erosion stages are defined by depth/volume removal or in some cases weight deductions. The methods used in this work aim to unravel the structural changes in the material caused by repeated cluster impact. The aluminium alloy and austenitic stainless steels were selected as model materials due to their low hardness and homogeneity. Aluminium alloys and austenitic steels are often used throughout the literature rehearsed as experimental materials both for erosion studies and methods of surface modifications. The innovative approach in this work simulates water cluster impact by controlling technological parameters of ultrasonically induced PWJ. This allows achievement of a high number of impacts in relatively short time.

This work aims to define more precisely the erosion incubation stage and elucidate the mechanisms leading to initial material removal. This research area is currently highly unexplored, especially in layer just below the surface. The work is profoundly focused on electron microscopy techniques supplemented by microhardness measurement to describe the surface and subsurface changes. The highlight of this work is the proposal of an inventive EBSD measurement methodology that allows to directly observe selected material grains before and after exposure to liquid cluster impacts. Compared to standard evaluation based on roughness this technique gathers information about induced misorientation inside the grains and provides information from a thin subsurface layer.

The devised flow chart of the experimental part of this work based on the research gap is presented in **Figure 34**. The flow chart is divided into experimental materials where aluminium alloy was used for preliminary studies. For rest of the experiments 316L austenitic stainless steel was chosen due to better homogeneity. Both experiments started with parametric optimization including variability in pressure and number of cluster impacts (controlled by feed rate). In the case of the 316L steel preliminary screening experiment was done to confirm the possibility of fatigue life improvement. The variable during this experiment was feed rate. Finally stationary erosion exposure was done first consisting of all erosion stages to determine the erosion curve. The experiment was then repeated only in the incubation erosion stage and innovative EBSD measurement methodology was applied to better quantify and qualify the effect of erosion exposure time during the incubation stage.

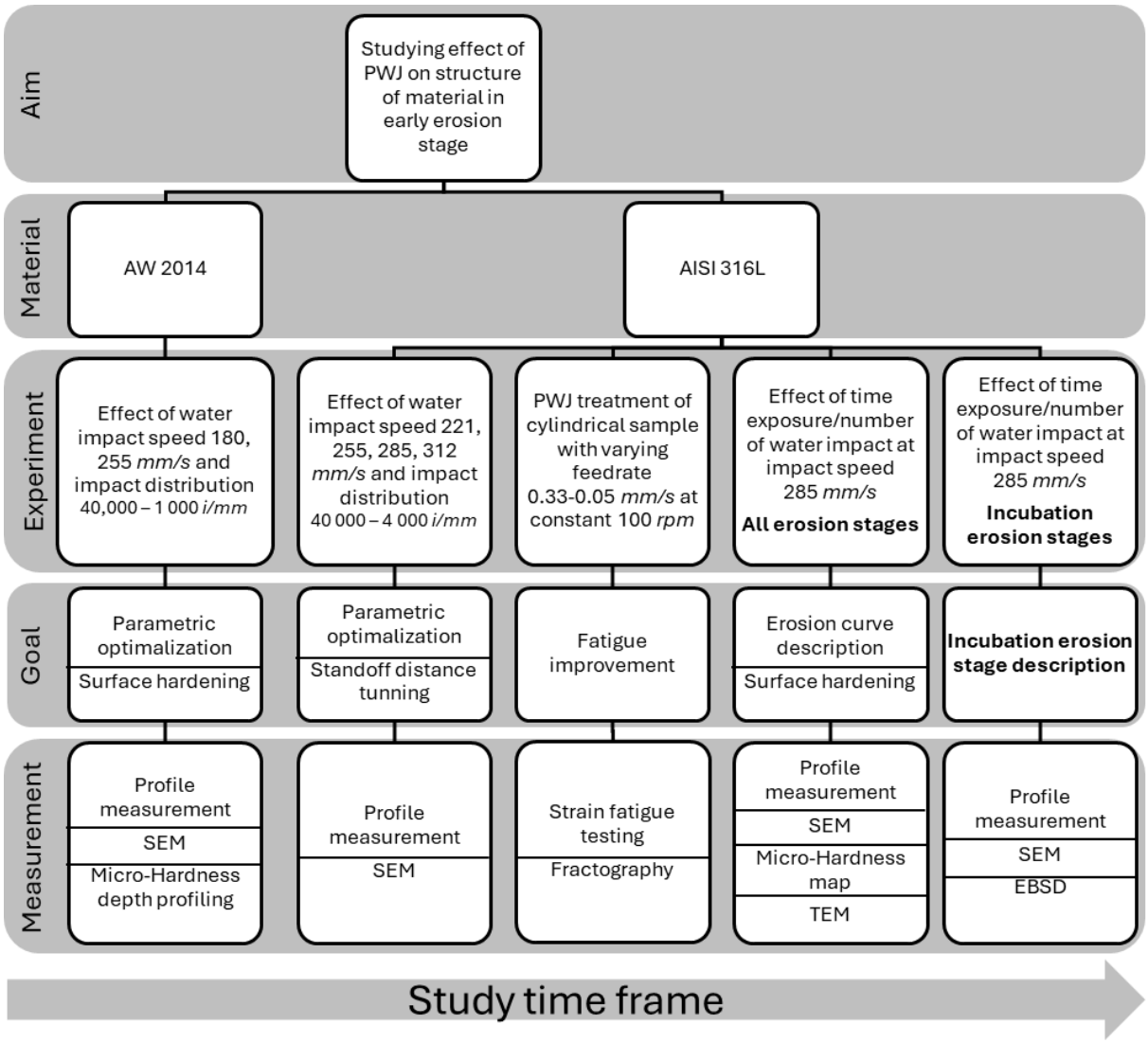

Figure 34 The flow chart of the experimental part of this thesis

3. Aims of the work

This work aims to study incubation erosion stage I and its transition to erosion stage II. The incubation erosion stage I precedes macroscopic material removal. Stages II and III contain different degrees of macroscopic material removal. From the literature overview it is evident that most researchers from early studies as well as current studies mostly focus on material removal stage. Erosion stages II and III from an exposure perspective and culmination regime from a standoff distance perspective. Compared to that the focus of this work is on the early erosion stage generally known as the incubation stage (erosion stage I) and the transition between this erosion stage and earliest signs of material removal. The first part of this work is focused on processes happening inside the material preceding macro-material removal and the second part is focused on using these processes in controlled manner. The main output of this study will be beneficial for understanding the early erosion processes based on exposure time and number of impacts. The next important area of this work is to describe the transition between erosion stage I and II. Finally, the technical use of this knowledge will be demonstrated as a mean of surface hardening and roughening. Knowledge of the effect of increasing number of water clusters impact on the surface of structural materials may in greater scope be used for more precise prediction of initial erosion rates.

A study of the effect of water cluster impact distribution will be evaluated on aluminium alloy AW-2014 as a preliminary study. The effect of impact distribution and standoff distance on the surface profile of 316L stainless steel will be evaluated. The knowledge learned will be used for further study of the incubation stage and incubation stage transition to stage II on austenitic stainless steel 316L with the following goals.

- The goal is to describe processes on the surface and subsurface of the material induced by water cluster impact in the erosion incubation stage.

- The processes leading to the transition between the incubation erosion stage and erosion stage II leading to macroscopic material removal will be described.

- The hardness profile caused by repeated water cluster impact will be evaluated in the case of selected materials.

- The surface roughening during the erosion incubation stage will be described based on liquid cluster parameters in the erosion incubation stage and transition to erosion stage II.

- The methodology for erosion incubation stage evaluation will be developed and tested.

4. Experiments

4.1. Experimental materials

Two experimental materials were selected for this study, austenitic stainless steel 316L stainless steel and aluminium alloy AW2014. Both material types are frequently used for PWJ based erosion experiments. The main reason for choosing both materials is their resistance to corrosion in the humid environment of tap water. The AW2014 alloy was used for the first set of experiments due to its ductility and low hardness, making it very sensitive to changes in PWJ process parameters. The 316L stainless steel was chosen due to its high plasticity and its structural homogeneity, making it a better candidate for incubation erosion stage testing. Both experimental materials are described in the next two chapters.

4.1.1 Aluminium alloy AW2014

The material was provided in the form of a wrought rod. A wrought aluminium alloy consists of alloying elements Cu, Si, Mn, and Mg. The alloy also contains a considerable amount of Fe impurities. Macro chemical composition as measured by optical emission spectroscopy is shown in **Table 4**. The distribution of particles inside the aluminium matrix is shown in **Figure 35**. The elasticity modulus of the alloy was measured from tensile test as 71 *GPa*. The microhardness was measured by 5 indents as 72 ± 1 HV0.2 Microhardness of untreated material was measured as 82.1 ± 1.9 HV0.005 as measured from 28 indents. The grain shows significant crystallographic texture as shown by the pole figure (**Figure 36**), expressed by the high value of MUD over 15. The <111> texture is strongest in the sample direction parallel to the rolling direction. The weaker <011> texture is found in direction perpendicular to rod axis. The material exhibits an elongated microstructure with the grain size of about 1.54 μm (as measured by the linear interception method) in a direction perpendicular to the rolling direction. The grains are elongated in a direction parallel to rod axis and form bands reaching hundreds of microns. During the experiment, the PWJ head was moving perpendicular to the rod axis. **Figure 37** shows the TEM micrographs of as received AW2014. The analysis shows roughly equiaxial grains in a foil plane (perpendicular to bar direction). Microstructure contains fine precipitates and small number of larger intrusive particles. These particles show the tendency of pinning dislocations as documented by **Figure 37**.

Table 4 Chemical composition of selected aluminium alloy in %wt measured by optical emission spectroscopy [61]

Element	Al	Cu	Mg	Mn	Si	Fe	Zn	Ni	Ti	Cr
Content wt.%	93.6	4.03	0.67	0.63	0.62	0.31	0.045	0.041	0.022	0.019
Standard deviation	0.031	0.024	0.003	0.006	0.003	0.007	0.001	0.0003	0.0004	0.0001

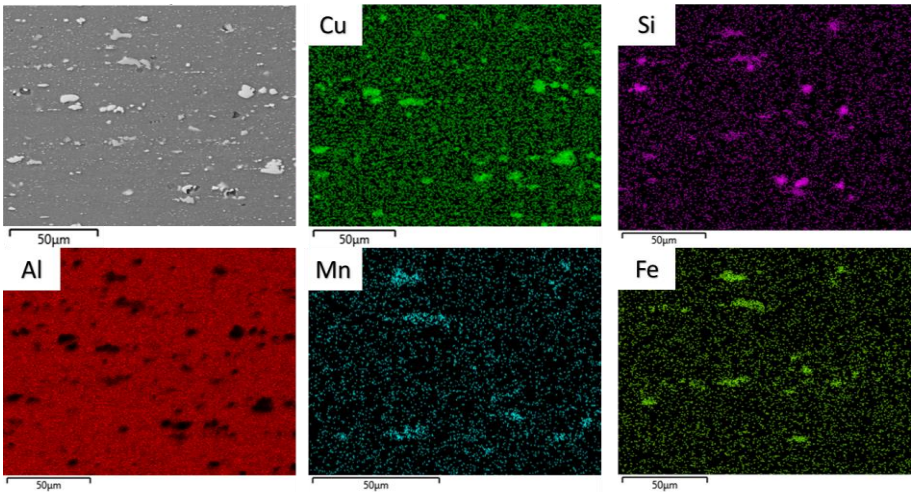

Figure 35 EDS measured particle distribution in the aluminium based matrix [61]

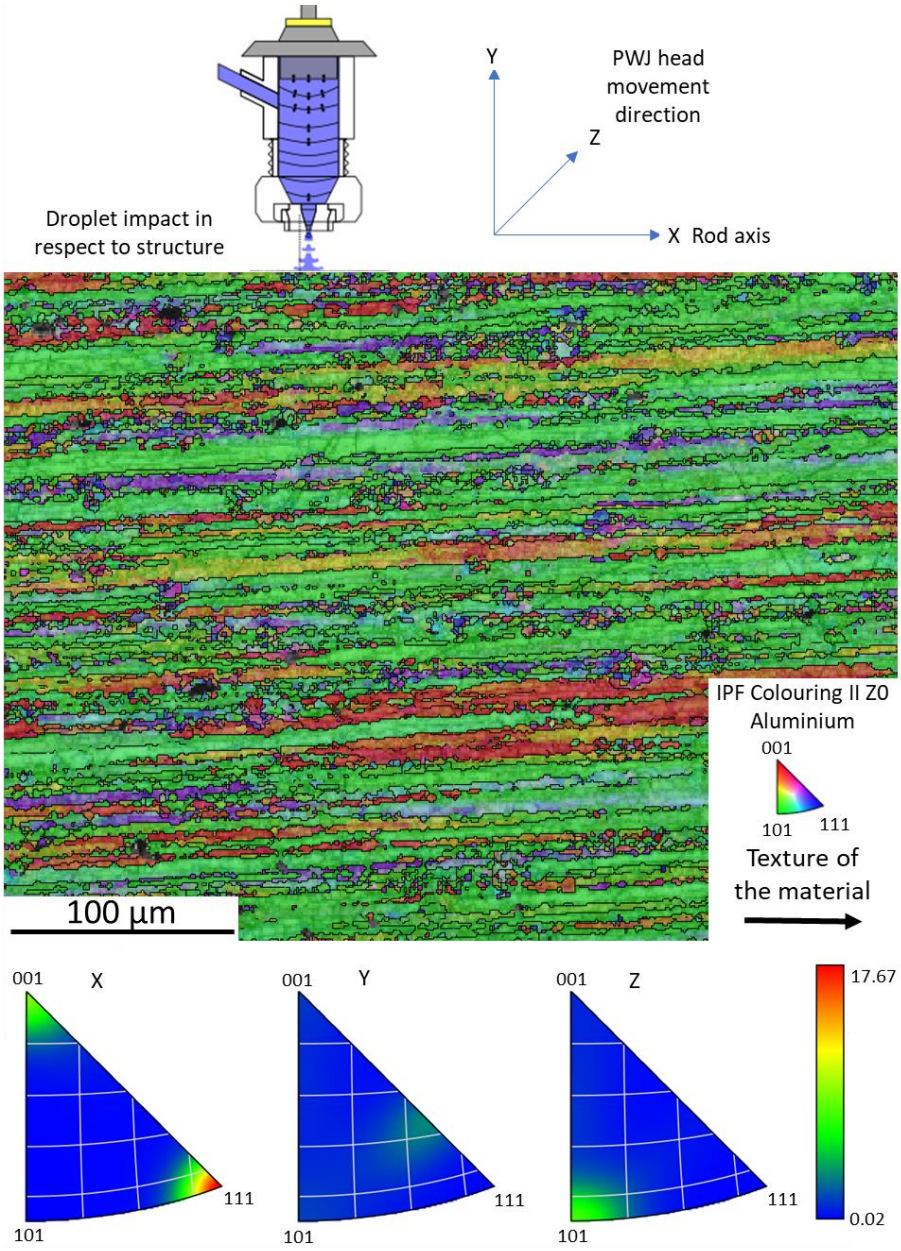

Figure 36 EBSD analysis of AW2014 cross-section parallel to rod axis, consisting of EBSD grain orientation map, Inverse pole figure, and indicated PWJ jet movement [61]

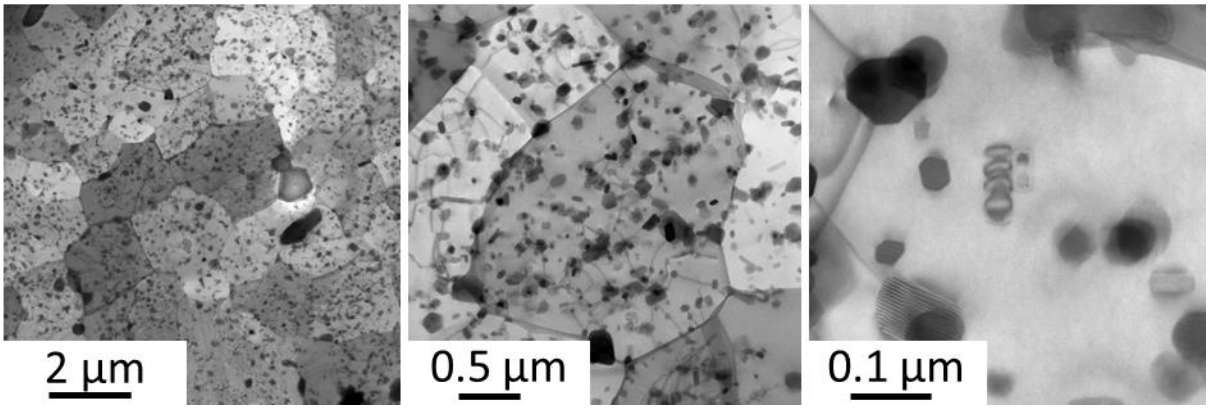

Figure 37 TEM of as-received AW2014 at three magnification levels showing overview of multiple grains, detail of single grain and detail of precipitates inside the grain

4.1.2 Austenitic stainless steel 316L

Austenitic stainless steel AISI 316L was supplied in the form of a hot-rolled plate. The austenitic stainless steel consists mostly of austenite a face-centred cubic (FCC) lattice with a small amount (up to 1.8 %) of residual δ ferritic phase with body centred cubic (BCC) lattice mostly in the form of elongated bands in a hot rolling direction. The material shows structural homogeneity. Therefore, it allows for precise and repeatable incubation erosion stage measurements such as microhardness measurement. The chosen properties of experimental material are shown in **Table 5** The grain size was evaluated using EBSD. The EBSD analysis yields over 95 % hit rate. To clean zero solutions 10 iterations of four neighbours zero solution removal method was used. The **Table 5** shows arithmetic mean values of equivalent circle diameter with and without special/twin boundaries. The arithmetic mean grain (equivalent circle diameter) size is 10.38±7.14 μm without joining special twin boundaries and 16.33±12.34 μm with the joining of special/twin boundaries. The area-weighted mean grain sizes measured on the same EBSD map are 19.86 μm and 32.42 μm without and with joining of special/twin boundaries. The phase composition was evaluated by the XRD method using the X-ray powder diffractometer Empyrean (Malvern PANalytical, UK). Hardness was measured using Duramin microhardness tester (Struers, Denmark) with a load of 1.96 N and tensile properties were evaluated using MTS 810 servo-hydraulic testing machine (MTS, USA).

Table 5 Selected properties of experimental material 316L steel

Material	Elasticity modulus *GPa*	Tensile yield strength *MPa*	Tensile ultimate strength *MPa*	Arithmetic mean grain size μm	Area weighted mean grain size μm	Hardness HV0.2
316L steel	198	322	625	*10.38 ± 7.14 16.33 ± 12.34	*19.86 ± 12.88 32.42 ± 20.57	184 ± 10

* A value that considers the twin boundaries as grain boundaries

Figure 38 shows an example of EBSD analysis of the surface of 316L stainless steel in the as received state. The scanning step size of EBSD analysis was chosen as 0.5 μm. The area of the scan was 700x200 μm. Furthermore, **Figure 38** shows an FSE image with PF next to it. The

pole figure analysis contains some preferred crystallographic plane orientations; however, the MUD reaches only value of 1.26, indicating very low crystallographic texture. The second row in **Figure 38** shows EBSD grain orientation map with grain boundaries marked, showing a considerable number of twin boundaries. The third row in **Figure 38** shows phase distribution with enhanced band contrast. The phase composition shows a small amount of δ-ferrite in the form of elongated bands following the grain boundaries of FCC austenite. **Figure 39** shows TEM analysis of as-received 316L stainless steel with a number of dislocations from multiple slip systems (**Figure 39**). The dislocations tend to form pile-ups at grain boundaries.

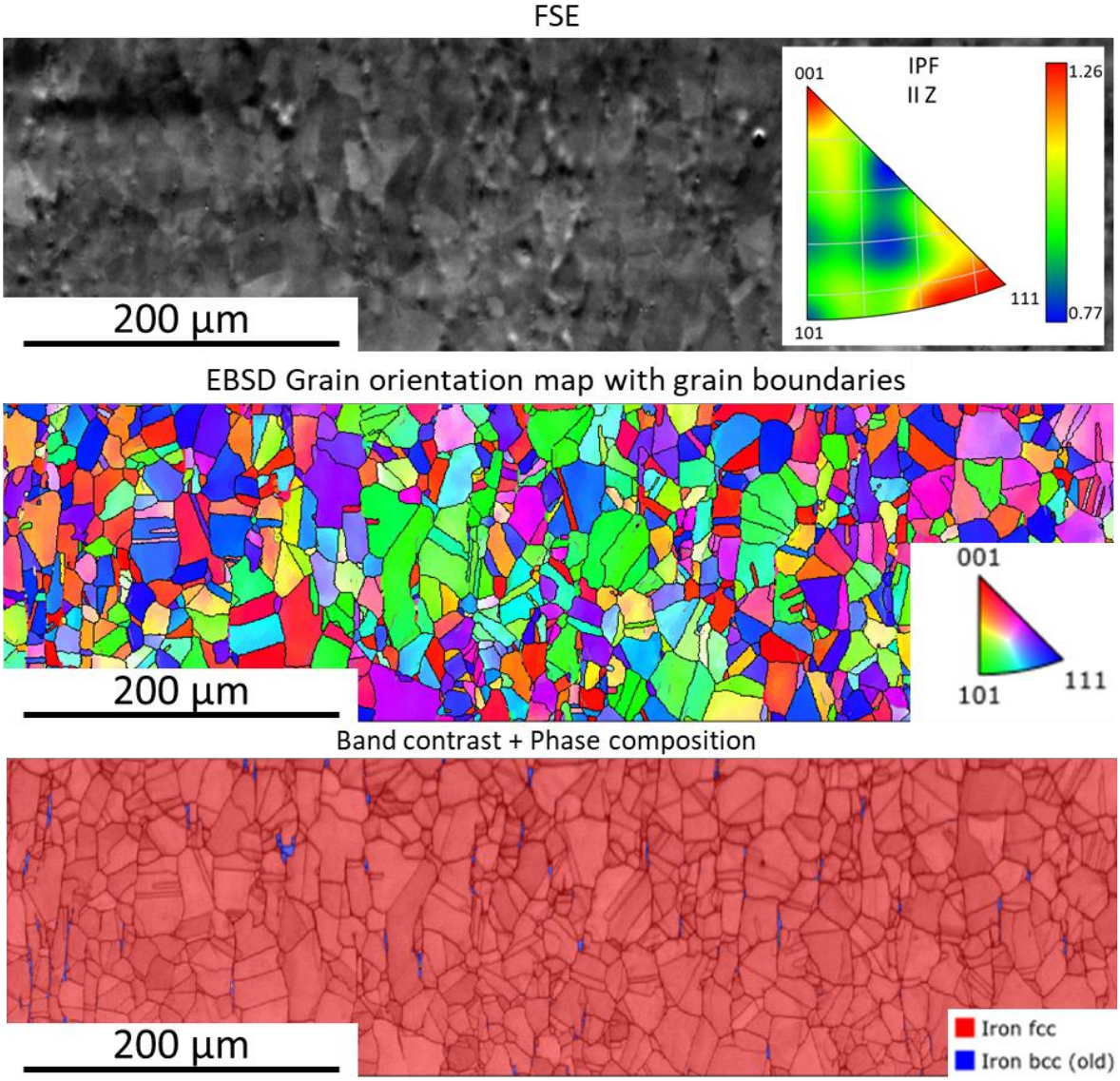

Figure 38 EBSD analysis of as received AISI316L surface to be treated by PWJ showing FSE image, EBSD grain orientation map with GB image and BC with phase composition image

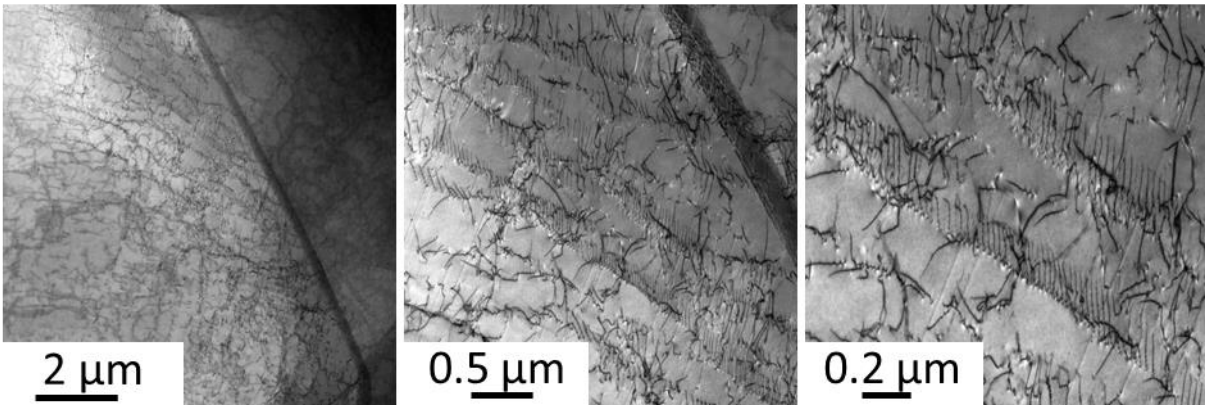

Figure 39 TEM micrographs of as-received hot rolled plate of 316L stainless steel showing 3 levels of magnification larger overview and details of dislocation structure.

4.2. Experimental treatment (PWJ, CWJ)

4.2.1 Overview of experiments

The technology used for water exposure of surfaces in this experiment is the PWJ system located at the Institute of Geonics UGN CAS. The principle of this technology is described in the **chapter 2.3**. The main part of the system is the water cluster generator with the sonotrode oscillating based on an acoustic generator ECOSON WJ-UG 630-40 (Ecoson, Slovakia) in the acoustic chamber. Schematic of the technology is depicted in **Figure 40a**, and the experimental setup is shown in **Figure 40b**. The sonotrode with the frequency of 40 *kHz* was chosen for this experiment and each subsequent experiment. The experiments are divided into sets based on development period and experimental goal.

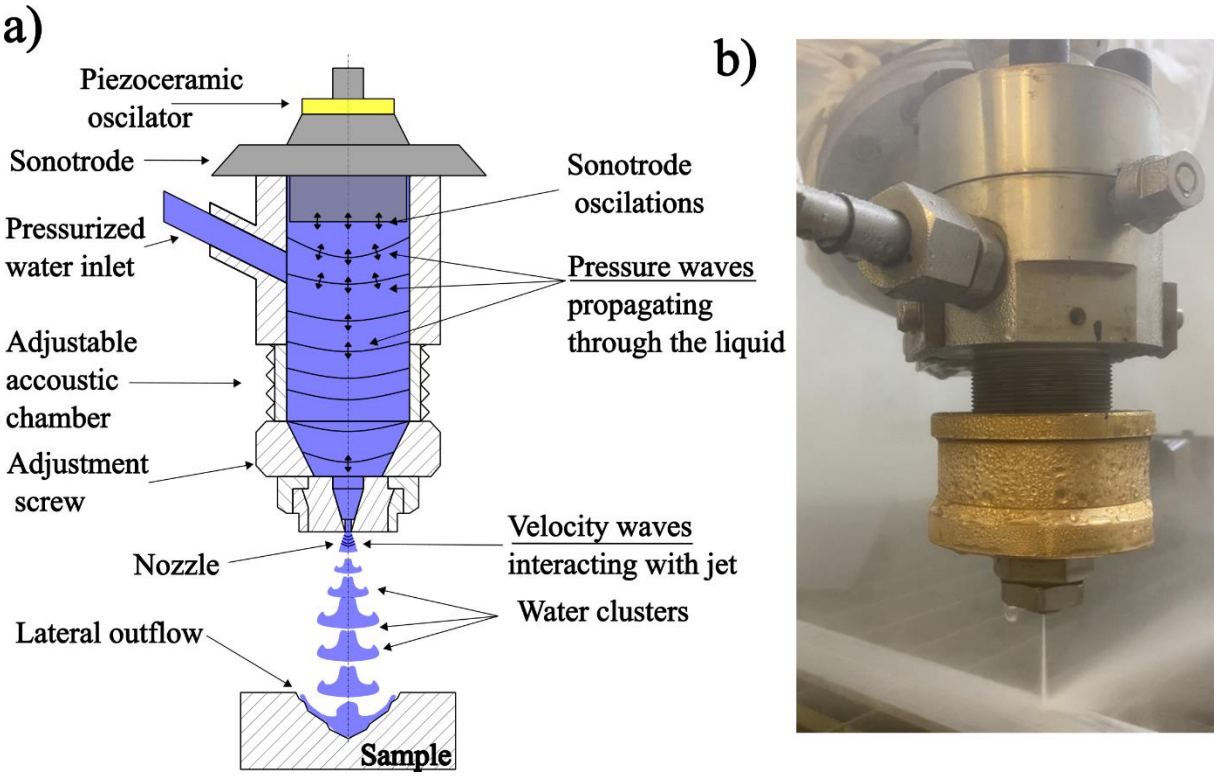

Figure 40. a) schematic of PWJ located over a sample, b) photo of PWJ moving over a sample

Hydraulic parameters such as flow rate, flow speed and hydraulic power for each experiment listed in tables are calculated based on the following equations. The flow speed is calculated as based on Eq. (12) with μ set as 0.9. The flow rate in m^3/s is then flow speed multiplied by the area of the nozzle by Eq. (19):

$$Q\left[\frac{m^3}{s}\right] = S.v_0 = \frac{\pi.d^2}{4}.\mu.\sqrt{\frac{2.p}{\rho_W}} \tag{19}$$

where *d* is nozzle diameter. Which is recalculated into l/min by Eq. (20):

$$Q\left[\frac{l}{min}\right] = 60\,000.Q\left[\frac{m^3}{s}\right] \tag{20}$$

and theoretical water cluster volume is estimated by Eq. (21):

$$\mathrm{v}_w[m^3] = Q\left[\frac{m^3}{s}\right].\frac{1}{f} \tag{21}$$

The first set of experiments (Table 6) deal with PWJ traveling on a line on austenitic stainless steel 316L stainless steel and aluminium alloy AW2014.

The 316L stainless steel was treated by four hydraulic pressure levels 30, 40, 50 and, 60 *MPa*. The standoff distance was varied in the first part of the experiment. The stair trajectory described by Hloch et al. [47] was used to estimate the optimal standoff distance in this experiment. After the optimal standoff distance was estimated for each pressure level, variations in water impact distribution were examined by variations in feed rate (1,5,10 *mm/s*). The feed rate in this experiment can be described as the travel speed of the working PWJ head over the material surface in a direction parallel to the surface.

The experiment on AW2014 was conducted at two pressure levels of 20 *MPa* and 40 *MPa*. The PWJ head was moving on the line trajectory at varying feed rates starting at 1 *mm/s*, followed by 5 *mm/s*, and then increased by 5 *mm/s* in each subsequent step until erosion was no longer visible. The obtained results contained all erosion stages from significant material removal through surface cracking and surface roughening to the erosion incubation stage.

Table 6 Experimental parameters of the first set of experiments

Experimental set No I											
Exp No.	Goal of experiment	p	f	Nozzle diameter	Flow speed	Flow rate	PWJ path	Optimal standoff	Feed rate	Impact exposure	Material
		MPa	*kHz*	*mm*	*m/s*	*l/min*	-	*mm*	*mm/s*	*i/mm*	-
1/1	parametric optimalization	30 40	40.7 40.5	0.5	220.7 254.8	2.6 3.0	line	28 30	1-5	40 000-8 000	316L steel
1/2	parametric optimalization	50 60	40.4 40.7	0.5	284.9 312.1	3.4 3.7	line	36 60	1-10	40 000-4 000	316L steel
1/3	surface hardening	20	40.7	0.5	180.2	2.1	line	16	1-10	40 000-4 000	AW2014
1/4	surface hardening	40	40.5	0.5	254.8	3.0	line	32	1-40	40 000-1 000	AW2014

The second set of experiments (**Table 7**) focused on the investigation of the early erosion stage in the 316L stainless steel. The area of interest was erosion stage I (known as incubation) and the description of the transition between erosion stages I and II. Experiments were carried out with 40 *kHz* sonotrode and 50 *MPa* pressure in a hydraulic chamber. This pressure and frequency level was chosen for the observation of early incubation stage, surface hardening and surface treatment of fatigue samples. The experiments of this set are controlled by a number of impacts on the surface of the treated area. This is achieved by variations in exposure time or feed rate. Each set of experiments is detailed below. The experiments will be more closely described in the following chapters.

Table 7 Experimental parameters of the second set of experiments

Experimental set No II											
Exp. No.	Goal of experiment	p	f	Nozzle diameter	Flow speed	Flow rate	PWJ path	Optimal standoff	Feed rate	Exposure	Material
		MPa	*kHz*	*mm*	*m/s*	*l/min*		*mm*	*mm/s*	*s*	-
2/5	surface hardening	50	40.7	0.4	284.9	2.15	spiral	60	0.33-0.05	X	316L steel
2/6	surface hardening	50	40.7	0.4	284.9	2.15	stationary	60	X	1-20s	316L steel
2/7	erosion observation	50	40.2	0.4	284.9	2.15	stationary	45	X	1-3s	316L steel

4.2.2 Experimental set I – effect of water impact distribution on surfaces of metals

The first set of experiments was designed to observe the effect of change in liquid impact distribution (controlled by feed rate) on the surface and to document all erosion stages. The main goal was to create a basic process map considering pressure, standoff distance, and feed rate.

Four pressure levels were chosen: 30 *MPa*, 40 *MPa* (**experiment 1/1**), and 50 *MPa*, 60 *MPa* (**experiment 1/2**) for treatment of 316L stainless steel at several standoff distance levels. The stair trajectory approach to estimate optimal standoff distance based on the work of Hloch et al. [47] was applied in this experiment. The PWJ head was moving on a stair trajectory (**Figure 41**) over the material surface at constant pressure. The surface treated by this trajectory was then measured by profilometer and optimal standoff distance for given pressure was evaluated based on Rz and Rv. The rest of experiment in this thesis was conducted on optimal standoff distance evaluated by this approach for given hydraulic pressure. Experimental runs with varying feed rates (1,5, 10 *mm/s*) were then done at optimal standoff distance for each selected pressure level. The goal was to observe the changes in the surface through all erosion stages using SEM.

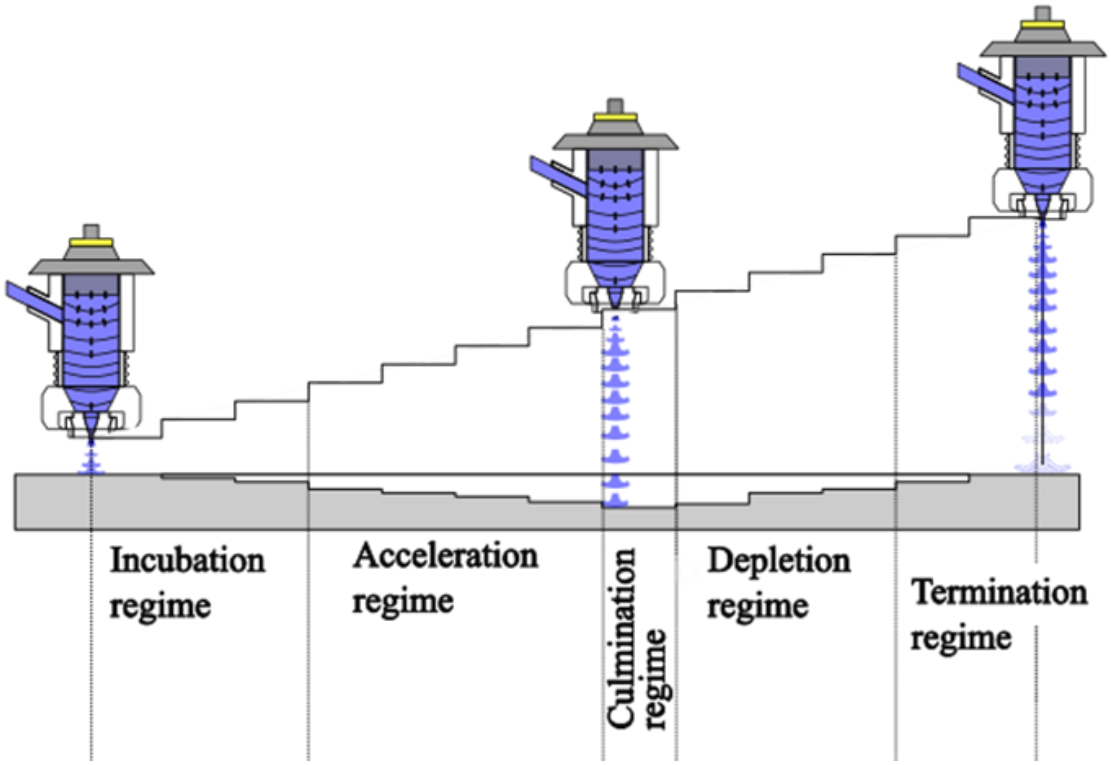

Figure 41 Stair trajectory of PWJ head devised to evaluate optimal standoff distance for hydraulic conditions specified in experiment 1/1 and 1/2

Aluminium alloy AW2014 was treated by two pressure levels of 20 *MPa* (**experiment 1/3**) and 40 *MPa* (**experiment 1/4**) and 0.5 *mm* nozzle diameter was selected. The pressure level of 20 *MPa* creates a theoretical volume of water cluster v_{d20} = 0.88 mm^3 with velocity v_w = 184 *m/s*. The pressure level of 40 *MPa* creates a theoretical volume of water cluster v_{d40} = 1.23 mm^3 moving at a velocity of a v_w = 260 *m/s*. The standoff distance was set to 16 *mm* and 32 *mm* for 20 *MPa* and 40 *MPa*, respectively.

The experiment consisted of the jet head travelling over the surface in a linear trajectory parallel to the surface. Experiments consisted of multiple experimental runs with decreasing water impact distribution (increasing feed rate). The feed rate of 1 *mm/s* was set as the reference of the experiment and the feed rate was then increased until the PWJ path was not visible. For 20 *MPa* the first, second, and third line was created with feed rates of 1 *mm/s* 5 *mm/s*, and 10 *mm/s* which equates to 40 000, 8000 and 4000 *i/mm* of the surface. The number of impacts per *mm* is based on the sonotrode native frequency of 40 *kHz*. The same conditions were repeated with a feed rate of 1 *mm/s* with pulses turned off, simulating the CWJ. For the pressure of 40 *MPa* the feed rate for the first line was 1 *mm/s*, (40 000 *i/mm*), for the second line 5 *mm/s* (8 000 *i/mm*) and each subsequent line was done with an increment in the feed rate of 5 *mm/s*, up to 40 *mm/s* (1 000 *i/mm*). One line was done with pulses turned off with feed rate of 1 *mm/s* to simulate the effect of CWJ. The experimental procedure is sketched in **Figure 42** as presented in previous work [61]. The edge of the sample for microhardness measurement was perpendicular to the feed rate direction (cross-section) and was then examined using SEM and hardness measurement. The surface profile was also measured to evaluate eroded depth or achieved roughness based on the feed rate.

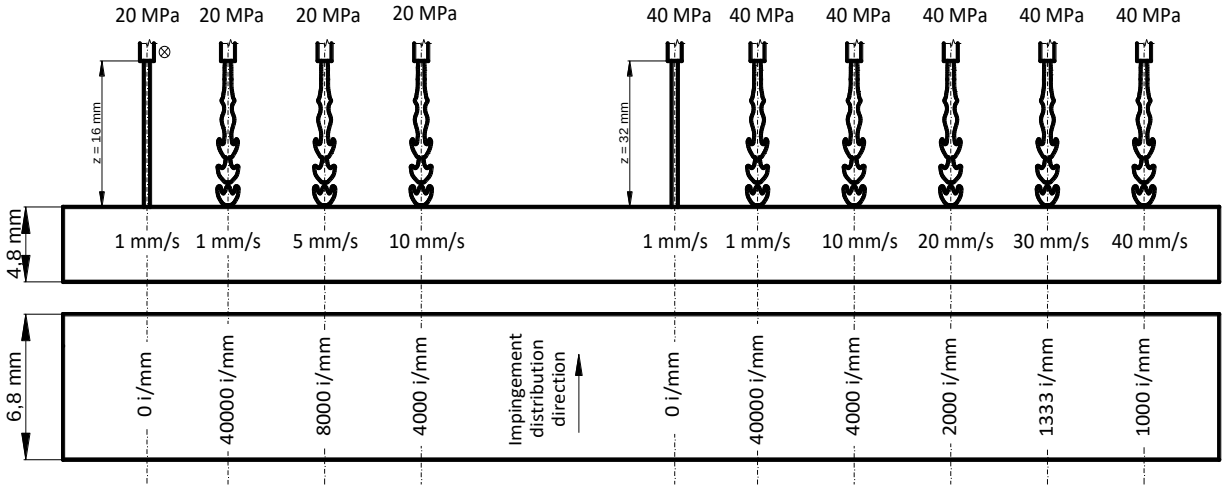

Figure 42 Experimental parameters for experiment 1/3 and 1/4: effect of feed rate (water impact distribution) for two constant water pressure levels 20 MPa and 40 MPa and two corresponding standoff distances 16 mm and 32 mm [61]

4.2.3 Experimental set II – early incubation stage effects

The second experimental set was done with hydraulic parameters set based on pressure of 50 *MPa* (**Table 7**). The main goal of these experiments was to evaluate the effect of PWJ on the surface of the material before the start of material removal.

The **experiment 2/5** consisted of the jet moving on a line trajectory with varying feed rates over fatigue sample rotating at 100 *rpm*. (**Figure 43**). Therefore, from the point of view of the sample the jet moves in a spiral. The fatigue samples were tested at three total strain amplitude levels. The goal was to create an S-N curve and compare the fatigue life of these samples with untreated material.

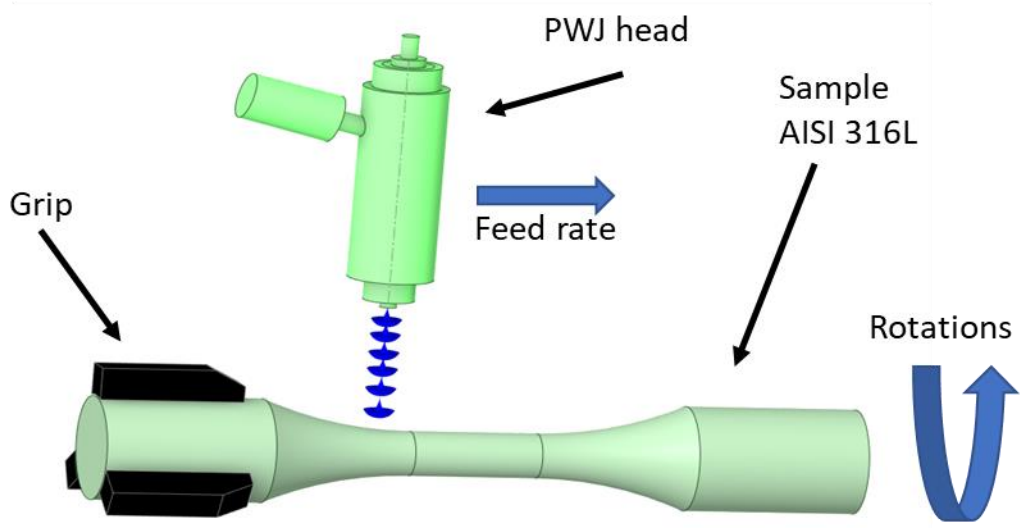

Figure 43 Treatment of fatigue rotational sample

Experiment no. 2/6 and 2/7 are based on PWJ exposure over a stationary position. The **experiment 2/6** exposure ranges from 1-20 s, ranging from surface roughening up to significant material removal. The surface was evaluated using SEM and confocal microscopy/optical profilometer and instrumented microhardness was measured on cross-section. Both microhardness and SEM results are supported by TEM analysis.

Experiment 2/7 considers surface roughening without material removal (exposure 1 to 3 s) The hydraulic parameters of the PWJ are the same as with static exposure **experiment 2/6**. Due to the time interwall between **experiment 2/6** and **experiment 2/7** and wear of sonotrode, change of nozzle etc. stair trajectory test was done before the experiment, and optimal standoff distance was evaluated to 45 *mm* for **experiment 2/7**.

Experiment 2/7 consisted of electrolytic polishing of the surface and then marking edges of selected areas on the surface with hardness indenters. The marked areas were then measured with EBSD. The PWJ was used to precisely treat the marked area for 1-3s. The experiment was evaluated from the top surface of the sample using Kernel average misorientations maps, pole figures, and inverse pole figures.

4.3. Measurement techniques

4.3.1 Flat sample preparation for PWJ treatment

The aluminium alloy rod was cut using an abrasive cutter Brilliant 220 (ATM Qness, Germany). The top surface of aluminium alloy samples before PWJ treatment was mechanically ground using SiC grinding papers with average grain sizes of 46 μm, 22 μm, 18 μm, and 15 μm. Polishing was done using diamond paste with grain sizes of 3, 1 and 0.25 μm. The grinding and polishing were done on manual grinding and polishing machines ATM Saphir 320 and Saphir 330 (ATM Qness, Germany). Chemical-mechanical polishing by oxide polishing suspension (OPS) for finer surface preparation using vibratory polisher Vibromet 2 (Buehler, USA) was the final step. The OPS used consisted of colloidal silica with a grain size of 40 nm. Preparation of cross-sectional cuts after PWJ treatment was carried out by precision abrasive cutter Brilliant 220 (ATM Qness, Germany). The cutting was done under a constant flow of cooling liquid based on water with the addition of alkaline antibacterial solution Blasorun 5 and ATM-CoolCut (ATM Qness, Germany). The cross-sectional cuts were then mounted into conductive cold mounting resin Technovit 5000 (Kulzer Technik, Germany) containing Cu. The mounted cross-sectional cuts were then grinded and polished the same way as the top surfaces.

Austenitic stainless-steel samples were prepared similarly. Mechanical grinding by abrasive paper of average grain sizes of 46 μm, 22 μm, 18 μm, and 15 μm was followed with polishing using diamond paste with grain size of 3 μm only. Both grinding and polishing were done on ATM Saphir 320 and Saphir 330 (ATM Qness, Germany). Electrolytic polishing was the final step for the preparation of EBSD compatible surfaces. Electrolytical polishing was done by the LectroPol-5 (Struers, Denmark). The electropolishing conditions were selected as 60 V, 40 s, and 0 °C, and polishing solution used consisted of ethanol, perchloric acid and nitric acid. Treated cross-sectional samples containing erosion craters were cut using precise electrical discharge machining. The cross-sectional samples were then mounted using hot mounting (180 °C) carbon filled resin Polyfast (Struers, Denmark). The cross-section was then grounded and polished in a similar manner as the top surface, but instead of electropolishing further mechanical polishing using diamond paste 1 μm and 0.25 μm was performed. Chemical mechanical polishing by OPS with the silica grain size of 40 nm was the final preparation step. Electrochemical polishing was not used because the intricate shape of eroded structures is preferentially etched away due to the edge effect. This would lead to the deformation of erosion relief.

4.3.2 Surface and subsurface observations

The quantification of the parameters of the treated surface (roughness profile, depth, removed volume) was evaluated using either non-contact profilometer MicroprofFRT (FormFactor, USA) or in case of a more precise evaluation of incubation stage by confocal microscope Olympus LEXT OLS 3100 (Olympus, Japan). The evaluation consisted of the measurement of kerf/crater depths in erosion stage III and surface roughness of traces in erosion stages I and II. The cut off frequency of $\lambda_c = 0.8$ *mm* was chosen during roughness evaluation. The cut off frequency divides the assessment lengths, from which the profile data are acquired, into several sampling lengths from which roughness parameters are evaluated [143]. The minimum length of the evaluated line was 2.5 *mm.* The parameters Ra and Rz were evaluated when the surface roughening was achieved. Advanced evaluation of the erosion incubation stage also consisted

of Ra and maximum peak to valley height (Rz) with the addition of skewness (Rsk) and kurtosis (Rku). Rku quantifies sharpness of the profile, while the Rsk quantify the symmetry of the profile around the mean line [143]. Rz was also divided into Rp (peak height) showing the maximum height of the profile above the mean line in the sampling length and Rv (valley depth) showing maximum depth of the profile below the mean line in the sampling length [143].

Detailed surface observation was conducted using a scanning electron microscope (SEM) Tescan Lyra 3 XMH FEG/SEMxFIB (Tescan, Czech Republic). The microscope is equipped with a focused ion beam (FIB) using gallium ions for milling, which was used for TEM lamellae preparation. The microscope is further equipped with the EBSD detector Symmetry, and XMax80 energy dispersive X-ray spectroscopy (EDS) both controlled by AZtec software (Oxford Instruments, United Kingdom). The SEM was used for top surface observations using secondary electrons and back scattered electrons detectors. The EDS was used for chemical characterization of the initial material. The top surface was observed in as treated state. If cleaning was needed ultrasound cleaning system was used while samples were submerged either in ethanol or toluene. The erosion kerf cross-section was observed by SEM after cutting and metallographic preparation described in the previous chapter.

For subsurface observation of dislocation distribution, lamellae were prepared from the selected surface location by FIB. The acceleration voltage of the FIB was set to 30 kV for rough milling and cutting of the lamellae. 5 kV was used for the final thinning of the lamellae. The places from which the lamellae were taken were chosen based on SEM SE observations. The lamellae were then observed using a TEM microscope JEOL JEM-2100F (Jeol, Tokyo, Japan) operating at an acceleration voltage of 200kV with the STEM possibility. The dislocation density was evaluated on micrographs with sufficient magnification using the interception method devised by Ham [144]. The method consists of drawing random lines in the micrograph and counting the number of intersections of lines and dislocations. Based on a number of intersections the dislocation density is estimated as $\rho = 2N/Lt$, where N is a number of intersections L is the length of lines and t thickness of the foils or lamellae is considered to be 100 nm, based on the setting of the FIB milling procedure.

The EBSD was used for surface measurement of phase composition, grain size, morphology and misorientations. The Kikuchi patterns [145] obtained by the EBSD detector are processed via Hough transformation [146] to determine the Euler angles[147, 148] . Based on Euler angles maps of material structure were generated. Basic EBSD analysis was carried out using Oxford instruments native software Aztec while more complex analysis was caried out using open source MTex v5.7.0 MATLAB toolbox. MTex was chosen as it contains a noise reducing half-quadratic filter designed specifically for EBSD data. Grain morphology analysis was done by EBSD grain orientation map. Texture changes in PWJ treated surface were quantified by inverse pole figures (IPF) and pole figures (PF) where the level of preferred orientation is expressed as multiples of uniform density (MUD). Forward scattered electron (FSE) and band contrast images were used for general grain visualization. Phase mapping was used to visualize phase distribution. Most importantly, surface, and subsurface deformation was evaluated based on Kernell average misorientation (KAM) maps. The KAM mapping show misorientation angle of the pixel and the selected degree of its neighbouring pixels (**Figure 44**). In this study, 1-

degree neighbours were considered. EBSD analysis can be according to some sources [149, 150] correlated to density of geometrically necessary dislocations.

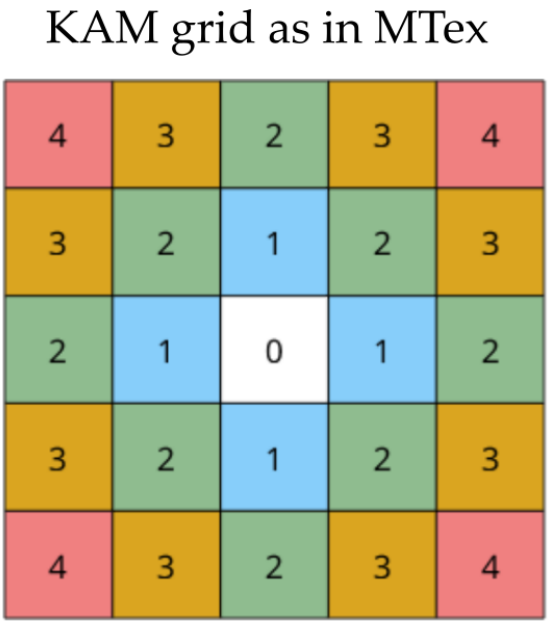

Figure 44 KAM grid incorporated in the MTex, the 1st degree neighbour misorientations are considered (the orientation of the centre pixel versus orientations of the first-degree neighbouring pixels

4.3.3 Hardness and microhardness measurements

The initial hardness of untreated materials was measured by the Vickers hardness testing method. The load of 0.2 kg was used for both stainless steel and aluminium alloy. Tests were done by the Duramin microhardness tester (Struers, Denmark) equipped for Vickers and Knoop hardness tests in loads ranging from 98.07 mN (10 g) to 19.61 *N* (2 kg).

The effect of PWJ on material microhardness was measured on cross-sectional cuts as described in chapter **4.3.1**. The microhardness tests were performed using instrumented Vickers type indenter. The Zwick Nanoindenter ZHN (Zwick Roell, Germany) with the maximum achievable force of 2 *N* was used for hardness measurement. The loading force was chosen to create indents with approx. 10 μm length of indent diagonal. The indent size was selected to measure close to the surface (30 μm) with minimal influence on the sample edge. The loading force was chosen 150 mN for austenitic stainless steel and 50 mN in the case of aluminium alloy. The load cycles for both metals are depicted on **Figure 45**. The load cycles consist of finding the surface, loading phase, and creep phase consisting of hold at maximum load, first unload phase, hold phase, and final unload phase. Microhardness 2D maps were created in Python 3.11.3 and interpolated by Scipy.interpolate method using linear interpolation.

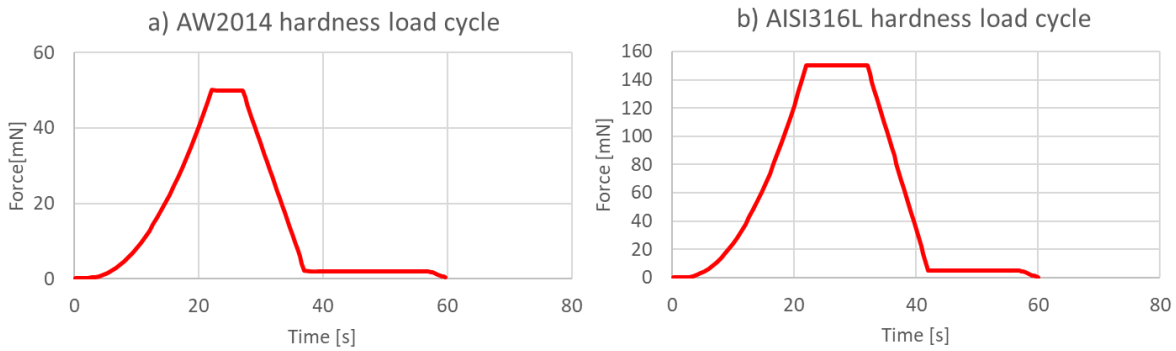

Figure 45 Hardness measurement load cycles used for a) AW2014 [61] and b) 316L stainless steel

Instrumented hardness measurement of PWJ treated AW2014 was done using the load of 50 mN on polished cross-sections. **Figure 46** shows the scheme of hardness measurement layout with distances from the surface and between indents. During the measurement X coordinates of indents were subjected to small corrections to avoid hardness measurement of visible constituent particles on the cross-section.

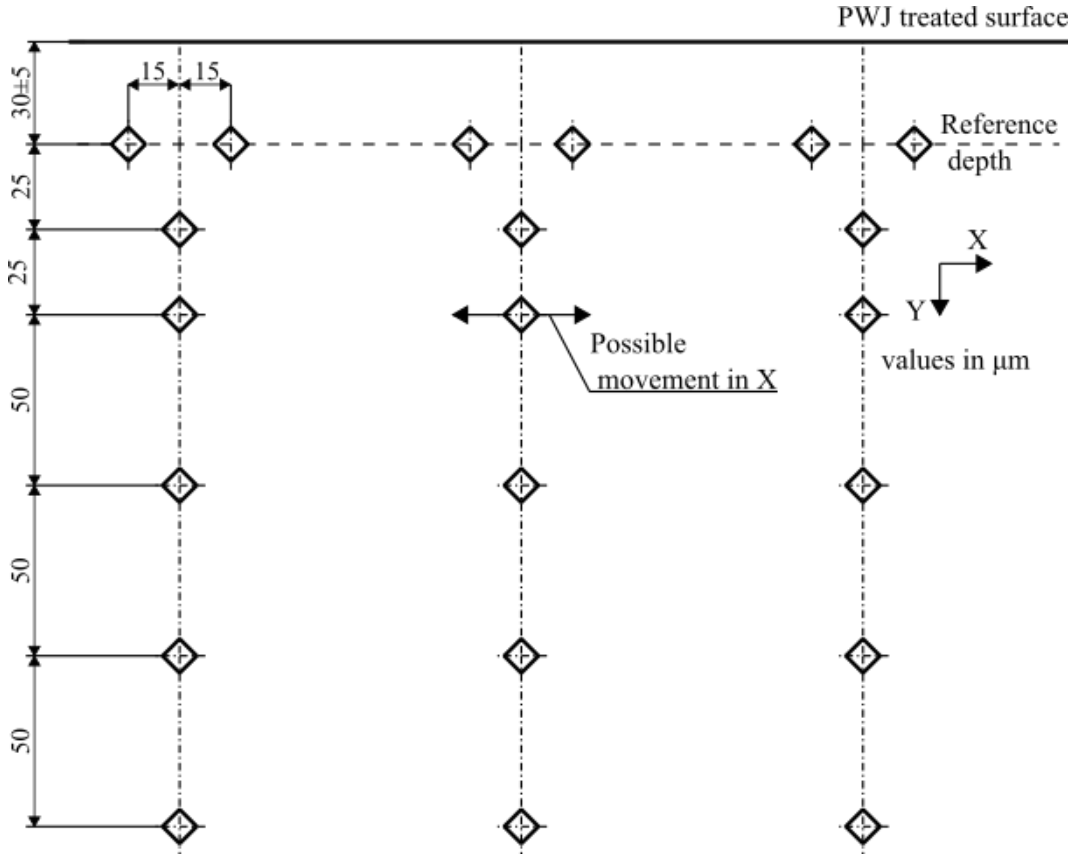

Figure 46 Microhardness measurement design with starting distance from the surface and distances between indents [61]

Microhardness measurement of profile under PWJ treated 316L stainless steel was performed. The measurement grit consisting of 15 rows of indents with 30 μm spaces between rows was used. A number of columns was adapted to the width of the affected area with distance of 40 μm in between columns. However, 15 columns were chosen as the minimum applied number of columns. The grid example can be seen in **Figure 47a**. The load force was chosen as 150 mN to achieve indent with a diameter size close to 10 μm. The small indent size is necessary to

measure hardness close to the surface or close to kerf edges. If the indent position was outside of material boundaries indent was not taken as seen schematically in **Figure 47b**.

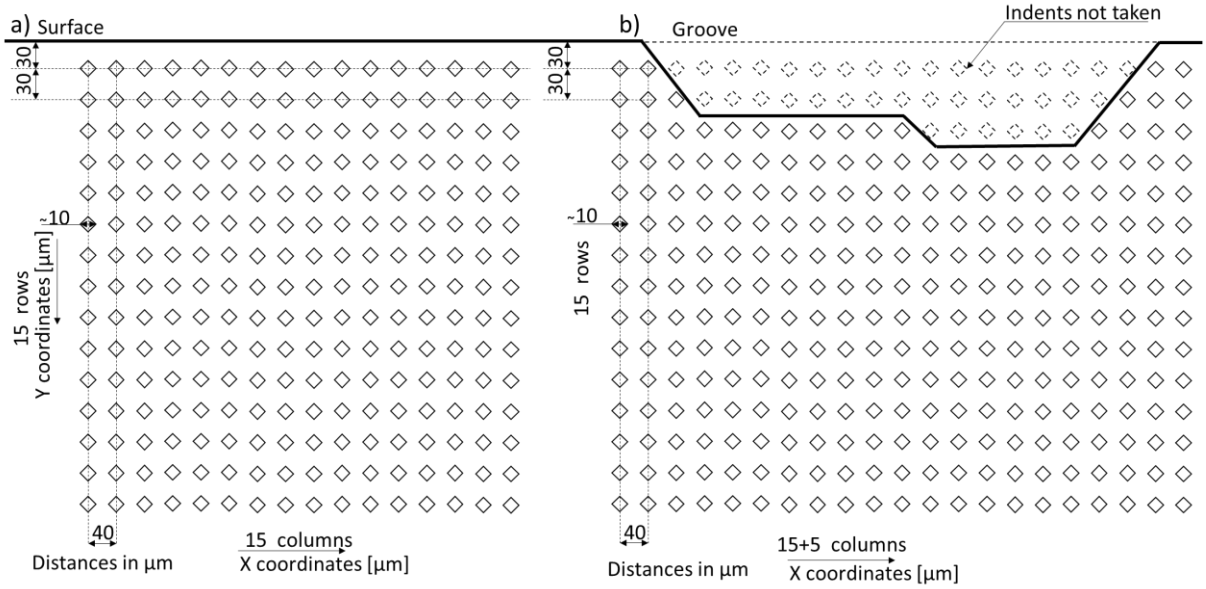

Figure 47 Schematic of hardness measurement on cross-section in case of a) roughening b) material removal by erosion

4.3.4 Fatigue testing methodology

The fatigue tests were performed using MTS 810 (MTS, USA) servo hydraulic testing machine on cylindrical samples with a gauge length of 15 *mm.* Fatigue samples were prepared using turning and grinding. The samples were not subjected to any sort of heat treatment after turning. The sample's axis was in the rolling direction (**Figure 48a**). The tests were done in symmetrical total strain (R = -1) controlled mode. **Figure 48b** shows the applied strain cycle with constant strain rate. The strain rate was chosen sufficiently high to reach 10^6 cycles in a reasonable time but sufficiently low for the relatively low thermal conductivity of austenitic steel. Thermocouples touching the specimens during loading were used for checking that the heating of the specimens is negligible. All tests were conducted at ambient temperature. The hydraulic grips were water cooled during the test . The strain was measured by the MTS contact axial extensometer. Fatigue tests were conducted to obtain the S-N curve and cyclic hardening softening curves.

The fatigue tests samples were polished using SiC paper with grit ranging from 120 to 4000. The last grinding step was done in a direction parallel to the sample axis. The preliminary samples were then polished using diamond paste with grain sizes 3 microns, 1 micron, and 0.25 microns. The samples were then treated by the PWJ. The preliminary fatigue samples were tested at strain amplitudes ε_a = 0.44; 0.32 and 0.28 % with a strain rate of $5x10^{-3}$ s^{-1}.

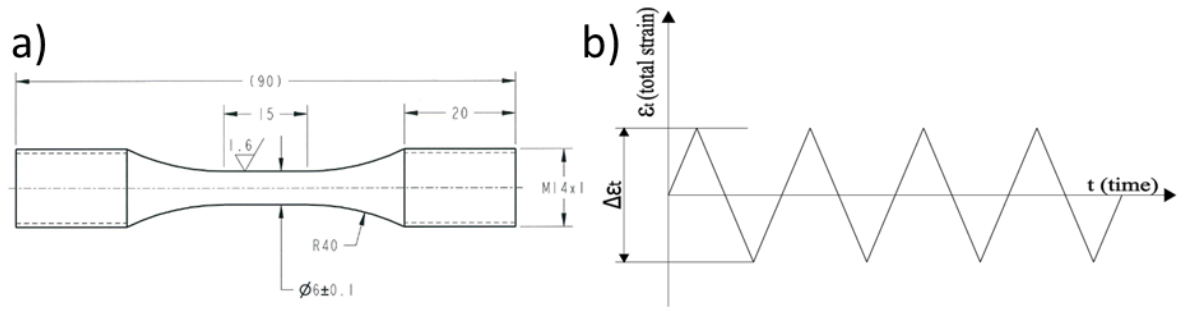

Figure 48 a) Fatigue sample geometry of 316L stainless steel samples treated with PWJ, b) Strain loading cycle

5. Results

The results described in following chapter were selected in order to create logically compact set of results following goals of this dissertation. Within the framework of cooperation with the Institute of Geonics, more results were obtained. Some of them are already published and other are used in papers in preparation.

5.1. Experimental set I

Experimental set I was conducted on both austenitic stainless steel and aluminium alloy. PWJ exposure of 316L stainless steel at four pressure levels with varying standoff distances was conducted during experiments 1/1 and 1/2 **(chapter 5.1.1**.) After establishing optimal standoff distance, experimental runs with varying water impact distribution (controlled by feedrate) were conducted. The 40 *kHz* sonotrode was used as it provides relatively accurate dosing of water clusters and smaller individual water cluster volume compared to the 20 *kHz* sonotrode.

The experiments 1/3 and 1/4 **(chapter 5.1.2)** were conducted on aluminium alloy AW2014 because its low hardness allows observation of erosion intensity due to changes in the PWJ process more readily compared to harder materials. The standoff distance was evaluated before the experiment and only the optimal standoff distance was considered. The experiment consisted of treating the surface of AW2014 at 2 pressure levels with varying water cluster impact distribution. The results presented in this chapter were already published in [61].

5.1.1 Effect of water impact distribution on the surface of 316L stainless steel

The effect of PWJ treatment on the response of austenitic stainless steel 316L was the topic of this part of PhD thesis. PWJ with parameters given in **chapter 4.2.2** was used for evaluation of pressure, standoff distance, and feed rate effect on the surface of steel samples.

The evolution of profile parameters based on standoff distance is depicted in **Figure 49**. The feed rate of PWJ was constant. However, changing of standoff distance led to significant changes in the achieved roughness parameter Ra. Four levels of pressure were applied. The pressure of 30 *MPa* creates a profile with Ra ranging from 1.48 μm up to 1.84 μm for standoff distance intervals from 26 to 32 *mm*. The pressure of 40 *MPa* led to a profile with Ra ranging from 2.32 up to 2.77 μm for standoff distance intervals from 26 to 38 *mm*. The pressure 50 *MPa* resulted in profile with Ra ranging from 2.36 μm up to 2.74 μm for standoff distance intervals

from 30 to 46 *mm.* Finally, profile Ra caused by 60 *MPa* pressure ranged from 2.27 μm up to 2.81 μm for standoff distance intervals from 40 to 68 *mm.* The largest value of the Ra parameter coincides mostly with the highest Rz parameter. The only exception from this trend is the surface created using pressure of 50 *MPa,* where the highest Rz was achieved by standoff distance z = 36 *mm,* while the highest Ra was achieved by z = 38 *mm.* The highest values of Rz achieved for each pressure level are Rz 13.64 μm at z = 28 *mm* for p = 30 *MPa,* Rz 20.65 μm at z = 30 *mm* for p = 40 *MPa,* Rz 21.48 μm at z = 36 *mm* for p = 50 *MPa,* Rz 21.98 μm at z = 54 *mm* for p = 60 *MPa*. Ra, Rz and Rv all show the existence of optimal standoff distance leading to the most intensive surface roughening. Exposure of PWJ with pressure 60 *MPa* leads to almost linear growth of the Rv parameter up to its maximum at z = 60 *mm.* Compared to these values it is hard to determine the common trend in Rsk or Rku values. Rsk for pressure of 30 *MPa,* 40 *MPa* and 50 *MPa* seems to be rather stable around values of 1; 0.8 and 0.6 respectively. Rku value for 30 *MPa,* 40 *MPa* and 50 *MPa* seems to show similar tendencies and keeps values of approximately 4.8; 4.2 and 4.2 respectively. PWJ at 60 *MPa* leads to a lowering of both Rsk and Rku values with an increase in standoff distance.

Based on the roughness parameter (Rz and Rv) evaluation, optimal standoff distances were selected as depicted in **Figure 50**. The selected optimal standoff distances are as follow: z = 28 *mm* for 30 *MPa,* z = 30 *mm* for 40 *MPa,* z = 36 *mm* for 50 *MPa* and z = 60 *mm* for 60 *MPa*. The standoff distance selected for 30 *MPa* and 40 *MPa* leads to the highest Ra and Rz at given pressure level, while for 50 *MPa* chosen standoff distance (z = 36 mm) leads to highest Rz and third highest Ra (first being achieved at z = 38 mm). The pressure of 60 *MPa* shows a more complicated increase of Ra and Rz, but a clear increasing trend in valley depth the Rv parameter. The increase in Rv parameter is generally attributed to water cluster actions. Therefore, z = 60 *mm* was selected as the optimal standoff distance for a pressure level of 60 *MPa*.

The surface of the steel sample was then treated at selected optimal standoff distances at each pressure level with increasing feed rate. An increase in feed rate leads to a controlled decrease in the total volume of cluster by decreasing impacts per millimetre *i/mm.* The chosen feed rate values were: 1 and 5 *mm* for 30 and 40 *MPa* (lower pressure levels) and 1, 5, 10 *mm/s* in the case of 50 and 60 *MPa* (higher pressure levels). Results are shown in the form of surface profile evaluation in **Figure 51**, and in the form of SEM micrographs in **Figure 52**.

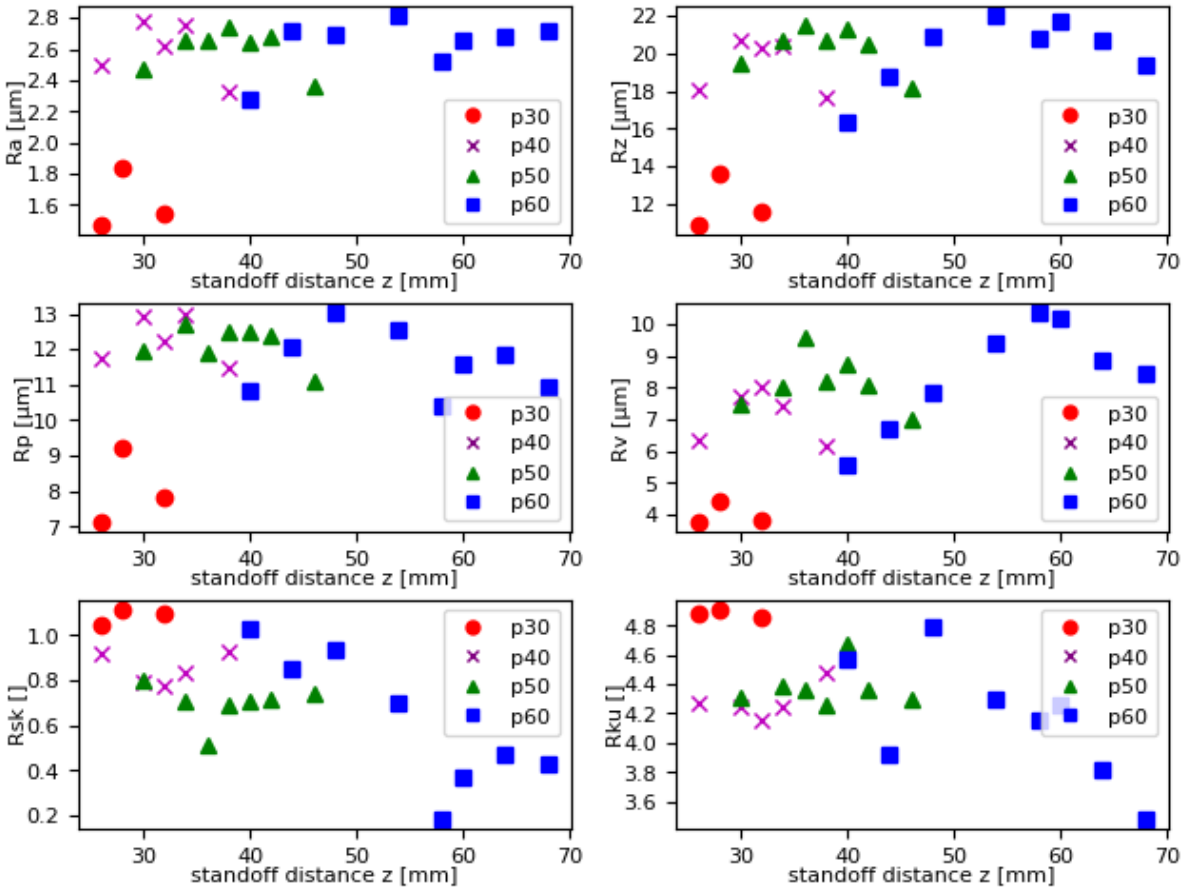

Figure 49 Roughness parameters Ra, Rz, Rp, Rv with Rsk and Rku of 4 pressure levels based on standoff distance z

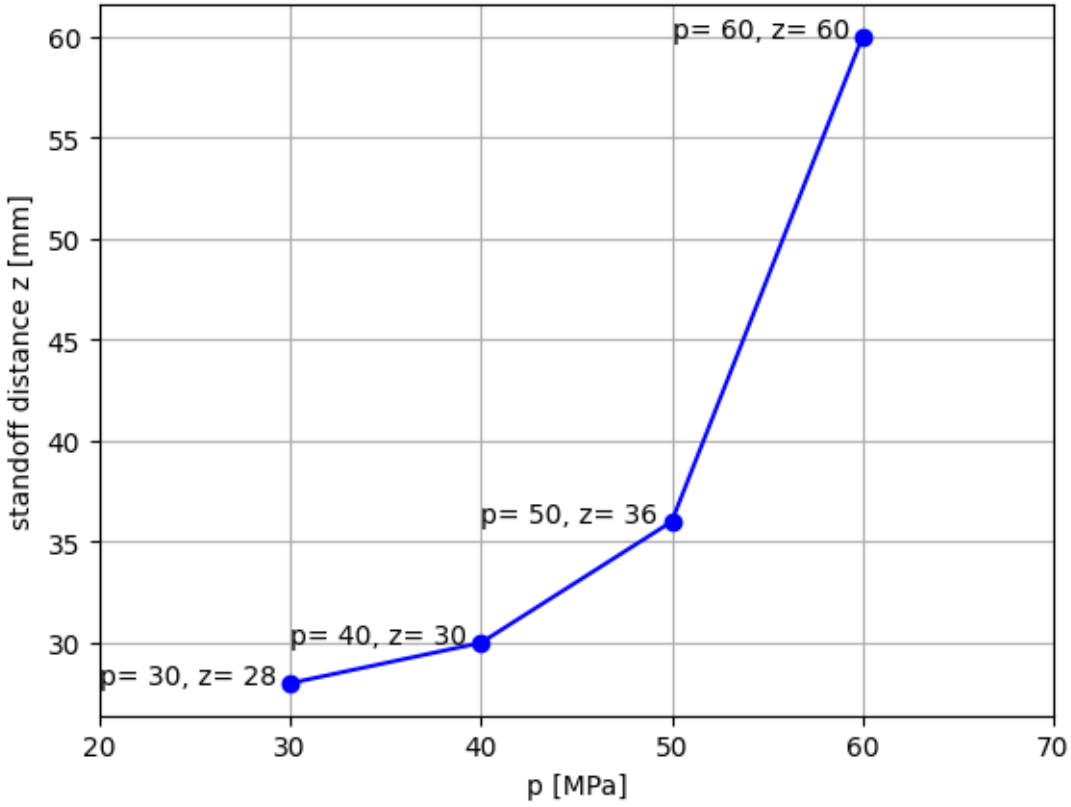

Figure 50 Optimal standoff distances selected for each pressure level

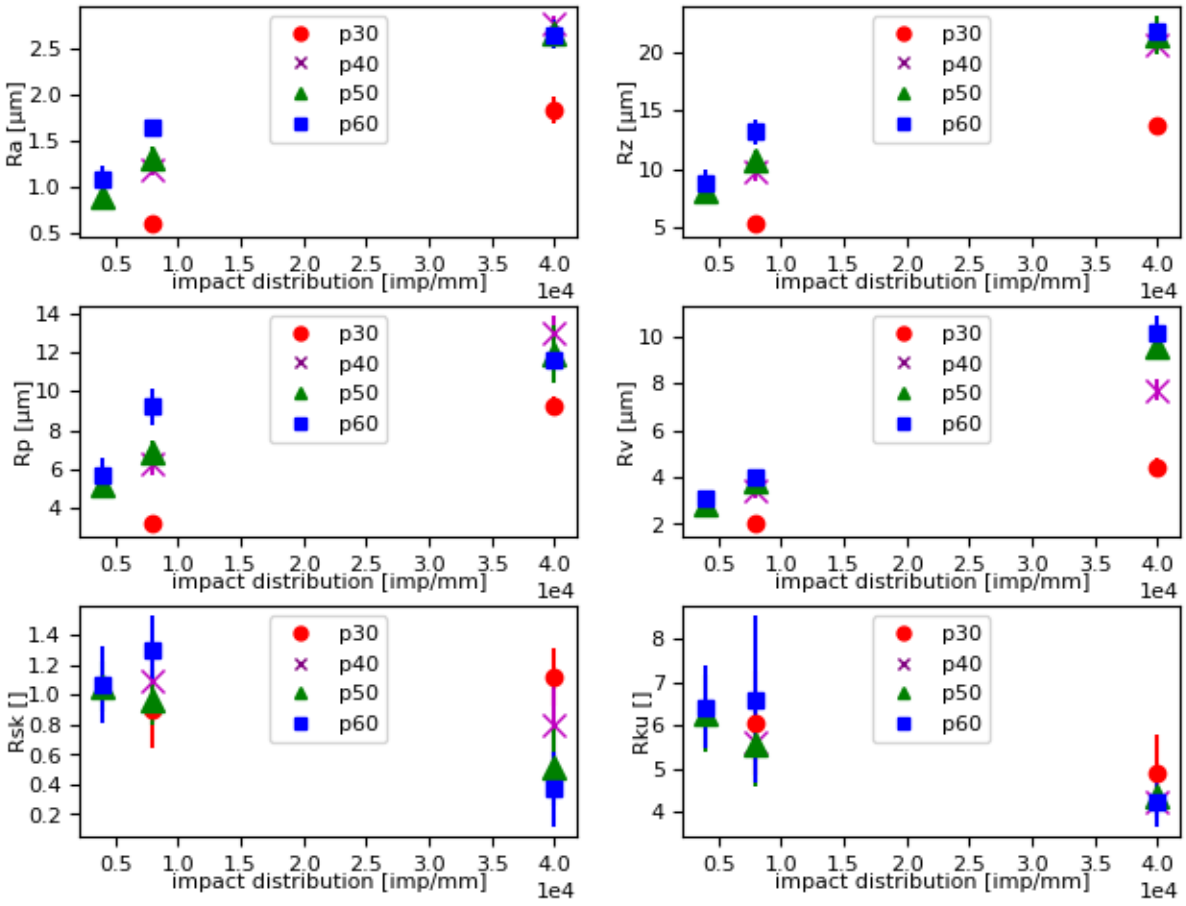

Figure 51 Roughness parameters Ra, Rz, Rp, Rv with Rsk and kurtosis Rku of 4 pressure levels based on feed rate v mm/s at optimal standoff distances z_{opt} selected for each pressure level p = 30, 40, 50, 60 MPa as 28, 30, 36, 60 mm respectively

Roughness parameters of Ra and Rz as well as Rv and Rp show strictly decreasing tendency with an increase in feed rate for all pressure levels. On the other hand, skewness parameter Rsk shows an increase between feed rate from 1 *mm/s* and 5 *mm/s*. It means that the profile is getting more peak dominant. An increase in kurtosis parameter Rku caused by an increase in feed rate from 1 to 5 *mm/s* means the increase in sharpness of the profile. **Figure 52** shows a SEM overview (print.mag 200x) of surfaces treated from optimal standoff distances based on stair trajectory. The effect of four pressure levels and the effect of increasing feed rate on erosion for each pressure level are visible in **Figure 52**. The pressure level variation at the feed rate of 1 *mm/s* leads to material roughening in cases of 60 *MPa*, 50 *MPa* and 30 *MPa* pressure. The PWJ treatment with 50 *MPa* pressure shows several places with significant material removal (similar to localized stage III). Material removal was also observed at 40 *MPa* and 1 *mm/s*, however, only sporadically. For 60 *MPa* significant surface roughening was observed. The feed rate of 5 *mm/s* caused surface roughening without visible material removal for all observed pressure levels. This is also the case for 10 *mm/s*.

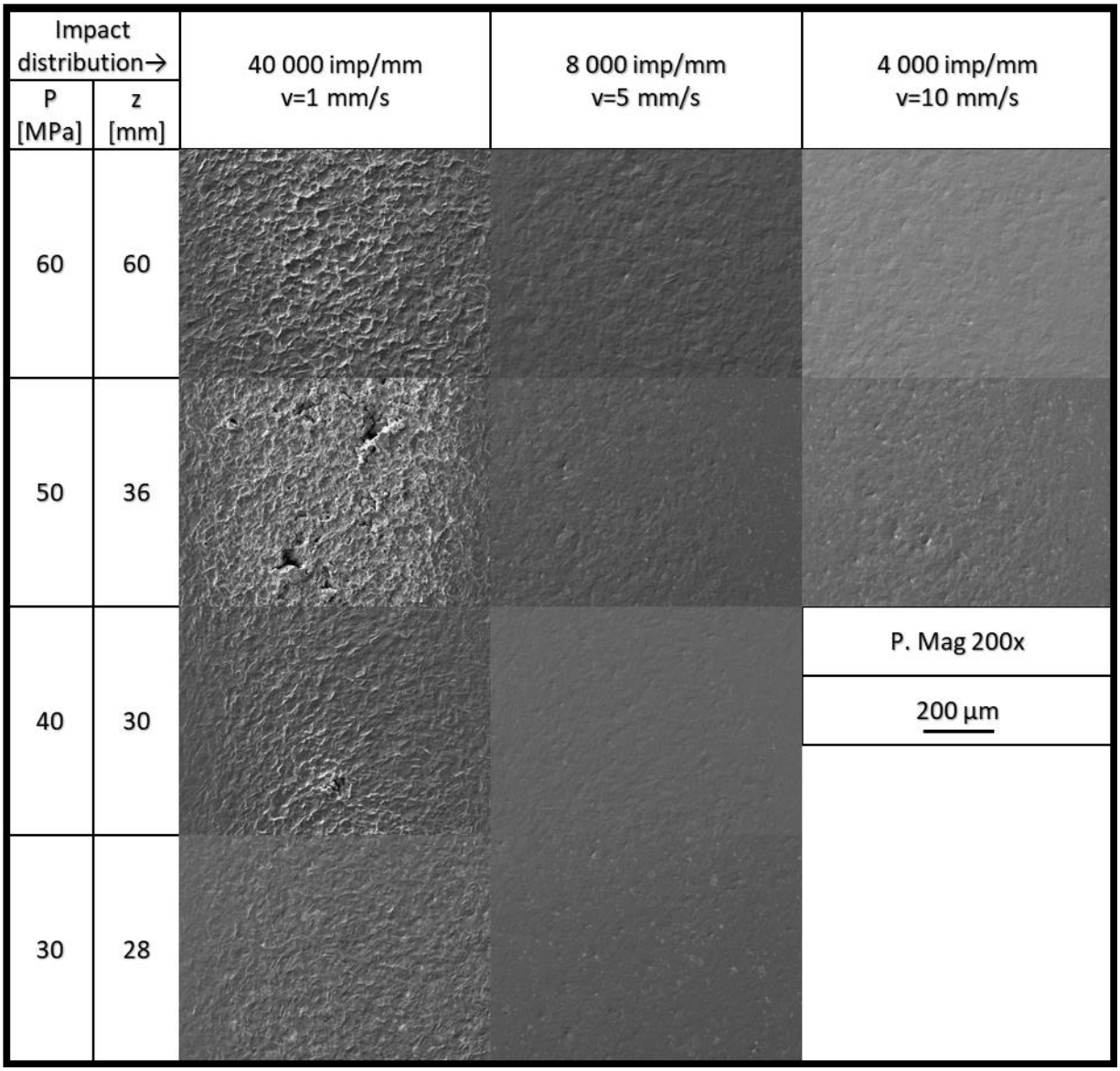

Figure 52 SEM overview of parametric optimization for the 316L steel considering pressure p standoff distance z and feed rate v with SEM print magnification of 200 x

The creation of grain boundary exposed relief can be observed in all four pressure levels (**Figure 53**). Rimmed grain boundaries can be observed at 60 and 50 *MPa* (1 *mm/s*). PWJ treatment with 60 *MPa* and 50 *MPa* also led to the creation of small cavities close to the elevated grain boundaries. A number of these cavities and their size are significantly larger at 50 *MPa*. PWJ treatment with 40 and 30 *MPa* led to grain boundary reveal as well, but not in such magnitude. Surfaces treated by these pressure levels (30 and 40 *MPa*) also show a number of surface steps, i.e., the creation of twins inside the treated grains. Surface steps related to twinning are also visible at the feed rate of 5 *mm/s* and in the case of 60 and 50 *MPa* also in the case of 10 *mm/s*.

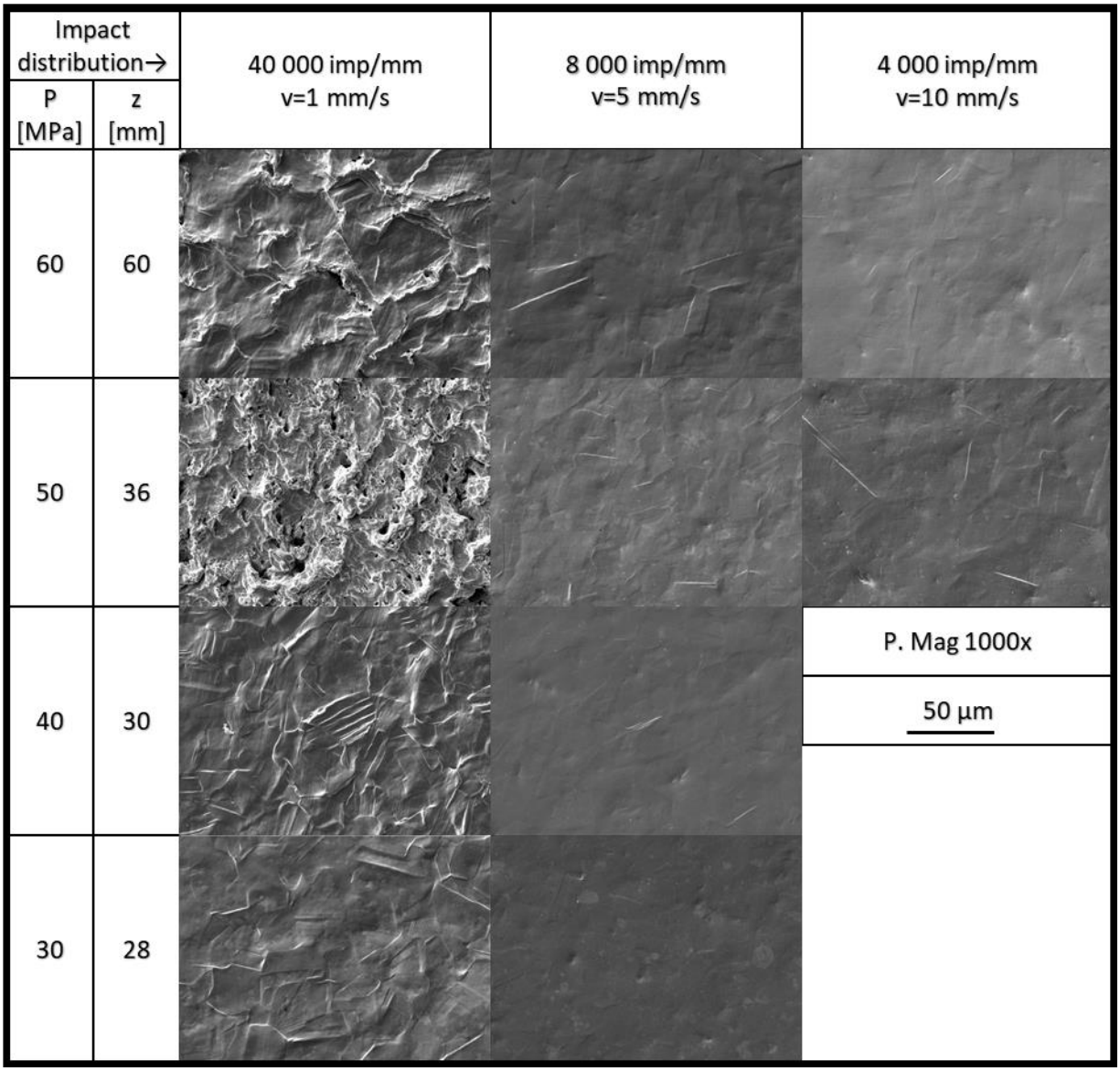

Figure 53 SEM detail of effect of parametric optimization considering pressure P standoff distance z and feed rate v with SEM print magnification of 1000 x

5.1.2 Effect of water impact distribution on the surface of Al alloy AW 2014

Experiment 1/3 conducted in this work was the evaluation of the effect of the distribution of liquid cluster impacts on the integrity of Al alloy. Two pressure levels were chosen for this experiment: 20 *MPa* and 40 *MPa*. Other process parameters (standoff distance, acoustic chamber length) were set to complement hydraulic pressure. The water impact distribution on the surface was controlled by the feed rate (movement velocity of PWJ head over the surface.)

The effect of the change of the total volume of liquid clusters impinging surface can be seen in **Figure 54**. Continuous kerf was created by 40 000 *i/mm* which equates to the feed rate of 1 *mm/s* by both 20 and 40 *MPa*. The pressure level of 20 *MPa* with the feed rate of 1 *mm/s*

(p = 20 MPa, v = 1 mm/s) created continuous kerf with fluctuations in width and small protrusion at the place where the jet impinged the material. The edges of the kerf also showed plastically upheaved material (pile-ups). Material removal was not visible by SEM at small magnification after 8 000 *i/mm (p = 20 MPa, v = 5 mm/s)*. Nonetheless, the jet path was still clearly visible due to surface roughening. There was no visible jet marking created by 4 000 *i/mm (p = 20 MPa, v = 5 mm/s)* at low magnification **Figure 54**.

The kerf created by 40 *MPa* at 40 000 *i/mm (p = 40 MPa, v = 1 mm/s)* was visibly wider and deeper. 40 *MPa* at this impact distribution also created visible pile-ups on the edges of the kerf and protrusion on sample surface where the kerf left the treated surface. At a smaller impact distribution 4 000 impacts per millimetre *(p = 40 MPa, v = 10 mm/s)*, the kerf showed significant disconnections on jet trajectory. However, some larger disconnected pits with visible material removal were observed along the jet path. The kerf cannot be considered connected as the amount of material loss fluctuates to zero along the jet path. With the further decrease of impact distribution to 2000 *i/mm*, 1333 *i/mm*, and 1 000 *i/mm* (v = 20 *mm/s*, v = 30 *mm/s* and v = 40 *mm/s*) there was no visible material removal at chosen magnification. The edge still shows protrusion at the entrance and exist point of the jet path.

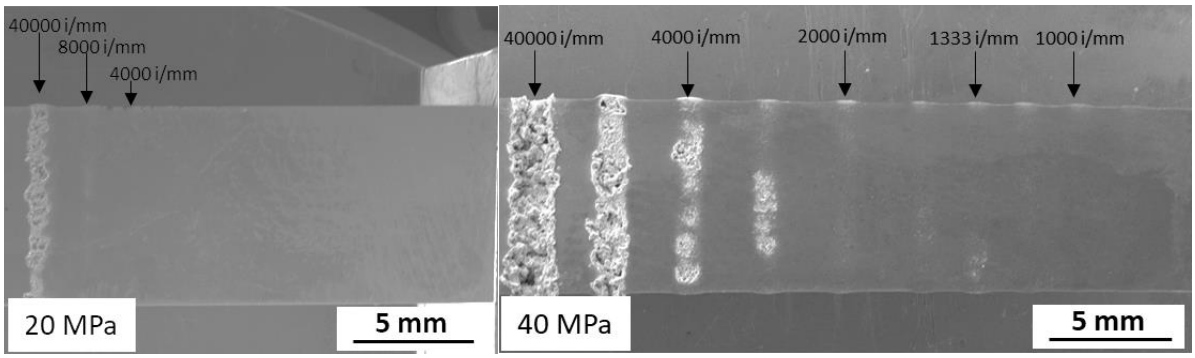

Figure 54 The overview of effect of decreasing total volume of clusters impinging the surface. The impact volume is controlled via feed rate ranging from 1 mm/s up to 40 mm/s which can be recalculated into 40 000 i/mm and 1000 i/mm [61]

The plots in **Figure 55** and **Figure 56** show profilometric measurements of depth of kerfs in aluminium alloy treated with PWJ equipped with 40 *kHz* sonotrode. The figures show variations of depth based on supply pressure and impact volume. The results follow the observations based on the SEM overview shown in **Figure 54**. The depth values are evaluated based on five equidistant locations along the kerf. The maximal and minimal depth is represented by the lower and upper limit of whisker lines visible in the figures. The median value is represented by the box interface and two box colours represent first and third quartile of the experimental run. The constant supply pressure increment in feed rate leads to decrease in depth achieved. The depth decrease is attributed to smaller volume of impacts impinging length unit of the treated material. In other words, the depth decrease can be attributed to lesser interaction time on the unit length of treated material. When supply pressure is doubled from 20 *MPa* (**Figure 55**) to 40 *MPa* (**Figure 56**) at constant feed rate of 1 *mm/s* the depth achieved increased from 227 *μm* to 625 *μm*. This can be attributed to an increase in cluster velocity from 180 m/s to 255 m/s, which leads to an increase in their kinetic energy.

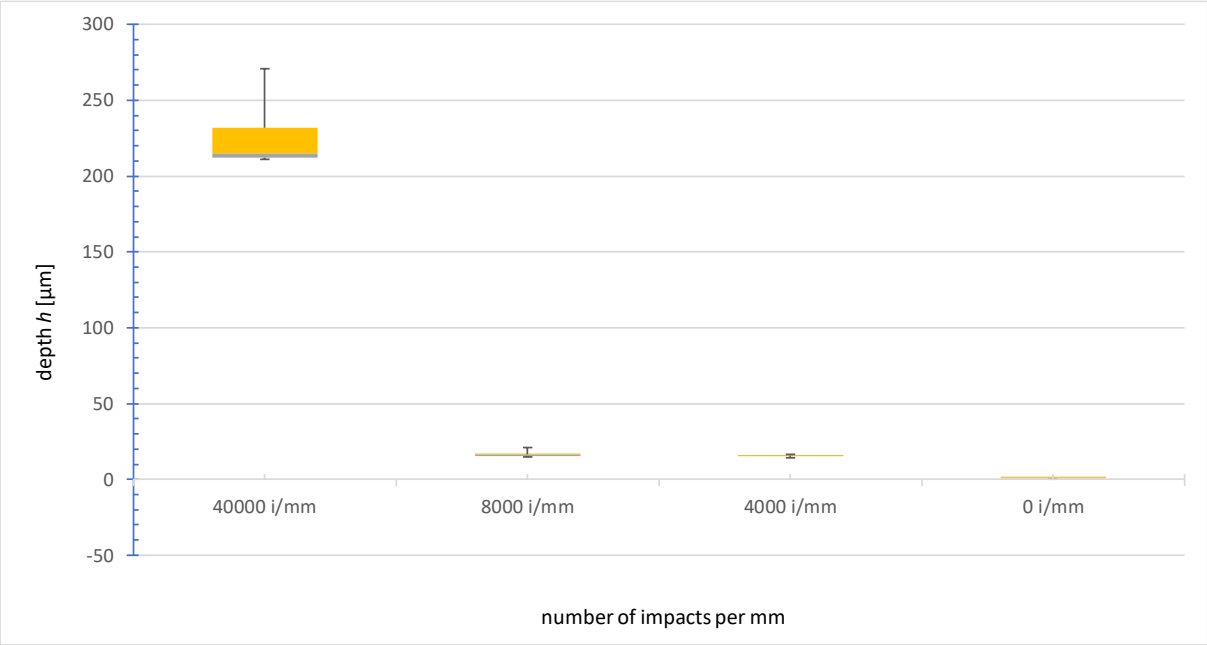

Figure 55 Dependence of impact volume (feed rate) on depth of kerf created. The constant conditions are hydraulic pressure 20 MPa, 40 kHz impact frequency and standoff distance 16 mm [61]

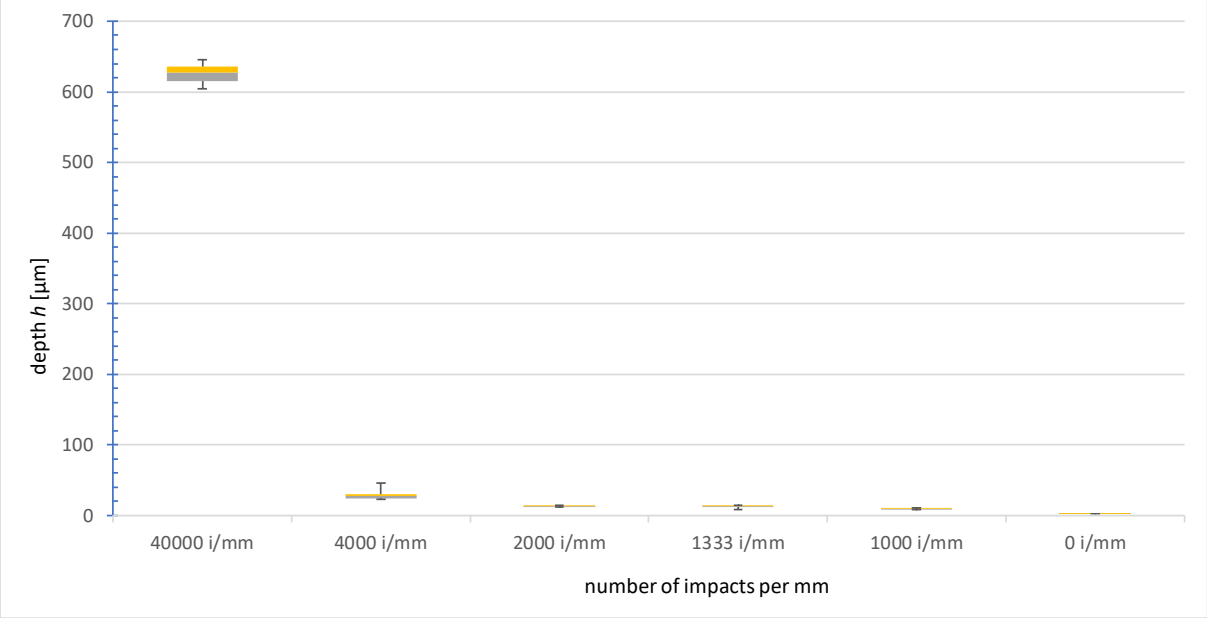

Figure 56 Dependence of impact volume (feed rate) on depth of kerf. The constant conditions are hydraulic pressure 40 MPa, 40 kHz impact frequency and standoff distance 32 mm [61]

Figure 57 shows a comparison of traces created by PWJ and CWJ with supply pressure of 20 *MPa* and the feed rate of 1 *mm/s*. The erosion kerf created by PWJ consisted of visible discontinuities along the jet path. CWJ footprint is almost unnoticeable at this magnification level (Rz = 8.89 μm). PWJ at feed rate of 10 *mm/s* resulted in roughening of the surface (Rz = 15.39 μm) with an irregular width of imprint along the trace

Figure 58 shows a comparison of traces of PWJ and CWJ created at supply pressure of 40 *MPa* and a feed rate of 1 *mm/s*. The erosion kerf created by PWJ is deep and continuous. CWJ creates a homogenously roughened surface (Ra = 2.35 μm, Rz = 14.54 μm) at the same feed rate. Kerf

created by PWJ with an increased feed rate to 10 *mm/s* shows visible discontinuity in eroded zones. Roughness parameters were evaluated for erosion footprint created using PWJ at 40 *MPa* and feed rate 20 *mm/s*. The roughness reached values of Ra 2.33 μm and Rz 12.87 μm. It is similar as roughening created by CWJ (with values reaching Ra 2.35 μm and Rz 14.54 μm) when the same supply pressure of 40 *MPa* was applied but with a significantly lower feed rate of 1 *mm/s*. This shows the increase of erosion effectivity of PWJ compared to CWJ where it is possible to achieve a similar roughness profile with 20 times increased feed rate when pulses are turned on. A faster process is more economically advantageous when used for real technical applications in practice. The feed rate of 40 *mm/s* creates only a roughened footprint with roughness values of Ra = 1.56 μm and Rz = 9.31 μm.

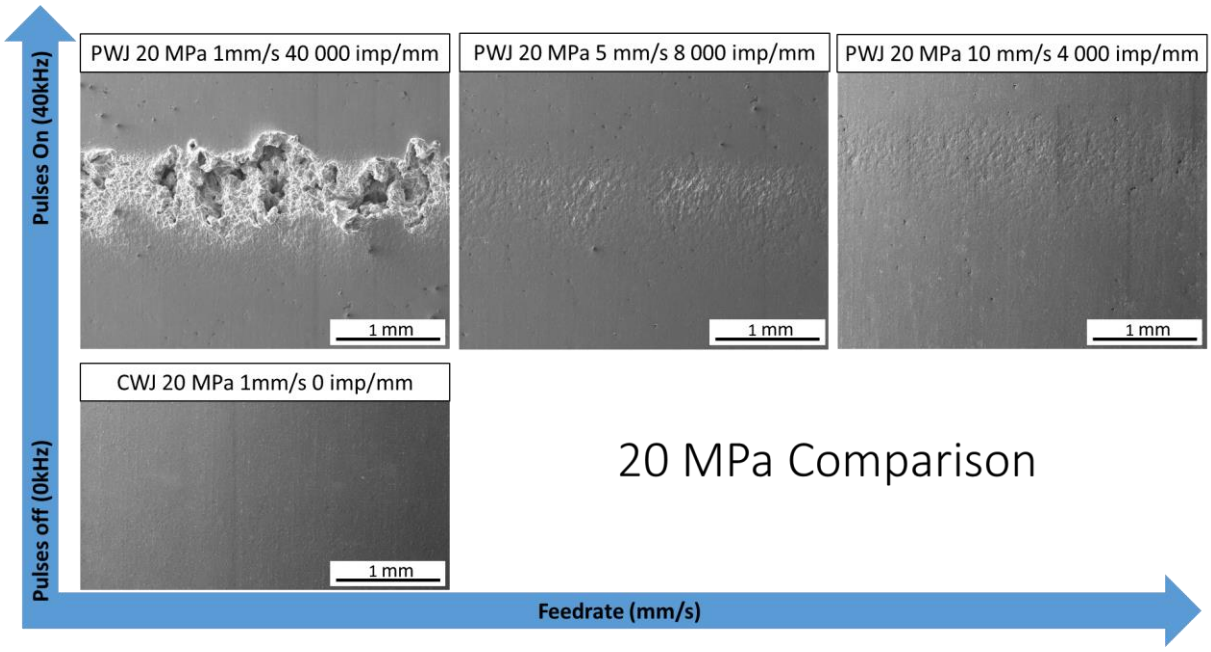

Figure 57 Overview comparison of PWJ and CWJ with the supply pressure of 20 MPa with variance in feed rate recalculated into droplet distribution using starting frequency 40 kHz. Modified from [61]

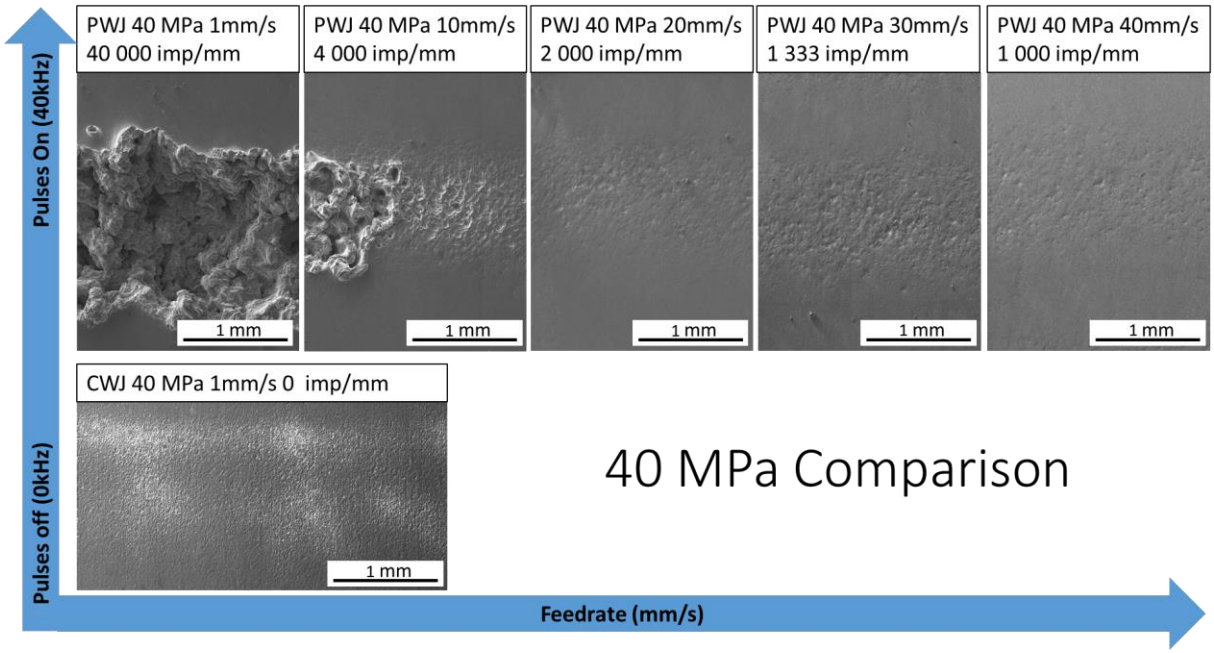

Figure 58 Overview comparison of PWJ and CWJ with the supply pressure of 40 MPa with variance in feed rate recalculated into droplet distribution using starting frequency 40 kHz. Modified from [61]

The erosion footprint created by PWJ at 20 *MPa* and frequency of 40 *kHz* can be seen in **Figure 59** and **Figure 60**. The difference between these kerfs is in the impact distribution controlled by feed rate. **Figure 59** shows the surface treated with the feed rate of 1 *mm/s* which equates to 40 000 impacts per millimetre, while roughening in **Figure 60** was achieved by the feed rate of 10 *mm/s* which equates to 4 000 impacts per millimetre. **Figure 59a** shows the jet footprints consisting of discontinuous paths of separate erosion kerfs. The prevalence of high pile-ups on the left side can hint at the direction of the jet movement (marked by the yellow arrow in the right corner of **Figure 59a**). The nozzle diameter is marked using white dashed lines. The eroded area is mainly between these lines, nevertheless with some erosion damage stochastically distributed also outside of the nozzle diameter area. The width of the affected are marked in **Figure 59a** by yellow dotted lines is approximately 2 times larger than the nozzle diameter.

Details in **Figure 59b, c, and d** are focused on the kerf borders. The area is full of small cavities. Small surface cavities show a number of marks on their edges possibly created by the effect of lateral flow jetting. The area close to the kerf shows a number of shallow microcavities, rifts and tears. Transient cavity exits can be also created as an escape point of lateral flow from the main kerf. This is visible in detail of **Figure 59d**.

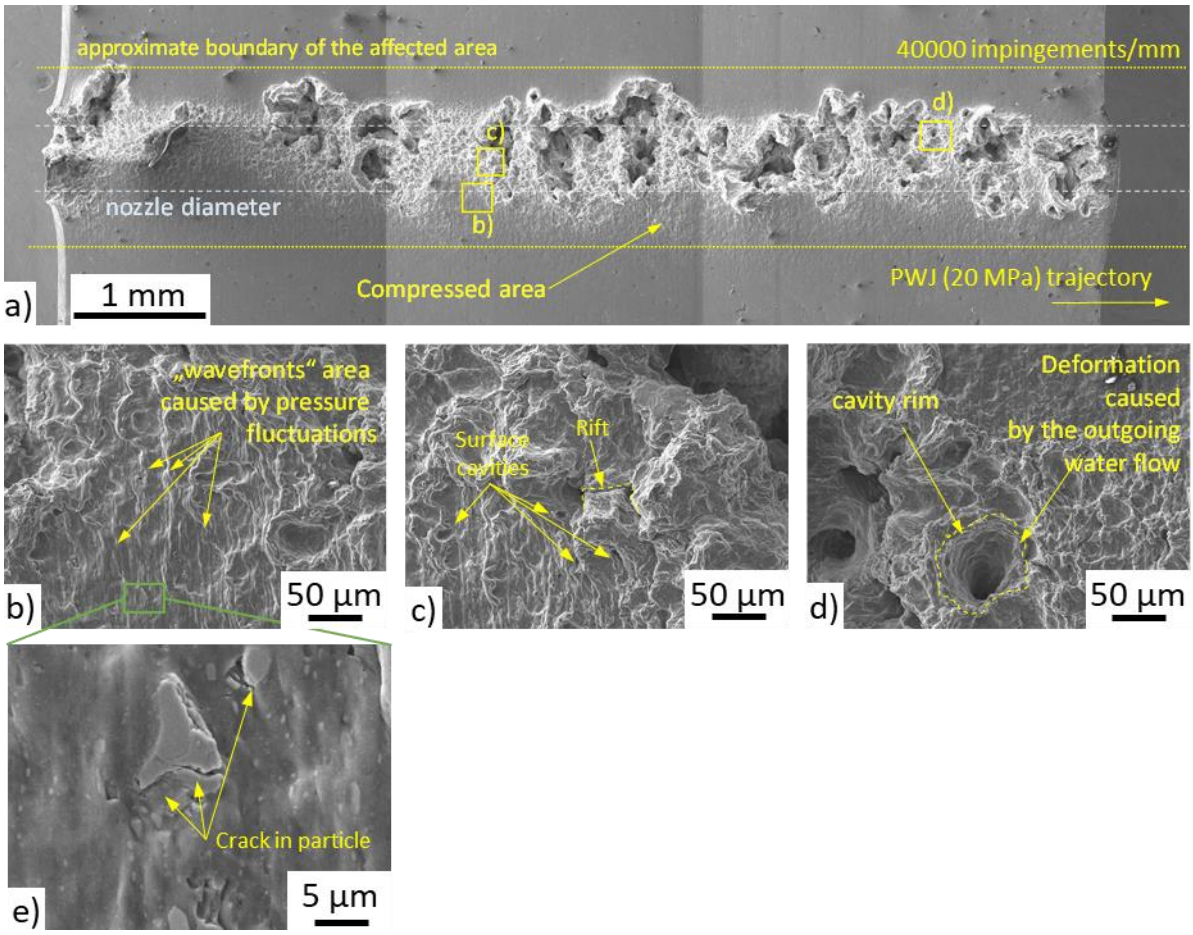

Figure 59 SEM observation of area treated with PWJ at supply pressure of 20 MPa and feed rate of 1 mm/s creating impact distribution of 40 000 i/mm. Figures are showing a) kerf overview. The underlying figures show details of b) adjacent area c) pile-up area and d) middle of the kerf showing cavity entrance

PWJ treatment of 20 *MPa* and feed rate 10 *mm/s* (4000 *i/mm*) created a roughened surface (**Figure 60**). The surface shows number of upheavals and depressions (**Figure 60a**). **Figure 60b** shows details of wavy surface deformed due to PWJ action. The only sign of material removal observed is the tilting of constituent particles in the aluminium matrix that can lead to cracking or even rollout of constituent particles (**Figure 60c)** and local depressions (**Figure 60d)**. The cracks propagating inside the constituent particle are detailed in **Figure 60e**.

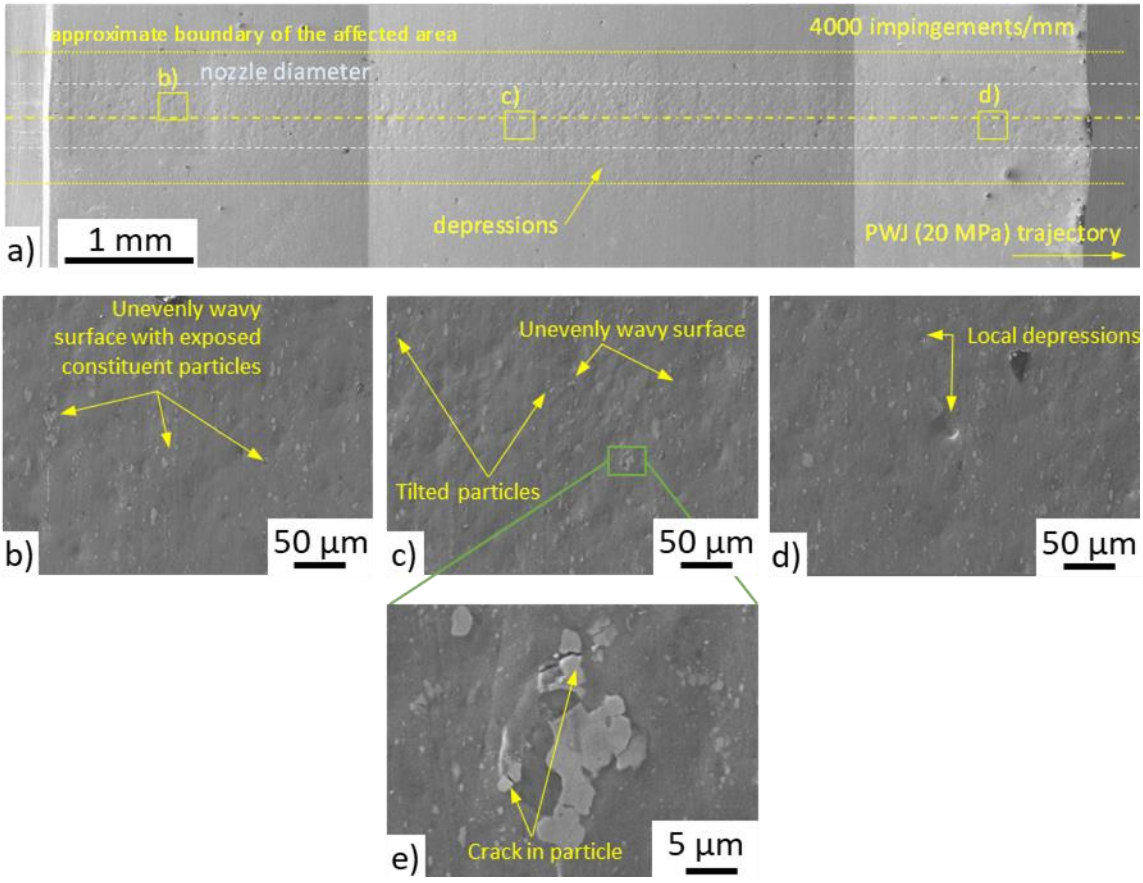

Figure 60 SEM observation of area treated with PWJ at supply pressure of 20 MPa and feed rate of 10 mm/s creating impact distribution of 4000 i/mm

Figure 61 shows the surface after PWJ treatment for the hydraulic pressure of 40 *MPa* and feed rate of 1 *mm/s*. The overview of the created kerf is shown in **Figure 61a**. The kerf is connected/continuous across the whole jet footpath. The kerf edges show significant pile-ups on both sides. The pile-up details are visible in **Figure 61b, c**. The material behind the pile-up shows no signs of material removal except rare cavity openings. The material at the outer footing of the pileup shows signs of deformation. Many cavity exits were observed. The cavity exits are rimmed with protruded material. The detail in **Figure 61b** shows the tearing off the top layer of aluminium alloy at the cavity exit. This detail also shows a gap in the pile-up with a relatively even surface. A similar cavity opening and compressed material near the pileup base can be seen in **Figure 61c**. **Figure 61a** shows also the kerf bottom. The kerf bottom is not uniform in height and contains a significant number of valleys and peaks. The detail in **Figure 61d** shows the vicinity of the crater in the centre of the kerf width. The detail shows the entrance to the subsurface cavity. The entrance is rimmed. On the top of the close peak, there are visible ductile dimples, i.e., signs of ductile fracture (noted with a yellow marking in the **Figure 61d**).

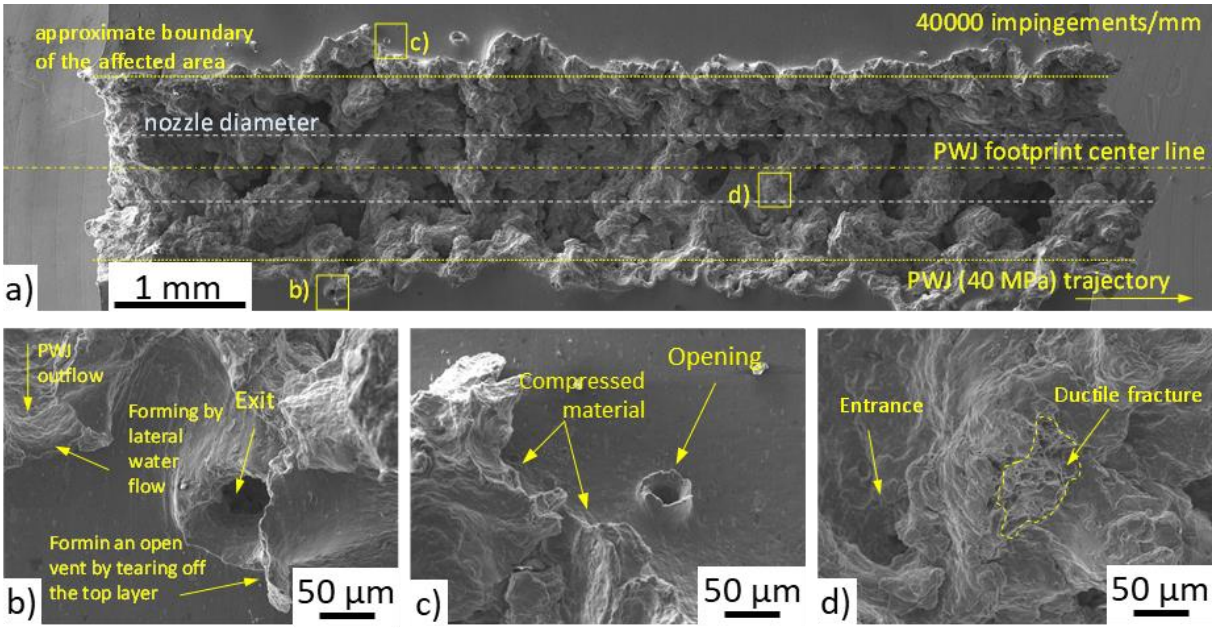

Figure 61 SEM observation of area treated with PWJ at supply pressure of 40 MPa and feed rate of 1 mm/s creating impact distribution of 40 000 i/mm. Modified from [61]

The water pressure of 40 *MPa* and higher feed rate of 40 *mm/s* created a roughened surface visible in **Figure 62**. The surface shows similar features as the surface created by 20 *MPa* and 10 *mm/s* (see **Figure 60**). The overview of the erosion footprint on the treated surface is in **Figure 62a**. The roughening is again approximately 2 times wider than the nozzle diameter. The detail in **Figure 62b** is from the area under the nozzle diameter and shows a local depression created along the jet path. The detail in **Figure 62c** shows the area from the outside of the nozzle diameter. Finally, detail in **Figure 62d** shows an area close to the path at the edge of the sample. The edge shows a visible protrusion to the side. The area close to the edge is visibly more roughened showing some local depressions formed into micropits.

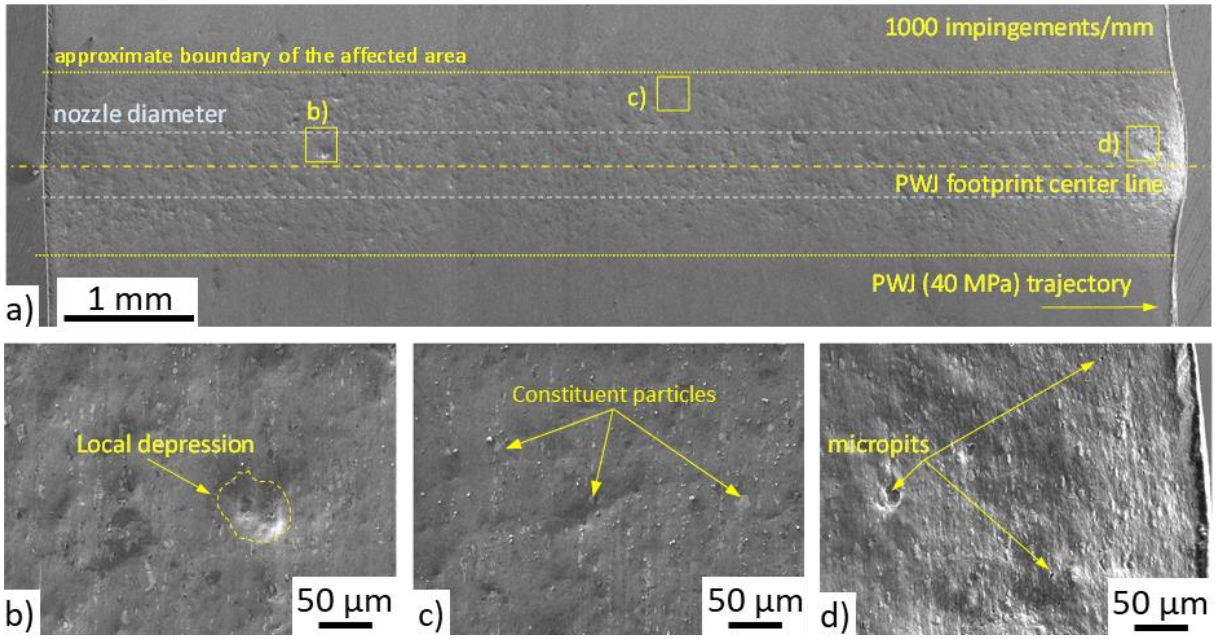

Figure 62 SEM observation of area treated with PWJ at supply pressure of 40 MPa and feed rate of 40 mm/s creating impact distribution of 1 000 i/mm

Figure 63 shows polished cross-sections of aluminium alloy samples treated by 40 *MPa* at feed rates of 1 *mm/s* and 10 *mm/s* which creates conditions for impact distribution of 40 000 and 4 000 *i/mm* respectively. The cross-section after the feed rate of 1 *mm/s* (**Figure 63a**) shows the depth of erosion kerf filled with metallographic mounting resin. The cross-section shows some voids seemingly disconnected from the main kerf. The cross-section also shows cracks of various sizes, filled with epoxy resins. The pile-ups at the kerf borders are also visible. The cross-sectional picture of the kerf created with higher feed rate of 10mm (**Figure 63b**) shows a smaller kerf with a small pile-up next to it created on the surface of aluminium alloy sample. On the other side of the peak, a visible local depression is present.

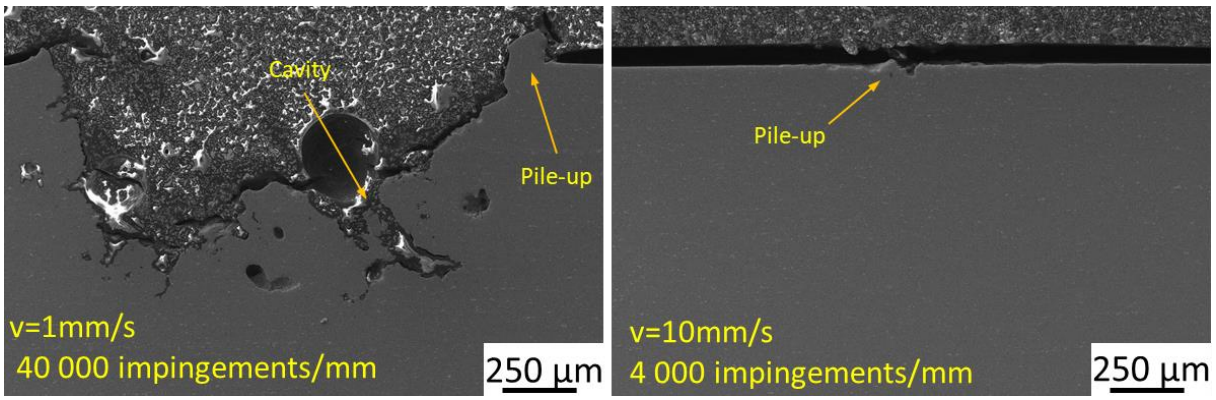

Figure 63 SEM observation of cross-section created with PWJ at supply pressure of 40 MPa, 40kHz and feed rate of a) 1 mm/s (40 000 i/mm) and b) 10 mm/s (4 000 i/mm)

The dependence of hardness on distance from the surface for AW2014 treated with waterjet (both PWJ and CWJ) using a varying feed rate and constant pressure of 20 *MPa* and 40 *MPa* is shown in **Figure 64** and **Figure 65**.

The highest hardness values were obtained in the subsurface layer. Treatment with pressure 20 *MPa* exhibits a visible increase in measured hardness 92.3 ± 3 HV 0.005 values in depth of 30

μm from the surface (**Figure 64**). The increment is the highest for PWJ with feed rate of 5 *mm/s*. The second highest hardness increment in the subsurface layer was observed in the case of treatment with feed rate of 10 *mm/s*. When pulses were turned off at the feed rate of 1 *mm/s* (as substitution of CWJ treatment) hardness values in the subsurface were close to surface hardness of original i.e., untreated state (in picture marked with red dashed line). The hardness decreases up to depth of 75 *μm*, where it becomes, within the experimental error, close to the untreated state.

Figure 65 shows the depth dependence of hardness HV 0.005 for treatment done by supply pressure 40 *MPa* with varying feed rates. One test was done with CWJ at the same supply pressure for comparison. The hardening is most significant for all PWJ treatments in the subsurface layer, i.e. at the depth of 30 *μm* from the surface, similarly as for pressure of 20 *MPa*. The highest hardness was observed for the feed rate of 20 *mm/s*, where hardness reached a value of 95 HV0.005 and then with dept the hardness slowly decreased. The same trend is visible for all PWJ variations. In the case of the CWJ variant, the 40 *MPa* pressure results are close to the hardness of untreated surface, similarly as for pressure 20*MPa*.

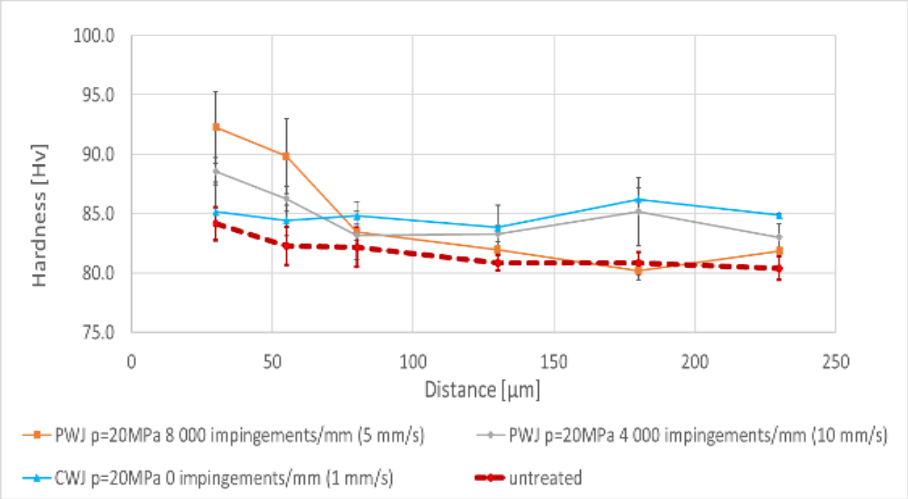

Figure 64 Hardness distribution as a function of distance from surface on the cross-section of a surface treated with PWJ and CWJ with feed pressure of 20 MPa with varying feed rates

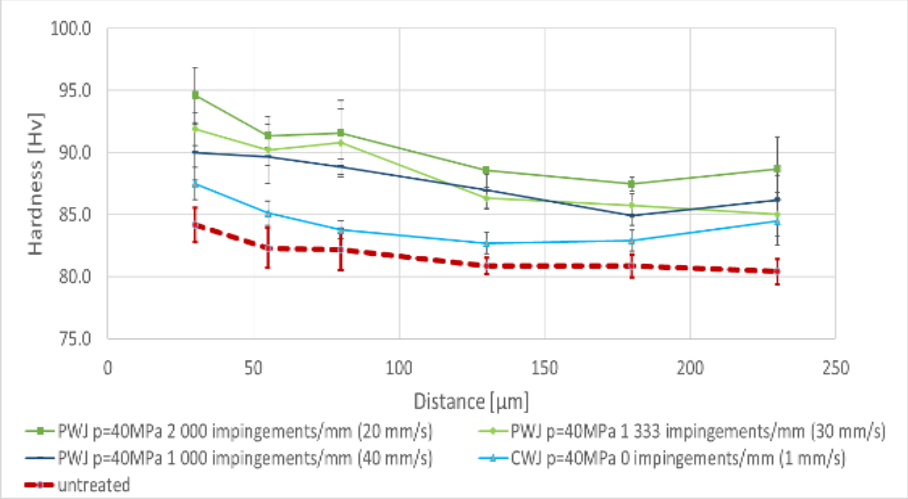

Figure 65 Hardness distribution as a function of distance from surface on the cross-section of a surface treated with PWJ and CWJ with feed pressure of 40 MPa with varying feed rates

5.2. Experiment set II

Experimental set II consists of PWJ treatment of exclusively 316L stainless steel. The treatment of rotatory fatigue samples was done by PWJ and compared with untreated material. The next experiment focused on changes to the surface and subsurface of the treated material caused by PWJ with varying exposure time. The last experiment focused on EBSD observation of incubation erosion stages caused by PWJ with varying exposure time.

5.2.1 Surface hardening – fatigue improvement

Two sets of PWJ treatments on samples used in fatigue tests were conducted. First fatigue samples were treated with PWJ with constant hydraulic pressure and variations in feed rate from v = 0.05 *mm/s* up to v = 0.33 *mm/s*. Fatigue tests were conducted on 3 strain levels for each treatment. The parameters of PWJ treatment are described in Chapter **4.2.3**. Details of the fatigue testing are described in Chapter **4.3.4**.

Figure 66 shows the dependence of a number of cycles to fracture N_f on total strain amplitude $\varepsilon_{at.}$ The fatigue curve of as received material was measured in large interval of total strain amplitudes (**Figure 66a**). Based on this curve three strain levels 0.44, 0.32 and 0.28% were selected for PWJ treated samples. The results are shown in detail in **Figure 66b**. Since the x-axis is plotted in logarithmic scale, the improvement of fatigue life due to the PWJ treatment is quite high. At the strain level of ε_{at} = 0.28%, two PWJ treatments with feed rates of 0.2 and 0.05 *mm/s* achieved a maximum number of cycles $7x10^5$. At this value of the applied number of cycles, the fatigue testing was interrupted/finished without the final fracture of the sample and the test was considered run-out. At the same strain level, the sample treated by PWJ at v = 0.33 *mm/s* reached a fatigue life of 106 589 cycles, which is a significant increase compared to 37 635 cycles of untreated material.

Figure 67 shows a dependence of a number of cycles to fracture on feed rate. The dependence is especially visible at the strain level ε_{at} = 0.32%. PWJ treatment at v = 0.33 *mm/s* led at ε_{at} = 0.32 % to fatigue life of N_f = 36 778 cycles, while lower values of the feed rate of v = 0.2, 0.1, and 0.05 *mm/s* led to fatigue lives of N_f = 78 176, N_f = 123 847 and N_f = 139 068 cycles respectively. The decrement in PWJ feed rate led to a number of cycles to failure increase. Similar dependence is also observed ε_{at} = 0.28%, however, precise effect of the feedrate at this strain level cannot be drawn on the basis of the data due to low number of experiments and presence of run-outs. Strain level ε_{at} = 0.44 % shows no clear dependence of PWJ feed rate on a number of cycles to failure, and all results are below N_f = 20 000.

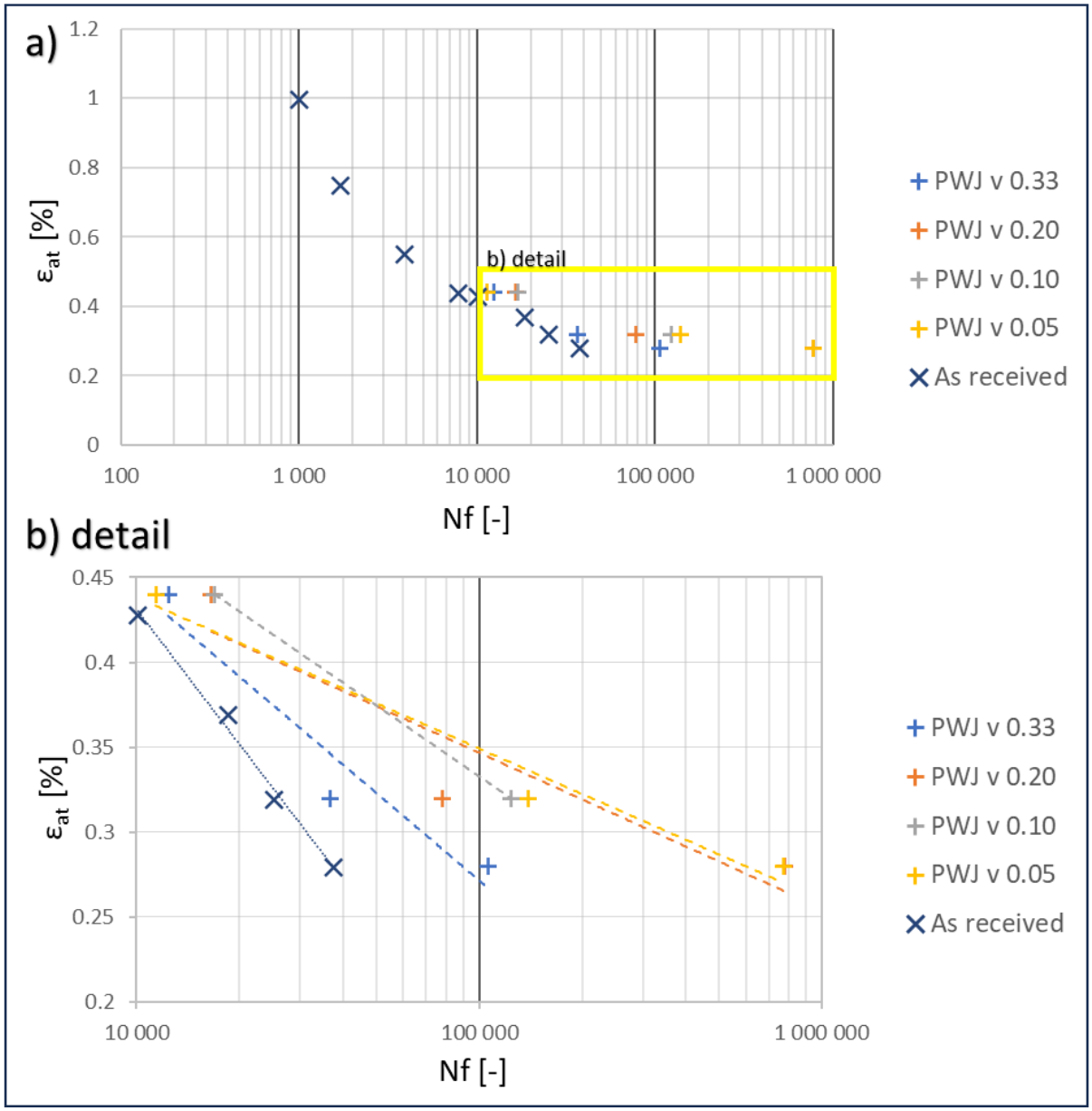

Figure 66 a) Fatigue life curves of FT 1 with variable PWJ feed rate with constant PWJ feed rate compared to fatigue life curve of untreated material. b) Detail of 10^4-10^6 area. Measurements are approximated by logarithmic trendline

Table 8 Fatigue lives of samples at three total strain amplitudes treated by PWJ compared to as-received material

	As received	PWJ treated at different feed rate			
v *mm/s*	0	0.33	0.2	0.1	0.05
ε 0.28 %	37 635	106 589	RO 777 050	-	RO 770 500
ε 0.32 %	25 154	36 778	78 176	123 847	139 068
ε 0.44 %	7 846	12 403	16 540	16 920	11 375

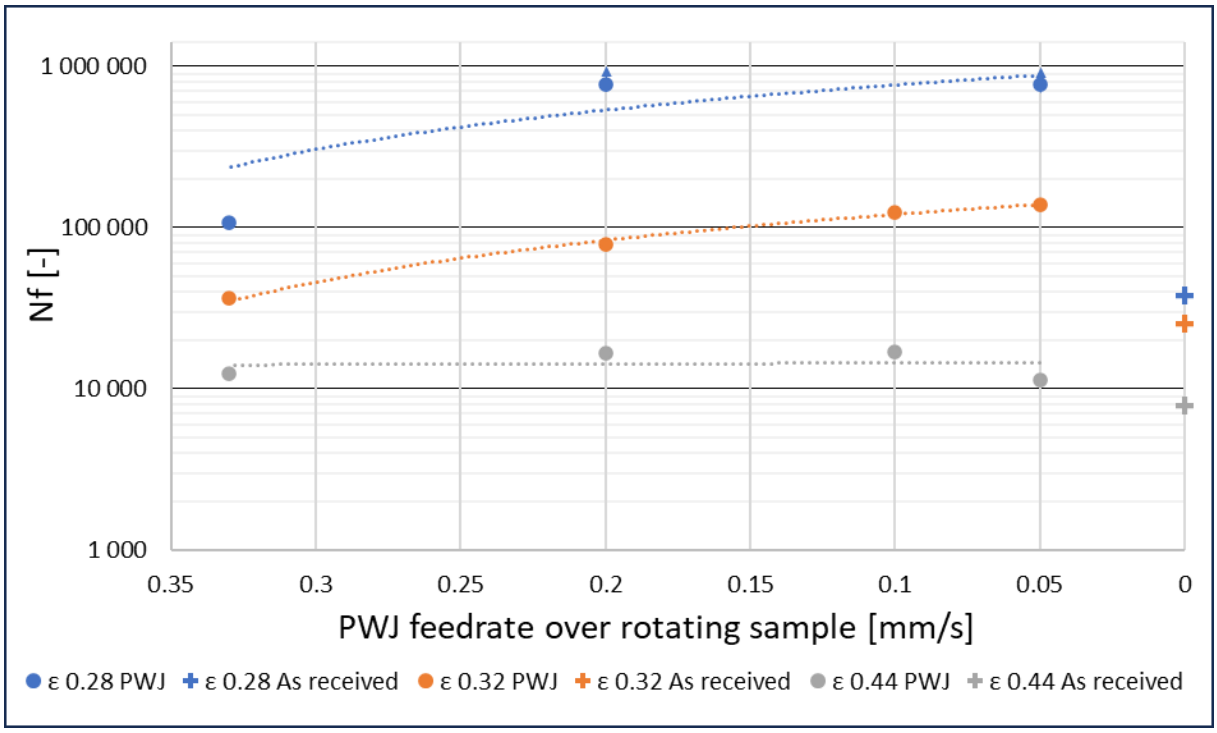

Figure 67 Number of cycles to failure dependence on the feed rate of PWJ treatment for several total strain amplitudes compared with untreated material

The cyclic hardening/softening curves for all three tested strain levels (0.28 %, 0.32 %, 0.44 %) are presented in **Figure 68a, b, c**. The initial cyclic hardening is more significant at lower strain levels and is followed by long period of cyclic softening and then secondary cyclic hardening appears. The length of secondary hardening differs significantly for particular treatments. It is evident that the start of secondary hardening appears after certain number of cycles. The existence and length of the secondary hardening is thus determined by the moment when the macrocrack is formed. I.e. the as-received sample at strain level $\varepsilon_{at,eq}$ = 0.28 % shows little to no secondary hardening before macrocrack propagation.

The length of the secondary hardening stage increases with a lower feed rate of PWJ treatment. The longest secondary hardening phase is observed for run-out samples (PWJ v = 0.2 *mm/s* and v = 0.05 *mm/s*) at ε_{at} = 0.28 %.

Samples tested at a strain level of ε_{at} = 0.32 % show similar behaviour. The secondary hardening of the as-received sample is almost negligible, The secondary hardening of PWJ v = 0.33 *mm/s* sample probably started, however, macrocrack propagation started soon after approx. $3x10^4$ cycles. The secondary hardening of the sample treated by PWJ at v = 0.2 *mm/s* was ended by macroscopic crack propagation at around $7x10^4$ cycles. Finally, the PWJ sample treated by v = 0.1 *mm/s*, v = 0.05 *mm/s* achieved over $10x10^5$ cycles at strain level ε_{at} = 0.32 %.

At the highest strain level ε_{at} = 0.44 %. all samples show fatigue life between $7x10^3$ cycles and $1.8x10^4$ cycles. Interestingly all samples show a visible secondary hardening stage.

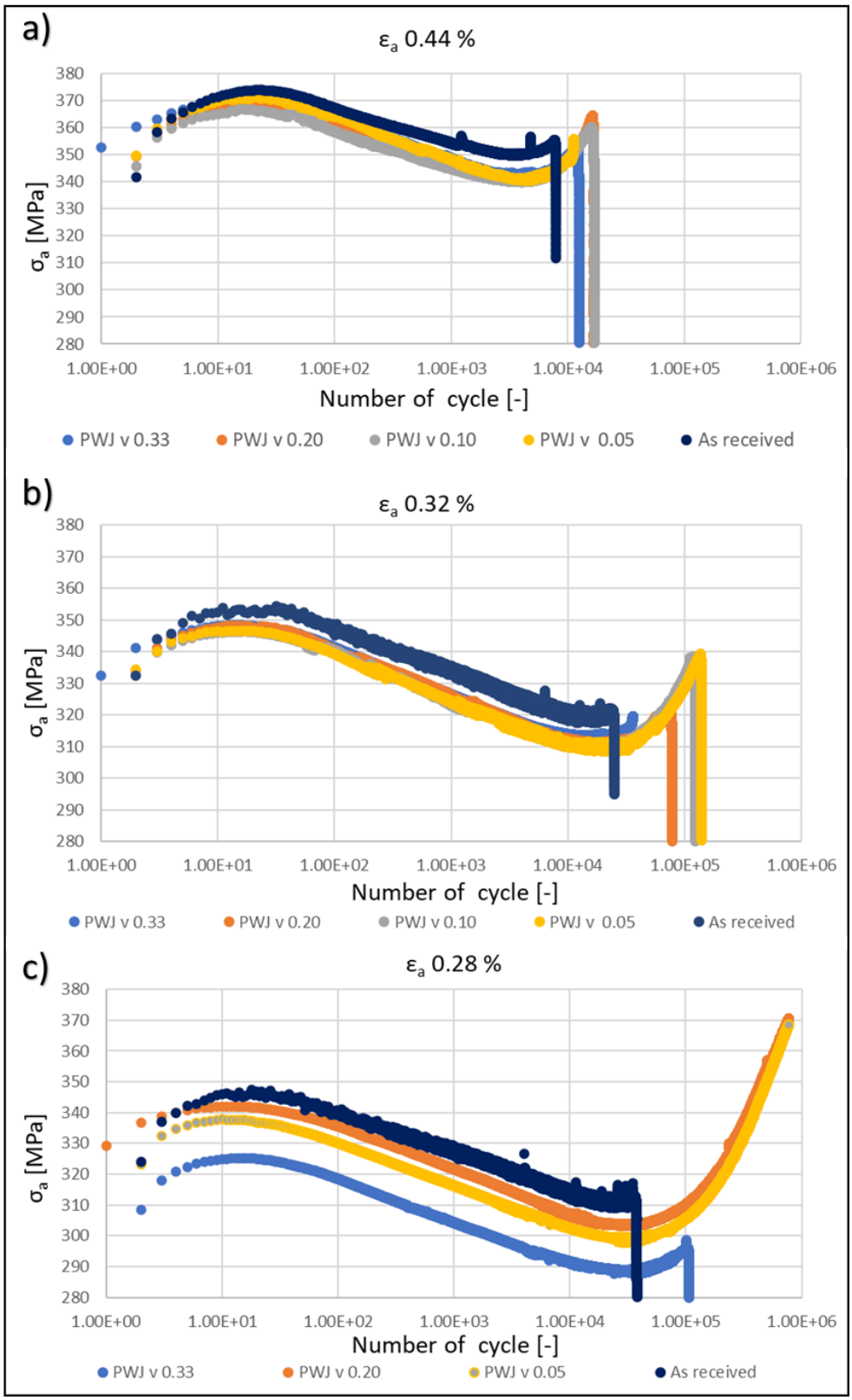

Figure 68 Hardening curve for total deformation amplitude of a) 0.28 %, b) 0.32 % and c) 044 % for 316L stainless steel PWJ treated samples

Based on the fatigue testing results the strain level of 0.32% was selected for fractography observation of fatigue life dependence on feed rate. Higher strain level does not exhibit strong fatigue life changes and at low strain of 0.28% due to the presence of run-out, the result can be considered as not conclusive. The PWJ feed rate of v = 0.33 *mm/s*, v = 0.10 *mm/s* and v = 0.05

mm/s were selected for fractography observations. Examples of fractography observation of samples treated by PWJ prior fatigue tests are in **Figure 69**. The upper row of micrographs shows an overview of the fracture surfaces of selected samples. From comparison it is evident, that a decrease in feed rate results in a decrease in the area of final fracture (marked by blue arrows). The fatigue crack initiation point of all three samples is marked by green arrows. The following two rows of micrographs in **Figure 69** show details of areas in the crack propagation region close to the initiation zone at two different magnification levels. The approximate location of the details is marked with yellow rectangles. These details show the presence of striations, i.e., characteristic morphologic features related to fatigue loading and crack growth direction and sometimes also to crack growth rate.

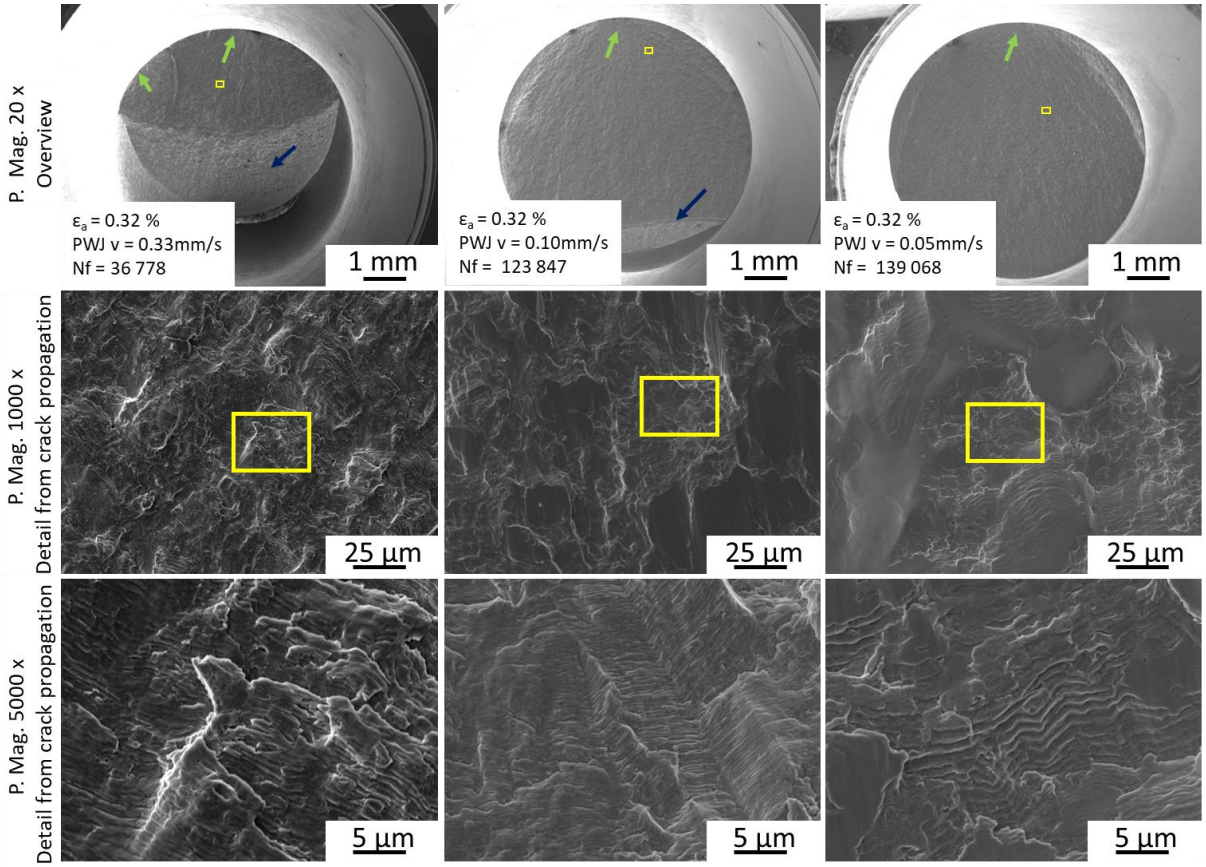

Figure 69 Fractography of samples after 0.32% total strain amplitude fatigue test. The first line shows an overview of the whole fracture, while second- and third lines show details from fatigue crack propagation area at two magnifications

5.2.2 Surface hardening – effect of time exposure

The hydraulic pressure of 50 *MPa* was selected for the time exposure test of 316L stainless steel. The only variable of the experiment is a number of impacts of water clusters, which is controlled by variations in exposure time. The surface morphology after given number of water impacts was observed using SEM and followed by subsurface observation using TEM. TEM observation was carried out for a better understanding of erosion induced changes in the subsurface. Therefore, several TEM lamellae were prepared using the FIB technique

from the central region of the eroded area. Microhardness was measured with force of 150 *mN*. Surface shape was evaluated using the MicroProfFRT non-contact profilometer.

Figure 70 shows the surface of steel samples observed using SEM and treated by PWJ for exposure times of 5 and 10 seconds, which is 205 000 and 410 000 impacts respectively. The experiment contains all 3 erosion stages because the evolution of erosion starts from surface roughening/deformation, then with increasing exposure time, it continues with a material removal at preferential sites and the creation of micropits up to the formation of coherent erosion crater under the jet.

Figure 70a shows the area subjected to PWJ for 5s. It corresponds to approximately 205 000 impacts. The centre of the eroded area shows a high level of deformation. Outside of the centre region the surface appears gradually less damaged. The detail of the centre area is shown in **Figure 70b**. The detail shows number of protruding regions. Occasional presence of microcavities was observed.

After 10 *s* of PWJ exposure (**Figure 70c**) which equates to about 410 000 impacts the roughened area is wider than the diameter of the used nozzle. The area gets gradually more deformed closer to the jet core. The area under the jet core shows a significant number of cracks and microcavities, as well as places of visible material removal. Detail in **Figure 70d** shows the centre of exposed area, where the material removal process is most apparent.

After 15 *s* of PWJ exposure (**Figure 71a**) area under the jet core is significantly eroded with obvious material removal. The crater is from top and side edges rimmed with pile-up. Detail **Figure 71b** focuses on this pile-up. The detail shows a visible pile-up surrounding the erosion crater. The pile-up is in several places disturbed by cavities. The region of compressed material is observable behind the pile-up.

A similar situation is observed after 20 *s* of PWJ exposure (**Figure 71c**) where the top and side edges of the erosion crater are also surrounded by the pile-up. However, the bottom part of the crater shows a gradual transition into a roughened area with no significant pile-up. The detail (**Figure 71d**) again focuses on pile-up on the top side of the erosion crater. There are visible surface steps behind the pile-up. The pile-up is also much more disturbed by surface cavities and visible tearing of the pile-up was observed.

The surface of steel samples was treated also by CWJ for comparison. It shows a roughening after 10 *s* of exposure (**Figure 72a**). The area shows some visible twinning (**Figure 72b**). The detail also shows a significant number of steps created on the CWJ treated surface. First signs of material removal are observed in **Figure 72c** after CWJ exposure of 20 s. Most of these early signs of material removal are observed under the jet core. **Figure 72d** shows the detail of the mentioned area under the jet core. The material removal starts at preferential sites which seems to correspond to surface steps observed under smaller erosion time. The material response to CWJ is significantly smaller than the material response caused by PWJ. PWJ exposure of the 20s leads to the creation of an erosion pit, while at the same time CWJ exposure leads only to starting of the material removal on preferential sites.

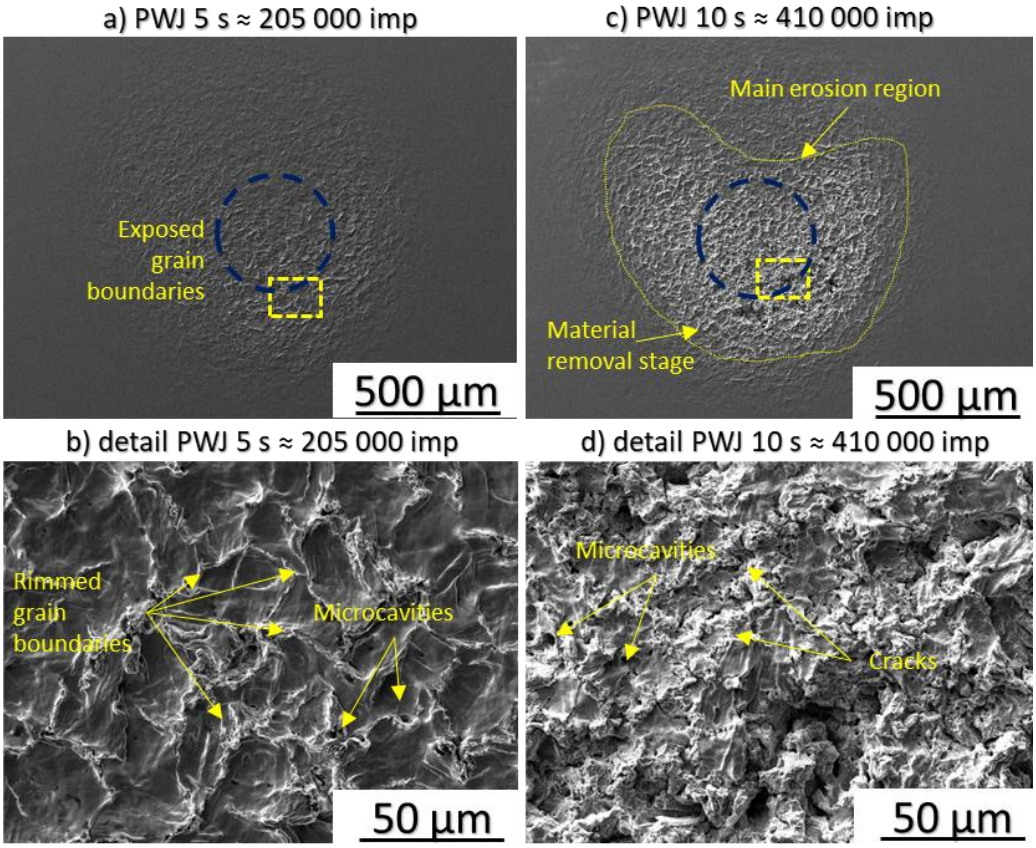

Figure 70 SEM analysis of surface treated with increasing time under water impacts at frequency of impacts of 41 kHz for erosion time of a)5 s b) 10 s. Blue circle mark jet diameter

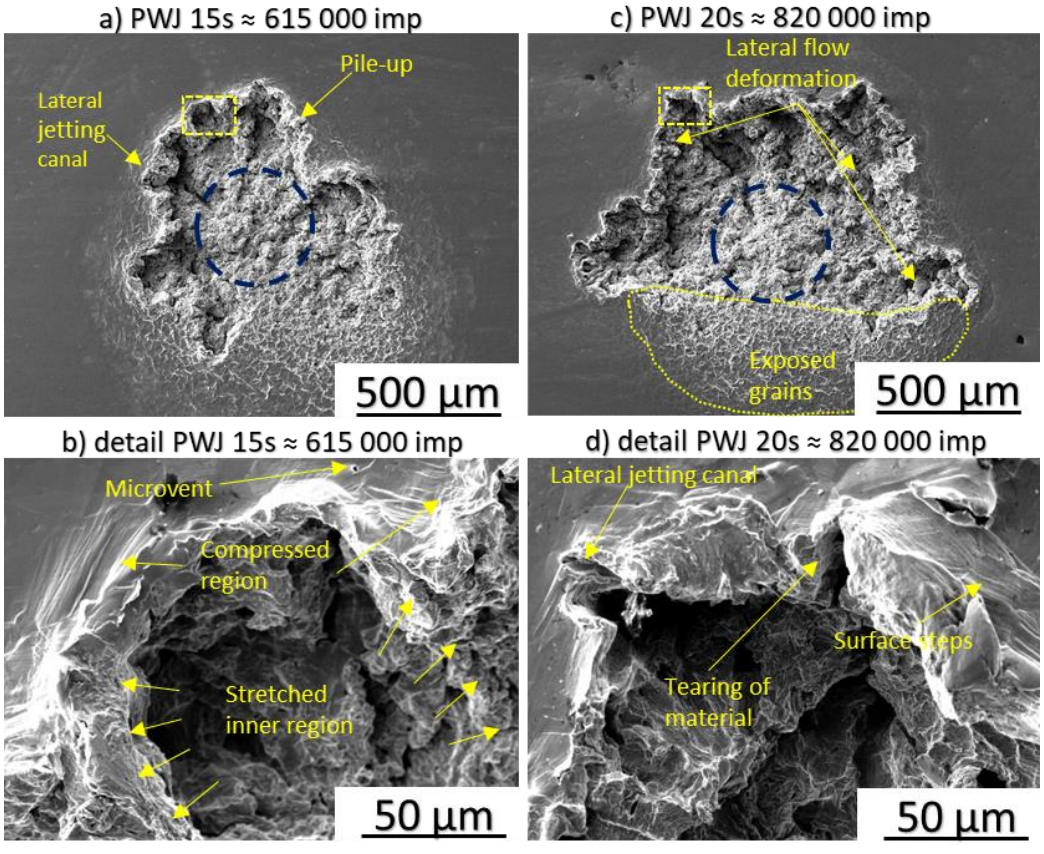

Figure 71 SEM analysis of surface treated with increasing time under water impacts at frequency of impacts of 41 kHz for erosion time of a)15 s b) 20 s Blue circle mark jet diameter

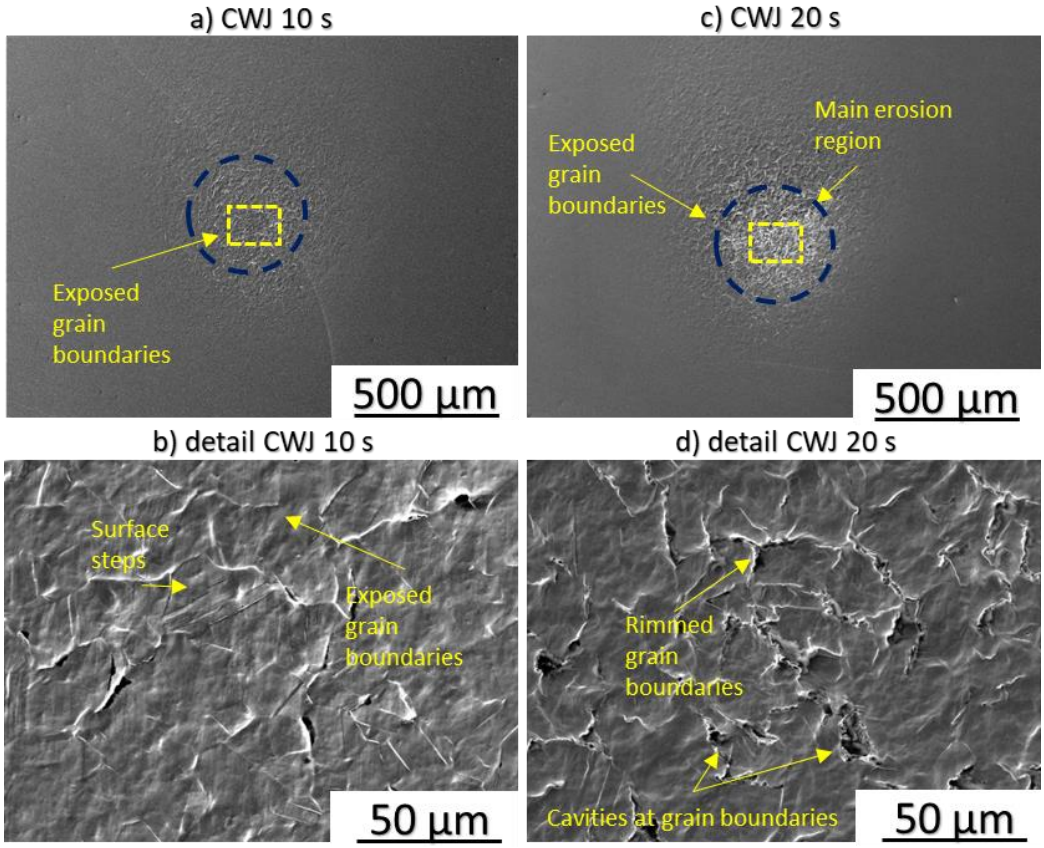

Figure 72 The surface treated by CWJ with an exposure time of a) 10 s showing roughened surface with a number of steps on the material and visible steps b) 20s shows the first cavities appearing in the centre of the exposed area. The blue circle mark jet diameter

The shape of the measured crater profile is shown in **Figure 73**. The measurement is taken from the centre of the erosion crater at the highest depth point. As reported above, the detectable depth in continuous single crater starts at 7s of PWJ exposure. Based on this observation, an exposure time of 7s was chosen as the point where roughness parameters evaluation will be replaced with depth and volume evaluation. **Figure 73** shows the deepening and widening of the crater concerning increasing erosion exposure time. The continuous single crater exceeds in its width the nozzle diameter at about 10s of PWJ exposure.

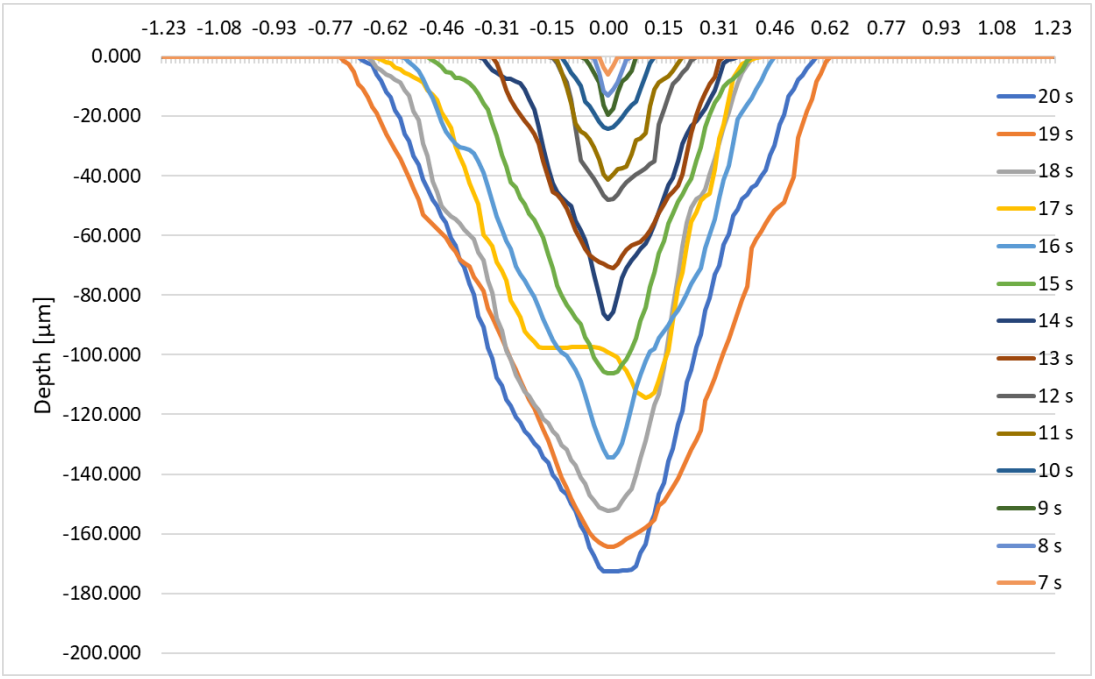

Figure 73 Visualization of PWJ exposed area profile based on exposure time. Exposure ranging from 7 s to 20 s

Figure 74 shows depth plot of the dependences of removal volume and erosion depth achieved by increasing the exposure time of PWJ from 1s up to 20 s. At a frequency of 41*kHz* the exposure time range corresponds to impact range from 41 000 to 820 000 impacts. Sufficient surface depression for detection using a profilometer is created roughly after 3s (123 000 *imp.*) of PWJ. However, evaluable material removal/depth starts at 7s (287 000 *imp.*) as apparent from the crater profile in **Figure 73** and in a graph showing evaluation of crater depth in **Figure 74**. The material erosion evaluated through depth and volume removed, grows gradually with an increase in exposure time (number of impacts) in the measured region. The erosion depth h increment was fitted with the curve defined by Eq. (22), where the only input is the exposure time (i.e., number of impacts):

$$h_e = 0.0112t^{3.3308} \qquad (22)$$

Removed volume can be then expressed by the Eq. (23):

$$v_r = 0.0034e^{0.1822t} \qquad (23)$$

where d_t is the depth in the μm, v_r is volume removed in mm^3 and t is time in s. The selected equation types were selected to maximize the fit and the R^2 values, shown in **Figure 74**.

For time exposure lesser than 7s, data presented in **Figure 74** are not sensitive to changes reached in the surface. Therefore, this stadium of erosion was evaluated also in the form of roughness parameters as presented in **Figure 75**, which shows roughness parameters evolution. Parameters of interest were Ra, Rz Rsk and Rku.

Parameters Ra, Rz showed similar increasing trend. Ra starts at exposure 1 s with value 0.505 μm that after 6 s of exposure increases to 2.53 μm. Rz value starts at 2.15 μm (1 s) and reaches 9.84 μm (6 s). At 6 s of exposure time both parameters show higher value spread. This is attributed to uneven roughness distribution across the treated area.

The skewness parameter Rsk is close to 0 and doesn't increase significantly during low levels of exposure time (1 – 6 s). The parameter stays in the range between 0 and 0.5 during selected time exposure interval. Skewness gives us information about the asymmetry of the profile, i.e., if it is valley or peak dominant. A value close to 0 signifies that valleys and peaks are equivalent. The Rsk parameter close to 0.5 shows us peak dominance over valleys. Based on the SEM images it can be attributed to upheaval of material or grain tilting.

The kurtosis value higher that 3 means a sharper roughness profile. The highest mean value of Rku of 4.4 was observed for an exposure time of 2 s. The increase in exposure time leads to standard normal profile distribution (mesokurtic). This can be attributed to the smoothening of sharp edges due to the effect of the lateral flow of the jet.

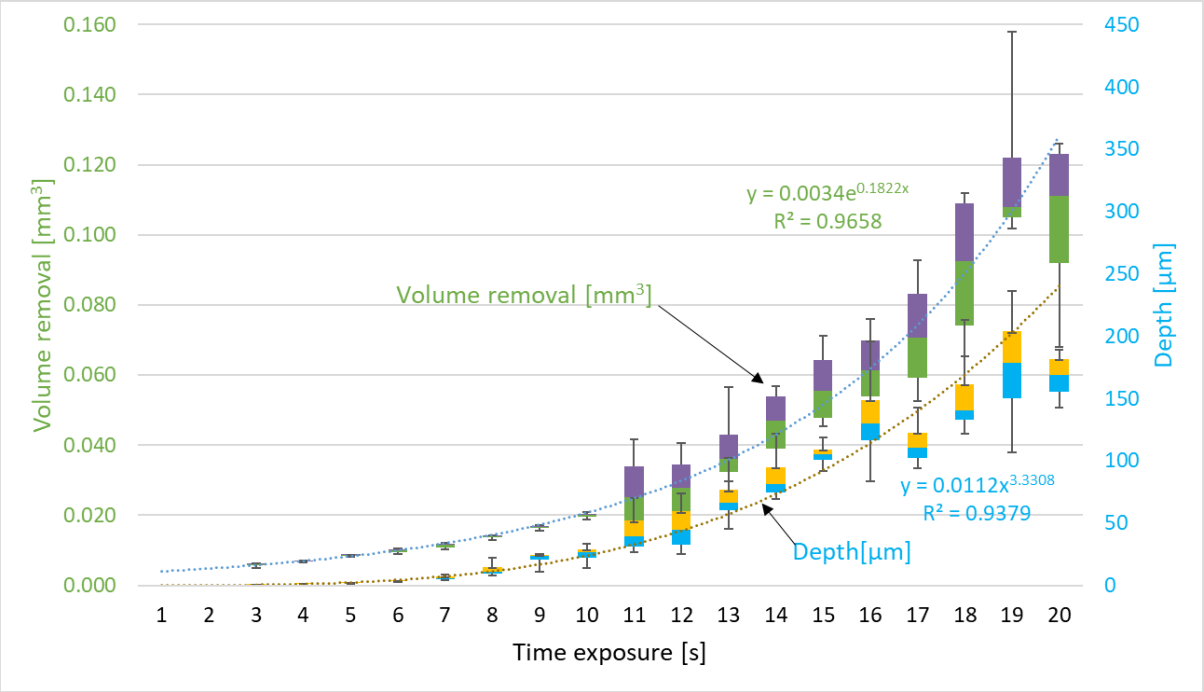

Figure 74 Box graph of depth and volume removal based on PWJ exposure ranging from 1s to 20 s

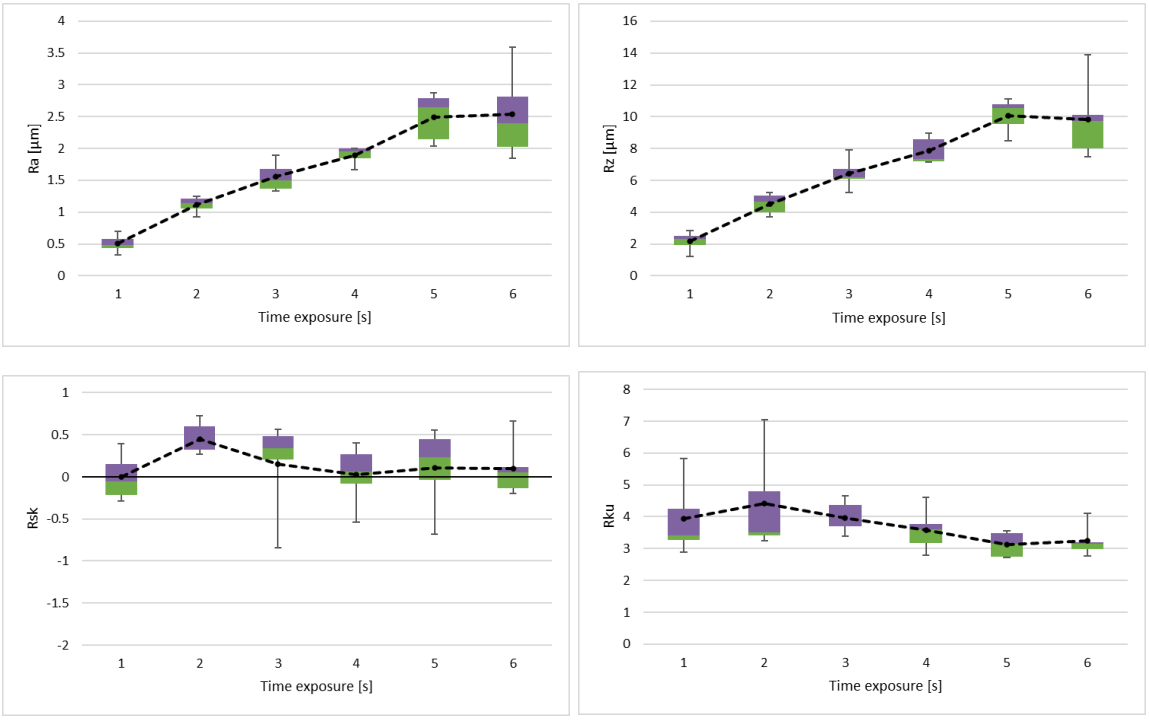

Figure 75 Graph showing roughness parameters (Ra, Rz, Rsk, Rku) based on PWJ exposure time for small exposure times from 1 to 6 s

The subsurface area hardness is shown in 2D visualization in **Figure 76**. The visualization was done by a software written in Python with linear interpolation between the points (linear interpolation is described in chapter **4.3.3**). The visualization shows the formation of the hardened layer under the first row of indents after 5 *s* of PWJ exposure. The first row is located 30 μm under the treated surface. It can be assumed based on the measured hardness gradient, that hardening increases closer to the surface. The first layer of indents shows stronger hardening after 10 *s* of PWJ exposure. Moreover, the hardened layer is more homogenously spread across all the indents in the first row and some indents of second row also show hardening. After 15 *s* of PWJ exposure, a significant erosion crater was created in the cross-section. From the first layer of indents under the crater the hardening can be observed, however homogenous hardened layer is missing. The most significant hardening is visible close to crater edges and radiuses in the first measured row under the crater. The treatment using 20 *s* of PWJ exposure results in similar situation as for 15 *s* exposure. The most significant hardening is in the first row of indents closest to the crater edges. The hardening is again concentrated in crater edges or radiuses. The underlying rows of indents show some non-uniformity in the hardness profile. A statistical approach was also followed and hardness in each row under the surface was averaged and plotted on the graph shown in **Figure 77** in the case of PWJ and **Figure 79** in the case of CWJ treatment. The graph in **Figure 78** shows the dependence of normalised hardness on depth under PWJ treated surface. Normalized hardness is obtained when, each averaged depth hardness is divided by the total hardness of the whole grid.

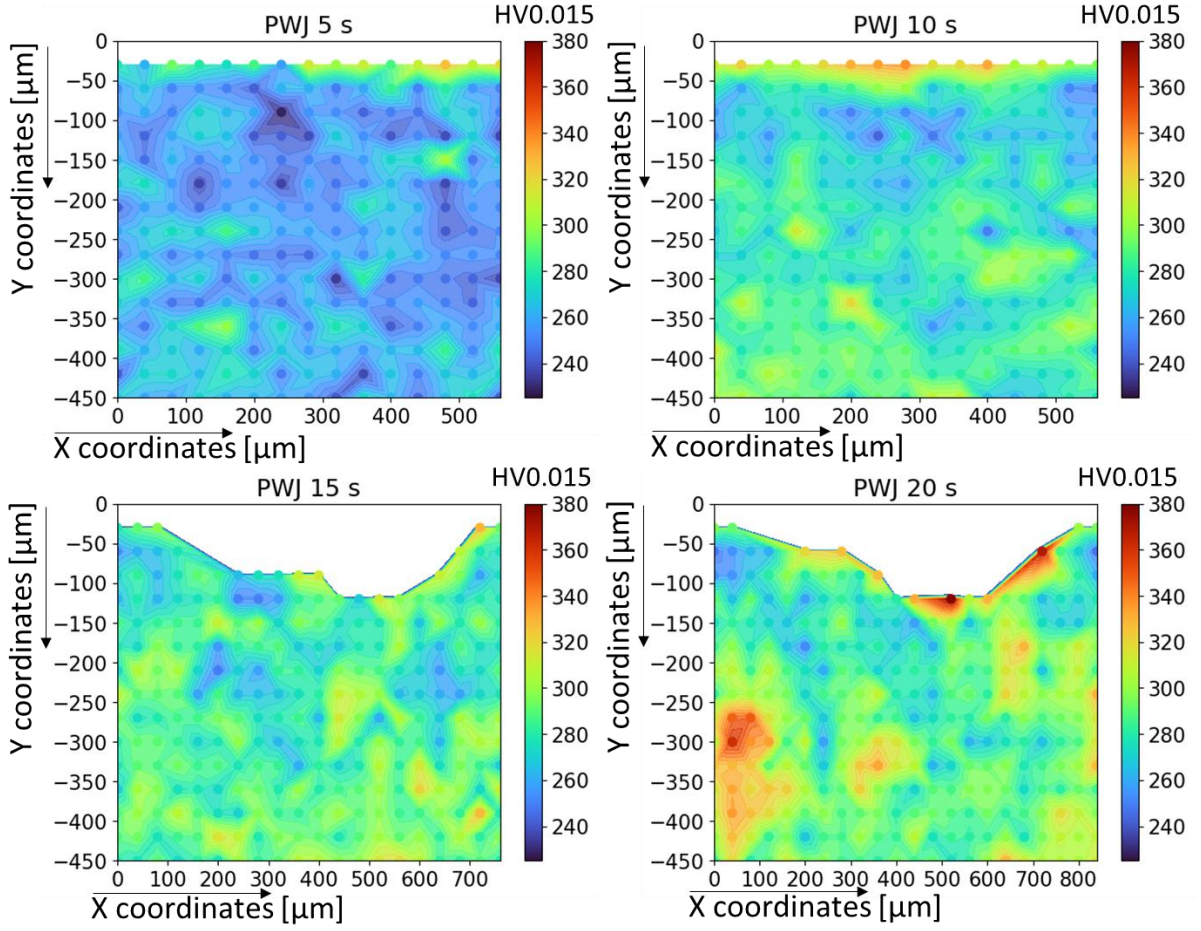

Figure 76 The 2D microhardness visualization under craters exposed to PWJ for increasing exposure time

The graph in **Figure 77**, shows depth dependence of the hardness for the surfaces treated with increasing exposure time to PWJ. The depth-hardness curves show an increase in area below 100 μm. From the original surface micro-hardness of 294 HV0.015, the hardness increased to 316 HV0.015 after 10 *s* of PWJ exposure. For other exposure times of 5 *s* 15 *s* and 20 *s* the surface hardness is similar from a statistical point of view to the untreated surface.

When the hardness is normalized by the whole grit hardness value (see **Figure 78**), the effects of sample preparation or material inhomogeneities decrease and treated surfaces therefore show a hardness increase relative to the measured area. In this case the surface of 5 *s* exposure of PWJ shows the most significant increase to the value of 1.13 in 30 μm below the surface followed by 10 *s* of PWJ exposure that shows the value of 1.12, while the original surface shows the value of 0.99.

The effect of CWJ on hardness is shown in **Figure 79**. In this case no hardening was observed in any of the measured exposure times (5, 10, 15, 20 s). The hardening was not observed even at the closest distance from the surface of 30 μm.

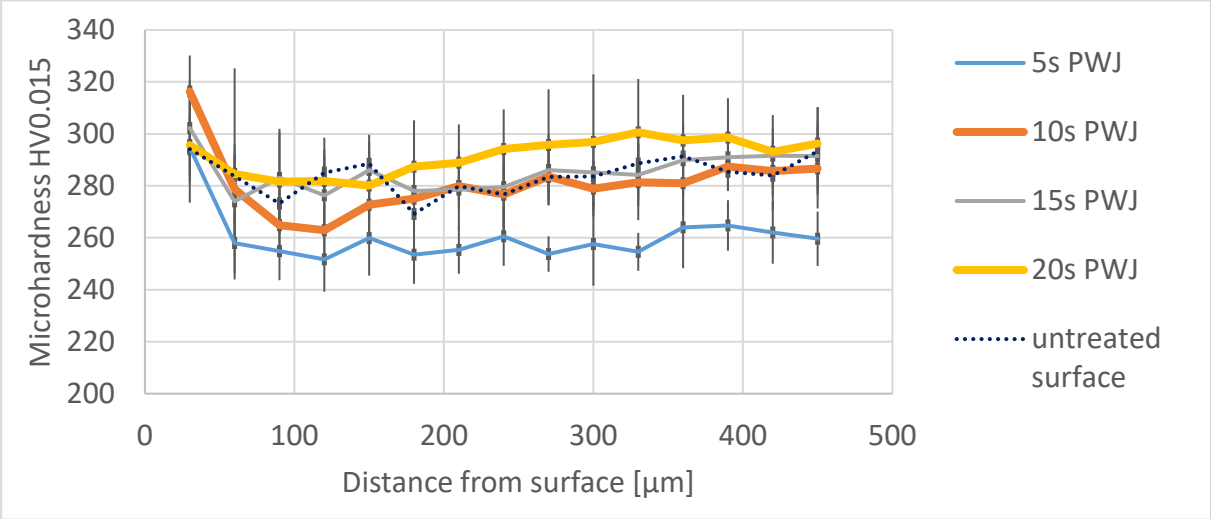

Figure 77 Hardness-depth profile of surface treated with different PWJ exposure times ranging from 5 s up to 20 s

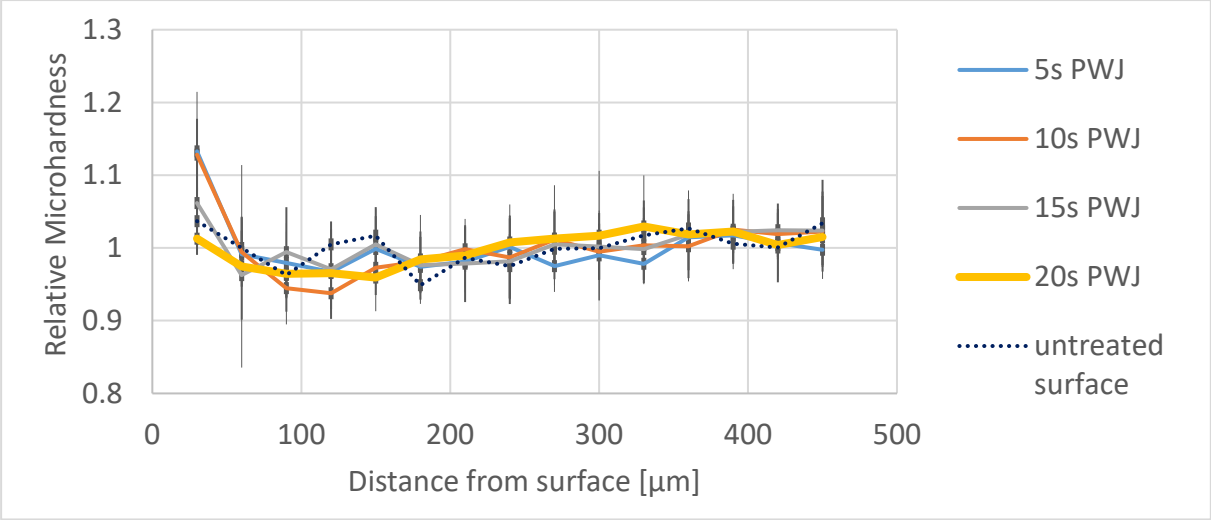

Figure 78 Relative Hardness-depth profile of surface treated with different PWJ exposure times ranging from 5 s up to 20 s. Each hardness value was divided by the averaged hardness of the whole measurement net

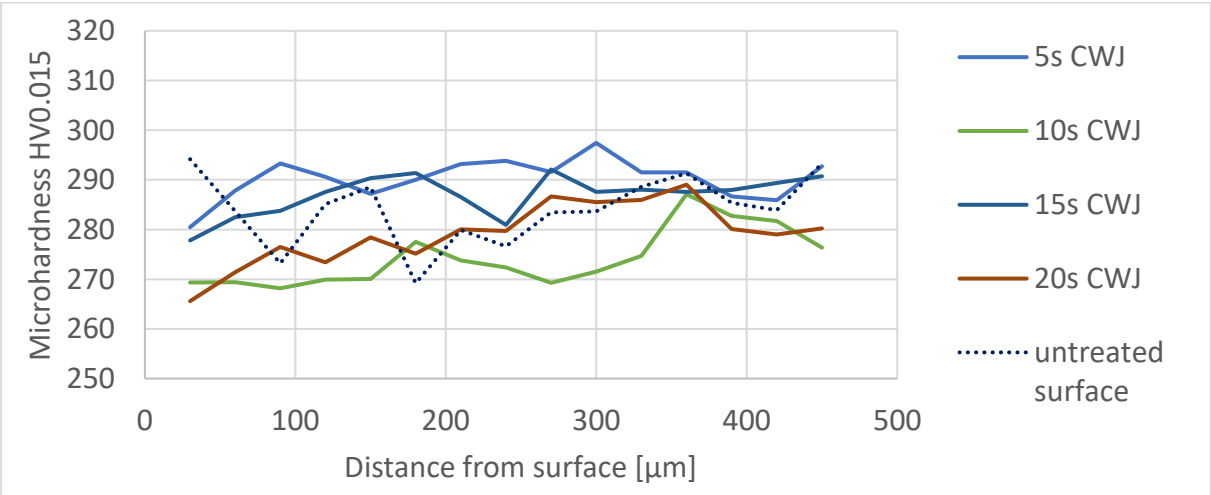

Figure 79 Hardness depth profile under surfaces treated by CWJ exposure

The biggest relative hardening was observed in the case of 5 *s* of PWJ exposure at a distance of 30 μm under the surface, therefore 2 TEM lamellae were extracted using the FIB technique from the sample surface and the results of dislocation structure were compared with the dislocation structure for as received (hot rolled) material (see **Figure 80**).

Figure 80a shows relatively high dislocation density approximately 10^{13} m^{-2} of material state before PWJ exposure contains due to manufacturing history (hot rolling). Dislocations gliding on multiple slip systems are relatively homogeneously distributed. Dislocation pile-ups can be observed close to grain boundaries. Furthermore, dislocations forming close packed nets were observed close to grain boundaries.

An example of dislocation structure after exposure to PWJ for 5 *s* is in **Figure 80b**. The grain in the picture is approximately 2 μm under the treated surface. It shows high density of dislocations estimated as 7.10^{14} m^{-2}. The dislocations are homogenously distributed without signs of arrangement into wall or cell structures often observed in cyclically loaded samples.

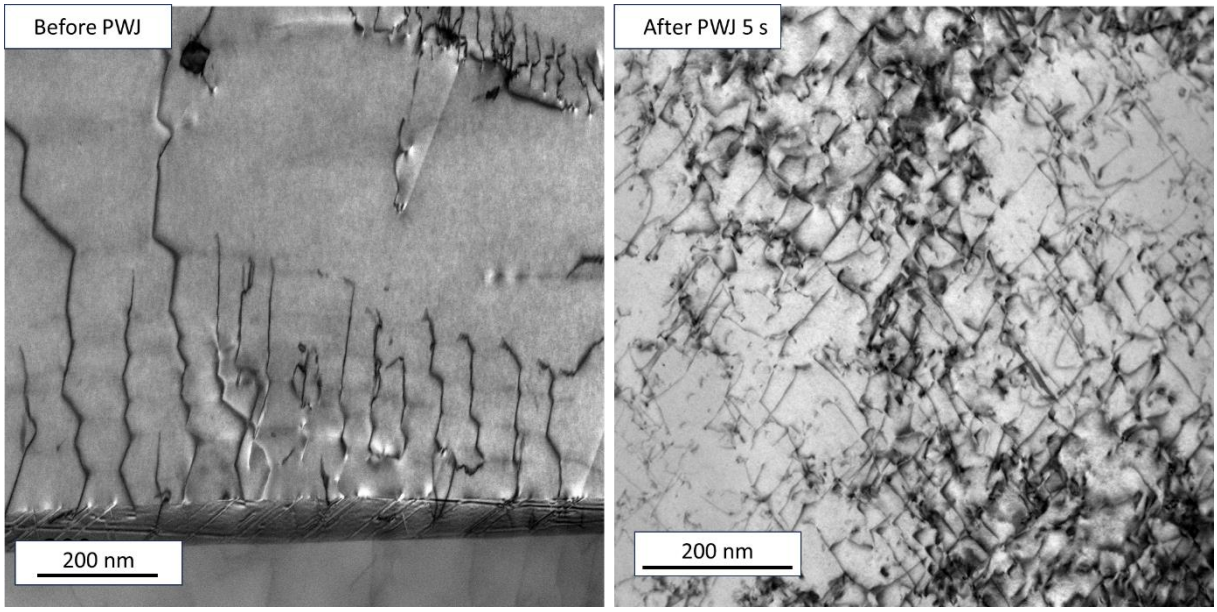

Figure 80 Comparison of dislocation structure observed by TEM in subsurface prior to PWJ treatment and after 5s of PWJ exposure

Other examples of subsurface dislocation structure created by 5 *s* PWJ exposure are in **Figure 81**. The FIB lamella was cut transversally to the treated surface. The top of **Figure 81a** shows the surface of the lamella. The area under the surface differs from the untreated state mainly by the substantial increase in dislocation density. At this magnification there is no visible gradient in dislocation density towards the bulk of the material. A high number of deformation induced twins is characteristic for this combination of the PWJ process and the material. Due to the high stress field the contrast is degraded, nonetheless, two microtwin systems are shown in **Figure 81b**. The diffractogram shown in the inset documents extra spots created by the twins along two {111} planes. The twins are highlighted in the TEM figure by orange dashed lines and marked as Twin 1 and Twin 2.

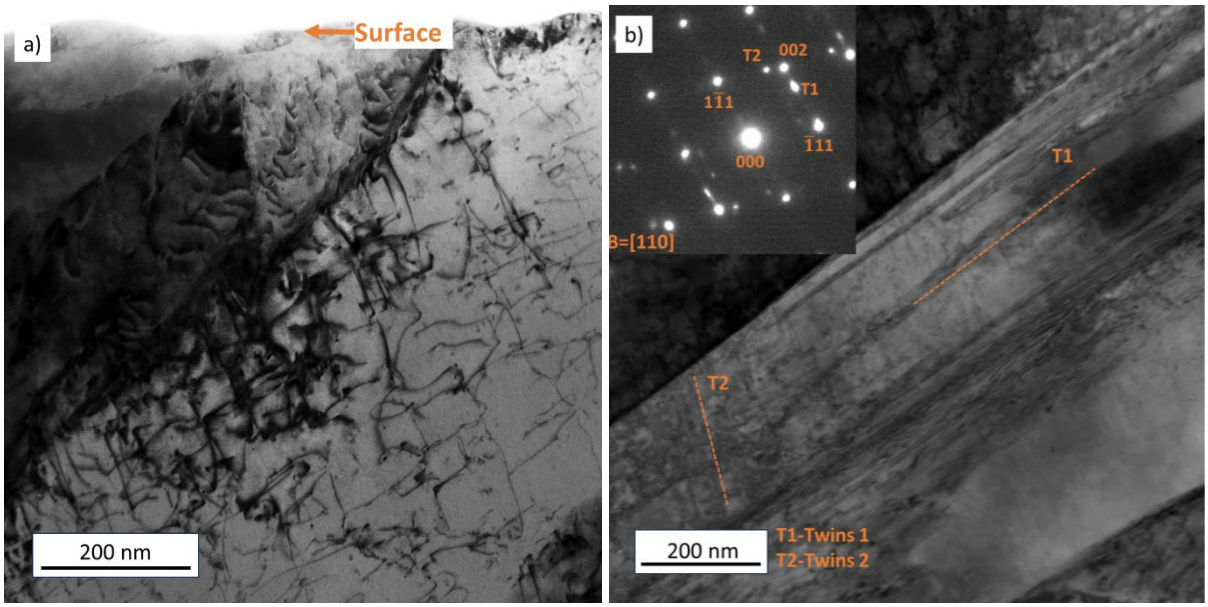

Figure 81 centre of PWJ 5s exposed area subsurface showing a) high dislocation density under the surface and b) multiple twins observed in the subsurface. Twins show multiple directions as is marked with lines on the figure. Twins are confirmed by diffraction pattern shown on inset of figure b

5.2.3 Erosion incubation stage EBSD observation

The experiment described in the previous chapter proved the hardening under the surface treated by PWJ, however only in a very thin layer under the surface. That is the reason why a new measurement methodology was derived to record changes in the layer closest to the surface. The surface of the samples was electrolytically polished and then marked by small hardness indents in a circle pattern according to the schematic shown in **Figure 82a**. **Figure 82b, c** show an OM micrograph of the marked surface in overview and detail. The marked areas were measured by EBSD prior to PWJ exposure. After EBSD measurement, areas were subjected to different exposure times of PWJ and then again analyzed using EBSD. Note how areas B and D were not treated in order to limit possibility of influence between adjacent areas

The process of scanning was performed inside the circular area in a cross pattern (see **Figure 83**) due to the inhomogeneity of water cluster distribution in PWJ. **Figure 83a** shows the polished marked area in secondary electrons with the EBSD map location highlighted. **Figure 83b** shows the same area in forward scattered electron (FSE) mode. In this mode individual grains can be easily distinguished. **Figure 83c** shows the same area but after 1.5s of PWJ exposure (61 500 impacts) in FSE. For every selected area (A,C,E,F), EBSD was measured before the PWJ exposure and at the exact same location after PWJ exposure.

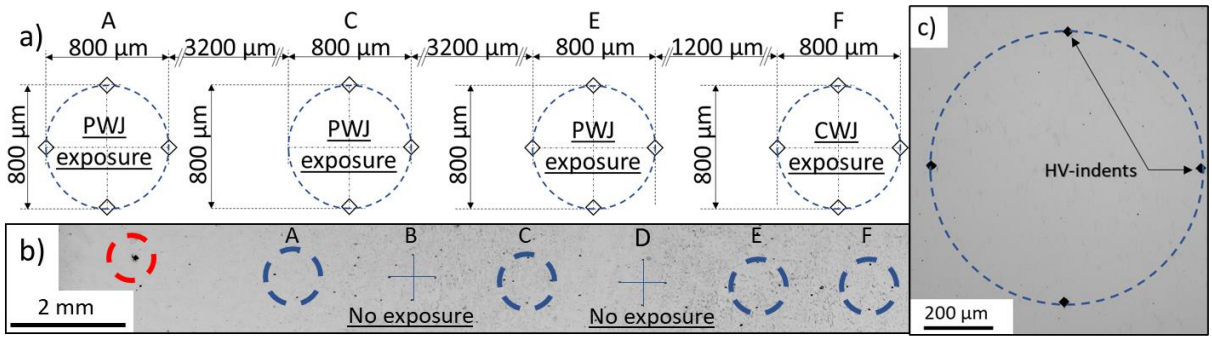

Figure 82 Schematic for EBSD measurement preparation showing a schematic of marking b) the electropolished surface prepared for EBSD with marking c) detail of marked area prepared for EBSD.

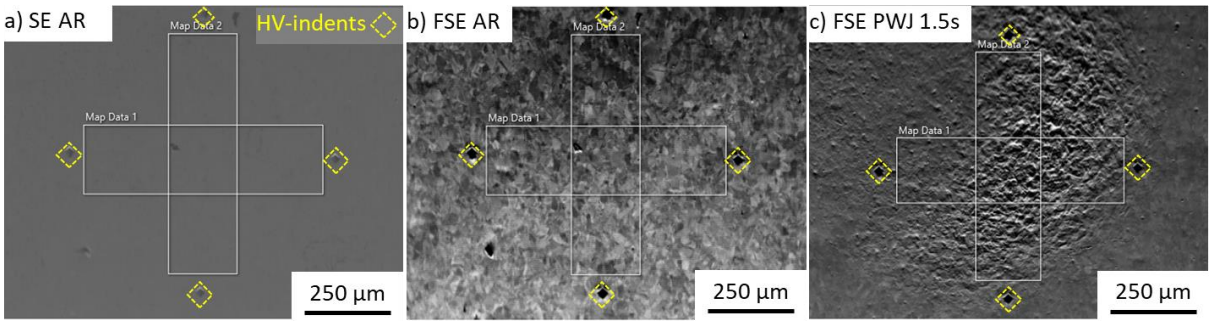

Figure 83 area prior to PWJ treatment shown in a) secondary electrons and b) forward scattered electron. Area treated by 1.5 s of PWJ exposure shown by c) forward scattered electrons

Figure 84 shows the area treated by PWJ with 3 *s* exposure which is the maximum exposure time used in this experiment. The EBSD grain orientation map overlay was inserted into the image. FSE mode highlights the localization of the PWJ effect. While the treated area is visibly circular, approximately half of the area is significantly roughened while the other half shows much lesser roughening. In the most roughened area, the EBSD overlay shows a number of black areas called un-indexed regions. In these regions, it was not possible to index the orientation of grains using the Kikuchi pattern. The reason is either because dislocation density under the treated areas was too high or the roughness of the surface was too high. Based on the nonuniformity of the eroded area shown by FSE (**Figure 84**). The treated area can be divided into the main erosion region and the secondary erosion region. **Figure 84** contains an approximate outline of the main erosion region.

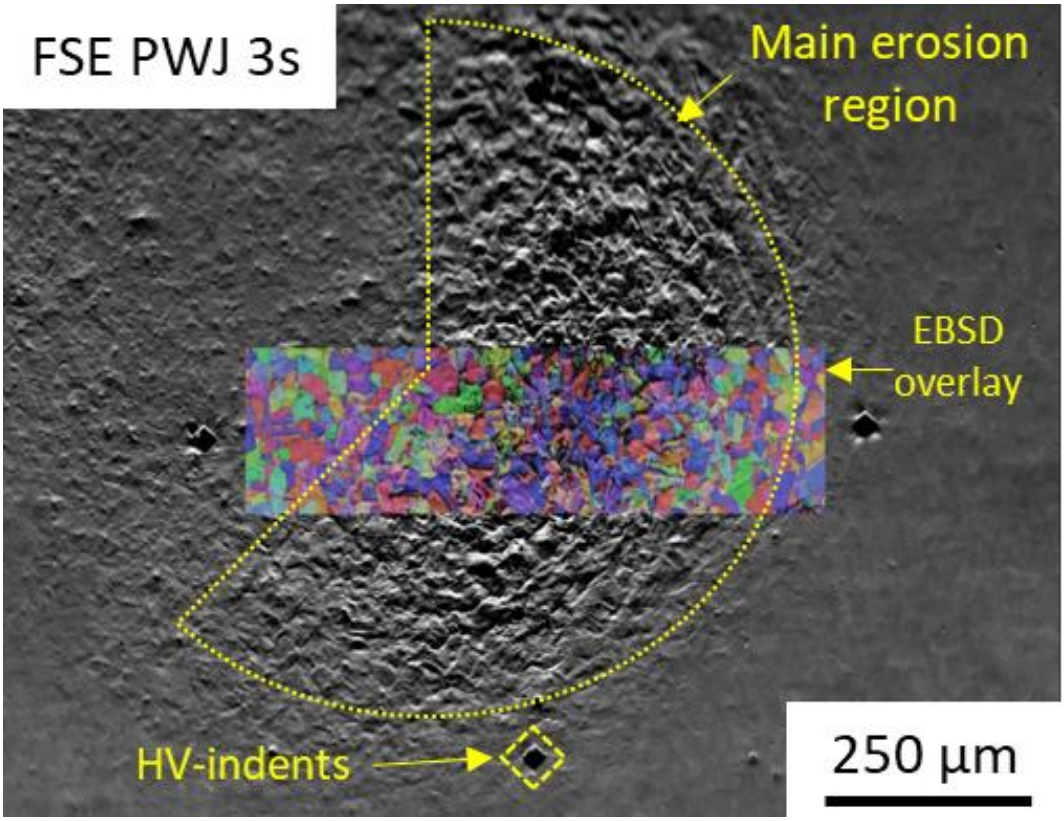

Figure 84 Surface treated with 3 s of PWJ shown by forward scattered electron with horizontal overlay showing EBSD grain orientation map

Figure 85 shows the evolution of PWJ treated surface by EBSD grain orientation map. This method displays the orientation of each grain by the colour. Pictures for as received state and for treatment with 1 *s* exposure (**Figure 83a, b**) are from the exact same place, so it is possible to directly evaluate changes created by 1 *s* of PWJ exposure. In the as received state, there is a quite high number of equiaxed grains. A small number of the grains include visible twin boundaries in their interior. The hit rate (number of successfully indexed regions) is exceptionally high in the as-received state (over 95 %). After one second of PWJ exposure, there is a visible increase in non-indexed regions (NIR), shown by black colour. The main part follows grain boundaries in the significantly roughened part of the PWJ treated area. The second significant change is a change in colour in some grains which corresponds to the change of orientation of these grains. These two aspects suggest that the grain tilting is mechanism that is behind the surface roughening. It is important to note that the backscattered electrons, bringing the information about the specimen's crystallography, comes from relatively thin surface layer less than 1μm. The observed change of crystallographic orientation due to PWJ exposure is related to this thin surface layer and no information is gained about the situation deeper from the surface. With increasing exposure time, the number and size of non-indexed regions further increased. After 1.5 *s* of PWJ exposure, the non-indexed regions grow into the interior of selected grains or follow twin boundaries. Some non-indexed regions are also observed outside of the main erosion region. After 3 *s* exposure, the non-indexed regions spread even more into interior of the grains especially in the main erosion region. Some grains in the main erosion region also show nonhomogeneous colour distribution, i.e., different shades of colour inside a single grain. This can be interpreted as an increasing change of orientation , i.e., misorientations of grains caused by increasing erosion exposure. The grain tilting was also evaluated using inverse pole figures.

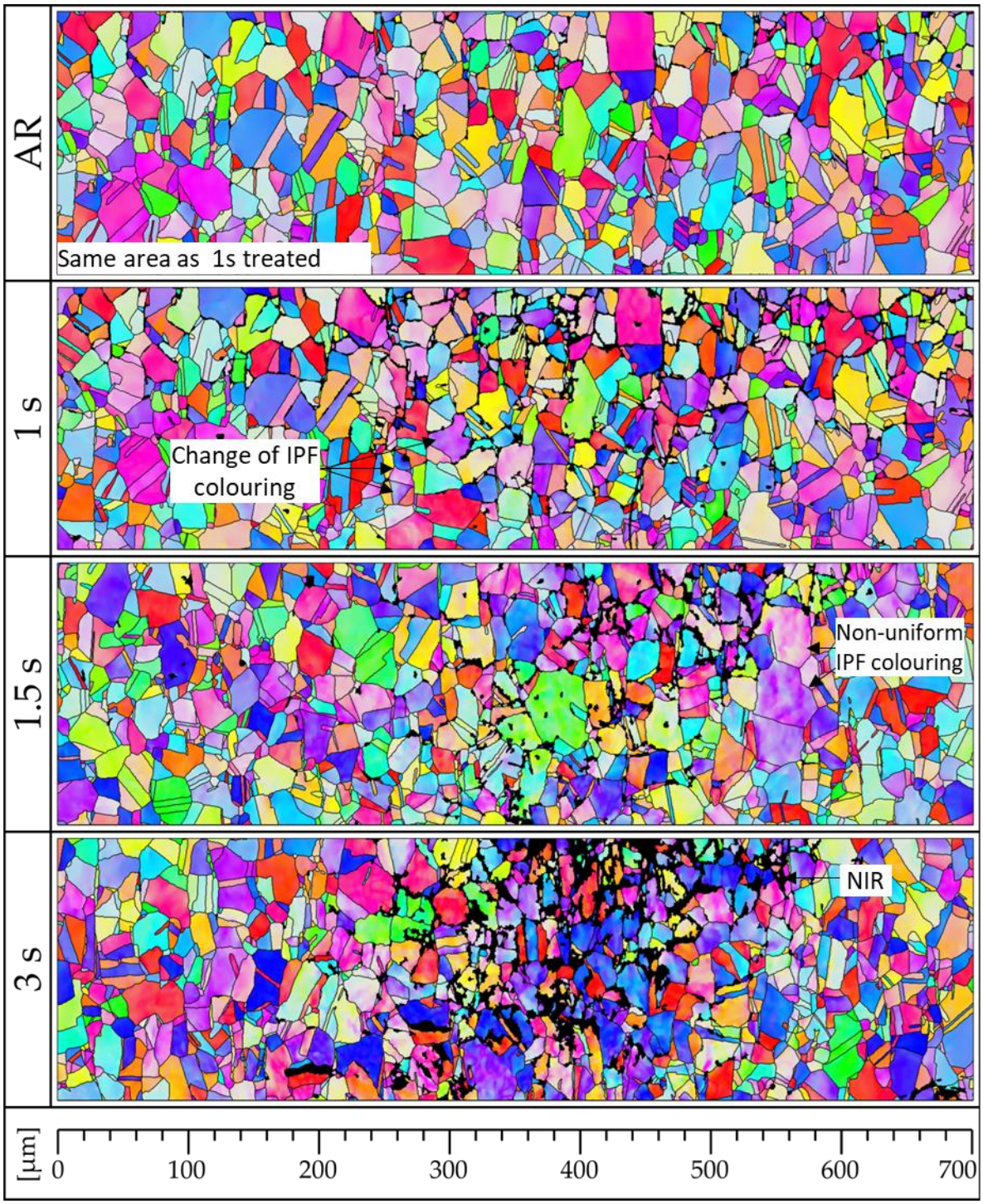

Figure 85 Several areas treated with increasing PWJ acting time measured by EBSD displayed by means of EBSD grain orientation map. As received state measurement is taken from the same area as 1s exposure for comparison. The time exposure ranged from 0 s up to 3s. Black regions are non-indexed regions (NIR)

Figure 86 shows the evolution of {111} plane pole figures from the as-received state (prior to PWJ treatment) to PWJ treated surfaces. The figures are displayed at uniform MUD ranging from 0.00 to 3.30 -. The pole figure shows almost no visible differences after 1 *s* PWJ treatment. In the case of 2 *s* and 3 *s* PWJ exposure the peak in MUD appears at the cross-section of the X and Y axis. The peaks reached MUD values close to 3.30. This shows global changes in grains

orientation. Since the maximum MUD is below 4 of the texture of the material is evident but not strong.

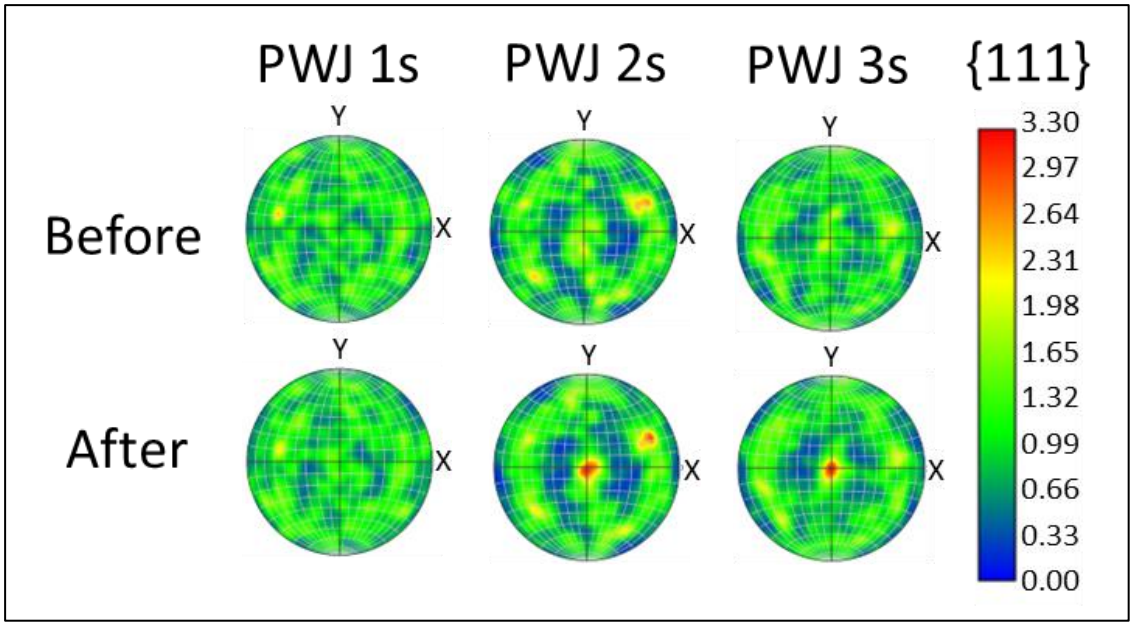

Figure 86 {111} plane pole figures of the EBSD measured areas before and after PWJ exposure of 1, 2 and 3s

For further quantification of misorientation inside grains, an analysis using kernel averaged misorientation was performed (KAM). KAM provides a possibility to characterize plastic deformation induced by PWJ by a number. **Figure 87** shows the increasing influence of PWJ on KAM as longer exposure time leads to more pronounced KAM. Picture for as received state is taken from the same area as picture for 1s of PWJ exposure. The red lines are grain boundaries or twins, while the colour gradient inside the grains displays misorientations inside the grains. There is a significant increase in KAM in the main erosion region, and smaller increase in KAM in the secondary erosion region. This trend continues up to 1.5 *s* of PWJ exposure. KAM increased further up to 3 seconds of PWJ exposure when a number of non-indexed regions appeared. Notably all KAM data measured inside grains exhibit a value of approximately 1°, i.e., the maximum misorientation of lattice in one grain is up to 1°. It means that used methodology is quite sensitive. KAM maps for PWJ exposure of 1.5s and 3s show concentration of misorientation i.e., plastic deformation into locations such as grain boundaries or sub-grains.

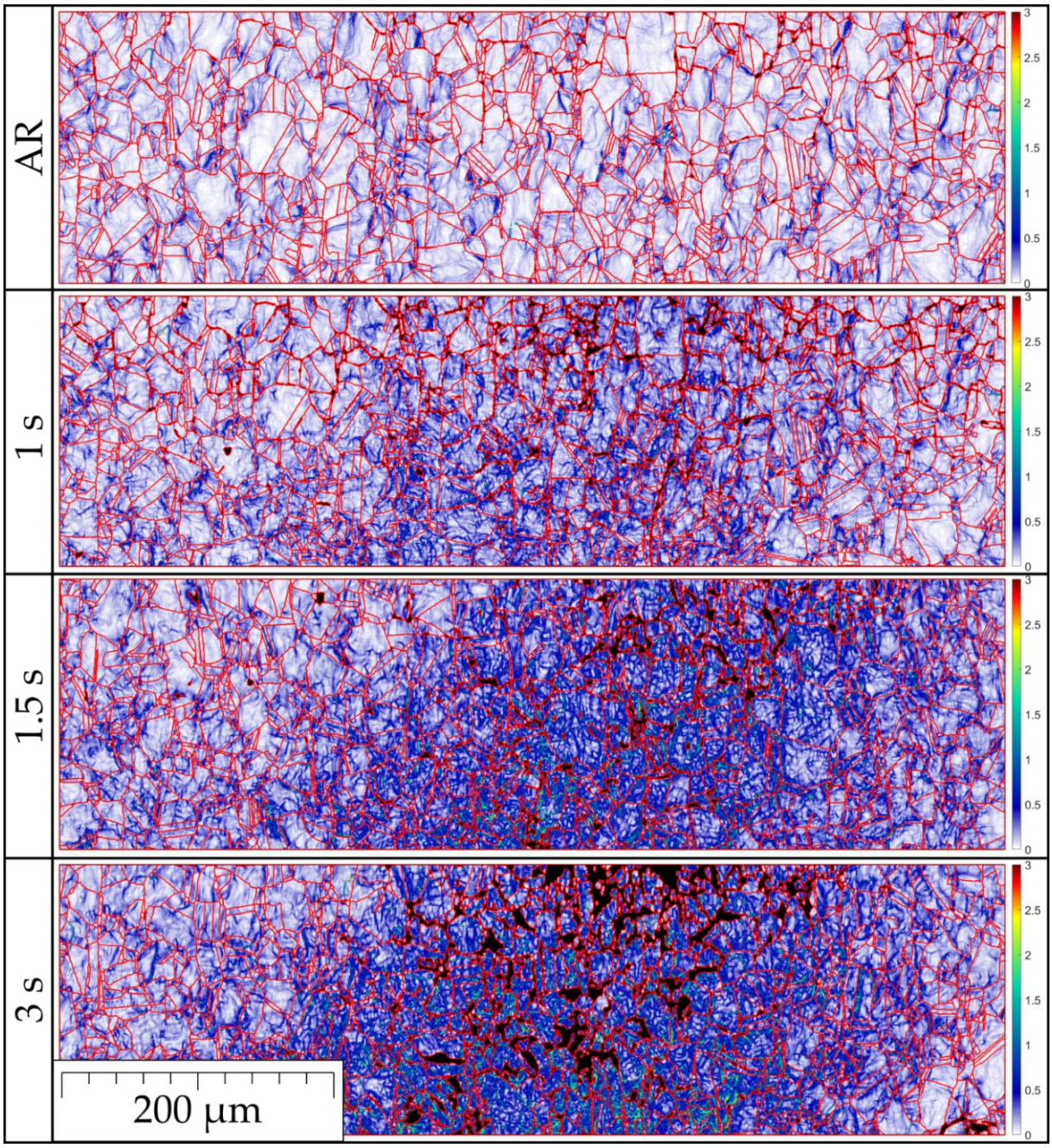

Figure 87 Several areas treated with increasing PWJ acting time measured by EBSD evaluated by KAM. Time exposure ranged from 0 s up to 3 s. As received state measurement is taken from the same area as 1s exposure for comparison. Red line mark high angle boundaries while blue lines shows low angle boundaries (misorientation below 15°)

The layout of **Figure 88** compares the detail of the EBSD grain orientation map and KAM analyses of the same area before and after exposure to PWJ for 1 and 3 s. The comparison of the EBSD grain orientation map of as-received and PWJ treated area allows direct observation of orientation changes in individual grains and precise evaluation of location of non-indexed regions. Detail for 1s exposure shows that non-indexed areas are present since this very short exposure, and they are concentrated mainly to the vicinity of grain boundaries. After 3s of PWJ exposure a misorientation induced inside grains is visible even in EBSD grain orientation map by colour gradients inside larger grains. These grains can be directly compared in KAM maps. It is necessary to notice that the KAM map shows some misorientations in the interior of the grains even in as received state, i.e., before PWJ treatment, however their presence is

significantly increased after PWJ exposure, mainly in form of low angle boundaries (LAB). Distinguishing of LAB formation is easier for the 1s of PWJ exposure, due to oversaturation in the case of PWJ 3 s. PWJ 3 *s* exposure leads to higher number of LABs. Furthermore, chosen misorientation scale, which is sufficiently sensitive in case of 1 *s* PWJ exposure leads in the case of 3s of PWJ exposure to oversaturation. The effect of PWJ is clearly visible especially in KAM maps. The increase in PWJ exposure time leads to increase in number of non-indexed regions. The most possible reason in our case is increase of roughness of the exposed surface. Non-indexed regions were observed mostly around grain boundary steps. PWJ exposure of 3s leads to high number of non-indexed regions. However, hit rate is still above 85 %.

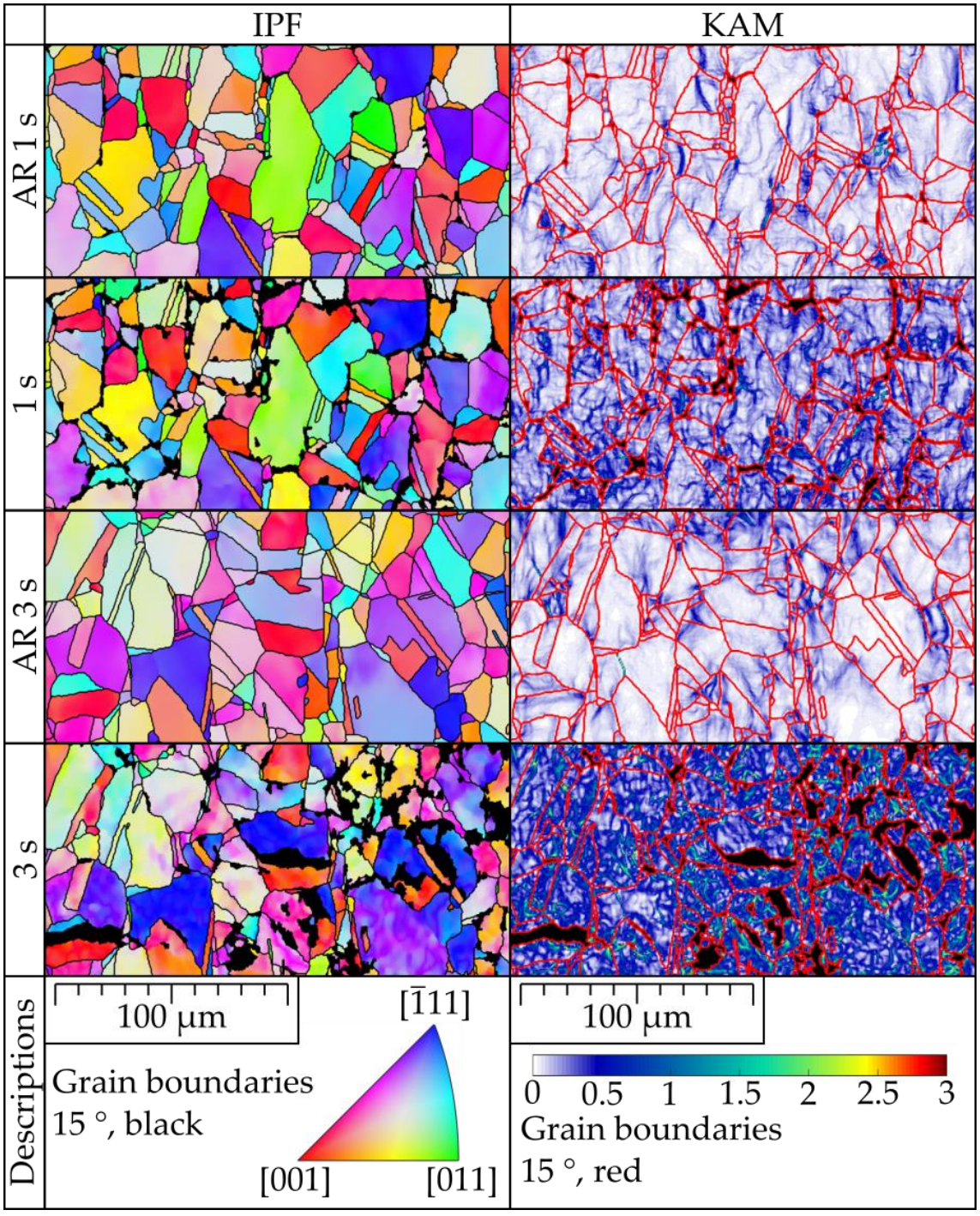

Figure 88 Comparison of area before PWJ treatment and after 1 s, 3 s of PWJ exposure. The area is observed by means of EBSD grain orientation map (right) and KAM (left)

Since the origin of NIR regions is of crucial importance, most prominent NIR regions on surface exposed to 3s of PWJ (**Figure 89a**) were closer examined by SE. The NIR regions selected for observation are marked in **Figure 89b**. **Figure 89c** show significant surface step surrounding one particle. At this image, it is evident that the step follows a grain boundary. Detail in **Figure 89d** shows small crack propagating from the corner of the surface step. The **Figure 89e** shows severely deformed surface step across the grain with detail shown in **Figure 89f**. Both of the examined NIR regions as well as overview photo suggest that NIR regions shown in **Figure 85** are not created by material removal. Rather these regions appear adjacent to surface steps which deviate the angle between the surface and the electron beam.

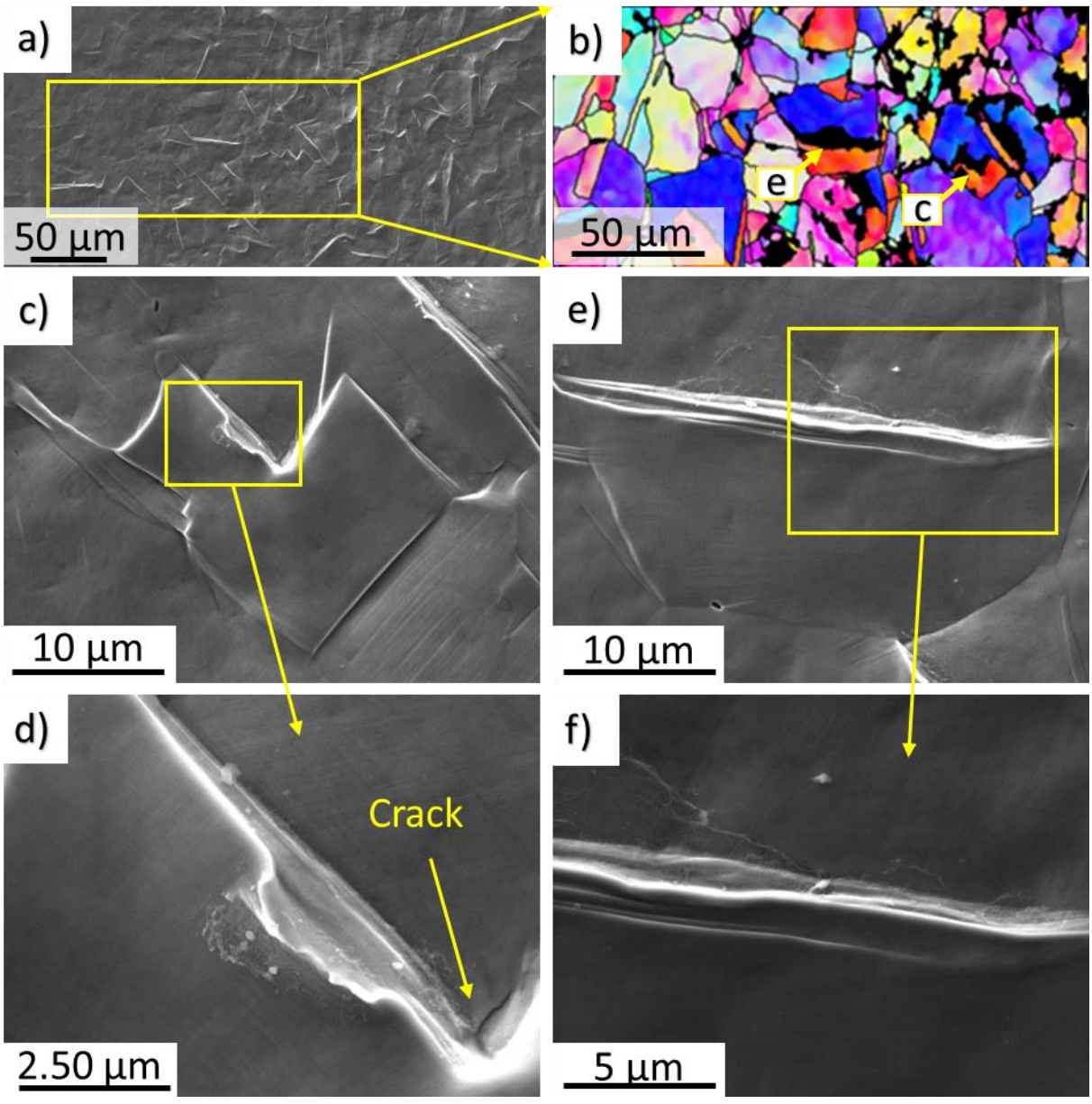

Figure 89 Detailed observation of NIR regions after 3s PWJ treatment using SE

Table 9 presents the results of EBSD analysis concerning the grain size of individual phases present in the microstructure of stainless steel before and after PWJ and CWJ treatment. The amount of BCC phase was also evaluated.

The KAM was averaged over the entire measured area to acquire numbers describing the state material state after PWJ. This value is shown along grain size and phase composition in **Table 9**. The grain size of the FCC phase does not change with increasing exposure time of PWJ. A small decrease after 3 *s* of PWJ exposure is caused by not-indexed regions copying grain boundaries. This causes grains to appear smaller. BCC is detected in the as received state in a small amount. The BCC amount is very small 0.98 % and is generally found in the form of thin needles between the FCC grains. The BCC content doesn't increase in the given exposure range according to measurement, at least within the margin of experimental scatter. It is in agreement with the TEM study, which does not reveal any deformation induced α´martensite. The KAM value of "PWJ average" is taken from the whole measured area while "PWJ max" is taken from the main erosion region.

Table 9 EBSD evaluation showing grain size (equivalent circle diameter) of FCC phase and volume fraction of BCC phase. The table also shows average and max KAM measured across the whole map, and inside the most eroded region respectively

t	d FCC	BCC	KAM average	KAM max
s	*μm*	%	°	°
0	10.8	0.98	0.12	0.12
		PWJ		
1	10.2	1.04	0.21	0.23
1.5	10.4	1.60	0.28	0.36
2	10.6	0.97	0.39	0.43
3	9.7	1.41	0.41	0.51
		CWJ		
3	11.0	1.06	0.18	0.20
6	10.7	1.25	0.25	0.30

The total KAM angle expresses the presence of misorientation of the entire examined area. The KAM value indicates the presence of dislocation walls that form subgrain like structures. Increasing exposure of PWJ and CWJ leads to an increase in plastic deformation i.e., both "PWJ max" and "PWJ average" value increase. The "CWJ max" and "CWJ average" are calculated in the same manner for the area treated by CWJ. The graph in **Figure 90** shows the increase in average KAM from 0.12° for as received state up to 0.21° after 1s of PWJ exposure, then further increase to 0.28° after 1.5 *s* of PWJ exposure. These values are comparable to 3 *s* of CWJ exposure 0.18° and 6 *s* of CWJ exposure 0.25°. PWJ exposure of 3 *s* leads to KAM 0.41°. This shows the clear advantage of PWJ over CWJ as a very effective method of material surface modification.

The profile of KAM distributed along the X coordinate of the EBSD map is shown in **Figure 91**. The figure shows the KAM gradient in influenced zones for all PWJ exposure times. **Figure 91a** shows the value for each X coordinate averaged along whole Y axis. **Figure 91b** fits these values with polynom of third order. Maximum fitted values reach values of 0.24 °, 0.43 °, 0.48 °, 0.52 ° for 1 s, 1.5 s, 2 *s* and 3 *s* PWJ exposure, respectively. Both figures prove, that the area under PWJ is deformed non homogenously and follows quite clear trend. The influence of PWJ is still present at the edges of the analyzed area but the KAM increases significantly at the jet core. This gradient can characterize PWJ in terms of tool shape.

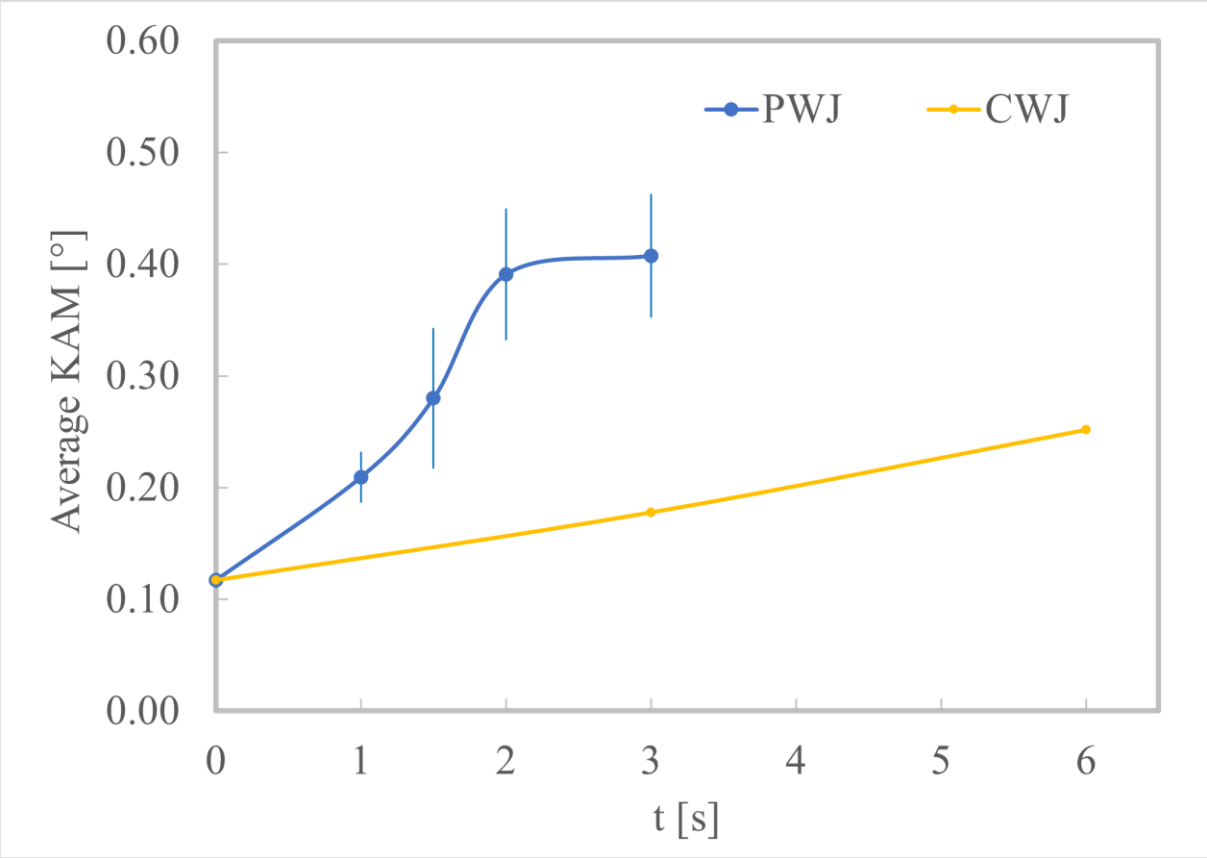

Figure 90 Dependence of averaged KAM of PWJ and CWJ on the exposure time

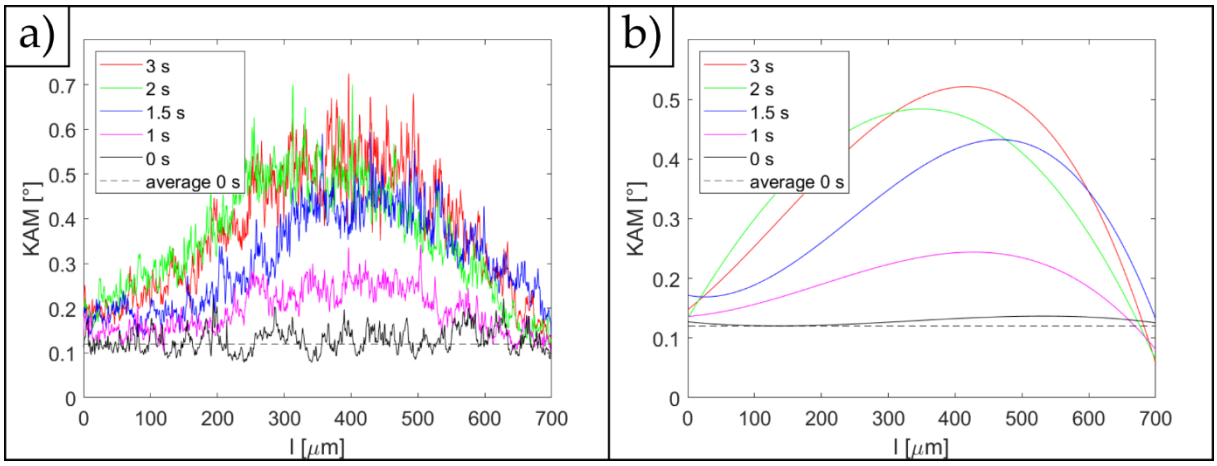

Figure 91. Averaged KAM calculated from EBSD map in dependence on X coordinates on the crater. The figure shows a) raw average based on X coordinate b) data fitted with polynom of 3rd degree

The EBSD measurement was accompanied by roughness analysis to achieve level of correlation between roughness measurements and EBSD measurements. Roughness measurement is the most used method of erosion incubation stage evaluation; therefore, the roughness measurement was done on measured samples for possible KAM-roughness correlation. The **Table 10** shows the evolution of selected profile parameters measured from whole eroded area. The parameters measured include Ra, Rz Rv, Rp, skewness Rsk and kurtosis Rku.

The effect of exposure time on profile parameters (Ra , Rp , Rv , Rsk and Rku). Both Ra and Rz parameters show an increasing trend with an increase of PWJ exposure (**Figure 92**). The Ra parameter increases from 0.45 μm for as received material to 1.72 μm after only 1 sec of PWJ exposure. The Ra parameter increased further to 3.97 μm after 3s of PWJ exposure. CWJ only reached Ra of 1.74 μm after 6s of exposure. An increasing trend is also observed in the Rz parameter that grows from 5.47 through 10.58 to 23.54 μm for PWJ exposures of 0 s, 1 *s* and 3 *s* respectively. Rz achieved by CWJ after 6s of exposure was 11.29 μm. Surface skewness Rsk was changed from 0.09 to -0.52 after 1s of PWJ exposure. With increase in exposure, it randomly stays under the -0.2 value meaning the profile show an asymmetrical distribution of peaks and valleys. The profile asymmetry is further supported by comparison of Rv and Rp parameters, where Rv is always higher than Rp after PWJ and CWJ exposure. However, in the case of the untreated profile Rp and Rv are roughly identical. This can be interpreted in early erosion stages as an increase in upheaved material created by grain tilting compared to the original surface. Kurtosis shows degree profile sharpness [143]. The kurtosis of the untreated surface reached 3.09 meaning the surface had sharp peaks. Kurtosis drops to 2.71 after 1s of PWJ exposure and further to 2.59 after further PWJ exposure (2s). This shows the blunting of the profile peaks. Kurtosis then grow with further PWJ exposure even above the initial value. This means peaks are smoothened at the start of PWJ exposure and then new sharp peaks are created with further water cluster action.

Table 10 Surface profile parameters documenting the erosion of the surface due to repeated impact of water clusters in early incubation stage

	PWJ					CWJ	
	Exposure time *s*						
	0	1	1.5	2	3	3	6
Ra *µm*	0.45±0.07	1.72±0.28	2.20±0.38	2.94±0.35	3.97±0.32	0.61±0.12	1.74±0.31
Rz *µm*	5.47±0.32	10.58±0.91	13.39±1.25	21.98±1.02	23.54±1.35	7.14±0.38	11.29±0.87
Rv *µm*	2.72±0.21	6.03±0.43	6.95±0.33	12.23±0.79	12.52±0.25	4.78±0.46	6.02±0.45
Rp *µm*	2.74±0.32	4.56±0.52	6.44±0.99	9.75±0.44	11.02±0.38	2.36±0.39	5.27±0.49
Rsk -	0.09±0.23	-0.52±0.19	-0.28±0.22	-0.37±0.17	-0.24±0.14	-1.76±0.18	-0.36±0.12
Rku -	3.09±0.11	2.71±0.29	2.59±0.31	3.39±0.39	2.75±0.43	2.88±0.22	2.78±0.31

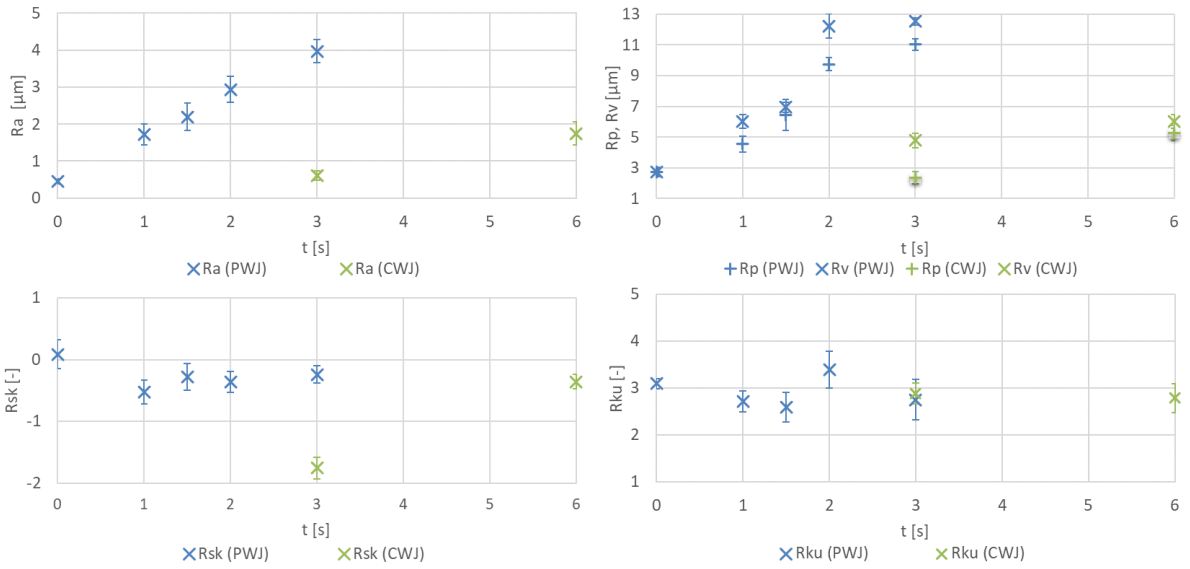

Figure 92. Surface measurement of the evolution of arithmetical mean height (Ra), mean peak height (Rp) and mean pit depth (Rv) as well as skewness (Rsk) and kurtosis (Rku) based on PWJ and CWJ exposure time

6. Discussion

6.1. Experiment set I

6.1.1 Effect of water impact distribution on the surface of 316L stainless steel

In the early years of the development of PWJ, the optimal standoff distance was evaluated based on the inclined trajectory test. The inclined trajectory was used in years 2019 by a number of researchers [48–50] and work by Srivastava et al. [114] considered stairs trajectory in the same year. Based on reasonable doubts about the effect of upward movement of the jet during the incline trajectory test, stair trajectory was selected for evaluation of optimal standoff distance in this thesis. The use of linear runs at constant standoff distance was chosen to avoid the contribution of upward movement velocity of the jet during the experiment $v_y = v_{PWJ}.\sin(\alpha)$ as would be the case of inclined trajectory. In 2020 Srivastava et al. published an article comparing the effect of both trajectories on erosion depth in article [51]. It should be noted that although the difference between the velocity of the jet head (1 *mm/s*) and the velocity of the water (337 *m/s*) is large, a significant difference in the depth of the kerfs was achieved. Since the publishing of this article most works considering the effect of standoff distance on erosion effectivity are based on stair trajectory [47, 52] and other experiment use test runs on stair trajectory to determine optimal standoff distance for the experiment [13, 56].

PWJ test runs were done on the surface of 316L stainless steel in ranges of hydraulic pressure of 30-60 *MPa*, standoff distance of 26 to 58 *mm* and feed rate in range from 1 *mm/s* to 10 *mm/s*. The selected PWJ parameters led to repeated impacts of the surface with subsonic water clusters. SEM observation shows number of exposed grain boundaries. Higher pressure parameters led to rimmed grain boundaries and in the case of hydraulic pressure 50 *MPa* even number of surface cavities was observed. The roughness parameters Ra and Rz show very small changes based on standoff distance in the case of hydraulic pressure 40 and 50 *MPa* as described in **Figure 51**. This may be caused by several factors. Austenitic steel with hardness close to 200 HV 0.2 is tested, while a number of researchers [48, 50] use softer aluminium alloys for optimal standoff distance evaluation. Second reason was that the pressure/nozzle combinations chosen led to impacts of the material at subsonic velocities at a moderate feed rate of 1 *mm/s*. Lastly, samples were in a polished state to evaluate the erosion incubation changes. However, Kirols et al. [151] concluded that improving initial surface roughness is a practical tool to delay water droplet erosion. Therefore, OPS or electrolytically polished surfaces help with the observation and evaluation of early erosion changes, but these surface preparation methods may also delay the onset of these changes. The SEM observation of 1 *mm/s* shows that the most significant damage was done by hydraulic pressure 50 *MPa*. The reason why hydraulic pressure 60 *MPa* did not reach such high erosion intensity may be due to the diminishing effect of the water hammer effect. Excessively high pressure levels may lead to insufficient formation of PWJ clusters [40]. Based on the roughness measured, it seems that the standoff distance needed for the creation of sufficiently separate water clusters increases with pressure, but at some point, interaction of the jet with the atmospheric drag causes severe degradation of the jet, before these clusters are sufficiently developed. The roughness measurement combined with SEM observation of the 50 *MPa* was selected as the most effective

pressure level for current conditions. Based on this analysis further experiment on 316L stainless steel in this work were done at a constant hydraulic pressure of 50 *MPa*.

The optimal standoff distance evaluated within this work should overlap with the culmination regime described by Hloch et al. [47], however the effectivity was determined by roughness parameters.

The effect of hydraulic pressure, standoff distance and feedrate was evaluated by means of surface measurements (Ra, Rz, Rp, Rv and Rsk, Rku). The decrease of droplet impact distribution show a strict decrease in achieved Rz. The increasing standoff distance causes an increase in Rz up to optimal standoff distance and then decreasing tendency. A similar development based on standoff distance was observed for removed volume on aluminium alloy by Foldyna et al. [54]. Finaly, pressure increase shows increasing tendency but diminishing returns after hydraulic pressure 40*MPa*. The results were supported by SEM. Based on these results Experiment Set II was designed.

6.1.2 Effect of water impact distribution on the surface of AW 2014

The effect of feed rate on erosion of Aluminium alloy AW 2014 was observed. The feed rate is the movement of the PWJ head over the surface of the sample parallel to the sample surface controlled by the robotic hand. The optimal standoff distance was evaluated by stair trajectory described in the previous experiment. The feed rate and frequency (40 *kHz*) are determining factors for water impact distribution on the surface of the PWJ treated material in the case of single lines. For the treatment of 2D surfaces, the overlapping factor must be also considered. Significant differences in results are reported by Stolárik et al. [13] based on selected pattern strategies while keeping constant water impact distribution.

The area between water clusters is filled with smaller discontinuous water bunches as visualized by Zeleňák et al. [45]. Therefore, total liquid clusters volume is better in term of erosion testing and prediction, but in the case of technical praxis for surface treatment or material removal, this parameter should be mainly controlled by feed rate or exposure time and frequency. The aluminium alloy is used for erosion testing and technology tuning of water jet technique by a number of studies [13, 47, 48, 50, 56, 152–154]. The aluminium alloys are used due to their low erosion resistance, it means that minor change in PWJ process parameters cause significant change of erosion intensity.

The low erosion resistance of aluminium also helps to determine current erosion regime based on the standoff distance. The problem with aluminium alloys is their inherent structural inhomogeneity caused by alloy additions and impurities [155]. It can create several problems when evaluating PWJ effectiveness. Some studies observing early erosion documented preferential sites of material removal, stronger material roughening or micropits. Studies where these features were reported on SEM micrographs are for example [13, 48, 50, 56]. Similar places of local depressions and micropits were observed in this thesis (**Figure 60**).

Furthermore, a number of cracked or partially removed constituent particles were observed during incubation erosion stages (see **Figure 62**). The places left after the particles are washed away as observed (**Figure 59e** and **Figure 60e**) may act as stress concentrators and could be also subjected to lateral outflow jetting. These factors create local changes in erosion intensity.

It can be concluded that constituent or other types of particles can influence the speed of material removal by the creation of preferential erosion areas. This can create uneven and unpredictable hardness distribution in close subsurface. It is also visible from cross-sectional measurement that these constituent particles also create inhomogeneities during microhardness measurement.

Hardness increment due to the PWJ treatment was documented on AW2014. PWJ with hydraulic pressure of 20 *MPa* caused significant hardening to depth over 50 μm. The hardening was most significant at feed rate of 1 *mm/s* and decreased with a higher feed rate. CWJ at the same conditions did not show any significant hardening. PWJ with the hydraulic pressure of 40 *MPa* achieved an even more significant hardness gradient. The hardness was measured on a cross-section in three lines. Cross-sectional hardness line measurement is often used to study the effects of AWJ [141, 156], CWJ [78] and PWJ [12, 56] and cavitation peening [110, 111] on the material surface. However, due to the complexity of PWJ interaction caused by kerf shape and elastic waves propagation 2D mapping is a more suited method. For these reasons, the line measurement was substituted by 2D hardness mapping in the **Experiment 2/7**.

Fully eroded kerfs observed in this thesis show standard PWJ features such as openings and exit of cavities similarly as documented in [55]. Significant pile-up (upheaving) on the edges of the kerf were observed in this thesis similar to pile ups observed in works [47, 51, 56]. Lateral outflow areas on a side of the kerfs were also observed in this thesis as described by [48]. The lateral outflow exits are possibly created by the material movement caused by the lateral outflow jetting. Based solely on SEM observations it is impossible to disapprove presence isolated of subsurface voids as presented by Hloch et al. [48]. However, all observed surface cavities show signs of flow directed deformation, hinting at tunnelling of the material. Protrusions of material were observed in this thesis at the entry and exit points of the jet from the sample. The creation of interconnected micro-cavities was later supported by CT in work [55]. A significant increase in the erosion rate of PWJ compared to CWJ was concluded from SEM observation and depth/roughness measurement.

This experiment documented the often-overlooked importance of constituent particles in early erosion stages. This is especially important because many studies [13, 47, 48, 50, 56, 152–154] use aluminium alloys as testing material for evaluation of PWJ properties, and aluminium alloys of commercial quality often have high number of structural inhomogeneities [155] such as constituent particles. The erosion of these particles creates preferential sites for lateral outflow action, which could lead to an earlier onset of material removal and uneven erosion intensity across the treated surface.

6.2. Experiment set II

6.2.1 Surface hardening – fatigue improvement

Cylindrical fatigue samples were treated by PWJ at the process parameter range selected for the experiments. The significant improvement of the fatigue life was achieved at total strain level $\varepsilon_{at} = 0.32\%$ using PWJ treatment. The number of cycles to failure increased with decreasing feed rate of PWJ treatment. The number of cycles to failure at this strain level were in the range of 10^4 to 10^5 . A similar trend was observed at $\varepsilon_{at} = 0.28\%$ and is even more

conclusive. The number of cycles to failure ranged from 3.10^4 for an untreated sample. Specimens treated by PWJ feed rates of 0.2 and 0.05 mm/s did not fracture and the tests were stopped after 7.10^5 cycles. Possible increase of the fatigue life after PWJ treatment was suggested in a preliminary study of the UGN group by Hlaváček et al. [117] who observed improvement from N_f = 166 190 to N_f = 439 590 at stress amplitude about 290 MPa. The main difference is that they used lower pressure and sonotrode oscillating at a lower frequency of 20 kHz. S-N curve presented in their case shows that the beneficial effect of PWJ treatment on fatigue life is more dominant in low amplitude high cycle area. This observation [117] was one of the motivation for the opening of this topics as the theme for this Ph.D. thesis. The obtained results confirm for the first time, according to our knowledge, the possibility to use the PWJ as an alternative method for prolonging fatigue life, similarly, to e.g. shot peening. It can be assumed that the fatigue life of samples was increased due to the introduction of the residual stresses into the surface layer of the material. Polák [157] described that compressive residual stresses may slow down fatigue crack initiation and propagation in its early stages. This may explain the positive effect of PWJ treatment at lower strain amplitudes and the lack of this effect at higher strain amplitudes. Most fatigue life is determined in the crack initiation stage at lower strain amplitude levels, while at higher strain amplitudes, fatigue life is mostly determined by the crack propagation stage. Such trend is also in agreement with effect of shot peening on the fatigue life [158, 159]

While pure WJ peening [64] and AWJ peening [101] are established technologies, the PWJ peening of cylindrical samples is a relatively novel research area. Most of the research considering subsurface hardness or residual stress improvement considered flat samples or welds [12, 13, 115]. The fatigue samples used for testing had low diameter of 6 *mm*. This means the effectivity of the lateral flow may be strongly diminished and more importantly, the experiment is very sensitive to misalignment of the jet and the sample axis.

To enlarge the knowledge about possible controlling of fatigue life to the case of flat parts, several steps in future research steps are recommended. The flat fatigue samples should be used. This modification will allow better comparison to all previously achieved results on flat surfaces [12, 13, 115]. As the next step, effect of lateral flow jetting on overall jet effectivity should be evaluated. The study of cylindrical samples should be also preceded by examining the effect of the angle of impact on the PWJ effect. According to Lee et.al. [160], the droplet impact angle influences erosion before craters are formed. The PWJ peening process carried out in this work is within the incubation erosion stage, therefore angle of impact will play a significant role. Ahmad et al. [3] confirmed that the maximum volume loss happens at perpendicular impact (referenced to volume loss of X20Cr13). The study of effect of impact angle should be followed by a study of the effect of the radius of the surface subjected to PWJ. Burson-Thomas et al. [35] predicted that initial compressible stage is significantly altered based on ratio between droplet size and radius size. The lateral flow may commence at varying times along the contact periphery, which could lead to asymmetric acting of the lateral outflow. There are cases in literature [101] where AWJ peening conditions for radial surface samples were selected based on flat surfaces exposure with results showing significant improvement in fatigue strength. **Until these steps are accomplished, the application of previous theoretical or experimental results obtained on flat surfaces to PWJ treatment of radial surfaces will involve significant uncertainty.**

6.2.2 Surface hardening – effect of time exposure

Erosion levels achieved during the **experiment 2/6** cover all three erosion stages as defined by [21, 36]. After 5 seconds cracks are observed only in the centre of the main erosion area. These cracks follow a clear pattern that can be linked to grain boundaries. Material removal is visible at 10 *s* of PWJ exposure in the main erosion area. The connected crater (erosion stage III) is created with further PWJ exposure. The difference between PWJ and CWJ is quite significant. Cracks and cavities are found stochastically distributed after 20s of CWJ exposure with the exact same parameters as PWJ. This shows the erosion rate increase of PWJ compared to CWJ. This is due to the repetitive acting of the water hammer compared to stagnation pressure. The work [56] tries to evaluate the difference between CWJ and PWJ. They used lower pressure and frequency on aluminium alloy. However, differences in the shape of CWJ caused erosion are apparent. In this thesis CWJ surface roughening is visible across the whole treated area, while in [56] most visible erosion is distributed along the outer diameter of the eroded area.

The PWJ in the first 2 stages observed in this thesis created similar erosion pattern as in [161]. These patterns hint at grain tilting as an early deformation mechanism. This will be further explained in the discussion of **experiment 2/7**. The 3rd erosion region shows pile-ups only in the upper and side parts of the erosion crater. Three quarters of the crater edge had pile-up and one quarter of the crater edge showed a continuous transition to unaffected material similarly as observed in [48]. The eroded area shows asymmetric erosion distribution. This asymmetry is visible also in the incubation erosion stage (**Figure 70**, **Figure 83**) This asymmetry can be attributed to several possible factors. Firstly, as seen in **Figure 40a** and **Figure 40b** the water inlet is on one side of the the acoustic chamber, while the sonotrode is in the PWJ jet axis. The discrepancy means that the acoustic waves could propagate asymmetrically through the acoustic chamber and therefore create asymmetry in the water clusters. The second possible cause is that even a slight deviation of perpendicularity between the jet and the treated surface may cause an asymmetric commence time of the lateral outflow similar to case of radial surfaces as described by Burson-Thomas et al. [35]. Also, imperfections in the geometry of the output nozzle can influence the shape of the jet.

The erosion pattern in the transition area between crater and untreated material again accentuates grain boundaries. Similar patterns are quite common in the incubation erosion stage in polycrystalline materials. These patterns are documented in [20–22, 37]

The profile measurement was done to evaluate the maximum depth μm achieved as well as the volume removed mm^3 by PWJ. The roughness parameters of the first stage of erosion were evaluated. Roughness parameters were evaluated up to exposure of 6 *s* in this study. The importance of the roughness to depth switch is shown in the schematic (**Figure 93**) In the case of the study in **experiment 2/6** switch between roughness measurement and volumetric measurement was done based on **Figure 74**. The switch should consider the transition from incubation erosion stage into second erosion stage and the roughness values achieved, to differentiate between the roughness evolution of the original surface and the roughness of created eroded fracture surface **Figure 73** can be also used as basis of the switch as it shows localized macroscopic material removal start at PWJ exposure of 7s.

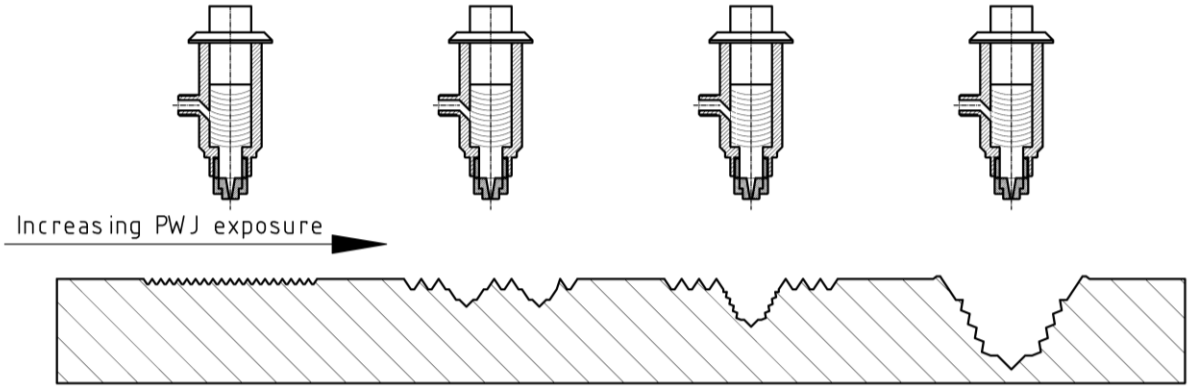

Figure 93 Schematic showing the importance of roughness/depth measurements change

The 2D hardness measurement grid was selected on cross section in **experiment 2/6** instead of line measurements for several reasons. Each point at the 2D hardness map is created from individual measurements (single indent). It means that individual measurements are not supported by statistics, and it may over or underestimate the hardness depending on local conditions. Results presented in this work (**Figure 76**) show no abrupt increase in hardness value so no point was omitted from the presented 2D hardness maps. The advantages of 2D hardness mapping far outweigh the disadvantages. Firstly, by averaging each individual indent high repetition (15-25) for averaged hardness for each depth is achieved. Secondly, 2D heat maps can document the effect of elastic waves propagating through the material after the water cluster impact.

According to the results of hardness measurement of 316L stainless steel supported by literature available hardness measurement following schematic of hardening can be drawn (**Figure 94**). The schematic shows that the material starts to harden due to the repeated impact of liquid clusters. This hardening affects mostly several layers of surface grains. When hardening reaches critical value and material plasticity is exhausted, cracks appear in this layer and material is locally removed by further liquid impacts. Newly exposed material then undergoes a similar cycle. However, since the initial surface was usually smoother than the newly exposed material, which is subjected to the effect of lateral outflow, roughening increases the rate of material removal. This results in the highest hardness directly under the surface in the case of roughened surfaces (5 *s* and 10 *s* of PWJ exposure in this thesis). While in the case of material removal (20 *s* of PWJ exposure in this thesis) hardened layer directly below the surface is eroded and higher hardness is observed deeper under the surface. PWJ exposure of 15s show combination of these two effects. Similar results were observed in the case of WJ peening by Azhari et al. [65], who observed that at higher roughness the maximum hardness values were shifted deeper under the surface.

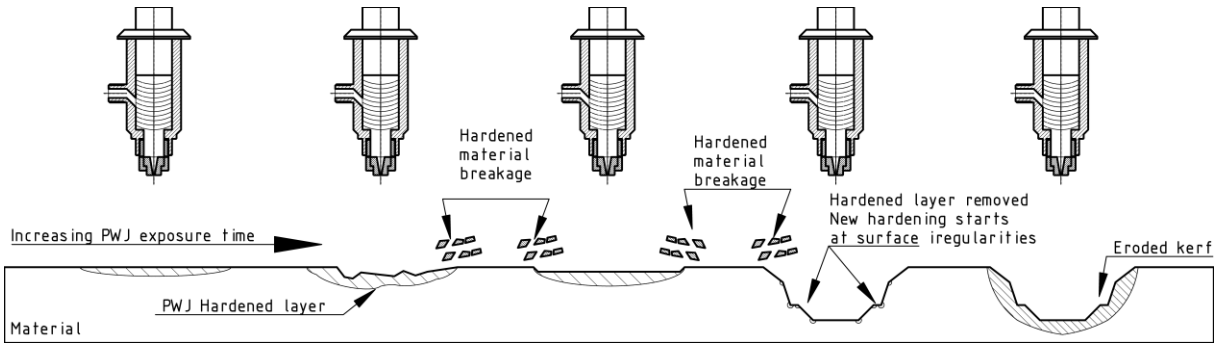

Figure 94 Schematic of repeated material hardening/removal process caused by liquid cluster impact

The most significant hardening in the case of 316L stainless steel is by 10 % of HV0.015 compared to average hardness (**Figure 78**). It seems to be surprisingly small increase; however, this value is representative for the material at depth of 30 μm. We can suppose that material just below the surface is hardened much more. A number of researchers [12, 13, 52, 53, 56, 59, 114, 116, 162] reported a hardening effect after PWJ but only one of these results was supported by electron microscopy. Therefore, the aim of the TEM analysis included in this experiment was to support these claims. A stationary jet was used instead of a line trajectory to concentrate water clusters on the single target location. The main erosion region in early stages is only around of about 180° of the central region as depicted in **Figure 72b**. Similar patterns after PWJ treatment were observed by [36, 43, 56]. SEM observation suggested that most of the surface peaks and valleys are close to grain boundaries. Grain tilting is therefore suggested as a main deformation mechanism in the erosion incubation stage. Furthermore, a number of depressions was found close to three grain junctions, which is supported by [163]. TEM observations show dislocation density gradient (Visible in **Figure 80** and **Figure 81**). Furthermore, before PWJ treatment mostly dislocations from one slip system are visible, while after PWJ exposure multiple slip systems appear active. The results suggest that the hardness increases significantly closer to the surface than 30 μm. The 2D hardness maps and measured hardness gradient confirm this finding. Based on these findings last experiments were designed to measure kernel averaged misorientation of surface treated by PWJ to quantify large area changes in the subsurface layer.

The following paragraph will describe the choice of hardness measurement load due to edge proximity. The current state of the art considers the hardened layer of thickness to be quite thin, which is in agreement with data measured in the experimental part of this work as well as in [52, 56]. Measurement of the hardness on the cross-section at such proximity to the edge requires a very low load for the indent to not be influenced by the edge. Most of the time microhardness or nanohardness measurement is necessary. According to ISO 6507-1 [164], the distance between the indent centre and the edge should be at least 2.5 times the mean diagonal length for steel copper and its alloys and at least 3 times the mean diagonal length for light metals and their alloys [164]. This is in many cases neglected when measuring the hardness profile created by PWJ as seen in [13, 116, 162]. The reason for using small loads is to get reliable measurements from as close to surface as possible, due to the steep gradient of the PWJ hardened layer. The small load however creates several problems. Firstly, according to ISO 6507-1 [164] decreasing the test force increases the scatter of the results of measurements [164]. Secondly, a smaller load leads to the more significant effect of quality of cross-section

preparation. Thirdly, indent is significantly more affected by structure properties such as grain boundaries, constituent particles etc., because only a small volume of material is responding to the penetration of the indent so no averaging of the properties on larger scale happens. Therefore, in this thesis micro hardness with a relatively low load force of 50mN (Al alloy) and 150 mN (316L steel) was evaluated to observe hardness development at depth of 30μm, even though it may be more susceptible to the cross-section preparation method. However, it can be concluded that even 30 μm is too high value to precisely evaluate the hardening of the surface layer. **Figure 95** shows relative hardness, which means hardness values divided by the average value of the measured region. This operation is done to reduce the effect of individual surface preparation. The added graphs on the left show each depth layer averaged into relative hardness value for a given depth. This should abate the higher scatter caused by low indentation force. In conclusion, graphs in **Figure 95** should be most representative of hardening this close to the edge, as they have a sufficiently low load to measure close to the PWJ treated surface, while at the same time high number of indents and mathematic operations reduce the limitations of the low load.

Hardness increment was measurable in wrought aluminium alloy to a depth of about 80 μm (**5.1.2**). A similar hardening depth was observed in the case of austenitic stainless steel (**5.2.2**). Hardening to depth below 100 μm has been observed in this work in this work on AW2014 and 316L stainless steel and a similar hardness depth was achieved by Chlupová et al. [52] on EA4T ferritic steel. **Figure 95** documents the creation of the hardened layer followed by its cyclic removal which supports hypothesis described in **Figure 94**. The depth of hardened layer observed in this work is quite shallow compared to shot peening or laser peening. The hardening profile cause by PWJ will now be compared to other methods of surface hardening. SP of 316L stainless steel led to an increase from 220HV to 405HV with a hardened layer depth of about 300 μm, as measured by Ahmed et al. [97]. A similar depth (~300 μm) was achieved by Maleki et al. on AISI 1060 using the Taguchi approach. LSP achieved over 600 μm for 316L stainless steel as measured by Wang et al. [137]. In the case of Ti alloys treated by LSP, a depth over 400 μm was achieved for Ti17 [131] and a similar depth in the case of Ti6Al4V [132]. Other authors studying ultrasonic PWJ either observed no change or statistically negligible change as is the case of Stolarik et al. [13] on EN-AW1050A or Nag et al. [56] on AW6060 . The hardening to a depth around 200 μm or deeper has been observed by Lehocka et al. [116], Hloch et al. [162] and Srivastava et al. [12, 59, 114] on AISI304 austenitic stainless steel. Interestingly, Lehocka et al. [116] compared 304 steel hardening depth which reached 250 μm to aluminium alloy EN AW 6060 where no significant hardening was observed.

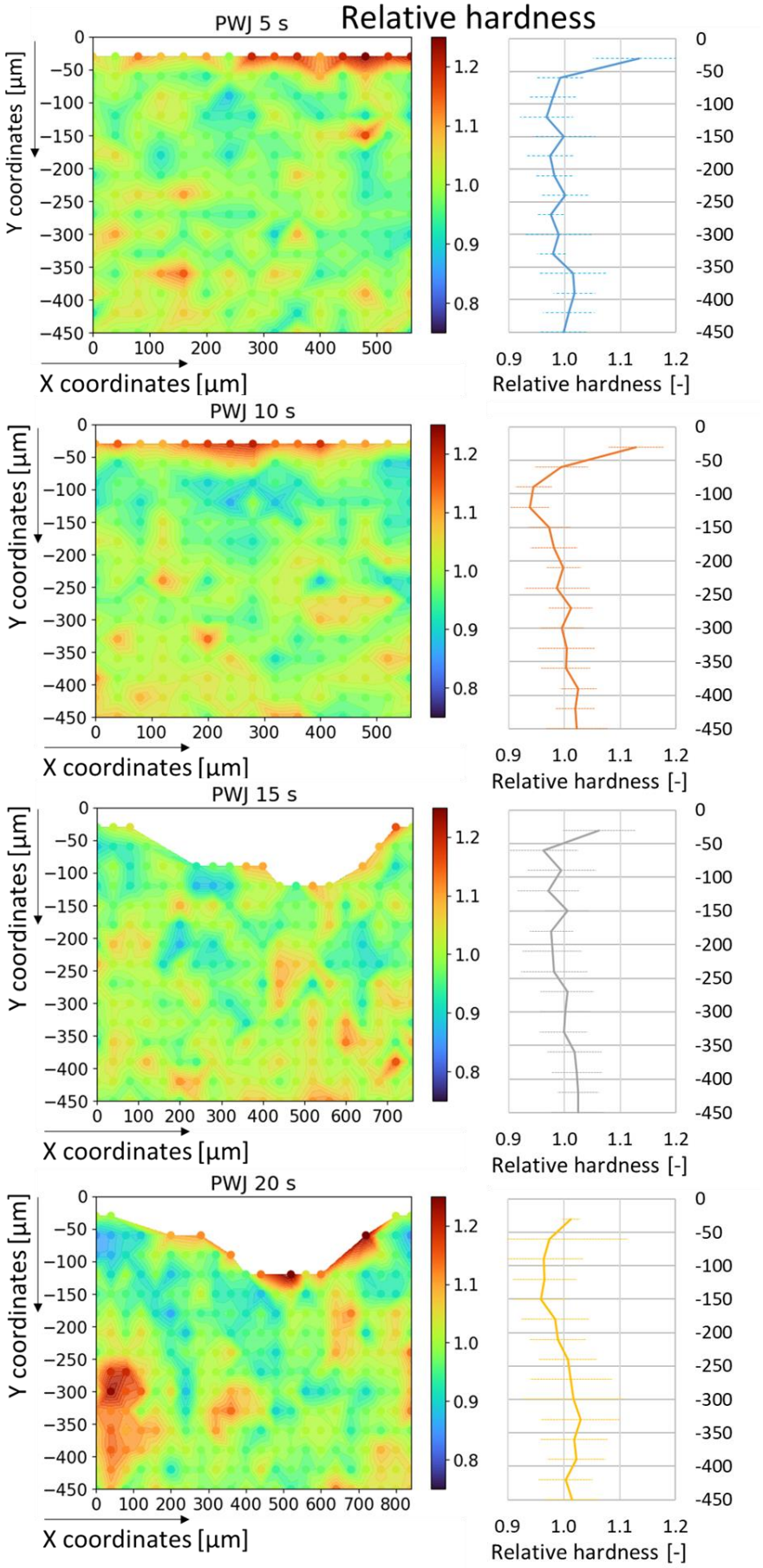

Figure 95 Relative 2D hardness maps with the addition of averaged values across each depth layer

6.2.3 Erosion incubation stage EBSD observation

SEM observations in this thesis as well as observations done by other authors [20–22, 37, 163], claim that the surface irregularities in the incubation erosion stage are created by grain tilting. EBSD measure the orientation of each pixel, replicating grain morphology in the form of an EBSD grain orientation map. Changes in grains in the EBSD grain orientation map (**Figure 88**) signify tiling of the grain. Comparison of as received state to state after PWJ treatment in inverse pole figure shows the grain tilted from their original direction. This means that grain tilting is proven response of tested material to water cluster impact. A number of surface irregularities may be attributed to grain tilting.

EBSD is scarcely used method of observation of PWJ treated surfaces, especially in the case of erosion incubation stage. The cross-sectional EBSD measurement is well established in the peening research [136, 137, 165, 166]. Most waterjet research focusing on CWJ [136, 167], AWJ [139, 168] or PWJ [71] used cross-sectional EBSD measurement after the WJ treatment (plane parallel with water direction). This study uses EBSD to observe the effect of PWJ on the treated surface (plane perpendicular to the water direction). To the author knowledge there is no study concerning PWJ treatment and EBSD surface (plane perpendicular to water direction) analysis.

The kernel averaged misorientation was evaluated from the EBSD data (explanation in **4.3.2**). There are some indications that KAM correlates with subsurface dislocation density [169] and a method to calculate geometrically necessary dislocations based on misorientation angle is already employed [170–172]. The EBSD before/after surface treatment also proved the creation of low-angle boundaries similar to subgrain boundaries with angles reaching 1°. The KAM can be averaged across the whole eroded area. **This gives researchers tool for effectively quantifying the incubation erosion stage.** In the next paragraph, the advantages and limitations of this method compared to other methods for incubation stage observations will be discussed.

The observation of PWJ treated surface by EBSD methodology (described in **4.2.3**) has been shown as an effective method for erosion incubation stage observations and quantifications. The method shows several specific requirements considering surface preparation. The advantages and limitations of the surface EBSD measurement methodology is summarized in **Table 11**. The method is also limited by the upper erosion limit. This limit will be determined in future works as a means of subsurface deformations and surface irregularities. The irregularities should be described by means of R_z, R_p or R_v. The method provides both qualitative and quantitative results. Qualitative analysis consists of observation of formations caused by erosion. Quantitative analysis can be done by averaging KAM in grains, lines or on whole eroded surfaces. The advantages compared to classic EBSD measurement done on cross-section are that no further treatment is required after PWJ treatment. Compared to XRD residual stress analysis, EBSD measure quite narrow subsurface layer. According to Wisniewski et al. [173] maximum informational depth of EBSD can reach 150 nm at an accelerating voltage of 30kV in low density materials, while XRD stress measurement reaches penetration depths in orders about $10^0 - 10^2\ \mu m$ based on angle ψ, radiation source used and examined metal [174]. It is necessary to measure thinner layer due to steep hardness gradient observed. A number of authors [172, 175] propose that KAM evaluation of EBSD measurement can be used to estimate

dislocation density. Liang et al. [172] compared methods for dislocation detection based on literature survey and concluded that XRD probe size typically ranges from hundreds of μm to several mm and the lower probe size of EBSD is about 100nm, while TEM allows the visualization of dislocation lines and dislocation density quantification at nanoscale.

The main advantage of the EBSD method over TEM is the area examined. TEM lamellae prepared by FIB are of dimensions of 10-15 μm width, 8-10 μm high and 50-100 nm thick according to [176]. So while TEM provides high accuracy of results up to analysis of single dislocations, it is local in nature which leads to poor statistical relevance [149].

The EBSD measured area in this work is 700x200 μm dimensions, which is not even the upper limit of the EBSD method. The EBSD may be the most suited method for statistical evaluation of the area subjected to the incubation erosion stage.

Table 11 advantages and limitations of the surface BSD measurement methodology

Advantages of EBSD/KAM	Limitations of EBSD/KAM
• Thin layer examined	• Quality of surface necessary
• No treatment after PWJ necessary	• Limited by speed/quality/size ratio
• Quantitative and qualitative data	• Control of PWJ location required
• Discover phase transformation	• Limited by surface roughness
• Estimation of dislocation density	• Limited by subsurface deformation
• Sensitive to early material changes	
• Effective for erosion incubation stage	

7. Summary and conclusions

The PWJ is a functional alternative to other surface treatment technologies with a clear environmental advantage. The hardened layer of the tested materials produced by PWJ is confirmed; however, the hardened layer depth reaches up to 100 μm only. Further PWJ parameters need to be altered to increase hardened layer depth. The surface roughening and further, surface erosion by PWJ is also observed in this work. The PWJ creates a high number of subsurface transient and blind cavities. From this perspective the technology may be suitable for surface roughening of bioactive surfaces. However, the use of PWJ for the study of erosion was the main topic of this thesis. PWJ is in this case used for generation of high frequency subsonic liquid cluster impacts. Within this work all three erosion stages are studied. Focus is given to the erosion incubation stage, which is hard to evaluate by conventional methods. The methodology of erosion incubation stage observation was proposed and tested. Below conclusions of each stage of experiments are given.

Effect of water impact distribution on the surface of 316L stainless steel

A similar experimental setup using a linear PWJ path with variance in feed rate to control water impact distribution was used for austenitic stainless steel. The experiment consisted of 4 hydraulic pressure levels 30, 40, 50 and 60 *MPa*. The influence of standoff distances was also examined for each pressure level concerning z = 26-32 *mm* for 30 *MPa*, z = 26-38 *mm* for 40 *MPa*, z = 30-46 *mm* for 50 *MPa* and z = 40-68 *mm* for 60 *MPa*.

Methodology of experiments and obtained results are as follows:

- Rz value in dependence on standoff distance shows increasing tendency up to culmination and then a decrease of values for pressure levels of 30, 40 and 50 *MPa*.
- In case of hydraulic pressure 60 *MPa*, the depth of valleys(Rv) increases significantly up to culmination at z = 58 *mm* and then decreases
- Based on surface profile measurement the optimal standoff distance for given hydraulic conditions was determined.
- The optimal standoff distances were then used for several runs with feed rate variations.
- The methodology for estimation of optimal standoff distance was proposed and applied.
- The increase in feed rate shows strictly decreasing tendencies in Rz Ra, Rp and Rv parameters.
- Hydraulic pressure level 50 *MPa* and v = 1 *mm/s* shows the highest number of disconnected erosion microcavities and voids.
- Detailed SEM observations show signs of material removal at hydraulic pressure 50 and 60 *MPa* at feedrate of v = 1 *mm/s*. Surface roughening was observed in all other cases. The severe surface roughening in case of low feed rates is accompanied by the creation of surface steps caused by twining. The cyclic behavior of hardening followed by saturation and removal of the hardened layer was explained.

Effect of water impact distribution on the surface of AW 2014

The evolution of surface area of AW2014 was described based on water cluster impact distribution, controlled by feedrate. The description includes topography analysis, surface analysis, dislocation analysis and hardness measurement Two PWJ processes at two pressure levels (40 *MPa* and 20 *MPa*) were compared with the CWJ method.

- Rz achieved by hydraulic pressure 40 *MPa* and number of cluster impacts 2 000 and 1 000 *i/mm* (v = 20 *mm/s* and v = 40 *mm/s*) was Rz = 12.87 and 9.31 μm respectively. In comparison, a lower hydraulic pressure level of 20 *MPa* led to a roughness value Rz = 15.39 μm at the number of cluster impacts 4 000 *i/mm* (10 *mm/s*). Rz values caused by CWJ at 1 *mm/s* were much lower reaching about Rz = 8.89 and 14.54 μm for 20 and 40 *MPa* respectively. It can be concluded that similar roughness is achieved by PWJ with the feed rate of 20 *mm/s* and CWJ with the feed rate of 1 *mm/s* at 40 *MPa*. At hydraulic pressure 20 *MPa* PWJ with the feed rate of 10 *mm/s* achieved a higher Rz parameter than CWJ at feed rate of 1 *mm/s*.
- PWJ shows almost 20 times faster surface roughening capabilities compared to CWJ at the hydraulic pressure of 40 *MPa*. Similarly, PWJ shows 10 times faster surface roughening capabilities compared to CWJ at a hydraulic pressure of 20 *MPa*.
- The earliest erosion damage signs were constituent particle cracking and removal. This leads to preferential erosion areas of lateral flow acting.
- The increase in surface micro-hardness was observed for both pressure levels. The maximum micro-hardness achieved for a pressure level of 40 *MPa* was 94.6 $HV_{0.005}$ in the case of v = 20 *mm/s*. Compared to the hardness of the as-received material 84.2 $HV_{0.005}$ the hardness was increased by over 10 %.
- Microscopy observation of incubation stage erosion concluded that the creation of localized surface damage is caused by interaction of water cluster impingement and constituent particles in the material. The interaction led to cracking and removal of the particles which create stress concentrator for lateral outflow.

Surface hardening – fatigue improvement

Next experiments were conducted using the pressure level of 50 *MPa* on austenitic stainless steel 316L. First PWJ was used to treat the round fatigue samples at varying cluster distribution.

- Specimens after PWJ treatment achieved significantly longer fatigue life in medium and low total strain amplitudes compared to untreated specimens.
- The increase in fatigue life showed clear dependence on the water impact distribution at ε_{at} = 0.32 %.
- Specimens treated by PWJ feed rates of 0.2 and 0.05 mm/s did not fracture at ε_{at} = 0.28 %. and the tests were stopped after 7.10^5 cycles.

Surface hardening – effect of time exposure

The next two experiments were both conducted using static PWJ head to obtain the exposure with the same hydraulic properties. The material used was 316L stainless steel. The first experiment focused on all three erosion stages. Surface evaluation was conducted by SEM and profile measurement. Subsurface microstructure was evaluated by TEM and cross-sectional hardness measurement.

The results can be summarized as follows:

- The surface roughness profile parameters Ra and Ry show an increase in magnitude with increasing PWJ exposure from 1 *s* to 6 *s*. At 6 *s*, the standard deviation of both parameters increases significantly as macroscopic material removal starts.

- The main observed erosion mechanism in incubation stage was grain tilting accommodated by twining.
- The first erosion damage has been observed at the depressed and elevated grain boundaries.
- The most intense primary hardening was observed below the eroded crater (30 μm). The hardening reached the highest values prior to start of material removal.

Erosion incubation stage EBSD observation

A methodology for quantification of the incubation erosion stage was proposed. The method uses EBSD observation of the exact surface before and after liquid clusters impact.

- The EBSD quantification method provided both qualitative and quantitative results in early incubation erosion stages and is already considered for further experiments.
- The KAM parameter calculated based on EBSD maps can be correlated with PWJ and CWJ exposure time for quantitative analysis of incubation erosion stage.
- The KAM distribution is nonhomogeneous among the treated area.
- EBSD grain orientation map proves that grain tilting is the mechanism behind surface roughening observed in this work during the incubation and pre-incubation erosion stage.
- The KAM evaluation shows misorientation localization into structures similar to sub-grain boundaries

Based on all the experiments the following main results has been established.

- Description of surface roughening or material removal in austenitic stainless steel and aluminium alloy based on water impact distribution and selected hydraulic parameters is provided. The mechanisms preceding material removal were evaluated.
- The processes leading to material removal were observed from the incubation stage to the earliest macroscopic pits formation
- The subsurface hardening was evaluated both in the case of austenitic stainless steel and aluminium alloy.
- The surface roughening in the erosion incubation stage has been thoroughly described by means of Ra, Rz Rv Rp as well as Rsk and Rku parameters.
- Increase of the fatigue life of specimens treated by PWJ with carefully chosen parameters is documented. This result show that PWJ is an alternative to known methods of surface hardening like shot peening.
- A new methodology consisting of surface EBSD measurement for evaluation of incubation and pre-incubation erosion changes in thin subsurface layer has been established and tested.

8. References

1. BARTOLOMÉ, Luis and TEUWEN, Julie. Prospective challenges in the experimentation of the rain erosion on the leading edge of wind turbine blades. *Wind Energy*. January 2019. Vol. 22, no. 1, p. 140–151. DOI 10.1002/we.2272.

2. ELHADI IBRAHIM, Mohamed and MEDRAJ, Mamoun. Water Droplet Erosion of Wind Turbine Blades: Mechanics, Testing, Modeling and Future Perspectives. *Materials*. 31 December 2019. Vol. 13, no. 1, p. 157. DOI 10.3390/ma13010157.

3. AHMAD, M., CASEY, M. and SÜRKEN, N. Experimental assessment of droplet impact erosion resistance of steam turbine blade materials. *Wear*. September 2009. Vol. 267, no. 9–10, p. 1605–1618. DOI 10.1016/j.wear.2009.06.012.

4. GOHARDANI, Omid. Impact of erosion testing aspects on current and future flight conditions. *Progress in Aerospace Sciences*. May 2011. Vol. 47, no. 4, p. 280–303. DOI 10.1016/j.paerosci.2011.04.001.

5. ZHANG, Huang, MA, Yue, HU, Guang and LIU, Qianfeng. Droplet impaction in nuclear installations and safety analysis: Phenomena, findings and approaches. *Nuclear Engineering and Design*. September 2020. Vol. 366, p. 110757. DOI 10.1016/j.nucengdes.2020.110757.

6. LEE, Y.S., LEE, S.H. and HWANG, K.M. Cause Analysis of Flow Accelerated Corrosion and Erosion-Corrosion Cases in Korea Nuclear Power Plants. *Corrosion Science and Technology*. 31 August 2016. Vol. 15, no. 4, p. 182–188. DOI 10.14773/CST.2016.15.4.182.

7. CHOI, Duk Hyun, KIM, Kyung Hoon and KIM, Hyung Joon. Long-term investigation of erosion behaviors on metal surfaces by impingement of liquid droplet with high-speed. *Journal of Mechanical Science and Technology*. March 2015. Vol. 29, no. 3, p. 1085–1091. DOI 10.1007/s12206-015-0220-0.

8. HONEGGER, E. *Corrosion and erosion of steam turbine blading*. 1924. *Brown Boveri Rev*. Vol. 12, p. 263-278.

9. SOURD, X., ZITOUNE, R., HEJJAJI, A., SALEM, M., HOR, A. and LAMOUCHE, D. Plain water jet cleaning of titanium alloy after abrasive water jet milling: Surface contamination and quality analysis in the context of maintenance. *Wear*. July 2021. Vol. 477, p. 203833. DOI 10.1016/j.wear.2021.203833.

10. YUAN, Yemin, CHEN, Jianfeng, GAO, Hang and WANG, Xuanping. An investigation into the abrasive waterjet milling circular pocket on titanium alloy. *The International Journal of Advanced Manufacturing Technology*. April 2020. Vol. 107, no. 11–12, p. 4503–4515. DOI 10.1007/s00170-020-05294-x.

11. KONG, M.C., AXINTE, D. and VOICE, W. Aspects of material removal mechanism in plain waterjet milling on gamma titanium aluminide. *Journal of Materials Processing Technology*. February 2010. Vol. 210, no. 3, p. 573–584. DOI 10.1016/j.jmatprotec.2009.11.009.

12. SRIVASTAVA, Madhulika, HLOCH, Sergej, KREJCI, Lucie, CHATTOPADHYAYA, Somnath, DIXIT, Amit Rai and FOLDYNA, Josef. Residual stress and surface properties of stainless steel welded joints induced by ultrasonic pulsed water jet peening. *Measurement*. October 2018. Vol. 127, p. 453–462. DOI 10.1016/j.measurement.2018.06.012.

13. STOLÁRIK, Gabriel, NAG, Akash, PETRŮ, Jana, SVOBODOVÁ, Jaroslava and HLOCH, Sergej. Ultrasonic Pulsating Water Jet Peening: Influence of Pressure and Pattern Strategy. *Materials*. 13 October 2021. Vol. 14, no. 20, p. 6019. DOI 10.3390/ma14206019.

14. FOLDYNA, Josef, SITEK, Libor, ŠVEHLA, Branislav and ŠVEHLA, Štefan. Utilization of ultrasound to enhance high-speed water jet effects. *Ultrasonics Sonochemistry*. May 2004. Vol. 11, no. 3–4, p. 131–137. DOI 10.1016/j.ultsonch.2004.01.008.

15. COOK, S. S. Erosion by water-hammer. *Proceedings of the Royal Society of London. Series A, Containing Papers of a Mathematical and Physical Character*. 2 July 1928. Vol. 119, no. 783, p. 481–488. DOI 10.1098/rspa.1928.0107.

16. SUMMERS, David A. *Waterjetting technology*. . 1st ed. London ; New York : E & FN Spon, 1995. ISBN 978-0-419-19660-0.

17. PEREC, Andrzej. Research into the Disintegration of Abrasive Materials in the Abrasive Water Jet Machining Process. *Materials*. 14 July 2021. Vol. 14, no. 14, p. 3940. DOI 10.3390/ma14143940.

18. FOWLER, G., SHIPWAY, P.H. and PASHBY, I.R. A technical note on grit embedment following abrasive water-jet milling of a titanium alloy. *Journal of Materials Processing Technology*. February 2005. Vol. 159, no. 3, p. 356–368. DOI 10.1016/j.jmatprotec.2004.05.024.

19. PARSONS, R.H. The Development of the Parsons Steam Turbine. *Nature*. 1 October 1936. Vol. 138, no. 3492, p. 567–568. DOI 10.1038/138567a0.

20. HANCOX, N. L. and BRUNTON, J. H. The Erosion of Solids by the Repeated Impact of Liquid Drops. *Philosophical Transactions of the Royal Society of London. Series A, Mathematical and Physical Sciences*. 1966. Vol. 260, no. 1110, p. 121–139.

21. THOMAS G. P. and BRUNTON, J. H. Drop impingement erosion of metals. *Proceedings of the Royal Society of London. A. Mathematical and Physical Sciences*. 27 January 1970. Vol. 314, no. 1519, p. 549–565. DOI 10.1098/rspa.1970.0022.

22. MARRIOTT, J. B., ROWDEN, G., HAMMITT, F. G., THOMAS, G. P., WEBB, A. W. O., TABOR, D., FYALL, A. A., SMITH, A. and BRUNTON, J. H. The Erosion of a Cobalt-Chromium Alloy by Liquid Impact [and Discussion]. *Philosophical Transactions of the Royal Society of London. Series A, Mathematical and Physical Sciences*. 1966. Vol. 260, no. 1110, p. 144–152.

23. MAHDIPOOR, M.S., TARASI, F., MOREAU, C., DOLATABADI, A. and MEDRAJ, M. HVOF sprayed coatings of nano-agglomerated tungsten-carbide/cobalt powders for water droplet erosion application. *Wear*. May 2015. Vol. 330–331, p. 338–347. DOI 10.1016/j.wear.2015.02.034.

24. MANN, B.S. and ARYA, Vivek. HVOF coating and surface treatment for enhancing droplet erosion resistance of steam turbine blades. *Wear*. April 2003. Vol. 254, no. 7–8, p. 652–667. DOI 10.1016/S0043-1648(03)00253-9.

25. GUJBA, Abdullahi K., MAHDIPOOR, Mohammad S. and MEDRAJ, Mamoun. Water droplet impingement erosion performance of WC-based coating sprayed by HVAF and HVOF. *Wear*. November 2021. Vol. 484–485, p. 203904. DOI 10.1016/j.wear.2021.203904.

26. BOWDEN F. P. and FIELD J. E. The brittle fracture of solids by liquid impact, by solid impact, and by shock. *Proceedings of the Royal Society of London. Series A. Mathematical and Physical Sciences*. 24 November 1964. Vol. 282, no. 1390, p. 331–352. DOI 10.1098/rspa.1964.0236.

27. BARGMANN, Heinz W. The mechanics of erosion by liquid and solid impact. *International Journal of Solids and Structures*. 1992. Vol. 29, no. 14–15, p. 1685–1698. DOI 10.1016/0020-7683(92)90162-M.

28. BURSON-THOMAS, Charles B., WELLMAN, Richard, HARVEY, Terry J. and WOOD, Robert J.K. Water droplet erosion of aeroengine fan blades: The importance of form. *Wear*. April 2019. Vol. 426–427, p. 507–517. DOI 10.1016/j.wear.2018.12.030.

29. KEEGAN, M H, NASH, D H and STACK, M M. On erosion issues associated with the leading edge of wind turbine blades. *Journal of Physics D: Applied Physics*. 25 September 2013. Vol. 46, no. 38, p. 383001. DOI 10.1088/0022-3727/46/38/383001.

30. VERMA, Amrit Shankar, CASTRO, Saullo G.P., JIANG, Zhiyu and TEUWEN, Julie J.E. Numerical investigation of rain droplet impact on offshore wind turbine blades under different rainfall conditions: A parametric study. *Composite Structures*. June 2020. Vol. 241, p. 112096. DOI 10.1016/j.compstruct.2020.112096.

31. KIROLS, H S, KEVORKOV, D, UIHLEIN, A and MEDRAJ, M. Water droplet erosion of stainless steel steam turbine blades. *Materials Research Express*. 16 August 2017. Vol. 4, no. 8, p. 086510. DOI 10.1088/2053-1591/aa7c70.

32. RYZHENKOV, V. A., LEBEDEVA, A. I. and MEDNIKOV, A. F. Erosion wear of the blades of wet-steam turbine stages: Present state of the problem and methods for solving it. *Thermal Engineering*. September 2011. Vol. 58, no. 9, p. 713–718. DOI 10.1134/S0040601511090138.

33. GUJBA, A.K., HACKEL, L., KEVORKOV, D. and MEDRAJ, M. Water droplet erosion behaviour of Ti–6Al–4V and mechanisms of material damage at the early and advanced stages. *Wear*. July 2016. Vol. 358–359, p. 109–122. DOI 10.1016/j.wear.2016.04.008.

34. FUJISAWA, Nobuyuki, YAMAGATA, Takayuki, HAYASHI, Kanto and TAKANO, Tsuyoshi. Experiments on liquid droplet impingement erosion by high-speed spray. *Nuclear Engineering and Design*. September 2012. Vol. 250, p. 101–107. DOI 10.1016/j.nucengdes.2012.06.022.

35. BURSON-THOMAS, Charles B., WELLMAN, Richard, HARVEY, Terry J. and WOOD, Robert J. K. Importance of Surface Curvature in Modeling Droplet Impingement on Fan Blades. *Journal of Engineering for Gas Turbines and Power*. 1 March 2019. Vol. 141, no. 3, p. 031005. DOI 10.1115/1.4041149.

36. FOLDYNA, Josef, KLICH, Jiří, ZELEŇÁK, Michal, ŠČUČKA, Jiří. Erosion of Metals by Pulsating Water Jet. *Tehnicki vjesnik - Technical Gazette*. March 2012. Vol. 19, no. 2. p. 381-386. DOI 10.17559/TV-20170327134630.

37. MA, Dina, MOSTAFA, Ahmad, KEVORKOV, Dmytro, JEDRZEJOWSKI, Pawel, PUGH, Martin and MEDRAJ, Mamoun. Water Impingement Erosion of Deep-Rolled Ti64. *Metals*. 18 August 2015. Vol. 5, no. 3, p. 1462–1486. DOI 10.3390/met5031462.

38. MOMBER, Andreas W. *Principles of Abrasive Water Jet Machining*. Springer London, 2012. ISBN 978-1-4471-1572-4.

39. RAKOWSKI, Zikmund. *Geomechanics 93: Strata mechanics, numerical methods, water jet cutting, mechanical rock disintegration proceedings of the International conference Geomechanics 93, Hradec, Ostrava, Czech Republic, 28-30 September 1993*. . Rotterdam Brookfield : A. A. Balkema, 1994. ISBN 978-90-5410-354-7. 624.151

40. ŘÍHA, Zdeněk, ZELEŇÁK, Michal, KRUML, Tomáš and POLOPRUDSKÝ, Jakub. Comparison of the disintegration abilities of modulated and continuous water jets. *Wear*. August 2021. Vol. 478–479, p. 203891. DOI 10.1016/j.wear.2021.203891.

41. KANTHA BABU, M and KRISHNAIAH CHETTY, O.V. A study on recycling of abrasives in abrasive water jet machining. *Wear*. April 2003. Vol. 254, no. 7–8, p. 763–773. DOI 10.1016/S0043-1648(03)00256-4.

42. BERGS, T., SCHÜLER, M., DADGAR, M., HERRIG, T. and KLINK, A. Investigation of Waterjet Phases on Material Removal Characteristics. *Procedia CIRP*. 2020. Vol. 95, p. 12–17. DOI 10.1016/j.procir.2020.02.319.

43. NAG, Akash, HVIZDOS, Pavol, DIXIT, Amit Rai, PETRŮ, Jana and HLOCH, Sergej. Influence of the frequency and flow rate of a pulsating water jet on the wear damage of tantalum. *Wear*. July 2021. Vol. 477, p. 203893. DOI 10.1016/j.wear.2021.203893.

44. LI, Deng, KANG, Yong, DING, Xiaolong, WANG, Xiaochuan and LIU, Wenchuan. Effects of feeding pipe diameter on the performance of a jet-driven Helmholtz oscillator generating pulsed waterjets. *Journal of Mechanical Science and Technology*. March 2017. Vol. 31, no. 3, p. 1203–1212. DOI 10.1007/s12206-017-0219-9.

45. ZELEŇÁK, Michal, ŘÍHA, Zdeněk and JANDAČKA, Petr. Visualization and velocity analysis of a high-speed modulated water jet generated by a hydrodynamic nozzle. *Measurement*. July 2020. Vol. 159, p. 107753. DOI 10.1016/j.measurement.2020.107753.

46. FOLDYNA, Josef. Recent Developments in Pulsating Water Jets. In : HLOCH, Sergej, KLICHOVÁ, Dagmar, KROLCZYK, Grzegorz M., CHATTOPADHYAYA, Somnath and RUPPENTHALOVÁ, Lucie (eds.), *Advances in Manufacturing Engineering and Materials*. Online. Cham : Springer International Publishing, 2019. p. 54–62. Lecture Notes in Mechanical Engineering. [Accessed 22 January 2023]. ISBN 978-3-319-99352-2.

47. HLOCH, Sergej, SRIVASTAVA, Madhulika, NAG, Akash, MÜLLER, Miroslav, HROMASOVÁ, Monika, SVOBODOVÁ, Jaroslava, KRUML, Tomáš and CHLUPOVÁ, Alice. Effect of pressure of pulsating water jet moving along stair trajectory on erosion depth, surface morphology and microhardness. *Wear*. July 2020. Vol. 452–453, p. 203278. DOI 10.1016/j.wear.2020.203278.

48. HLOCH, Sergej, ADAMČÍK, Pavel, NAG, Akash, SRIVASTAVA, Madhulika, ČUHA, Dominik, MÜLLER, Miroslav, HROMASOVÁ, Monika and KLICH, Jiří. Hydrodynamic ductile erosion of aluminium by a pulsed water jet moving in an inclined trajectory. *Wear*. June 2019. Vol. 428–429, p. 178–192. DOI 10.1016/j.wear.2019.03.015.

49. RAJ, Piush, HLOCH, Sergej, TRIPATHI, Rupam, SRIVASTAVA, Madhulika, NAG, Akash, KLICHOVÁ, Dagmar, KLICH, Jiří, HROMASOVÁ, Monika, MULLER, Miroslav, MILOSLAV, Linda, CHATTOPADHYAYA, Somnath and ADAMCIK, Pavel. Investigation of sandstone erosion by continuous and pulsed water jets. *Journal of Manufacturing Processes*. June 2019. Vol. 42, p. 121–130. DOI 10.1016/j.jmapro.2019.04.035.

50. NAG, Akash, HLOCH, Sergej, ČUHA, Dominik, DIXIT, Amit Rai, TOZAN, Hakan, PETRŮ, Jana, HROMASOVÁ, Monika and MÜLLER, Miroslav. Acoustic chamber length performance analysis in ultrasonic pulsating water jet erosion of ductile material. *Journal of Manufacturing Processes*. November 2019. Vol. 47, p. 347–356. DOI 10.1016/j.jmapro.2019.10.008.

51. SRIVASTAVA, Madhulika, NAG, Akash, CHATTOPADHYAYA, Somnath and HLOCH, Sergej. Standoff Distance in Ultrasonic Pulsating Water Jet. *Materials*. 27 December 2020. Vol. 14, no. 1, p. 88. DOI 10.3390/ma14010088.

52. CHLUPOVÁ, Alice, HLOCH, Sergej, NAG, Akash, ŠULÁK, Ivo and KRUML, Tomáš. Effect of pulsating water jet processing on erosion grooves and microstructure in the subsurface layer of 25CrMo4 (EA4T) steel. *Wear*. July 2023. Vol. 524–525, p. 204774. DOI 10.1016/j.wear.2023.204774.

53. SRIVASTAVA, Madhulika, HLOCH, Sergej, MULLER, Miroslav, HROMASOVÁ, Monika, CAIS, Jaromír, CHATTOPADHYAYA, Somnath, DIXIT, Amit Rai and KLICH, Jiří. Effect of Frequency Change During Pulsed Waterjet Interaction with Stainless Steel. In : HLOCH, Sergej, KLICHOVÁ, Dagmar, KROLCZYK, Grzegorz M., CHATTOPADHYAYA, Somnath and RUPPENTHALOVÁ, Lucie (eds.), *Advances in Manufacturing Engineering and Materials*. Online. Cham : Springer International Publishing, 2019. p. 85–96. Lecture Notes in Mechanical Engineering. [Accessed 22 January 2023]. ISBN 978-3-319-99352-2.

54. FOLDYNA, J., SITEK, L., ŠČUČKA, J., MARTINEC, P., VALÍČEK, J. and PÁLENÍKOVÁ, K. Effects of pulsating water jet impact on aluminium surface. *Journal of Materials Processing Technology*. November 2009. Vol. 209, no. 20, p. 6174–6180. DOI 10.1016/j.jmatprotec.2009.06.004.

55. HLOCH, Sergej, SOUČEK, Kamil, SVOBODOVÁ, Jaroslava, HROMASOVÁ, Monika and MÜLLER, Miroslav. Subsurface microtunneling in ductile material caused by multiple droplet impingement at subsonic speeds. *Wear*. February 2022. Vol. 490–491, p. 204176. DOI 10.1016/j.wear.2021.204176.

56. NAG, Akash, SRIVASTAVA, Madhulika, PETRŮ, Jana, VÁŇOVÁ, Petra, SRIVASTAVA, Ashish Kumar and HLOCH, Sergej. Comparison of Continuous and Pulsating Water Jet during Piercing of Ductile Material. *Materials*. 6 May 2023. Vol. 16, no. 9, p. 3558. DOI 10.3390/ma16093558.

57. KLICH, Jiri, KLICHOVA, Dagmar, FOLDYNA, Vladimir, HLAVACEK, Petr and FOLDYNA, Josef. Influence of Variously Modified Surface of Aluminium Alloy on the

Effect of Pulsating Water Jet. *Strojniški vestnik - Journal of Mechanical Engineering*. 15 October 2017. Vol. 63, no. 10, p. 577–582. DOI 10.5545/sv-jme.2017.4356.

58. LEHOCKÁ, Dominika, BOTKO, František, SIMKULET, Vladimír, MITAĽ, Dušan, BREZÍKOVÁ, Katarína and ZAJAC, Branislav. Study of Surface Topography of CW004A Copper after PWJ Disintegration. In : *Proceedings of the 2nd EAI International Conference on Management of Manufacturing Systems*. Online. Starý Smokovec, Slovakia : EAI, 2018. [Accessed 22 January 2023]. ISBN 978-1-63190-158-4. DOI 10.4108/eai.22-11-2017.2274347.

59. SRIVASTAVA, Madhulika, HLOCH, Sergej, TRIPATHI, Rupam, KOZAK, Drazan, CHATTOPADHYAYA, Somnath, DIXIT, Amit Rai, FOLDYNA, Josef, HVIZDOS, Pavol, FIDES, Martin and ADAMCIK, Pavel. Ultrasonically generated pulsed water jet peening of austenitic stainless-steel surfaces. *Journal of Manufacturing Processes*. April 2018. Vol. 32, p. 455–468. DOI 10.1016/j.jmapro.2018.03.016.

60. TRIPATHI, Rupam, HLOCH, Sergej, CHATTOPADHYAYA, Somnath, KLICHOVÁ, Dagmar, ŠČUČKA, Jiří and DAS, Alok Kumar. Application of the pulsating and continous water jet for granite erosion. *International Journal of Rock Mechanics and Mining Sciences*. February 2020. Vol. 126, p. 104209. DOI 10.1016/j.ijrmms.2020.104209.

61. POLOPRUDSKÝ, Jakub, NAG, Akash, KRUML, Tomáš and HLOCH, Sergej. Effects of liquid droplet volume and impact frequency on the integrity of Al alloy AW2014 exposed to subsonic speeds of pulsating water jets. *Wear*. January 2022. Vol. 488–489, p. 204136. DOI 10.1016/j.wear.2021.204136.

62. TRIPATHI, Rupam, HLOCH, Sergej, CHATTOPADHYAYA, Somnath, KLICHOVÁ, Dagmar and KLICH, Jiří. Influence of frequency change during sandstone erosion by pulsed waterjet. *Materials and Manufacturing Processes*. 25 January 2020. Vol. 35, no. 2, p. 187–194. DOI 10.1080/10426914.2019.1669800.

63. LEHOCKÁ, D., KLICH, J., BOTKO, F., FOLDYNA, J., HLOCH, S., KEPIČ, J., KOVAĽ, K., KREJČI, L. and STORKAN, Z. Pulsating water jet erosion effect on a brass flat solid surface. *The International Journal of Advanced Manufacturing Technology*. July 2018. Vol. 97, no. 1–4, p. 1099–1112. DOI 10.1007/s00170-018-1882-4.

64. AZHARI, Azmir, SCHINDLER, Christian, KERSCHER, Eberhard and GRAD, Patrick. Improving surface hardness of austenitic stainless steel using waterjet peening process. *The International Journal of Advanced Manufacturing Technology*. December 2012. Vol. 63, no. 9–12, p. 1035–1046. DOI 10.1007/s00170-012-3962-1.

65. AZHARI, Azmir, SCHINDLER, Christian and LI, Bo. Effect of waterjet peening on aluminum alloy 5005. *The International Journal of Advanced Manufacturing Technology*. July 2013. Vol. 67, no. 1–4, p. 785–795. DOI 10.1007/s00170-012-4522-4.

66. WANG, J and GUO, D.M. The cutting performance in multipass abrasive waterjet machining of industrial ceramics. *Journal of Materials Processing Technology*. February 2003. Vol. 133, no. 3, p. 371–377. DOI 10.1016/S0924-0136(02)01125-1.

67. GRINSPAN, A. Sahaya and GNANAMOORTHY, R. A novel surface modification technique for the introduction of compressive residual stress and preliminary studies on Al alloy AA6063. *Surface and Coatings Technology*. October 2006. Vol. 201, no. 3–4, p. 1768–1775. DOI 10.1016/j.surfcoat.2006.03.002.

68. KLICHOVA, Dagmar, NAG, Akash, POLOPRUDSKÝ, Jakub, FOLDYNA, Josef, PUDE, Frank, SITEK, Libor and HLOCH, Sergej. Utilising of water hammer effect for surface roughening of Ti6Al4V. *The International Journal of Advanced Manufacturing Technology*. June 2023. Vol. 126, no. 11–12, p. 5633–5647. DOI 10.1007/s00170-023-11521-y.

69. STOLÁRIK, Gabriel, SVOBODOVÁ, Jaroslava, KLICHOVÁ, Dagmar, NAG, Akash and HLOCH, Sergej. Titanium surface roughening with ultrasonic pulsating water jet. *Journal of Manufacturing Processes*. March 2023. Vol. 90, p. 341–356. DOI 10.1016/j.jmapro.2023.02.013.

70. AMEGADZIE, M.Y., MOREAU, E.D., CHRISTENSEN, B., DONALDSON, I.W., TIEU, A., VIJAY, M.M. and PLUCKNETT, K.P. Ultrasonic pulsed waterjet surface peening of an industrial aluminum-based metal matrix composite. *Surface and Coatings Technology*. November 2021. Vol. 426, p. 127795. DOI 10.1016/j.surfcoat.2021.127795.

71. SIAHPOUR, P., AMEGADZIE, M.Y., TIEU, A., DONALDSON, I.W. and PLUCKNETT, K.P. Ultrasonic pulsed waterjet peening of commercially-pure titanium. *Surface and Coatings Technology*. November 2023. Vol. 472, p. 129953. DOI 10.1016/j.surfcoat.2023.129953.

72. FOLDYNA, Josef, RÍHA, Zdeněk, SITEK, Libor and SVEHLA, Branislav. Numerical simulation of transmission of acoustic waves high-pressure system. In : *Proceedings of the Interntional Congress on Ultrasonics*. Online. Vienna University of Technology, 2007. [Accessed 22 January 2023]. DOI 10.3728/ICUltrasonics.2007.Vienna.1456_foldyna.

73. KAMKAR, N., BRIDIER, F., BOCHER, P. and JEDRZEJOWSKI, P. Water droplet erosion mechanisms in rolled Ti–6Al–4V. *Wear*. April 2013. Vol. 301, no. 1–2, p. 442–448. DOI 10.1016/j.wear.2013.01.005.

74. STEEVES, A J, VARIOLA, F, VIJAY, M, TIEU, A, YAN, W, XU, M and DANIELS, B. In Vitro Response of Osteoblastic and Fibroblastic Cells to Water-Jet Treated Titanium Surfaces. In: *2019 WJTA Conference and Expo*. November 2019.

75. HLOCH, Sergej, NAG, Akash, PUDE, Frank, FOLDYNA, Josef and ZELEŇÁK, Michal. On-line measurement and monitoring of pulsating saline and water jet disintegration of bone cement with frequency 20 kHz. *Measurement*. December 2019. Vol. 147, p. 106828. DOI 10.1016/j.measurement.2019.07.056.

76. VARIOLA, Fabio, BRUNSKI, John B., ORSINI, Giovanna, TAMBASCO DE OLIVEIRA, Paulo, WAZEN, Rima and NANCI, Antonio. Nanoscale surface modifications of medically relevant metals: state-of-the art and perspectives. *Nanoscale*. 2011. Vol. 3, no. 2, p. 335–353. DOI 10.1039/C0NR00485E.

77. DARVELL, B.W., SAMMAN, N., LUK, W.K., CLARK, R.K.F. and TIDEMAN, H. Contamination of titanium castings by aluminium oxide blasting. *Journal of Dentistry*. October 1995. Vol. 23, no. 5, p. 319–322. DOI 10.1016/0300-5712(94)00003-X.

78. BARRIUSO, S., LIEBLICH, M., MULTIGNER, M., ETXEBERRIA, I., ALBERDI, A. and GONZÁLEZ-CARRASCO, J.L. Roughening of metallic biomaterials by abrasiveless waterjet peening: Characterization and viability. *Wear*. April 2011. Vol. 270, no. 9–10, p. 634–639. DOI 10.1016/j.wear.2011.01.024.

79. ANSELME, K. and BIGERELLE, M. Statistical demonstration of the relative effect of surface chemistry and roughness on human osteoblast short-term adhesion. *Journal of Materials Science: Materials in Medicine*. May 2006. Vol. 17, no. 5, p. 471–479. DOI 10.1007/s10856-006-8475-8.

80. KALLIECHARAN, D, TIEU, A, DANIELS, B, YAN, W, XU, M, VIJAY, M and MONCHESKY, T L. Surface modification of medical grade titanium alloy by forced pulsed water jet (FPWJ). In: *BHR Group at Water Jetting 2016: 23rd International Conference on Water Jetting*. November 2016. Vol. 23

81. TURSKI, M., CLITHEROE, S., EVANS, A. D., RODOPOULOS, C., HUGHES, D. J. and WITHERS, P. J. Engineering the residual stress state and microstructure of stainless steel with mechanical surface treatments. *Applied Physics A*. June 2010. Vol. 99, no. 3, p. 549–556. DOI 10.1007/s00339-010-5672-6.

82. SOYAMA, Hitoshi, CHIGHIZOLA, Christopher R. and HILL, Michael R. Effect of compressive residual stress introduced by cavitation peening and shot peening on the improvement of fatigue strength of stainless steel. *Journal of Materials Processing Technology*. February 2021. Vol. 288, p. 116877. DOI 10.1016/j.jmatprotec.2020.116877.

83. PEYRE, P., FABBRO, R., MERRIEN, P. and LIEURADE, H.P. Laser shock processing of aluminium alloys. Application to high cycle fatigue behaviour. *Materials Science and Engineering: A*. June 1996. Vol. 210, no. 1–2, p. 102–113. DOI 10.1016/0921-5093(95)10084-9.

84. MARTINEZ, Luis Lopez. Fatigue Life Extension Procedure by Ultrasonic Peening. In: *Swedish Conference on Light Weight Optimised Welded Structures*. March 2010.

85. DELOSRIOS, E, WALLEY, A, MILAN, M and HAMMERSLEY, G. Fatigue crack initiation and propagation on shot-peened surfaces in A316 stainless steel. *International Journal of Fatigue*. October 1995. Vol. 17, no. 7, p. 493–499. DOI 10.1016/0142-1123(95)00044-T.

86. TORRES, M. An evaluation of shot peening, residual stress and stress relaxation on the fatigue life of AISI 4340 steel. *International Journal of Fatigue*. August 2002. Vol. 24, no. 8, p. 877–886. DOI 10.1016/S0142-1123(01)00205-5.

87. ZHOU, J., RETRAINT, D., SUN, Z. and KANOUTÉ, P. Comparative study of the effects of surface mechanical attrition treatment and conventional shot peening on low cycle fatigue of a 316L stainless steel. *Surface and Coatings Technology*. September 2018. Vol. 349, p. 556–566. DOI 10.1016/j.surfcoat.2018.06.041.

88. ZUM GAHR, Karl-Heinz. *Microstructure and wear of materials*. . Amsterdam New York : Elsevier, 1987. Tribology series, 10. ISBN 978-0-444-42754-0.

89. BEGHINI, M. and BERTINI, L. Fatigue crack propagation through residual stress fields with closure phenomena. *Engineering Fracture Mechanics*. January 1990. Vol. 36, no. 3, p. 379–387. DOI 10.1016/0013-7944(90)90285-O.

90. PIPPAN, R. and HOHENWARTER, A. Fatigue crack closure: a review of the physical phenomena: Fatigue Crack Closure. *Fatigue & Fracture of Engineering Materials & Structures*. April 2017. Vol. 40, no. 4, p. 471–495. DOI 10.1111/ffe.12578.

91. MAIYA, P.S. Geometrical characterization of surface roughness and its application to fatigue crack initiation. *Materials Science and Engineering*. January 1975. Vol. 21, p. 57–62. DOI 10.1016/0025-5416(75)90198-6.

92. MONTROSS, C. Laser shock processing and its effects on microstructure and properties of metal alloys: a review. *International Journal of Fatigue*. October 2002. Vol. 24, no. 10, p. 1021–1036. DOI 10.1016/S0142-1123(02)00022-1.

93. MALEKI, Erfan and UNAL, Okan. Optimization of Shot Peening Effective Parameters on Surface Hardness Improvement. *Metals and Materials International*. September 2021. Vol. 27, no. 9, p. 3173–3185. DOI 10.1007/s12540-020-00758-x.

94. TOSHA, Katsuji. Influence of residual stresses on the hardness number in the affected layer produced by shot peening. In : *Asia-Pacific Forum on Precision Surface Finishing and Deburring Technology*. July 2002. p. 48–54.

95. OMARI, Mohammad A., MOUSA, Hamzah M., AL-OQLA, Faris M. and ALJARRAH, Mohammad. Enhancing the surface hardness and roughness of engine blades using the shot peening process. *International Journal of Minerals, Metallurgy, and Materials*. August 2019. Vol. 26, no. 8, p. 999–1004. DOI 10.1007/s12613-019-1818-5.

96. CHEN, Jun S, DESAI, Dawood A, HEYNS, Stephan P and PIETRA, Francesco. Literature review of numerical simulation and optimisation of the shot peening process. *Advances in Mechanical Engineering*. March 2019. Vol. 11, no. 3, p. 168781401881827. DOI 10.1177/1687814018818277.

97. AHMED, Aymen A., MHAEDE, Mansour, BASHA, M, WOLLMANN, Manfred and WAGNER, Lothar. The effect of shot peening parameters and hydroxyapatite coating on surface properties and corrosion behavior of medical grade AISI 316L stainless steel. *Surface and Coatings Technology*. October 2015. Vol. 280, p. 347–358. DOI 10.1016/j.surfcoat.2015.09.026.

98. GUJBA, Abdullahi and MEDRAJ, Mamoun. Laser Peening Process and Its Impact on Materials Properties in Comparison with Shot Peening and Ultrasonic Impact Peening. *Materials*. 10 December 2014. Vol. 7, no. 12, p. 7925–7974. DOI 10.3390/ma7127925.

99. HE, LI, ZHAO, CUI, LI, YU, CHEN, and FU. Mathematical Model and Verification of Residual Stress Induced by Water Jet Peening. *Metals*. 27 August 2019. Vol. 9, no. 9, p. 936. DOI 10.3390/met9090936.

100. HE, Zhanshu, YU, Huixin, ZHAO, Shusen, XING, Jiaqi, LI, Dalei, LI, Chao, CHEN, Lei and WANG, Shuai. An experimental and numerical analysis of water jet peening of Al6061-T6. *The International Journal of Advanced Manufacturing Technology*. April 2020. Vol. 107, no. 9–10, p. 3833–3845. DOI 10.1007/s00170-020-05282-1.

101. AROLA, D., ALADE, A. E. and WEBER, W. IMPROVING FATIGUE STRENGTH OF METALS USING ABRASIVE WATERJET PEENING. *Machining Science and Technology*. July 2006. Vol. 10, no. 2, p. 197–218. DOI 10.1080/10910340600710105.

102. HASHIMOTO, Tadafumi, OSAWA, Yusuke, ITOH, Shinsuke, MOCHIZUKI, Masahito and NISHIMOTO, Kazutoshi. Long-Term Stability of Residual Stress Improvement by Water Jet Peening Considering Working Processes. *Journal of Pressure Vessel Technology*. 1 June 2013. Vol. 135, no. 3, p. 031601. DOI 10.1115/1.4023417.

103. BALAMURUGAN, K., UTHAYAKUMAR, M., GOWTHAMAN, S. and PANDURANGAN, R. A study on the compressive residual stress due to waterjet cavitation peening. *Engineering Failure Analysis*. October 2018. Vol. 92, p. 268–277. DOI 10.1016/j.engfailanal.2018.05.012.

104. SOYAMA, Hitoshi. Surface mechanics design of metallic materials on mechanical surface treatments. *Mechanical Engineering Reviews*. 2015. Vol. 2, no. 1, p. 14- 00192-14–00192. DOI 10.1299/mer.14-00192.

105. SOYAMA, Hitoshi. Cavitation Peening: A Review. *Metals*. 19 February 2020. Vol. 10, no. 2, p. 270. DOI 10.3390/met10020270.

106. BRENNEN, Christopher E. *Cavitation and bubble dynamics*. . New York : Oxford University Press, 1995. Oxford engineering science series, 44. ISBN 978-0-19-509409-1.

107. ŚWIETLICKI, Aleksander, SZALA, Mirosław and WALCZAK, Mariusz. Effects of Shot Peening and Cavitation Peening on Properties of Surface Layer of Metallic Materials—A Short Review. *Materials*. 27 March 2022. Vol. 15, no. 7, p. 2476. DOI 10.3390/ma15072476.

108. JANKA, Styková, MILOŠ, Müller and JAN, Hujer. The improvement of the surface hardness of stainless steel and aluminium alloy by ultrasonic cavitation peening. DANČOVÁ, P. (ed.), *EPJ Web of Conferences*. 2017. Vol. 143, p. 02119. DOI 10.1051/epjconf/201714302119.

109. BAI, Fushi, SAALBACH, Kai-Alexander, WANG, Liang, WANG, Xiaogeng and TWIEFEL, Jens. Impact of time on ultrasonic cavitation peening via detection of surface plastic deformation. *Ultrasonics*. March 2018. Vol. 84, p. 350–355. DOI 10.1016/j.ultras.2017.12.001.

110. SEKI, Masanori, SOYAMA, Hitoshi, KOBAYASHI, Yuji, GOWA, Daisuke and FUJII, Masahiro. Rolling Contact Fatigue Life of Steel Rollers Treated by Cavitation Peening and Shot Peening. *Journal of Solid Mechanics and Materials Engineering*. 2012. Vol. 6, no. 6, p. 478–486. DOI 10.1299/jmmp.6.478.

111. KIM, Seong-Jong, HYUN, Koang-Yong and JANG, Seok-Ki. Effects of water cavitation peening on electrochemical characteristic by using micro-droplet cell of Al–Mg alloy. *Current Applied Physics*. September 2012. Vol. 12, p. S24–S30. DOI 10.1016/j.cap.2012.02.013.

112. JU, D.Y. and HAN, B. Investigation of water cavitation peening-induced microstructures in the near-surface layer of pure titanium. *Journal of Materials Processing Technology*. June 2009. Vol. 209, no. 10, p. 4789–4794. DOI 10.1016/j.jmatprotec.2008.12.006.

113. HE, Peiyu, LI, Fuzhu, GUO, Jun, CHEN, Shangshuang, GUO, Yuqin, WANG, Yun and TAN, Zhongrui. Research on the water cavitation peening process and mechanism of TC4 titanium alloy. *The International Journal of Advanced Manufacturing Technology*. January 2021. Vol. 112, no. 5–6, p. 1259–1269. DOI 10.1007/s00170-020-06566-2.

114. SRIVASTAVA, Madhulika, HLOCH, Sergej, GUBELJAK, Nenad, MILKOVIC, Marijana, CHATTOPADHYAYA, Somnath and KLICH, Jiri. Surface integrity and residual

stress analysis of pulsed water jet peened stainless steel surfaces. *Measurement*. September 2019. Vol. 143, p. 81–92. DOI 10.1016/j.measurement.2019.04.082.

115. SRIVASTAVA, Madhulika, HLOCH, Sergej, KREJCI, Lucie, CHATTOPADHYAYA, Somnath, GUBELJAK, Nenad and MILKOVIC, Marijana. Utilizing the water hammer effect to enhance the mechanical properties of AISI 304 welded joints. *The International Journal of Advanced Manufacturing Technology*. March 2022. Vol. 119, no. 3–4, p. 2317–2328. DOI 10.1007/s00170-021-08357-9.

116. LEHOCKA, Dominika, KLICH, Jiri, BOTKO, Frantisek, SIMKULET, Vladimir, FOLDYNA, Josef, KREJCI, Lucie, STORKAN, Zdenek, KEPIC, Jan and HATALA, Michal. Comparison of ultrasonically enhanced pulsating water jet erosion efficiency on mechanical surface treatment on the surface of aluminum alloy and stainless steel. *The International Journal of Advanced Manufacturing Technology*. August 2019. Vol. 103, no. 5–8, p. 1647–1656. DOI 10.1007/s00170-019-03680-8.

117. HLAVÁČEK, Petr, KRUML, Tomáš, FOLDYNA, Jozef, TOBIÁŠ, Jiří, MAN Jiří. Effect of Pulsating Water Jet Peening on 316L Stainless Steel. In: Water Jet 2015 – *Research Development, Applications.* October 2015.p.29–36. ISBN: 978-80-86407-56-2.

118. CHAN, Wai Luen and CHENG, Henry Kuo Feng. Hammer peening technology—the past, present, and future. *The International Journal of Advanced Manufacturing Technology*. January 2022. Vol. 118, no. 3–4, p. 683–701. DOI 10.1007/s00170-021-07993-5.

119. MALAKI, Massoud and DING, Hongtao. A review of ultrasonic peening treatment. *Materials & Design*. December 2015. Vol. 87, p. 1072–1086. DOI 10.1016/j.matdes.2015.08.102.

120. DELGADO, P., CUESTA, I.I., ALEGRE, J.M. and DÍAZ, A. State of the art of Deep Rolling. *Precision Engineering*. October 2016. Vol. 46, p. 1–10. DOI 10.1016/j.precisioneng.2016.05.001.

121. MOSTAFA, Ayman M., HAMEED, Mohamed F. and OBAYYA, Salah S. Effect of laser shock peening on the hardness of AL-7075 alloy. *Journal of King Saud University - Science*. October 2019. Vol. 31, no. 4, p. 472–478. DOI 10.1016/j.jksus.2017.07.012.

122. FAIRAND, B.P. and CLAUER, A.H. Effect of water and paint coatings on the magnitude of laser-generated shocks. *Optics Communications*. September 1976. Vol. 18, no. 4, p. 588–591. DOI 10.1016/0030-4018(76)90327-8.

123. FAIRAND, B. P., CLAUER, A. H., JUNG, R. G. and WILCOX, B. A. Quantitative assessment of laser-induced stress waves generated at confined surfaces. *Applied Physics Letters*. 15 October 1974. Vol. 25, no. 8, p. 431–433. DOI 10.1063/1.1655536.

124. FABBRO, R., FOURNIER, J., BALLARD, P., DEVAUX, D. and VIRMONT, J. Physical study of laser-produced plasma in confined geometry. *Journal of Applied Physics*. 15 July 1990. Vol. 68, no. 2, p. 775–784. DOI 10.1063/1.346783.

125. NAKANO, Hitoshi. Femtosecond Laser Peening of Stainless Steel. *Journal of Laser Micro/Nanoengineering*. April 2009. Vol. 4, no. 1, p. 35–38. DOI 10.2961/jlmn.2009.01.0007.

126. EBRAHIMI, Mohammad, AMINI, Saeid and MAHDAVI, Seyed Mohammad. The investigation of laser shock peening effects on corrosion and hardness properties of ANSI 316L stainless steel. *The International Journal of Advanced Manufacturing Technology*. February 2017. Vol. 88, no. 5–8, p. 1557–1565. DOI 10.1007/s00170-016-8873-0.

127. ZHOU, Liucheng, HE, Weifeng, LUO, Sihai, LONG, Changbai, WANG, Cheng, NIE, Xiangfan, HE, Guangyu, SHEN, XiaoJun and LI, Yinghong. Laser shock peening induced surface nanocrystallization and martensite transformation in austenitic stainless steel. *Journal of Alloys and Compounds*. January 2016. Vol. 655, p. 66–70. DOI 10.1016/j.jallcom.2015.06.268.

128. KASHAEV, Nikolai, VENTZKE, Volker, HORSTMANN, Manfred, CHUPAKHIN, Sergey, RIEKEHR, Stefan, FALCK, Rielson, MAAWAD, Emad, STARON, Peter, SCHELL, Norbert and HUBER, Norbert. Effects of laser shock peening on the microstructure and fatigue crack propagation behaviour of thin AA2024 specimens. *International Journal of Fatigue*. May 2017. Vol. 98, p. 223–233. DOI 10.1016/j.ijfatigue.2017.01.042.

129. LU, J.Z., WU, L.J., SUN, G.F., LUO, K.Y., ZHANG, Y.K., CAI, J., CUI, C.Y. and LUO, X.M. Microstructural response and grain refinement mechanism of commercially pure titanium subjected to multiple laser shock peening impacts. *Acta Materialia*. April 2017. Vol. 127, p. 252–266. DOI 10.1016/j.actamat.2017.01.050.

130. QIAO, Hongchao, ZHAO, Jibin and GAO, Yu. Experimental investigation of laser peening on TiAl alloy microstructure and properties. *Chinese Journal of Aeronautics*. April 2015. Vol. 28, no. 2, p. 609–616. DOI 10.1016/j.cja.2015.01.006.

131. HONGCHAO, Qiao. Experimental investigation of laser peening on Ti17 titanium alloy for rotor blade applications. *Applied Surface Science*. October 2015. Vol. 351, p. 524–530. DOI 10.1016/j.apsusc.2015.05.098.

132. KUMAR, Dharmesh, NADEEM AKHTAR, Syed, KUMAR PATEL, Anup, RAMKUMAR, J. and BALANI, Kantesh. Tribological performance of laser peened Ti–6Al–4V. *Wear*. January 2015. Vol. 322–323, p. 203–217. DOI 10.1016/j.wear.2014.11.016.

133. ZHANG, X.C., ZHANG, Y.K., LU, J.Z., XUAN, F.Z., WANG, Z.D. and TU, S.T. Improvement of fatigue life of Ti–6Al–4V alloy by laser shock peening. *Materials Science and Engineering: A*. June 2010. Vol. 527, no. 15, p. 3411–3415. DOI 10.1016/j.msea.2010.01.076.

134. ZHANG, Zhifen, DU, Zhengyao, QIN, Rui, LI, Geng and WEN, Guangrui. Surface hardness monitoring of laser shock Peening: Acoustic emission and key frame selection. *Measurement*. August 2022. Vol. 199, p. 111560. DOI 10.1016/j.measurement.2022.111560.

135. SOYAMA, Hitoshi and KORSUNSKY, Alexander M. A critical comparative review of cavitation peening and other surface peening methods. *Journal of Materials Processing Technology*. July 2022. Vol. 305, p. 117586. DOI 10.1016/j.jmatprotec.2022.117586.

136. KUMAGAI, Masayoshi, CURD, Matthew E., SOYAMA, Hitoshi, UNGÁR, Támas, RIBÁRIK, Gábor and WITHERS, Philip J. Depth-profiling of residual stress and microstructure for austenitic stainless steel surface treated by cavitation, shot and laser peening. *Materials Science and Engineering: A*. May 2021. Vol. 813, p. 141037. DOI 10.1016/j.msea.2021.141037.

137. WANG, Z.D., SUN, G.F., LU, Y., CHEN, M.Z., BI, K.D. and NI, Z.H. Microstructural characterization and mechanical behavior of ultrasonic impact peened and laser shock peened AISI 316L stainless steel. *Surface and Coatings Technology*. March 2020. Vol. 385, p. 125403. DOI 10.1016/j.surfcoat.2020.125403.

138. MURUGANANDHAN, R., MUGILVALAVAN, M., THIRUMAVALAVAN, K. and YUVARAJ, N. Investigation of water jet peening process parameters on AL6061-T6. *Surface Engineering*. 3 April 2018. Vol. 34, no. 4, p. 330–340. DOI 10.1080/02670844.2017.1394564.

139. WANG, Zhao, MA, Zhelun, CHEN, Tao, FAN, Cheng, YU, Tianbiao and ZHAO, Ji. Experimental investigation into the effect of process parameters on the Inconel 718 surface integrity for abrasive waterjet peening. *Surface and Coatings Technology*. February 2023. Vol. 454, p. 129186. DOI 10.1016/j.surfcoat.2022.129186.

140. BALAJI, D.S. and JEYAPOOVAN, T. Multi-objective optimization in abrasive water jet peening on AA6063 alloy. *Materials Today: Proceedings*. 2021. Vol. 45, p. 1928–1933. DOI 10.1016/j.matpr.2020.09.220.

141. LIU, Jiawei, HAN, Jingtao, LU, Ruilong, WANG, Yu and LIU, Cheng. Effect of abrasive water pressure on the surface layer characteristics of duplex stainless steel 2205. *Materials Research Express*. 1 April 2023. Vol. 10, no. 4, p. 046516. DOI 10.1088/2053-1591/accd3f.

142. SATHYAJITH, S., KALAINATHAN, S. and SWAROOP, S. Laser peening without coating on aluminum alloy Al-6061-T6 using low energy Nd:YAG laser. *Optics & Laser Technology*. February 2013. Vol. 45, p. 389–394. DOI 10.1016/j.optlastec.2012.06.019.

143. WHITEHOUSE, David. *Surfaces and their measurement*. 1. publ. London : HPS, 2002. ISBN 978-1-903996-01-0.

144. HAM, R. K. The determination of dislocation densities in thin films. *Philosophical Magazine*. September 1961. Vol. 6, no. 69, p. 1183–1184. DOI 10.1080/14786436108239679.

145. NISHIKAWA, S. and KIKUCHI, S. Diffraction of Cathode Rays by Mica. *Nature*. June 1928. Vol. 121, no. 3061, p. 1019–1020. DOI 10.1038/1211019a0.

146. DUDA, Richard O. and HART, Peter E. Use of the Hough transformation to detect lines and curves in pictures. *Communications of the ACM*. January 1972. Vol. 15, no. 1, p. 11–15. DOI 10.1145/361237.361242.

147. SLABAUGH, Gregory G. Computing Euler angles from a rotation matrix. January 1999.

148. NOLZE, Gert. Euler angles and crystal symmetry. *Crystal Research and Technology*. February 2015. Vol. 50, no. 2, p. 188–201. DOI 10.1002/crat.201400427.

149. MOUSSA, C., BERNACKI, M., BESNARD, R. and BOZZOLO, N. Statistical analysis of dislocations and dislocation boundaries from EBSD data. *Ultramicroscopy*. August 2017. Vol. 179, p. 63–72. DOI 10.1016/j.ultramic.2017.04.005.

150. RUGGLES, T.J., YOO, Y.S.J., DUNLAP, B.E., CRIMP, M.A. and KACHER, J. Correlating results from high resolution EBSD with TEM- and ECCI-based dislocation

microscopy: Approaching single dislocation sensitivity via noise reduction. *Ultramicroscopy*. March 2020. Vol. 210, p. 112927. DOI 10.1016/j.ultramic.2019.112927.

151. KIROLS, H.S., KEVORKOV, D., UIHLEIN, A. and MEDRAJ, M. The effect of initial surface roughness on water droplet erosion behaviour. *Wear*. November 2015. Vol. 342–343, p. 198–209. DOI 10.1016/j.wear.2015.08.019.

152. RAMULU, M., KUNAPORN, S., AROLA, D., HASHISH, M. and HOPKINS, J. Waterjet Machining and Peening of Metals. *Journal of Pressure Vessel Technology*. 1 February 2000. Vol. 122, no. 1, p. 90–95. DOI 10.1115/1.556155.

153. KUNAPORN, S., RAMULU, M. and HASHISH, M. Mathematical Modeling of Ultra-High-Pressure Waterjet Peening. *Journal of Engineering Materials and Technology*. 1 April 2005. Vol. 127, no. 2, p. 186–191. DOI 10.1115/1.1857934.

154. LEHOCKÁ, D., KLICHOVÁ, D., FOLDYNA, J., HLOCH, S., HVIZDOŠ, P., FIDES, M. and BOTKO, F. Comparison of the influence of acoustically enhanced pulsating water jet on selected surface integrity characteristics of CW004A copper and CW614N brass. *Measurement*. November 2017. Vol. 110, p. 230–238. DOI 10.1016/j.measurement.2017.07.005.

155. AHMAD, Zaki (ed.). *Recent Trends in Processing and Degradation of Aluminium Alloys*. Online. InTech, 2011. [Accessed 14 March 2024]. ISBN 978-953-307-734-5.

156. AROLA, D. and RAMULU, M. Material removal in abrasive waterjet machining of metals Surface integrity and texture. *Wear*. September 1997. Vol. 210, no. 1–2, p. 50–58. DOI 10.1016/S0043-1648(97)00087-2.

157. POLÁK, Jaroslav. *Cyclic plasticity and low cycle fatigue life of metals*. . Prag : Academia, 1991. ISBN 978-80-200-0008-8.

158. BAGHERIFARD, Sara and GUAGLIANO, Mario. Fatigue behavior of a low-alloy steel with nanostructured surface obtained by severe shot peening. *Engineering Fracture Mechanics*. February 2012. Vol. 81, p. 56–68. DOI 10.1016/j.engfracmech.2011.06.011.

159. MALEKI, Erfan, UNAL, Okan, GUAGLIANO, Mario and BAGHERIFARD, Sara. Analysing the Fatigue Behaviour and Residual Stress Relaxation of Gradient Nano-Structured 316L Steel Subjected to the Shot Peening via Deep Learning Approach. *Metals and Materials International*. January 2022. Vol. 28, no. 1, p. 112–131. DOI 10.1007/s12540-021-00995-8.

160. LEE, Byeong- Eun, RIU, Kap- Jong, SHIN, Se- Hyun and KWON, Soon- Bum. Development of a water droplet erosion model for large steam turbine blades. *KSME International Journal*. January 2003. Vol. 17, no. 1, p. 114–121. DOI 10.1007/BF02984292.

161. POLOPRUDSKÝ, Jakub, CHLUPOVÁ, Alice, ŠULÁK, Ivo, KRUML, Tomáš and HLOCH, Sergej. Surface and Subsurface Analysis of Stainless Steel and Titanium Alloys Exposed to Ultrasonic Pulsating Water Jet. *Materials*. 10 September 2021. Vol. 14, no. 18, p. 5212. DOI 10.3390/ma14185212.

162. Strengthening Effect after Disintegration of Stainless Steel Using Pulsating Water Jet. *Tehnicki vjesnik - Technical Gazette*. Online. August 2018. Vol. 25, no. 4. [Accessed 12 June 2023]. DOI 10.17559/TV-20170327134630.

163. KAMKAR, N., BRIDIER, F., JEDRZEJOWSKI, P. and BOCHER, P. Water droplet impact erosion damage initiation in forged Ti–6Al–4V. *Wear*. January 2015. Vol. 322–323, p. 192–202. DOI 10.1016/j.wear.2014.10.020.

164. ISO 6507-1:2005. *Metallic materials - Vickers hardness test - Part 1: Test method*.

165. BAGHERIFARD, Sara, SLAWIK, Sebastian, FERNÁNDEZ-PARIENTE, Inés, PAULY, Christoph, MÜCKLICH, Frank and GUAGLIANO, Mario. Nanoscale surface modification of AISI 316L stainless steel by severe shot peening. *Materials & Design*. July 2016. Vol. 102, p. 68–77. DOI 10.1016/j.matdes.2016.03.162.

166. HOLMBERG, Jonas, BERGLUND, Johan, WRETLAND, Anders and BENO, Tomas. Evaluation of surface integrity after high energy machining with EDM, laser beam machining and abrasive water jet machining of alloy 718. *The International Journal of Advanced Manufacturing Technology*. February 2019. Vol. 100, no. 5–8, p. 1575–1591. DOI 10.1007/s00170-018-2697-z.

167. ZHUANG, Dong-Dong, ZHANG, Shu-Hao, LIU, Hai-Xia and CHEN, Jie. Cavitation erosion behaviors and damage mechanism of Ti-Ni alloy impacted by water jet with different standoff distances. *Engineering Failure Analysis*. September 2022. Vol. 139, p. 106458. DOI 10.1016/j.engfailanal.2022.106458.

168. MIESZALA, M., TORRUBIA, P. Lozano, AXINTE, D.A., SCHWIEDRZIK, J.J., GUO, Y., MISCHLER, S., MICHLER, J. and PHILIPPE, L. Erosion mechanisms during abrasive waterjet machining: Model microstructures and single particle experiments. *Journal of Materials Processing Technology*. September 2017. Vol. 247, p. 92–102. DOI 10.1016/j.jmatprotec.2017.04.003.

169. CARNEIRO, Íris and SIMÕES, Sónia. Recent Advances in EBSD Characterization of Metals. *Metals*. 13 August 2020. Vol. 10, no. 8, p. 1097. DOI 10.3390/met10081097.

170. KONIJNENBERG, P.J., ZAEFFERER, S. and RAABE, D. Assessment of geometrically necessary dislocation levels derived by 3D EBSD. *Acta Materialia*. October 2015. Vol. 99, p. 402–414. DOI 10.1016/j.actamat.2015.06.051.

171. MOUSSA, C, BERNACKI, M, BESNARD, R and BOZZOLO, N. About quantitative EBSD analysis of deformation and recovery substructures in pure Tantalum. *IOP Conference Series: Materials Science and Engineering*. 7 August 2015. Vol. 89, p. 012038. DOI 10.1088/1757-899X/89/1/012038.

172. LIANG, X.Z., DODGE, M.F., JIANG, J. and DONG, H.B. Using transmission Kikuchi diffraction in a scanning electron microscope to quantify geometrically necessary dislocation density at the nanoscale. *Ultramicroscopy*. February 2019. Vol. 197, p. 39–45. DOI 10.1016/j.ultramic.2018.11.011.

173. WISNIEWSKI, Wolfgang, SAAGER, Stefan, BÖBENROTH, Andrea and RÜSSEL, Christian. Experimental evidence concerning the significant information depth of electron backscatter diffraction (EBSD). *Ultramicroscopy*. February 2017. Vol. 173, p. 1–9. DOI 10.1016/j.ultramic.2016.11.004.

174. FITZPATRICK, M E, FRY, A T, HOLDWAY, P, KANDIL, F A, SHACKLETON, J and SUOMINEN, L. NPL good practice guide no. 52: determination of residual stresses by

X-ray diffraction Vol. 2 National Physical Laboratory Teddington, Middlesex, United Kingdom) September 2005. ISSN 1744-3911.

175. ZRIBI, Zahra, KTARI, Hassan Houcin, HERBST, Frédéric, OPTASANU, Virgil and NJAH, Nabil. EBSD, XRD and SRS characterization of a casting Al-7wt%Si alloy processed by equal channel angular extrusion: Dislocation density evaluation. *Materials Characterization*. July 2019. Vol. 153, p. 190–198. DOI 10.1016/j.matchar.2019.04.044.

176. LANGFORD, Richard M. Focused ion beams techniques for nanomaterials characterization. *Microscopy Research and Technique*. July 2006. Vol. 69, no. 7, p. 538–549. DOI 10.1002/jemt.20324.

9. List of symbols and abbreviations

Abbreviation	**Meaning**
AWJ	Abrasive water jet
AWJP	Abrasive water jet peening
BCC	Body centred cubic
CAS	Czech Academy of Sciences
CWJ	Continuous water jet
EBSD	Electron back scattered diffraction
EDM	Electrical discharge machining
FCC	Face centred cubic
FSE	Forward scattered electrons
GROD	Grain reference orientation deviation
IPF	Inverse pole figure
KAM	Kernel average misorientations
LSP	Laser shock peening
MUD	Multiples of uniform density
NIR	Non-indexed region
PF	Pole figure
PWJ	Pulsating water jet
PWJP	Pulsating water jet peening
Rpm	Rotations per minute
SP	Shot peening
UCP	Ultrasonic cavitation peening
UIP	Ultrasonic impact peening
UPT	Ultrasonic peening treatment
WJ	Water jet
WJCP	Water jet cavitation peening
WJP	Water jet peening

Symbol	**Basic dimension**	**Meaning**
C	*m/s*	Velocity of compression wave in liquid
C_s	*m/s*	Velocity of compression wave in solid
d	*m*	Nozzle diameter
E_k	*J*	Kinetic energy
E_p	*J*	Potential energy
f	*Hz*	Frequency
g	m/s^2	Gravity constant
h	*m*	Height, depth
Δh	*m*	Thickness of water layer
I_d	*i/m*	Impact distribution
I_n	*i*	Number of cluster impacts
p	*Pa*	Pressure
p_{at}	*Pa*	Atmospheric pressure
p_S	*Pa*	Stagnation pressure
p_{WH}	*Pa*	Water hammer pressure
Q	m^3/s	Flow rate
r	*m*	Radius

Ra	m	Profile arithmetic mean height
Rku	-	Kurtosis
Rp	m	Maximum profile peak height
Rsk	-	Skewness
Rv	m	Maximum profile valley depth
Rz	m	Profile maximum height
t	s	Exposure time
T	s	Duration of water hammer effect
v	m/s	Velocity
v_0	m/s	Effective water-jet velocity
v_{0th}	m/s	Theoretical velocity of exiting water jet
v_{pipe}	m/s	Focus flow velocity
V_r	m^3	Volume removed
V_w	m^3	Theoretical water cluster volume
x_0	m	Radius of area of water hammer effect
z	m	Standoff distance
β	Pa^{-1}	Compressibility
ε_a	-	Strain amplitude
λ_c	m	Cut-off frequency
μ	-	Coefficient of momentum losses
ρ	kg/m^3	Density

10. List of publications in impacted journals

H index reached to date 2.4.2024 in Scopus/WOS: 4/4

Number of citations reached to date 2.4.2024 in Scopus/WOS 56/51:

Publications in journals with impact factor

1) POLOPRUDSKÝ, Jakub, GAMANOV, Štěpán, CHLUPOVÁ, Alice, KLICHOVÁ, Dagmar, NAG, Akash, STOLÁRIK, Gabriel and HLOCH, Sergej. Water droplet erosion assessment in the initial stages on AISI 316 L using kernel average misorientation. Tribology International. March 2024. Vol. 191, p. 109165. DOI 10.1016/j.triboint.2023.109165.(D1, Elsevier)
2) POLOPRUDSKÝ, Jakub, NAG, Akash, KRUML, Tomáš and HLOCH, Sergej. Effects of liquid droplet volume and impact frequency on the integrity of Al alloy AW2014 exposed to subsonic speeds of pulsating water jets. Wear. January 2022. Vol. 488–489, p. 204136. DOI 10.1016/j.wear.2021.204136. (Q1, Elsevier)
3) SOJKOVÁ, Tereza, GRÖGER, Roman, POLOPRUDSKÝ, Jakub, KUBĚNA, Ivo, SCHNEEWEISS, Oldřich, SOJKA, Martin, ŠIŠKA, Zuzana, PONGRÁCZ, Jakub and PIZÚROVÁ, Naděžda. Kinetics of spontaneous phase transitions from wüstite to magnetite in superparamagnetic core–shell nanocubes of iron oxides. Nanoscale. 2024. Vol. 16, no. 11, p. 5551–5560. DOI 10.1039/D3NR06254F. (Q1 Royal Society of Chemistry)
4) HLOCH, Sergej, SVOBODOVÁ, Jaroslava, SRIVASTAVA, Ashish Kumar, SRIVASTAVA, Madhulika, POLOPRUDSKÝ, Jakub and NAG, Akash. Submerged pulsating water jet erosion of ductile material. Wear. February 2024. Vol. 538–539, p. 205243. DOI 10.1016/j.wear.2024.205243. (Q1, Elsevier)
5) HLOCH, Sergej, POLOPRUDSKÝ, Jakub, ŠIŠKA, Filip, BABINSKÝ, Tomáš, NAG, Akash, CHLUPOVÁ, Alice and KRUML, Tomáš. Erosion development in AISI 316L stainless steel under pulsating water jet treatment. Engineering Science and Technology, an International Journal. February 2024. Vol. 50, p. 101630. DOI 10.1016/j.jestch.2024.101630. (Q1, Elsevier)
6) ŠULÁK, Ivo, CHLUPOVÁ, Alice, POLOPRUDSKÝ, Jakub and SVOBODA, Jiří. Cyclic plastic response of rotary swaged Fe-14Cr-10Al-4Y2O3 ODS alloy at 1000–1200 °C. Materials Characterization. January 2024. Vol. 207, p. 113519. DOI 10.1016/j.matchar.2023.113519. (Q1, Elsevier)
7) ŘÍHA, Zdeněk, ZELEŇÁK, Michal, NAG, Akash, POLOPRUDSKÝ, Jakub, KRUML, Tomáš and HLOCH, Sergej. A study of the erosion characteristics of an EN AE-6060 aluminium alloy processed using middle and high power continuous and modulated water jets. Wear. January 2024. Vol. 536–537, p. 205154. DOI 10.1016/j.wear.2023.205154. (Q1, Elsevier)
8) STOLÁRIK, Gabriel, KLICHOVÁ, Dagmar, POLOPRUDSKÝ, Jakub, NAG, Akash and HLOCH, Sergej. Assessment of surface irregularities created by controlled liquid droplet on the surface of stainless steel AISI 304L. Engineering Science and Technology, an International Journal. November 2023. Vol. 47, p. 101558. DOI 10.1016/j.jestch.2023.101558. (Q1, Elsevier)
9) ŘÍHA, Zdeněk, ZELEŇÁK, Michal, KRUML, Tomáš and POLOPRUDSKÝ, Jakub. Comparison of the disintegration abilities of modulated and continuous water jets. Wear. August 2021. Vol. 478–479, p. 203891. DOI 10.1016/j.wear.2021.203891. (Q1, Elsevier)

10) POLOPRUDSKÝ, Jakub, CHLUPOVÁ, Alice, ŠULÁK, Ivo, KRUML, Tomáš and HLOCH, Sergej. Surface and Subsurface Analysis of Stainless Steel and Titanium Alloys Exposed to Ultrasonic Pulsating Water Jet. Materials. 10 September 2021. Vol. 14, no. 18, p. 5212. DOI 10.3390/ma14185212. (Q2, MDPI)

11) KLICHOVA, Dagmar, NAG, Akash, POLOPRUDSKÝ, Jakub, FOLDYNA, Josef, PUDE, Frank, SITEK, Libor and HLOCH, Sergej. Utilising of water hammer effect for surface roughening of Ti6Al4V. The International Journal of Advanced Manufacturing Technology. June 2023. Vol. 126, no. 11–12, p. 5633–5647. DOI 10.1007/s00170-023-11521-y. (Q2, Springer)

12) POLOPRUDSKÝ, Jakub, CHLUPOVÁ, Alice, ŠULÁK, Ivo and OBRTLÍK, Karel. Effect of heat treatment on the microstructure and fatigue behaviour of AISI 4130 steel. Kovove Materialy-Metallic Materials. Online. 31 October 2023. Vol. 61, no. 6. DOI 10.31577/km.2023.6.401. (Q4, Institute of Materials and Machine Mechanics, Slovak Academy of Sciences, Bratislava)

Published conference proceedings

1) VRAŽINA, Tomáš, ŠULÁK, Ivo, POLOPRUDSKÝ, Jakub, ZÁBRANSKÝ, Karel, GEJDOŠ, Pavel, HADRABA, Hynek and ČELKO, Ladislav. Influence of the Deposition Parameters on Microstructure and Properties of HVOF Sprayed WC-Crc-Ni Coating. In : METAL 2022. Online. 2022. p. 487–492. [Accessed 2 July 2023]. DOI 10.37904/metal.2022.4421.

2) POLOPRUDSKÝ, Jakub, CHLUPOVÁ, Alice, KRUML, Tomáš and HLOCH, Sergej. Identification of Local Microplasticity on Ti6Al4V After Impingement of Periodically Acting Water Clusters. In : HLOCH, Sergej, KLICHOVÁ, Dagmar, PUDE, Frank, KROLCZYK, Grzegorz M. and CHATTOPADHYAYA, Somnath (eds.), Advances in Manufacturing Engineering and Materials II. Online. Cham : Springer International Publishing, 2021. p. 63–74. Lecture Notes in Mechanical Engineering. ISBN 978-3-030-71955-5.

3) POLOPRUDSKÝ, Jakub, CHLUPOVÁ, Alice, KRUML, Tomáš, HLOCH, Sergej, HLAVÁČEK, Petr and FOLDYNA, Josef. Effect of Standoff Distance on the Erosion of Various Materials. In : KLICHOVÁ, Dagmar, SITEK, Libor, HLOCH, Sergej and VALENTINČIČ, Joško (eds.), Advances in Water Jetting. Online. Cham : Springer International Publishing, 2021. p. 164–171. Lecture Notes in Mechanical Engineering. ISBN 978-3-030-53490-5.

Conference speaking engagements

2019	Water jet 2019	CZ
2021	Water jet 2021	CZ
2022	ICMEM 2022	SK
2022	Metal 2022	CZ
2023	ICMEM 2023	SK
2023	MK2	CZ
2023	Water jet 2023	CZ
2023	ICMFM-XXI	CZ